Master Thesis

Linear Induction Motor (LIM) for Hyperloop Pod Prototypes

Author(s):
Timperio, Christopher

Publication Date:
2018-07

Permanent Link:

https://doi.org/10.3929/ethz-b-000379531 →

ETH zürich

Linear Induction Motor (LIM) for Hyperloop Pod Prototypes

MASTER THESIS

In collaboration with:

Presented by: Christopher Louis Timperio

Supervised by: Prof. Dr. Jasmin Smajic

Prof. Dr. Juerg Leuthold

swissloop

July 2018

Institute of Electromagnetic Fields (IEF)

This page is intentionally left blank.

LINEAR INDUCTION MOTOR (LIM) FOR HYPERLOOP POD PROTOTYPES

A thesis submitted to attain the degree of

MASTER OF SCIENCE of ETH ZÜRICH

(MSc ETH Zürich)

presented by

CHRISTOPHER LOUIS TIMPERIO

BSc ECE, Georgia Institute of Technology

born on 17.12.1990

United States of America

accepted on the recommendation of

Prof. Dr. Jasmin Smajic, examiner

Prof. Dr. Juerg Leuthold, co-examiner

July 2018

Institute of Electromagnetic Fields (IEF)

This page is intentionally left blank.

Eidgenössische Technische Hochschule Zürich
Swiss Federal Institute of Technology Zurich

Declaration of originality

The signed declaration of originality is a component of every semester paper, Bachelor's thesis, Master's thesis and any other degree paper undertaken during the course of studies, including the respective electronic versions.

Lecturers may also require a declaration of originality for other written papers compiled for their courses.

I hereby confirm that I am the sole author of the written work here enclosed and that I have compiled it in my own words. Parts excepted are corrections of form and content by the supervisor.

Title of work (in block letters):

Authored by (in block letters):

For papers written by groups the names of all authors are required.

Name(s):	**First name(s):**

With my signature I confirm that

- I have committed none of the forms of plagiarism described in the 'Citation etiquette' information sheet.
- I have documented all methods, data and processes truthfully.
- I have not manipulated any data.
- I have mentioned all persons who were significant facilitators of the work.

I am aware that the work may be screened electronically for plagiarism.

Place, date	**Signature(s):**

For papers written by groups the names of all authors are required. Their signatures collectively guarantee the entire content of the written paper.

This page is intentionally left blank.

Table of Contents

Abstract

Mobility is one of the main dilemmas facing a sustainable, clean-energy future. How can people and cargo be transported over long distances, without expending large amounts of fossil fuel energies or producing a large carbon footprint? How can this be done quickly and efficiently? Finding a mode of transportation which is energy-efficient, inexpensive, and even offers passenger transport is the task which the Swissloop team is striving towards each day. We as a team are currently focused on building the first ever Swiss solution for the Hyperloop. We are proud to say that our Swissloop product aims to be the fastest form of ground transportation ever conceived.

Swissloop's long term vision is to find ways to propel its pod capsules at speeds in excess of 1,000 km/h or 600 mi/h, while at the same time, having the smallest impact possible on our environment. These incredibly fast, yet energy-efficient ground speeds are to be realized by means of a magnetic linear accelerator. Therefore, we at Swissloop are researching and developing a linear induction motor prototype to be the foundation for future high-speed linear propulsion drives for Hyperloop-like systems.

Developing an efficient yet powerful Linear Induction Motor (LIM) is key to Swissloop's future as a sustainable Hyperloop transportation company. Passenger and cargo capsules need to be accelerated via some form of a high-speed linear accelerator – and a LIM is believed to be one of the best options for such a system. Before such a feat can be accomplished, scalable prototype motors should be developed in the short to medium term to help understand and formulate future, more complex linear accelerator systems. Therefore, the aim of the thesis is to develop a prototype LIM – providing Swissloop with a first iteration of a sustainable and efficient, yet powerful linear drive system.

"I could spend years trying to discover the origin of these mystic forces of electromagnetism, but as an engineer I haven't got time to do this." October 1972

Professor Eric Roberts Laithwaite – "Father of Maglev"

(1921 – 1997)

1 Introduction

The need to revolutionize current transportation systems towards a faster, more energy-efficient and environmentally sustainable solution will be one of the defining goals of this generation. When thinking of transport, a loss of time, crowded trains with delays, cancelled flights, missed connections, traffic jams on packed freeways, pollution and an overall unpleasant obstacle come to mind. The most common mode of transport today is the automobile or car. It's reliable, convenient, gets us to where we need to be in a relatively short time span, and is generally affordable for the average middle-class family. However, the most obvious and well-known downside of the car, is soul-crushing traffic.

In addition to the car, the other two most popular modes of transport include trains and planes. Railways are efficient and simple to arrange travel with, but tend to arrive slow to the destination, when compared with planes or cars. Air travel is known for its negative impact on the environment and airport security is probably one of the most dreadful encounters to experience. Each have their obvious downsides, however, they have become the norm in our current way of thinking about transport, such as Figure 1.1.

Fig. 1.1: Traffic Congestion – one of the main components leading to a rise in global Greenhouse Gas Emissions [1]

Besides the notion that transport with current technologies is an endurance which causes unwanted stress in an already stressful world, a larger and arguably more important issue is the heavy burden of pollutants on our environment created from existing transportation systems. One could argue that the world currently faces a climate change pandemic caused by the rise in greenhouse gases directly tied to transportation systems. An article from the BBC discussed the future of transport and what possible future transportation systems could look like: it was stated that by 2050 transport emissions

are projected to double due to a strong increase in demand for cars in developing countries. There could be as many as 2.5 billion cars on the road at that time, with most of them concentrated in large cities [2]. More cars would mean huge increases in the amount of global carbon emissions.

The Organization for Economic Co-operation and Development (OECD) conducted a study in 2010, which found that global carbon levels have reached 30.6 gigatonnes, and that by 2050, current greenhouse gas emissions will increase by another 50% [3]. The OECD also projects that atmospheric concentration of greenhouse gas emissions will reach almost 685 parts per million (ppm) CO2-equivalents by 2050. This amount is well over the concentration level of 450 ppm, which is the upper bound for having a 50% chance of stabilizing the climate at a 2°C global average temperature increase [3]. Transportation systems are one of the leading causes of this ever-increasing concentration of greenhouse gas emissions.

The U.S. Global Change Research Program, which includes federal government organizations such as NASA, NOAA, DoD, Dept. of Transportation, Dept. of Commerce, Dept. of Energy, and other U.S. federal organizations, – have launched a National Climate Assessment with the sole purpose of assessing and summarizing the impacts of climate change on the United States, now and into the future. The assessment stated that current transportation systems contribute to changes in the climate through emissions [1]. In 2010, the U.S. transportation sector accounted for 27% of total U.S. greenhouse gas emissions, with passenger cars and trucks accounting for 65% of that total. Furthermore, petroleum accounts for 93% of the nation's transportation energy use [1]. These findings indicate that policies and behavioral changes – aimed at reducing greenhouse gas emissions – will have significant implications for the various components of future transportation sectors.

As one studies the topic of current transportation systems, it becomes very clear, that if the goal is a sustainable future – one in which greenhouse gas emissions are decreasing instead of increasing – a new mode of transportation is required. For example, a transportation system which at its core, operates on a clean propulsion technology. Such a solution would need to be both economically viable into the long term and environmentally sustainable – producing low or no carbon emissions.

MunichRe; one of the world's largest insurance companies has recently performed a comprehensive risk analysis study on Hyperloop Transportation Technologies (HTT) – one of the leading Hyperloop companies focusing on passenger and cargo transport – to see if the overarching Hyperloop technology is feasible. They not only evaluated the company itself, but also the many risks and challenges in developing a full-scale Hyperloop system. After evaluating the company and its core competencies, they came to the conclusion that the Hyperloop technology is in indeed feasible, and also insurable in the medium term [4]. Also stated in [4]; "The analysis constitutes a milestone for the future success of HTT's Hyperloop technology and of the company itself." Having a world-renowned insurance company classify the Hyperloop technology as feasible and state that a future based on the technology's success is possible, is extremely optimistic and promising. Some renderings of what a possible Hyperloop future might look like – as imagined by HTT – can be seen below in Figure 1.2.

Fig. 1.2: Hyperloop Transportation Technologies (HTT) renderings of a possible future Hyperloop System – declared feasible and insurable by Munich Re [4]

A Hyperloop system such as the one deemed feasible my Munich Re, could very well be the solution to this generations transportation dilemma. This new energy-efficient form of travel could transport passengers and goods in capsules travelling at very high speeds in a low-pressure environment using a form of linear electric propulsion. Passengers and cargo would arrive at their destination faster and at a lower emissions cost, than any other transportation method currently available.

Therefore, the aim of this thesis will be to research a powerful new high-speed, yet efficient linear electric drive system to be the principal propulsion mechanism at the center of this new transportation technology. Creating such a novel energy efficient and powerful motor is in and of itself a challenge, however, such an electric drive must also operate in a low-pressure environment. This added design criterion makes the design of such a motor even more challenging.

Nonetheless, it appears such a linear motor is greatly needed at the moment. In particular, the motor appears to be the only technology within the Hyperloop which is not fully yet solved – and is therefore hindering the deployment of a fully-scaled system. The linear electric motor is also the central technology around which the Hyperloop is based, and represents the main propulsion mechanism driving the technology onward.

For this reason, this thesis focuses on the development of a linear electric motor, which as the name suggests, provides the linearly directed movement necessary for Hyperloop-like systems. Therefore,

this thesis offers a prototype design of a linear induction motor (LIM) with the potential to be the foundation for future linear motor development for the Hyperloop. A LIM could be scaled up and deployed into future full-scale Hyperloop systems. Further explanation into why a linear induction motor has been chosen, is discussed further in Appendix A. Several iterations of the design have been studied and simulated, and an optimized version has been selected. The final LIM that has been built, has also been optimized for speed and performance, on a specified track.

The linear motor presented here has been designed and manufactured in Switzerland. It has been designed to operate at approximately half the speed of a full-scale Hyperloop: 500 km/h. It weighs a total of 80kg and generates a peak thrust of 4.69kN. This yields a thrust-to-weight ratio of 3 – similar to that of the Space Shuttle.

The motor is planned to be mounted onto a prototype testing Pod weighing roughly 250kg. This testing Pod comes complete with avionics, telemetry, stability and braking systems. This means that the required telemetry data from sensors can be collected without added engineering. The mechanical design is also complete, and the Pod runs well on the selected track. After testing on an open-air test track facility in Dübendorf Switzerland, top speeds will be measured and recorded.

Additionally, the motor's operation will be tested in a low-pressure environment of pressurized conditions around 8mbar. Together with a design top speed of 500 km/h, a thrust-to-weight ratio of 3 and low-pressure operation, this linear induction motor prototype is the fastest, most powerful, robust, and efficient LIM prototype to date – for the application of the Hyperloop.

1.1 Project Background – The Hyperloop Concept

The Hyperloop concept as it is known today, was introduced back in 2013 by Elon Musk [5]. Musk talked about a cheaper, faster and more environmentally friendly alternative to the roughly $70 billion USD California high-speed rail project, and introduced the Hyperloop; as a fifth mode of transportation [5]. To which – if developed properly – could revolutionize cargo and passenger transportation and travel as we know it today. A sketch of the original Hyperloop idea from Musk can be seen below in Figure 1.3.

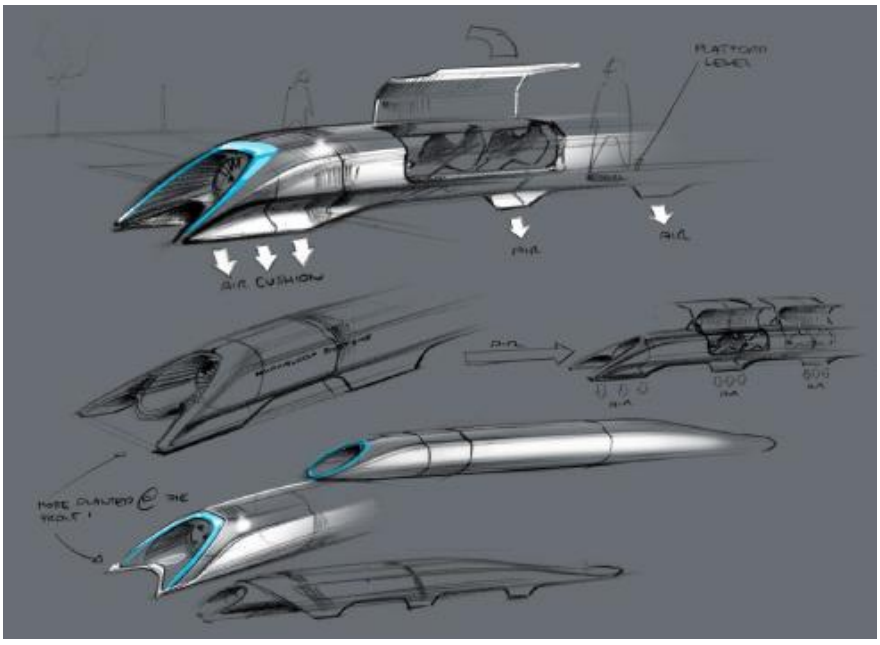

Fig. 1.3: Early Hyperloop Sketch [5]

Musk calculated that a Hyperloop system would offer the lowest energy per passenger per journey travel of any current known transportation technology [5]. As a consequence, realization of such a system would redefine the barriers of time and distance. This energy cost breakdown can be seen below in Figure 1.4 for an example route between Los Angeles and San Francisco: the Hyperloop clearly consumes less energy than the other existing modes of transportation.

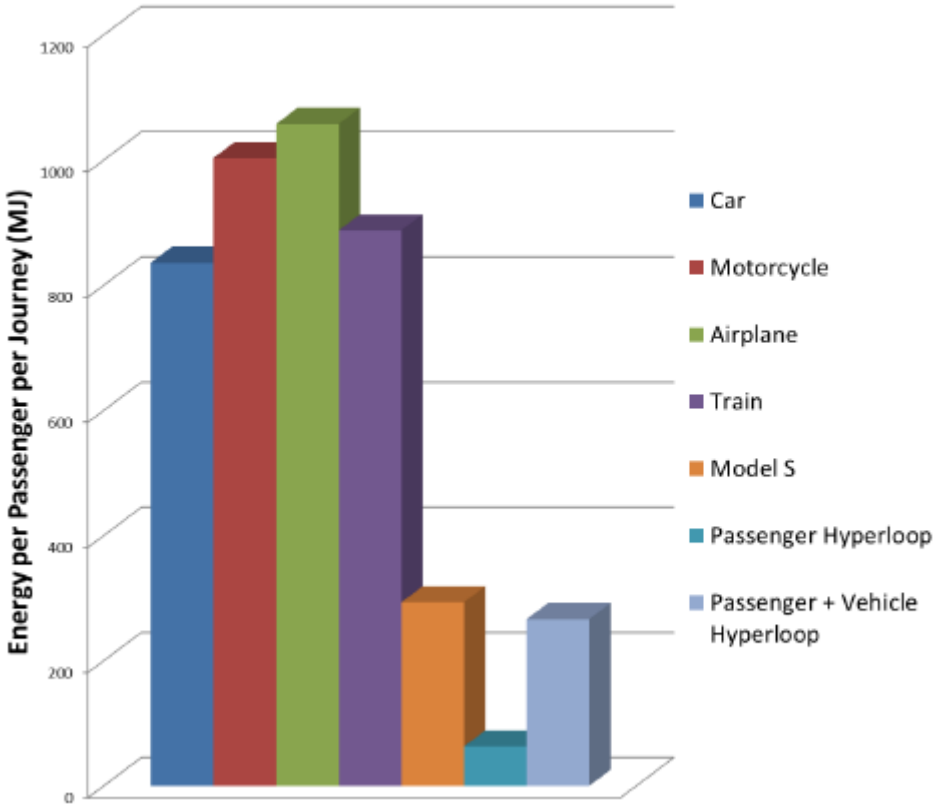

Fig. 1.4: Energy cost per passenger for a journey between Los Angeles and San Francisco for various modes of transport [5]

The only other system that comes close to matching the low energy requirements of Hyperloop is the fully electric Tesla Model S [5]. The reason the Hyperloop would be an ideal alternative for high-speed transportation comes down to its core technologies – which can be broken down into three main facets.

1. Vacuum or Low-pressure Environment: considerable reduction of air drag allows for smooth travel with speeds of up to 1,000 km/h. The energy required to sustain this low-pressure environment can be created by the solar panels lining the surface of the Hyperloop tube, creating an energy-independent system [5].
2. Levitation or Hovering: further reduction of the drag on the vehicle is achieved by removing the rolling resistance on the wheels and stress to bearings at high speeds through contact-less gliding. Passive, emission-free magnets or air bearings under the vehicle will be the enabling technology. Both methods are emission-free and consume little to no energy.
3. High-speed and Efficient Linear Accelerator: the acceleration mechanism propels vehicles or pods at high speeds, while having the least impact possible on our environment.

These three fundamental technologies make the Hyperloop an attractive choice for a future transportation solution. Although it seems appealing to replace all modes of transport with Hyperloop-like systems, the Hyperloop is only an ideal choice for certain cases. Situations that would benefit most would be transport between cities having very high frequency travel and on routes below 1500 km or 900 miles in separation [5]. In these instances, use of a Hyperloop-like system would greatly optimize travel and decrease the frequency of dramatic delays due to overpopulated areas, traffic jams, and the unnecessary added pollutants to our carbon footprint. However, for longer distances, it appears as though air travel is still most advantageous.

Although Elon Musk has recently pioneered this technology, and popularized the idea to the mainstream public, the idea of traveling at high speeds inside evacuated tunnels dates back to even the 19th century. Inventors such as Alfred Beach – most notably known for Beach Pneumatic Transit, which was New York City's first attempt at a subway – pictured a future where commuting could be both fast and reliable [6]. More specifically, Beach thought to combine the efficiency of modern-day railway systems with the speed of air travel, while at the same time, keeping environmental impact to a minimum. However, Musk re-energized the idea, and initiated a movement with the public which in turn, has brought this idea of the Hyperloop closer to fruition. A sketch of Beach's idea for the Beach Pneumatic Transit NYC railway line can be seen below in Figure 1.5.

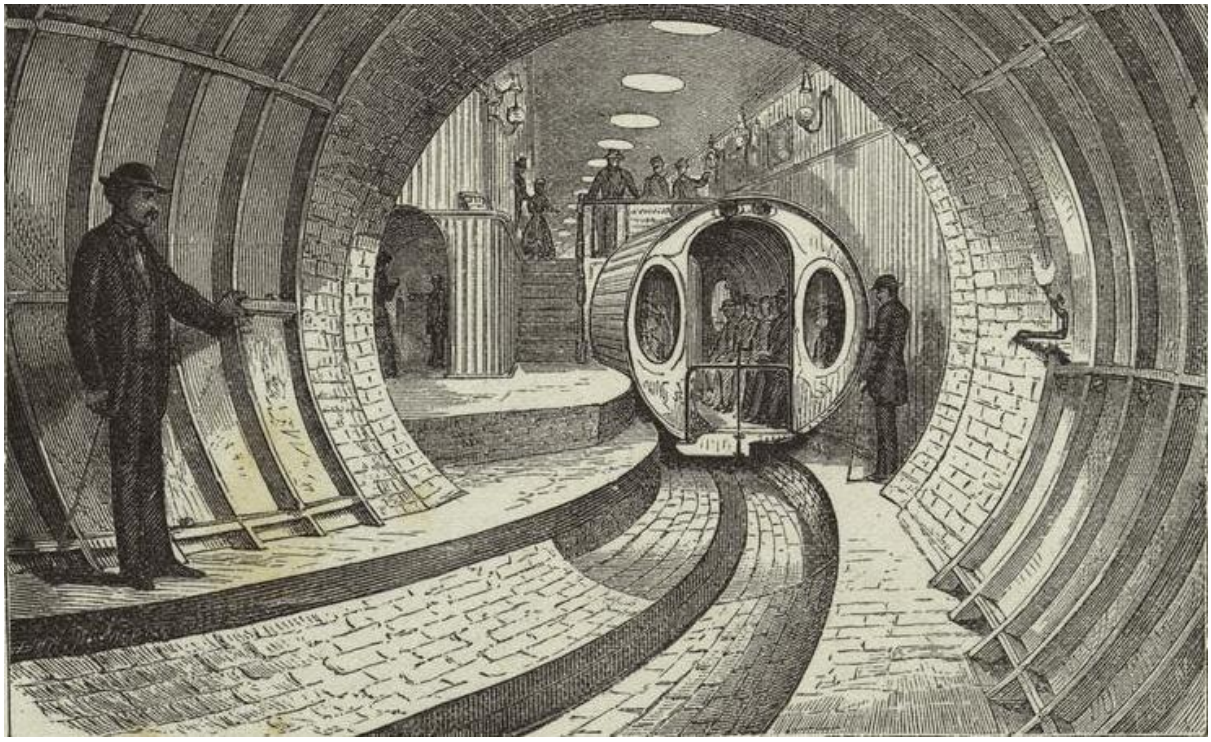

Fig. 1.5: Beach Pneumatic Transit NYC Underground Railway – showing a vehicle docked at a station [6]

1.2 Project Motivation

It was stated above that the main factor holding back the deployment of a full-scale Hyperloop is the development of a powerful, yet efficient linear drive. Upon solving this technological issue, there is no reason why Hyperloop systems can't begin deployment around the globe.

A fast and very public way to display the feasibility of the technology and its existence, is a live test or demonstration of the motor operating in a Hyperloop-like scenario. Such a venue already exists at SpaceX Headquarters in Hawthorne, California; as the official *SpaceX Hyperloop Pod Competition* [7].

This competition is open to university students all over the world, giving them the opportunity to develop and test Hyperloop Pod prototypes, and Hyperloop technology in general, under the guidance of experienced SpaceX engineers. It's an engineering competition which encourages students to get involved with and help grow the principal components behind the Hyperloop technology (such as its key propulsion or levitation systems). Growing the different technologies, helps drive the overall goal of bringing the Hyperloop closer to reality. The SpaceX Hyperloop tube can be seen below in Figure 1.6, and a technical drawing of the inside cross-section of 1.25km long tube and I-beam track can be seen below in Appendix B, [7].

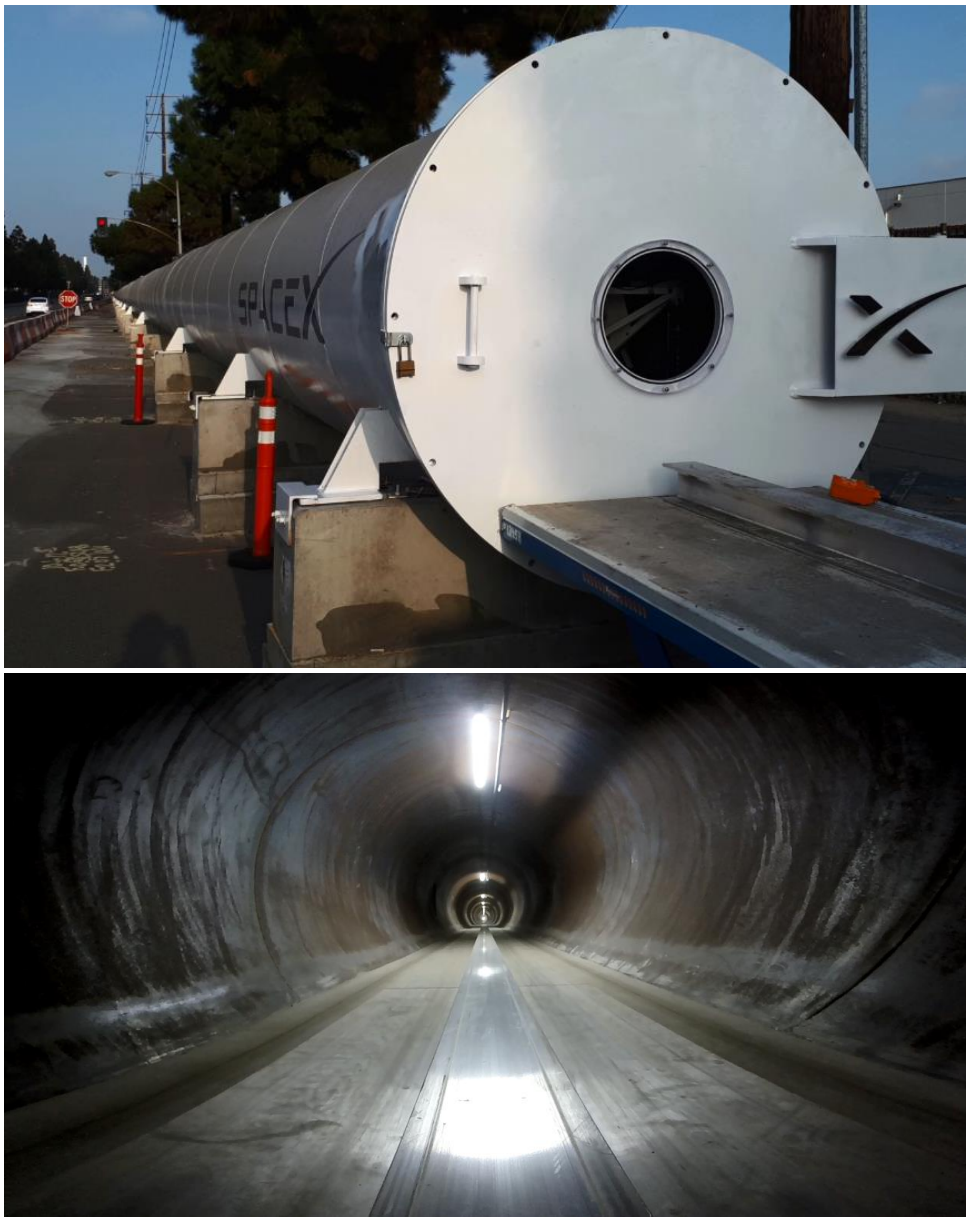

Fig. 1.6: SpaceX Hyperloop Tube in Hawthorne, California; outside (above) and inside (below)

Another useful element of the competition is the added design constraint of a fixed track geometry – which simplifies the design process as it is one less detail to consider. This means that the motor was designed and built around an already existing design for a Hyperloop-like track. Using this existing design is an important point since an endeavor of such size is estimated to cost in the tens of millions [4]. Therefore, the most cost-effective solution is to simply use an already designed and built track.

This also means, the motor can be brought to any one of the numerous testing facilities that uses this common track geometry, and the motor system can be tested with ease.

Therefore, the competition is the perfect test bench to test and measure such a prototype motor as the one developed in this thesis. This standardization ensures the availability of a known track to test the motor upon its completion. In addition to the SpaceX tube, which can be fully evacuated down to low-pressures, there is also open-air test track at the Swissloop testing facilities in Dübendorf Switzerland. The test track at the Dübendorf testing facility can be seen below in Figure 1.7, and the technical drawing of this track layout can be seen in Appendix C.

Fig. 1.7: Test Track at Dübendorf Testing Facility

This test track can be used to test the linear motor in ambient pressure before testing inside a more realistic Hyperloop tube – such as the SpaceX tube – which can operate under a low-pressure environment.

Using such test tracks will help validate the motor design, and optimize performance and efficiency through such testing – therefore reaching the speed goal of 500 km/h. If this speed goal is reached here – in a university thesis – there is no telling what could be accomplished within a few years of additional development.

In addition to the incentive of using the Hyperloop tube at SpaceX as a test bench for the prototype linear motor, the competition also provides an open and transparent viewing of the most current Hyperloop technology to the public. A competition with such a large audience will help grow the overall Hyperloop technology faster and make the Hyperloop more realistic and deployable.

Therefore, another goal of this thesis to inform the public about linear induction motors. Since the linear motor is the key technology behind making a sustainable and efficient new mode of transportation possible, it seems unfair to keep this technology hidden from those who might be able to even further advance it.

1.3 State of the Art

The state of the art can be broken into two different categories; 1) Complete *Linear Induction Motors* designed specifically for Hyperloop-like systems – and 2) *Linear Induction Motors* designed for

applications other than that of the Hyperloop, but can still be used as starting designs of linear motors for Hyperloop-like systems.

Since this thesis focuses on developing a complete linear induction motor specifically for Hyperloop-like systems, this is the technology that will be focused on first in this State of the Art Section.

1.3.1 EPFL and SwissMetro

As this thesis is taking place in Switzerland, it seems only fitting that the first state of the art linear motor technology to be discussed, is the technology developed in 1970 for the SwissMetro project at the Swiss Federal Institute of Technology Lausanne (EPFL) [8], [9].

The technology developed at EPFL from the late 1970's to the early 2000's made great strides in linear motor technology. The project went into the early stages of development and feasibility studies for the Swiss Federal Department of the Environment, Transport, Energy and Communications (DETEC) were even completed to request funding to build a pilot system with this linear motor technology in Switzerland – connecting Geneva - Lausanne [8]. This very well could have been the very first Hyperloop-like system ever built.

The SwissMetro system was very similar to the Hyperloop idea that Musk envisioned back in 2013. The project was designed to be a system in a low-pressure environment, using a form of linear motor with magnetic levitation. Sadly, due to funding reasons, the SwissMetro project was not given priority to build this system. However, design, manufacturing, and testing of linear induction motors to be used in such systems still took place at EPFL during this time. An 84m long test track was even built in Lausanne, Switzerland to experimentally test and measure the linear induction motor prototypes which were built [10]. A photograph of this test track can be seen in Fig. 1.8, and two prototype linear induction motors that were built can also be seen in Fig. 1.9.

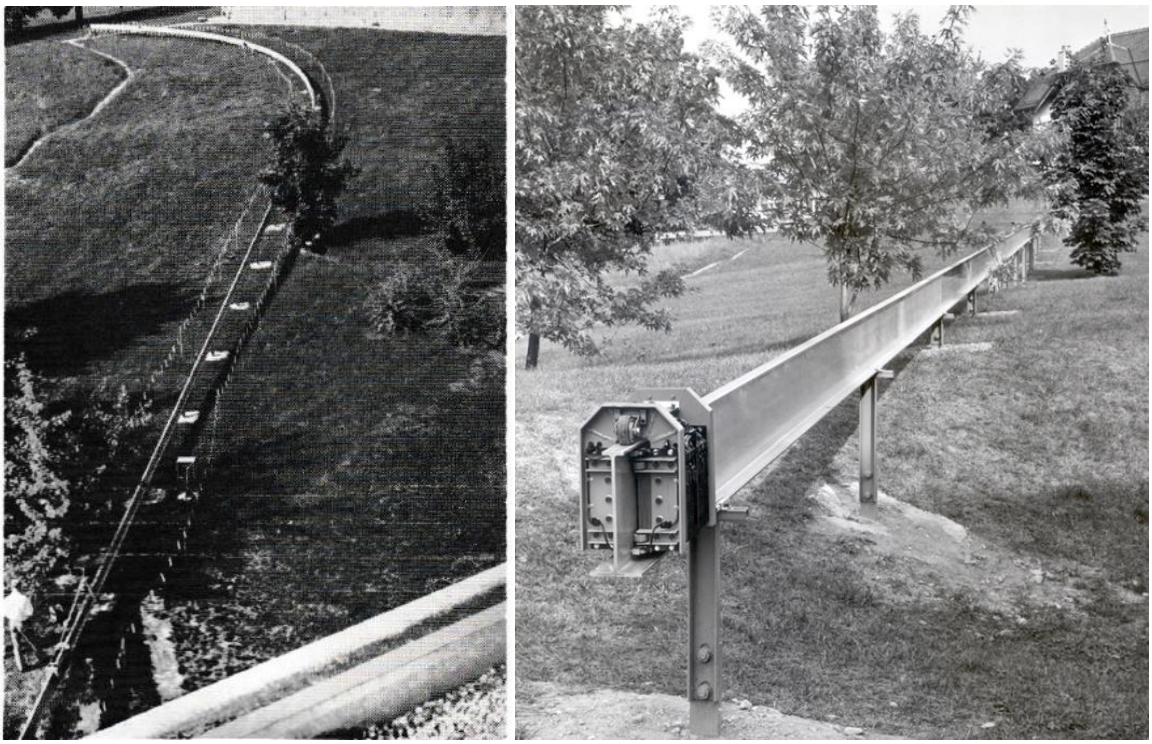

Fig. 1.8: 84 m dynamic test track for 15 and 30 kVA motors – capable of reaching speeds of 80kph [10]

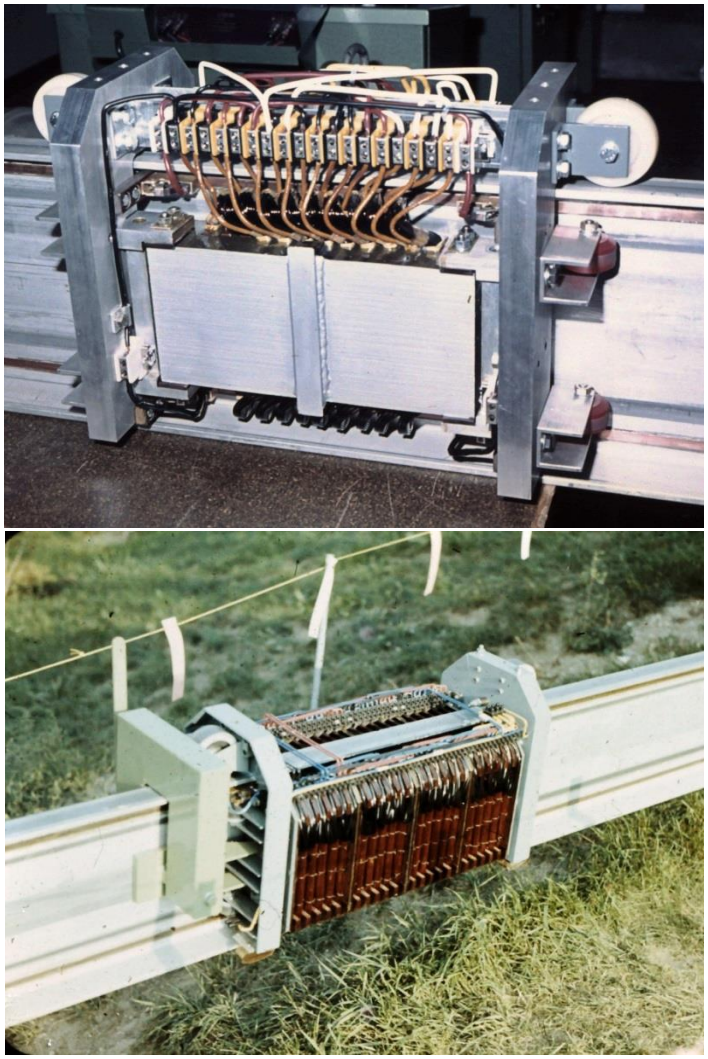

Fig. 1.9: Prototype Linear Induction Motors – EPFL 1970's [10]

The linear induction motors produced by EPFL were capable of generating speeds of approximately 80 km/h [10]. Although these motors were very advanced for their time – being developed in the 1960's and 1970's – they would not be fitting for a Hyperloop-like system to be developed today. The main reason being that the speeds reached and the masses capable of being moved are just too low for that of a prototype Hyperloop pod.

Additionally, since it was extremely difficult to achieve a variable frequency drive back in the 1970's, these motors were not frequency variable. This greatly decreases the motors performance without having the possibility to vary the frequency throughout acceleration. Nevertheless, these motors were a great achievement in the field of linear motors and are a great state of the art to build from today.

1.3.2 Virgin Hyperloop One

More recently, Virgin Hyperloop One has been getting a lot of media attention as the main Hyperloop company pursuing Hyperloop technology. They seem to be the farthest along compared to any other Hyperloop company today. However, not much is known from their linear motor technology – as they keep most of the information and technical specifications proprietary and confidential. This returns to one of the main points of this thesis – to make the technology of a linear induction motor which could be used in a Hyperloop system – open and more accessible to those who wish to know.

What is known from the Virgin Hyperloop One system, is that they use a linear induction accelerator with coils integrated into the track [11]. This configuration is known to be energy efficient as the energy needed for driving (for example; batteries), does not need to be transported. Instead, the track is powered only during certain sections to supply the motor with the necessary energy to drive. Therefore, the pod is not using energy accelerating for the entire length of track. The Open-Air and Hyperloop DevTube systems can be seen in Fig. 1.10.

Fig. 1.10: Hyperloop One Open-Air Test Track and Prototype Pod (top), Hyperloop DevTube (middle) and inside Hyperloop DevTube (bottom) – Nevada, USA [11]

It is known that Virgin Hyperloop One has been able to achieve speeds up to 385 km/h with their system on their approximately 500m test track [11]. Any further technical specifications of the motor are not exactly known at this time.

1.3.3 Tracked Hovertrain

Probably the most influential linear induction motor up until this point would be the one developed for vehicle propulsion in September 1969 [12]. It was Professor Eric Laithwaite at Imperial College London who published the first patent for linear induction motors to be used in vehicle systems as the core propulsion mechanism. Professor Laithwaite made great strides in linear induction motor development, and has even been named the Father of Maglev after patenting several surrounding technologies. Professor Laithwaite can be seen below in Figure 1.11 demonstrating a prototype double-sided LIM.

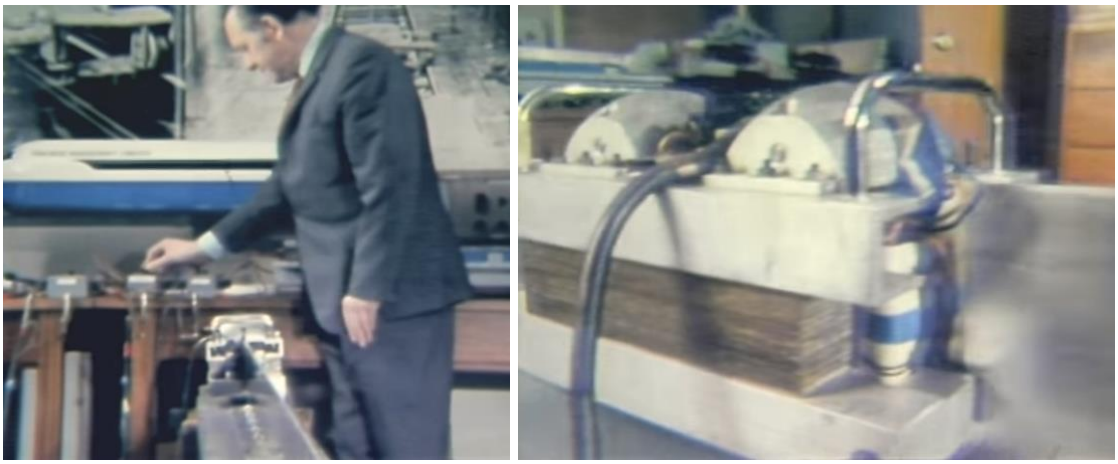

Fig. 1.11: Professor Eric Laithwaite showing his double-sided LIM prototype around an upside-down T-beam, 1972 [13]

In April 1966, he and his team constructed a 2m long "Hover-Pod" to test a prototype LIM which reached speeds of 50 km/h [13]. The LIM was a double-sided, short stator built around an upside-down T-beam track, and used 3-phase alternating current. It was noted even back then that scaled up, this LIM would have the potential to reach speeds of 600 km/h. This prototype Pod can be seen below in Figure 1.12.

A scaled-up project of the Hovertrain called *RTV 31* began in 1970 with the purpose of implementing a high speed, large scale "train-like" system using a double-sided LIM as the propulsion mechanism. However, before this project, only small-scale models were built and tested at low speeds (less than 100 km/h). Several issues were discovered when trying to scale up to larger vehicles with higher speeds and higher power requirements. Issues included material weakness in the rotor blade due to unsymmetrical forces from the double-sided stator windings, heating issues due to the high-power supplies, and power limitations. Looking back, it seems the technology of the time could not keep up with this idea of the linear induction motor. These problems eventually led to the cancellation of projects funding in February 1973 [13].

Although this system looked promising, and most of the issues, which ultimately caused the project to be cancelled – could easily be fixed today – the system was not imagined to operate in a low-pressure environment. Nonetheless, Laithwaite's and his team's work provides an ideal place to continue research on double-sided LIMs; and using a similar design, it is possible to envision a system that functions with much higher powers and even in a low-pressure environment.

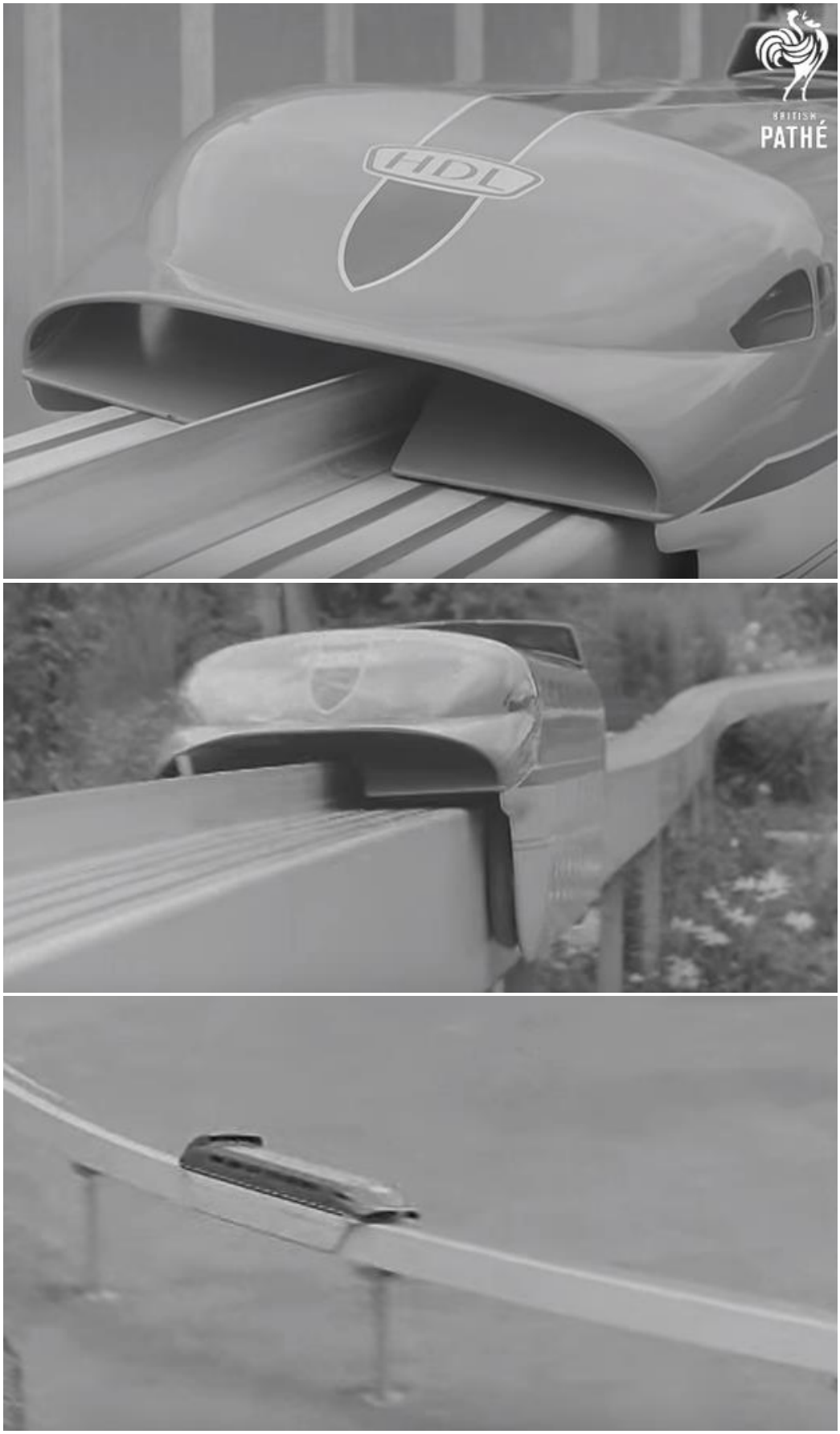

Fig. 1.12: Double-Sided Linear Induction Motor powering "Hovertrain" Prototype reaching speeds of about 50 km/h, April 1966 [13]

1.3.4 Small Precision Linear Induction Motors

As stated above, some companies just focus on small linear motor drives purely capable of small precise movements such as for conveyer belt or manufacturing applications. An example of this can be seen in Fig. 1.13.

Fig. 1.13: Example of Small Linear Induction Motor Drives, ETEL [14]

This technology – although it is still a type of linear induction motor – is not the technology needed in Hyperloop-like systems. The performance specifications such as the masses these motors can drive, the range, power limitations, and the achievable speeds – all make such motors non-ideal for a Hyperloop system. This is not to say that these drives perform worse, they are simply designed for a different application. As a matter of fact, they tend to be much more precise in their movements – down to the micrometer range in some cases. In general, such a precise movement would be highly desirable, however, precision is a parameter that is not needed in a Hyperloop-like system.

Therefore, this thesis aims to fill the gaps in the linear induction motor technologies described here. Speed is a main goal of this thesis, where a maximum speed of 500 km/h is the goal. Also, the motor should be able to reach this speed while transporting prototype Hyperloop Pods with masses weighing approximately 250kg. And again lastly, the knowledge or information learned here in this thesis should be open and publicly available.

The motor designed in this thesis needs to not only meet the current state of the art specifications, but also surpass them. SwissMetro / EPFL built a prototype motor with a top speed of 80 km/h (not in a low-pressure environment), and Hyperloop One's top speed is 385 km/h. The motor developed in this thesis will advance further and even set a new top speed record for Hyperloop Pods.

2 Theory

To help better understand the linear motor to be presented, a brief theoretical background on linear induction motors and their underlying fundamental principles is provided here.

2.1 Maxwell's Equations

Maxwell's Equations are the governing equations for any electromagnetics problem, and thus are the fundamental equations behind the linear induction motor and its operating principles. Maxwell's Equations are shown below in Eqn. 2.1 – Eqn. 2.4 in differential form [15].

$$\nabla \times \vec{E} = -\frac{\partial \vec{B}}{\partial \mathrm{t}} \tag{2.1}$$

$$\nabla \times \vec{H} = \vec{J} + \frac{\partial \vec{D}}{\partial \mathrm{t}} \tag{2.2}$$

$$\nabla \cdot \vec{D} = \rho_v \tag{2.3}$$

$$\nabla \cdot \vec{B} = 0 \tag{2.4}$$

Where $\vec{E}$ is the electric field strength, $\vec{H}$ is the magnetic field strength, $\vec{D}$ is the electric flux density, $\vec{B}$ is the magnetic flux density, $\vec{J}$ is the electric current density, and ρ_v is the local charge density [15].

Eqn. 2.4 – which can be derived from Gauss's Law for Magnetism [15] – states that all magnetic fields must begin and end on themselves. Therefore, for any closed surface, the sum of the total number of magnetic field lines entering and exiting that surface i.e., the net flux through that surface, will be zero. In other words, all field lines that exit this surface, must re-enter it. This leads to the inference that no magnetic monopoles or charges exist.

However, electric charges do exist and produce electric field lines that do not close on themselves. Therefore, summing the total number of electric field lines over some surface, gives the total charge density over that surface (or volume). In this case, the net charge dictates the total flux out of any given volume or surface. This yields Eqn. 2.3, which again is derived from Gauss's Law [15].

Eqn. 2.1 can be derived from Faraday's Law and states that a changing (time-varying) magnetic field produces and sustains an electric field. Eqn. 2.2 can be described by Ampere's Law, and states that a changing (time-varying) electric field produces and sustains a magnetic field. Additionally, Ampere's Law states that currents can also produce and sustain magnetic fields. The currents inferred here can either be a conduction current density or convection current density. Therefore, $\vec{J}$ in Eqn. 2.2 is comprised of both $\vec{J}_{cd} = \sigma\vec{E}$ (conduction) and $\vec{J}_{cv} = \rho_v\vec{v}$ (convection) [15].

Eqn. 2.1 and Eqn. 2.2 are the most important physical laws for the LIM, as they act to induce the currents which is the underlying fundamental force that generates movement – or *Thrust* – in the induction motor. A detailed derivation for this force follows in the Lorentz Force Section below.

These are Maxwell's Equations in differential form and assume the presence of time-varying fields, with current and charge distributions ($\vec{J}$ and ρ_v) in the system. If this were not the case, these terms would tend towards zero, as the system would be source-free, which is the case in a perfect vacuum (free-space).

Additionally, the following material (constitutive) relations hold in Eqn. 2.5 – Eqn. 2.7 [15];

$$\vec{D} = \varepsilon \vec{E} \tag{2.5}$$

$$\vec{B} = \mu \vec{H} \tag{2.6}$$

$$\vec{J} = \sigma \vec{E} \tag{2.7}$$

with ε and μ being the absolute permittivity and permeability properties. These values are in turn comprised of the relative or material permittivity and permeability quantities (ε_r and μ_r), and the free space or vacuum permittivity and permeability quantities (ε_0 and μ_0).

2.1.1 Quasi-Static Approximation

Low-frequency electric or magnetic fields do not propagate in the same manner as electromagnetic waves of higher frequencies do. These low frequency fields oscillate slowly and therefore have not yet evolved into time dependent fields or propagating waves. This is because an insufficient amount of time has elapsed over too short a distance [16]. In other words, the fields are oscillating so slowly due to their low frequency that the time-dependent portion of the fields is negligible. These slowly oscillating fields can even be thought of as DC magnetic or electric fields, which once generated, remain stationary.

The magnetic fields generated in the motor (more specifically the stator) operate at such low frequencies that a "Quasi-static Approximation" can be employed [16], [15]. The quasi-static approximation gives simplifications for a low frequency field and states that the time dependent electric or magnetic field terms drop out of their respective equations.

To clarify, any field terms "dropped" from an equation are still technically there: they just do not add a noticeable contribution to the total field and are thus negligible. However, this condition only holds true above a certain threshold. This threshold is the quasi-static approximation, which can be seen in Eqn. 2.8 below [16].

$$\frac{L}{c} \ll \tau \quad \text{or} \quad \omega L \ll c \tag{2.8}$$

Eqn. 2.8 states that the ratio of a field's propagation length L to its velocity c, must be much less than τ: the characteristic time constant for the sinusoidal steady state response of an oscillating signal [16]. Stated differently, the field with angular frequency ω traveling over some length L, must be slower than the speed of light. Unless this condition is met, low frequency field terms cannot be removed, as they are too large to be neglected [16].

The quasi-static approximation can be employed for the time derivative of the electric flux density term in Ampere's Law, given in Eqn. 2.2. This term, $\partial\vec{D}/\partial$t, can be re-written as $\vec{J}_d$, and denoted as the displacement current density. The displacement current density can be thought of as the currents moving back and forth in some volume. When considering motors and the low frequency stator magnetic field, this term is so small compared to the other currents in Eqn. 2.2, that under the quasi-static approximation, it can be neglected.

$$\nabla \times \vec{H} = \vec{J} + \cancelto{0}{\vec{J}_d} \tag{2.9}$$

Thus, with this displacement current density term neglected, Ampere's Law takes on the magnetoquasistatic (MQS) form of Eqn. 2.10 [16], [15].

$$\nabla \times \vec{H} = \vec{J} \tag{2.10}$$

Eqn. 2.10 is the form of Ampere's Law used when working with the magnetic stator fields of this LIM. Let it be noted that the remaining Maxwell Equations are still used in their time-varying forms.

2.2 Electric Drives

In general, an electrical drive or motor is designed to convert electrical energy – say from a battery or electrical source – to a form of mechanical motion. In a conventional rotary motor, this motion is transferred rotationally, and commonly turns an axle in a car – which rotates the wheels, turns water pumps, fans, or anything requiring rotational motion. However, in the linear drive case, this motion is now generated and transferred linearly, which is exactly the type of motion desired in a Hyperloop-like system.

To understand how motion is transferred in a linear direction and how a forward thrust is generated, a simple breakdown of rotational motors is necessary. Next, a discussion of how the transformation to the linear motor is accomplished follows, and then finally the equations and theory needed to design a linear motor are presented.

2.2.1 Motor Basics

A conventional rotary motor is comprised of two main parts; the stator and the rotor. The stator (generally, and in most cases) remains stationary, while the rotor rotates inside of the stator, as its function is to transfer the input energy (from the stator) to a rotational mechanical output; hence its name. A basic design of a rotary induction motor can be seen below in Figure 2.1, showing both the stator and the rotor.

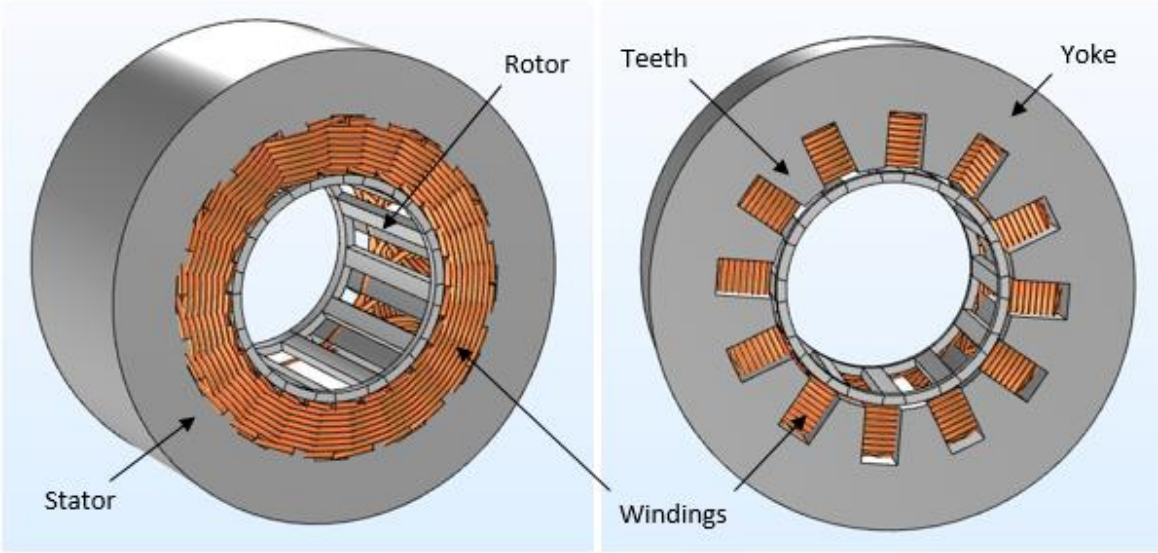

Fig. 2.1: Stator and Rotor shown for common Rotary Electric Motor – showing the different parts of the stator

As shown, the stator consists of a few parts, all labeled in Figure 2.1. The windings act as the input to the motor, delivering the electrical power, and wrap around the teeth of the stator core. Sometimes these windings are referred to as the armature of the motor – as they are the "power-producing" component of the electric machine [17]. The stator core itself is comprised of the yoke and the teeth. In between the rotor and stator is an air gap, which is very important for the operation of the induction motor.

In a rotary induction motor, the stator's task is to produce a rotating magnetic field that interacts with the rotor by inducing eddy currents. These induced currents produce an equal and opposite magnetic

field that is attracted to the source magnetic field produced by the stator. Thus, an attractive force, or torque in the rotary case, between the magnetic fields is generated and causes the rotor to rotate [17].

The stator material is most commonly iron. The need for induction (i.e., currents induced in the rotor), however, does not dictate that the stator be made of iron. On the other hand, performance increases dramatically with an iron core. The stator core has historically been made of iron because it – or any other magnetically permeable material – helps constrain the field to the shape of the stator. By constraining the field so that it flows through the stator core and the stator teeth, the strength of the magnetic field increases in the air gap. If the stator core does not consist of a magnetically permeable material, the magnetic field will simply flow freely through the air. This phenomenon is illustrated below in Figure 2.2.

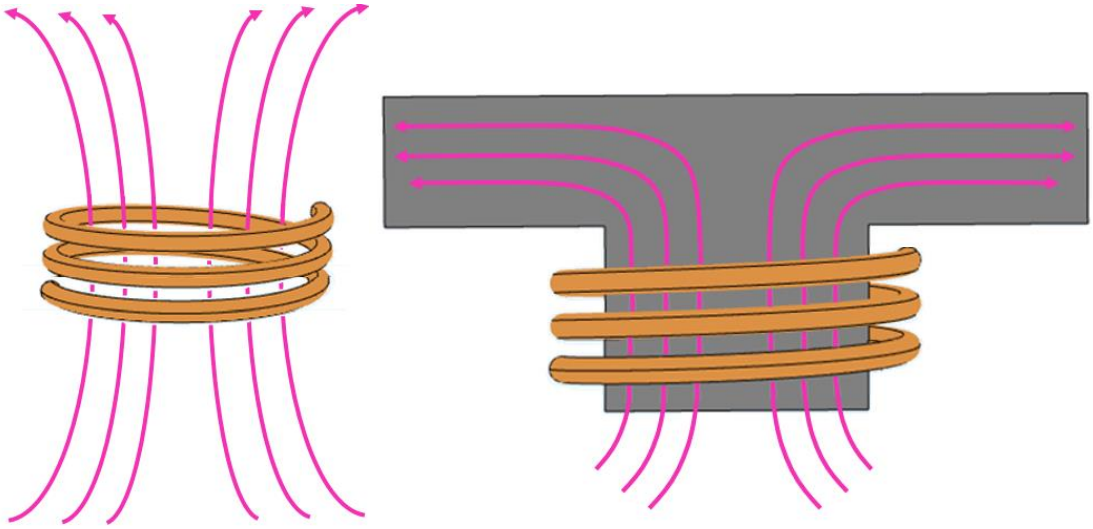

Fig. 2.2: A coil of windings in air producing a magnetic field (in magenta) is shown on the left, and on the right is a coil of windings wound around a magnetically permeable material – such as iron. The field produced from the coil on the left can be seen to be much less "constrained" than the field from the coil on the right – which is wound around an iron core. This is because of the magnetic permeability and reluctance properties of the iron material.

The same conclusion can be reached from Ampere's Law in (quasi-static) integral form, which is shown below in Eqn. 2.11.

$$\oint_{(c)} \vec{H} \cdot d\vec{l} = \iint_{S} \vec{J} \cdot d\vec{S} \tag{2.11}$$

It can be seen that when the closed path of the magnetic field lines ($d\vec{l}$) increases, the magnetic field strength, $\vec{H}$, decreases. Therefore, a larger $d\vec{l}$ (e.g., a longer distance, like a path through air) yields a lower magnetic field strength. This analysis gives insight into how the path length through a non-magnetically permeable material reduces the magnetic field strength, but not as to why a magnetically permeable material gives a "shorter" path in the first place. This is due to a property called *magnetic reluctance*, which is analogous to electrical resistance in a circuit; in that current flows through the path of least electrical resistance. The same is true for magnetic resistance or reluctance. This will be explained in more detail in the Magnetic Flux Density Section below.

In addition, the magnetic permeability of the material itself plays a role and will also affect the magnetic field strength, as a higher magnetically permeable material will always "push" the concentration of the field to that of a lower magnetically permeable material – as from iron to air. This will also be discussed in more detail below in Magnetic Flux Density Section.

The rotor is often (and traditionally) referred to as a "*Squirrel Cage Rotor*" because it resembles a wheel in which a squirrel or hamster might run in [17]. This squirrel cage rotor is essentially a conductive cage short-circuited at both ends with conductive end rings. These end rings create a low impedance circuit or path with the rotor bars through which the induced eddy currents flow. It is the combination of these induced eddy currents with the rotating stator field that generates a torque, forcing the rotor to rotate. An illustration of the rotor can be seen below in Figure 2.3.

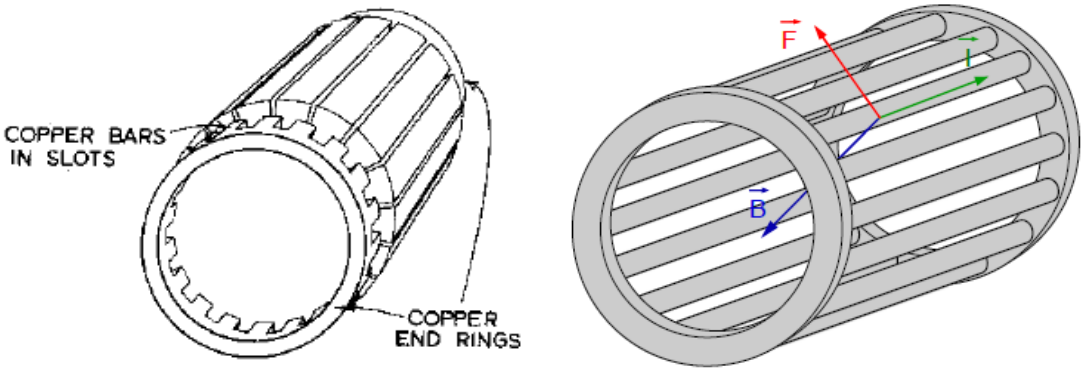

Fig. 2.3: Squirrel Cage Rotor with short-circuited end-rings connected to rotor conductive bars [13], [18] – showing the stator B-field in blue, induced eddy current flow direction in green, and Lorentz force produced as the product of eddy currents and stator B-field in red.

Looking at the rotor on the right in Figure 2.3, the stator magnetic field can be seen in blue: it passes through the rotor cage and induces the eddy currents (green), which together act to produce an attractive torque (red). Thus, the alternating stator magnetic field causes the rotor to continuously move and that's how rotational motion is generated in the rotary induction motor case. As for the operation of the linear induction motor, more theory into how the linear thrust is produced will be provided in following sections.

2.2.2 Linear Motor Evolution

The operation of the linear motor is similar to that of the rotary motor, except that the generated motion now translates into a linear direction. The linear driving force is the result of one key aspect: *the induction of a travelling stator field from polyphase excitation*.

To create a linear motor, one can imagine slicing the rotary motor from the previous section down its center, stopping in the middle, and then "rolling out" the split stator and rotor. A linear motor can be seen in Figure 2.4 with the different parts of the stator labelled for completeness.

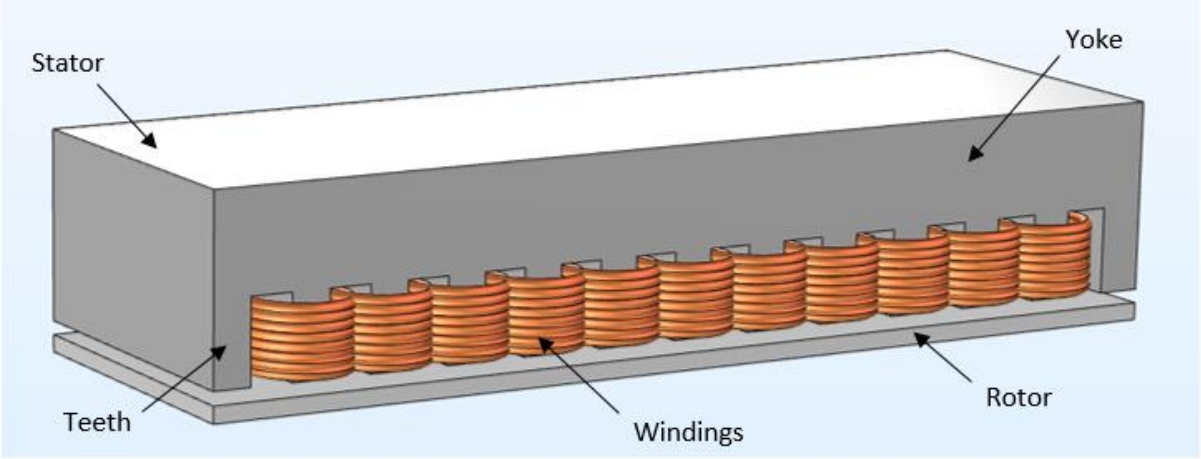

Fig. 2.4: Linear Motor Evolution from Rotary Motor – showing the Stator and Rotor, and different parts of the stator

As indicated, all parts of the rotary motor are still there, the only difference being that the shape of the stator and rotor are now exactly as the name implies, *linear*.

The biggest difference in the linear motor when compared to the rotary motor is at the ends of the linear motor. The motor is no longer a continuous object, but instead has open-ended air gaps at each end, which do not exist in the rotary motor. These air gaps at the end lead to "end-effects" at both ends of the LIM that cause unwanted losses and decrease performance [19]. The study of end-effects is a very specialized and deep topic in and of itself and will therefore not be covered in-depth in this thesis. However, some of the key issues associated with end-effects will be investigated and discussed in the End-Effects Section below.

Another difference in the linear motor is that the long conductive bars or end rings of the rotor, in the rotary case, which allowed eddy currents to flow around in a low-impedance circuit, are not present in the linear case. In the linear case, a simplified conductive "plate" or "blade" is used as the rotor. The solid conductive plate of the linear case distributes the travelling stator field continuously, according to Maxwell's Equations, the field cannot be influenced. In the rotary case, this can be designed for, and chosen how or where the eddy currents are induced.

The main motivation for adding bars in the rotary case is to give an "entrance" for the field to induce currents. If the rotor were just a solid plate as in the linear case, the field would flow around the rotor and not interact as well with it. Instead rotor bars are designed so that when the field passes through these bars, currents are induced in them and flow through in a low impedance path. This effect is not that large in the linear case, as the field does not avoid the rotor. An efficiency comparison between the "Squirrel Cage Rotor" and the "Blade Rotor" can be seen below in Figure 2.5 [13].

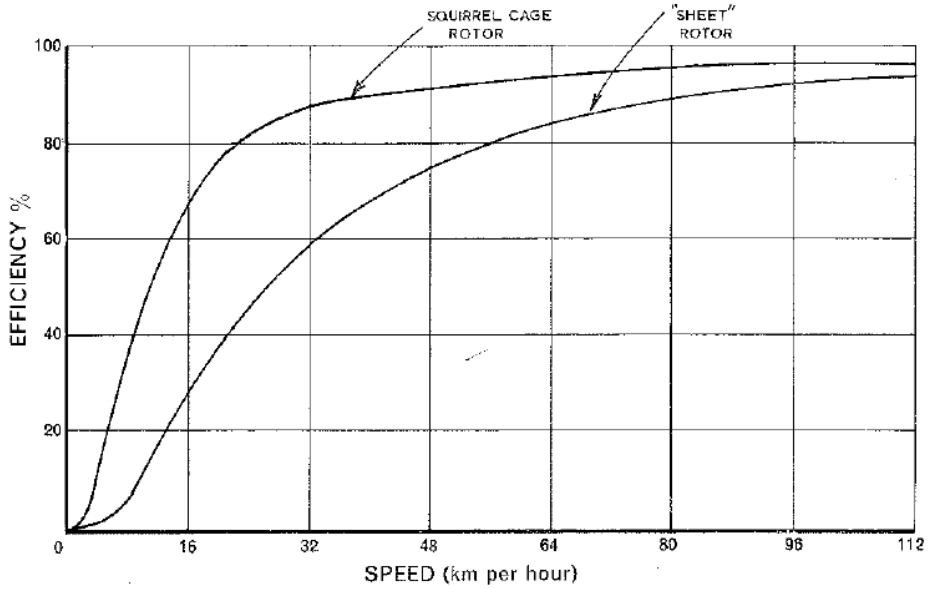

Fig. 2.5: Efficiency comparison between the conventional rotary squirrel cage rotor, and linear blade rotor – also denoted as a "Sheet Rotor" [13]

As can be seen, at higher speeds, the sheet rotor is not significantly less efficient than the squirrel cage rotor, perhaps only by 5-10% [13]. Nevertheless, one might try to recover this efficiency by slicing optimized holes in the linear rotor blade[1], so that a path is created for induced eddy currents to flow.

[1] This would also reduce the mass of the rotor blade, thus helping with weight saving or weight constraints that might exist in high performance Hyperloop-like systems. Such optimized holes are shown in Musk's Hyperloop Alpha Whitepaper [5].

However, this significantly increases design complexity and manufacturing and does not noticeably improve performance. The induced eddy currents still flow in the plate, but unfortunately not as well as in the rotary case. Therefore, this "sheet" geometry is simply a design tradeoff between manufacturing and design simplicity.

Additionally, in the rotary motor, the stator is conventionally fixed in place, while the rotor rotates in place[2]. One difference for the linear motor is that depending on the application, it might be advantageous to switch which part of the motor is moving and which is fixed in place. As an example, a Pod or Hyperloop vehicle can have the stator fixed onboard the moving Pod, while the rotor blade is fixed to the track. In this case, the rotor is the part that is fixed, while the stator is technically moving. This grants extra design options when deciding which motor configuration to choose.

Several different configurations or types of linear motors exist. The classification can be split into two main types, Synchronous and Asynchronous [17], [20]. Asynchronous motors can also be referred to as induction motors: the two terms are used interchangeably and refer to the same type of motor. Therefore, the type of motor presented in this thesis can also be referred to as a linear asynchronous motor; however, by convention it is referred to as a linear induction motor.

An Asynchronous motor was chosen for this thesis because the design is much less complex than that of a synchronous motor, which involves the use of permanent magnets to create an attractive Lorentz force that is otherwise generated with induction. Thus, from a design perspective alone, the LIM offers a good starting point for a prototype, because it is much simpler than it synchronous counterpart. The different topologies or linear motor classifications can be seen below in Figure 2.6.

Since, the linear motor developed in this thesis is a linear induction motor, the theory discussed in the following sections focuses on the topics necessary for understanding induction or asynchronous motor theory. Nevertheless, it is informative to show the other linear motor types to indicate that many other choices or options for linear motor configurations exist.

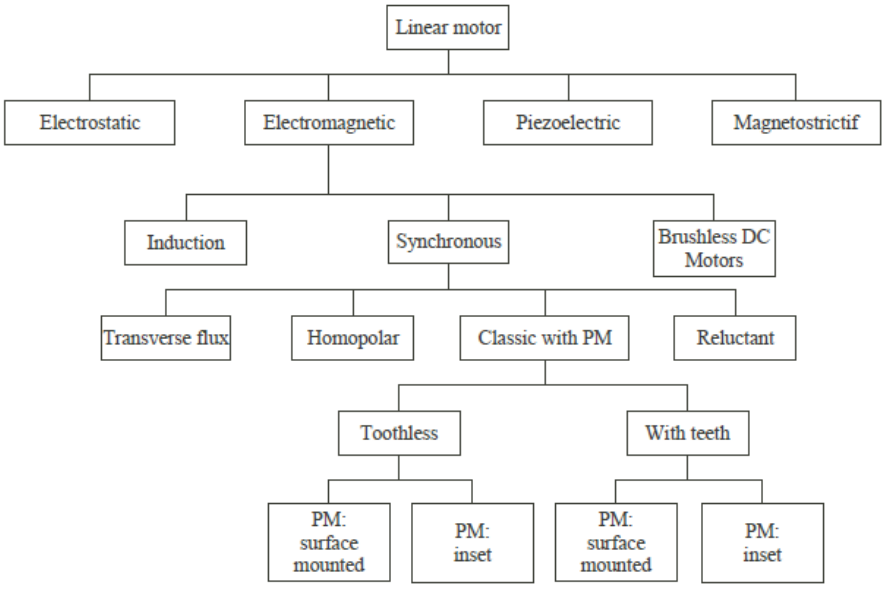

Fig. 2.6: Classification of Linear Motor Types – showing Asynchronous or Induction and how it is categorized [20]

[2] This is not always the case, there can be a moving outer stator with a fixed inner rotor – often used in race car applications where the motor is fixed directly inside of the car's wheels. However conventionally, the stator is stationary, and the rotor rotates.

Earlier it was mentioned that the key aspect behind the linear force for a linear induction motor is the travelling stator field produced from a polyphase excitation. Both principles are discussed below.

2.2.3 Polyphase Excitation

The stator of a rotary induction motor produces a rotating magnetic field that interacts with the rotor by generating a torque, thus causing the rotor to rotate. In a linear motor, the field produced from the stator is now one of a travelling or sweeping field due to its rolled out or linear geometry. The excitation method however, is the same between rotary and linear: this travelling (linear) or rotating (rotary) field is produced by polyphase excitation.

Simply put, polyphase excitation is an excitation where the input is split amongst multiple signals of equal amplitude, but varying phase delays. As shown in Figure 2.6, linear motors can either be excited by a DC or an AC source. Induction motors are excited via some AC electrical source. With a single AC input approximated by a sine wave, the maximum of the signal would only be for a short period in time (i.e., only when the sine wave is near its maximum). For the rest of the time, the sine wave oscillates between its maximum and minimum. A single-phase sine wave is shown below in Figure 2.7 to help illustrate this point; where the maximas and minimas are labelled by red dots.

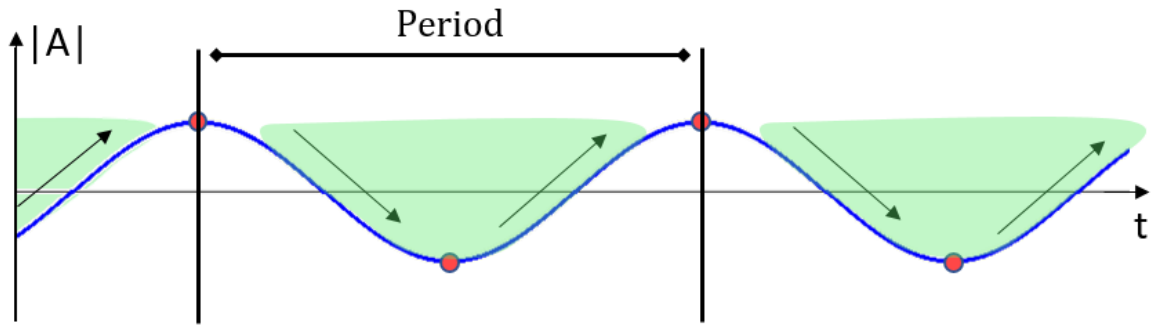

Fig. 2.7: Single-Phase Sine wave oscillating as some AC source to the LIM – showing amplitude vs. time

The contribution from the field at its maximum is very strong and interacts well with the rotor to rotate it. However, during the rising and falling of the sine wave, the field weakens greatly and does not contribute much to the overall torque turning the rotor (in the rotary case) or thrust attracting or "pulling" the rotor (in the linear case). This effect can be seen in Figure 2.7: when the field is at a maximum, the thrust is strongest. The long non-contributing "breaks" in the signal in-between the sine wave's periods are highlighted in green.

These periods during which the sine wave alternates between its positive maximum and negative minimum are uneven transitions between cycles and can be thought of as "signal dropouts". To prevent this, additional input signals, of equal amplitude but shifted phase delays, can be used to achieve more uniform transitions between maximums (cycles). The excitation shall be some number of AC input signals, each having a corresponding and different phase delay.

When distributed evenly, these differences in phase delays allow the maximum of the field to constantly alternate between each input. In this way, a travelling field is produced, as there is always some maximum point traveling along the excitation path of the motor. To achieve this uniform field distribution, it is necessary for the difference in phase delays between input signals to be as evenly distributed as possible.

As one can imagine, the input could be split into as many as 10 or even 20 inputs to have almost indistinguishable input transitions. However, there are tradeoffs between number of input phase

delays and the design complexity. As the number of inputs increases, the system becomes more complex to design. Additionally, at some point, the difference in performance and efficiency will almost be indistinguishable. Therefore, there exisits a balance between design complexity and number of inputs. Considering the rotary case, an even distribution around the motor is most commonly achieved by splitting the input into three equal amplitude signals with equal phase delay between each input. This configuration equates to three inputs, each of which have a 120° phase delay between them.

$$360°/3 = 120° \tag{2.12}$$

This 120° phase shift gives the most uniform field distribution at the lowest "cost" for a simultaneously rotating/travelling field. Figure 2.8 depicts the inputs as currents of varying phase delays and shows how they vary during the motor's operation as it cycles through the three phases.

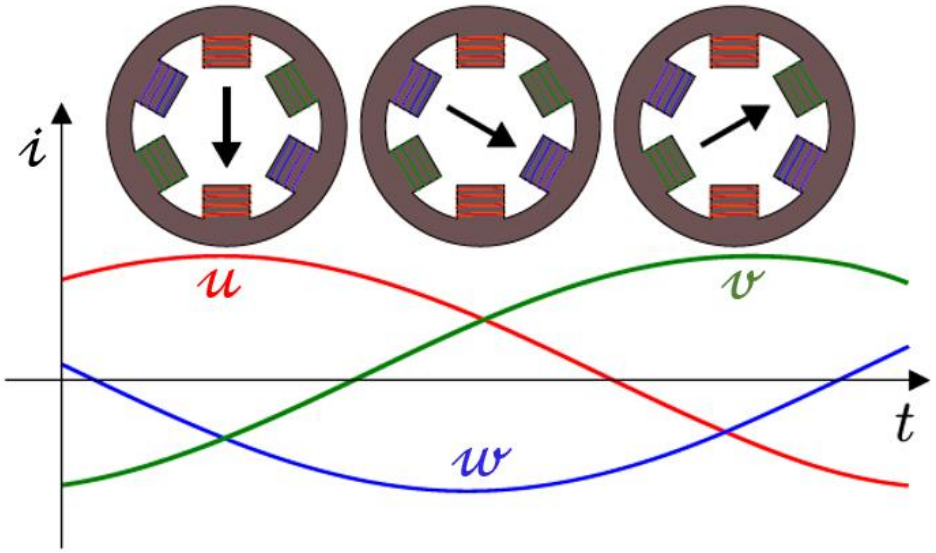

2.8: 3-phase Equal Amplitude Voltage Excitation vs. Time – showing how there is always one phase at maximum [18]

Figure 2.8 shows that there is always some point in time when one phase provides the maximum force during operation. This behavior creates a more uniform or "steady" field for the rotary motor. The same holds true for the excitation of the linear motor. The three excitation currents are listed below for completeness.

$$i_u = I \cdot \cos(wt) \tag{2.13}$$

$$i_v = I \cdot \cos(wt + 120°) \tag{2.14}$$

$$i_w = I \cdot \cos(wt + 240°) \tag{2.15}$$

All three inputs have the same amplitude and frequency during operation, with the phase shift being the only difference between them. If the amplitudes or frequencies were different, there would be asymmetries introduced in the system. These three alternating 120° phase offset currents can be seen again in Figure 2.9, where it can be seen that the motor always experiences some maximum point.

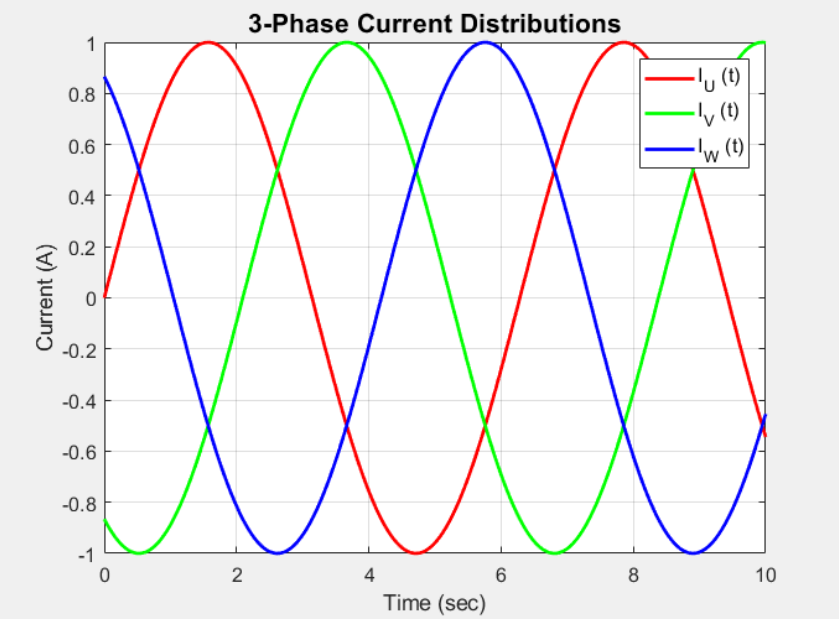

Fig. 2.9: 3-Phase Current Distributions – showing a 120° phase offset for the input currents, where one phase is always at a maximum

Further observation of these currents shows that for any instance in time, the total instantaneous current (i.e., input to the motor), would actually be zero. This can be analyzed further with some simple algebra.

$$I_{U1} + I_{W1} + I_{V1} \equiv 0 \tag{2.16}$$

$$1A + (1A \angle 120°) + (1A \angle 240°) \equiv 0 \tag{2.17}$$

$$1A + \left(-\frac{1}{2} + \frac{\sqrt{3}}{2}i\right)A + \left(-\frac{1}{2} - \frac{\sqrt{3}}{2}i\right)A \equiv 0 \tag{2.18}$$

$$1A - 1A + \frac{\sqrt{3}}{2}i\,A - \frac{\sqrt{3}}{2}i\,A \equiv 0 \tag{2.19}$$

$$0 \equiv 0 \tag{2.20}$$

After performing these steps, it can be shown that at any given moment, the total instantaneous current input to the motor is zero. The phase diagram of these three 120° offset currents can be seen below in Figure 2.10.

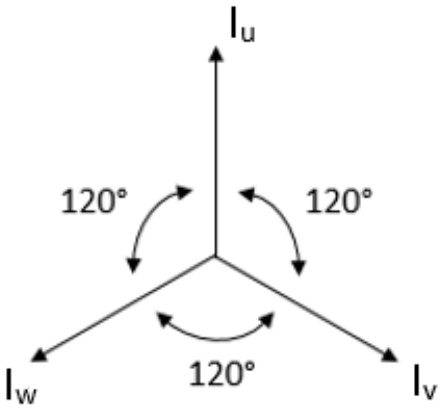

Fig. 2.10: 3-Phase Currents with Equal 120° Separation

This diagram shows the 120° separation between the 3-phase currents. It is this 3-phase excitation that leads to the creation of a travelling stator field. [21]

2.2.4 Travelling Stator Field

Having analyzed how the stator field is produced from a varying 3-phase supply, a formulation of the stator field can be investigated further. The time-varying "traveling" or "sweeping" magnetic stator field that sweeps across a conductive rotor secondary is produced when electrical current is excited through the stator windings. After the windings have current flowing through them, they produce and sustain a magnetic field according to Ampere's Law. The magnetic field can be quantified by taking a path around a single coil of a single phase. This can be seen below in Figure 2.11, where a closed loop encloses a coil of a single phase, and the corresponding magnetic field strength for each part of the path is observed.

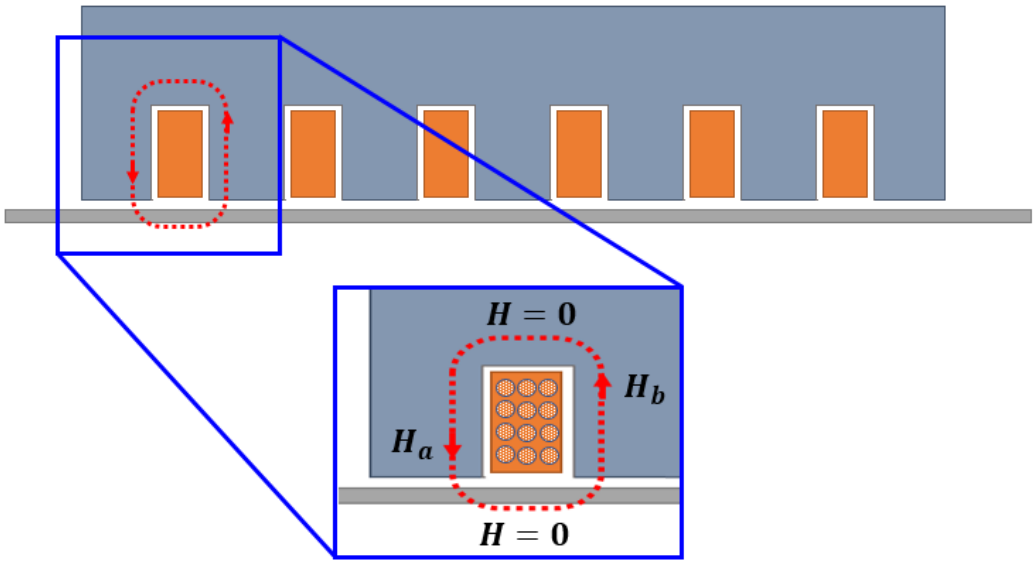

Fig. 2.11: Path taken around a current carrying coil of N windings to calculate the closed line integral of the H-Field for a simple 6-Slot single-sided LIM

Solving the line integral of Ampere's Law around this closed path shown in red yields the magnetic field strength in the air gap for a single phase of this field. The corresponding field can be seen below after using Ampere's Law in magneto quasi-static form, listed here again for reference.

$$\oint_{(c)} \vec{H} \cdot d\vec{l} = \iint_{S} \vec{J} \cdot d\vec{S} \tag{2.21}$$

The magnetic field strength, H, can be determined and shown below in Eqn. 2.22 for the path around the winding, if the field is summed according to Figure 3.1.

$$H_a \cdot g - H_b \cdot g = N \cdot I \tag{2.22}$$

Eqn. 2.22 indicates that the magnetic field strength of the closed path around the winding is summed for the given air gap distance, g, and then equated to the turn number, N, of the winding, and the current passing through the windings, I. In other words, the closed path taken around the windings is equal to the current enclosed by that path multiped by the number of windings of that path. Let it be noted, that Eqn. 2.22 solves for the magnetic field strength in the air gap, g [21].

Summing the magnetic field strengths of the path shows that the tangential field components are zero, but that the normal field components are opposite in sign to one another. Using this principle, a substitution can be made for the field components to simplify the equation.

$$H_a = -H_b \tag{2.23}$$

From here, some simple algebra can be performed to equate the magnetic field strength to the enclosed current of N windings.

$$H_a \cdot g + H_a \cdot g = 2H_a \cdot g = N \cdot I \tag{2.24}$$

$$H_1 = \widehat{H} = \frac{NI}{2g} \tag{2.25}$$

Rearranging the equation and setting the total magnetic field strength to $\widehat{H}$, the magnetic field strength in the air gap is determined. Since g is the distance of the air gap, the magnetic field strength found from Eqn. 2.25 passes twice through this air gap. Observation of Figure 3.1 shows that the field has two contributions from the air gap because the path of the line integral enclosing the winding must close on itself. The total length of the path plays an important role in determining the magnetic field strength and will be discussed later in the Magnetic Flux Density and Motor Design Sections.

To produce a time-varying magnetic stator field, Eqn. 2.26 and Eqn. 2.27 are introduced to add time and space varying components to the equation.

$$\sin(\omega t) \tag{2.26}$$

$$\sin\left(\frac{\pi y}{\tau_p}\right) \tag{2.27}$$

Eqn. 2.25 can be multiplied by Eqn. 2.26 and Eqn. 2.27 to produce a time- and space-varying magnetic field strength similar to the actual field [21]. y is the horizontal or linear direction in which the linear motor translates when thrust is generated and τ_p is the pole pitch of the motor, which is described in more detail in its own section below. However, for now τ_p is referred to as the half period of the stator sine wave [21], illustrated below in Figure 2.12.

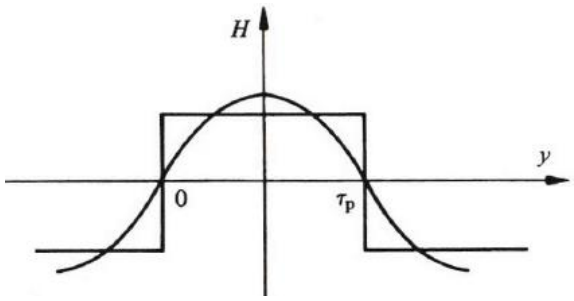

Fig. 2.12: Pole Pitch Identified as the half period of the stator sine wave [21]

Combining the time and space varying components above with Eqn. 2.25 yields the following time-varying magnetic field strength for a single phase, u, of the motor.

$$H_u(y,t) = \frac{4}{\pi} \cdot \widehat{H} \cdot \sin\left(\frac{\pi y}{\tau_p}\right) \cdot \sin(\omega t) \tag{2.28}$$

$$H_u(y,t) = \frac{4}{\pi} \cdot \frac{NI}{2g} \cdot \sin\left(\frac{\pi y}{\tau_p}\right) \cdot \sin(\omega t) \tag{2.29}$$

Assuming a 3-phase input comprised of three equal amplitude 120° (corresponding to $^{2\pi}/_{3}$ radians) phase shifted magnetic fields, the remaining two phases of the input are listed below.

$$H_u(y,t) = \frac{4}{\pi} \cdot \frac{NI}{2g} \cdot \sin\left(\frac{\pi y}{\tau_p}\right) \cdot \sin(\omega t) \tag{2.30}$$

$$H_v(y,t) = \frac{4}{\pi} \cdot \frac{NI}{2g} \cdot \sin\left(\frac{\pi y}{\tau_p} + \frac{2\pi}{3}\right) \cdot \sin\left(\omega t + \frac{2\pi}{3}\right) \tag{2.31}$$

$$H_w(y,t) = \frac{4}{\pi} \cdot \frac{NI}{2g} \cdot \sin\left(\frac{\pi y}{\tau_p} - \frac{2\pi}{3}\right) \cdot \sin\left(\omega t - \frac{2\pi}{3}\right) \tag{2.32}$$

t can be seen that there are now three 120° offset stator fields that vary in time and space (position). To create the total stator field that sweeps the distance of the stator and induces eddy currents in the rotor for thrust production, these 3-phase fields can be summed together. However, first it is desirable to decompose the sines into cosines to make the math less complex. This decomposition process can be completed to produce the final 3-phase cosine fields seen below.

$$H_u(y,t) = \frac{4}{\pi} \cdot \frac{NI}{2g} \cdot \left(\cos\left(\frac{\pi y}{\tau_p} - \omega t\right) - \cos\left(\frac{\pi y}{\tau_p} + \omega t\right)\right) \tag{2.33}$$

$$H_v(y,t) = \frac{4}{\pi} \cdot \frac{NI}{2g} \cdot \left(\cos\left(\frac{\pi y}{\tau_p} - \omega t\right) - \cos\left(\frac{\pi y}{\tau_p} + \omega t + \frac{4\pi}{3}\right)\right) \tag{2.34}$$

$$H_w(y,t) = \frac{4}{\pi} \cdot \frac{NI}{2g} \cdot \left(\cos\left(\frac{\pi y}{\tau_p} - \omega t\right) - \cos\left(\frac{\pi y}{\tau_p} + \omega t - \frac{4\pi}{3}\right)\right) \tag{2.35}$$

Finally, the superposition of all three phases yields the total sweeping or travelling magnetic stator field.

$$H_{tot}(y,t) = \frac{6}{\pi} \cdot \frac{NI}{2g} \cdot \cos\left(\frac{\pi y}{\tau_p} - \omega t\right) \tag{2.36}$$

This field is the total magnetic stator field seen in the air gap of the motor that travels or sweeps across the stator to induce eddy currents in the rotor.

The total magnetic stator field sweeps across the rotor and resembles a cosine or sine-like distribution. It will be seen in the subsequent Winding Configuration Section how this sine-like distribution is achieved or approximated. However, if these separate 3-phase and total fields are plotted as a function of position, it can be seen how the total resulting stator field is created and sweeps in position. Figure 3.3 shows these equations plotted in Matlab for a generic air gap spacing and pole pitch value.

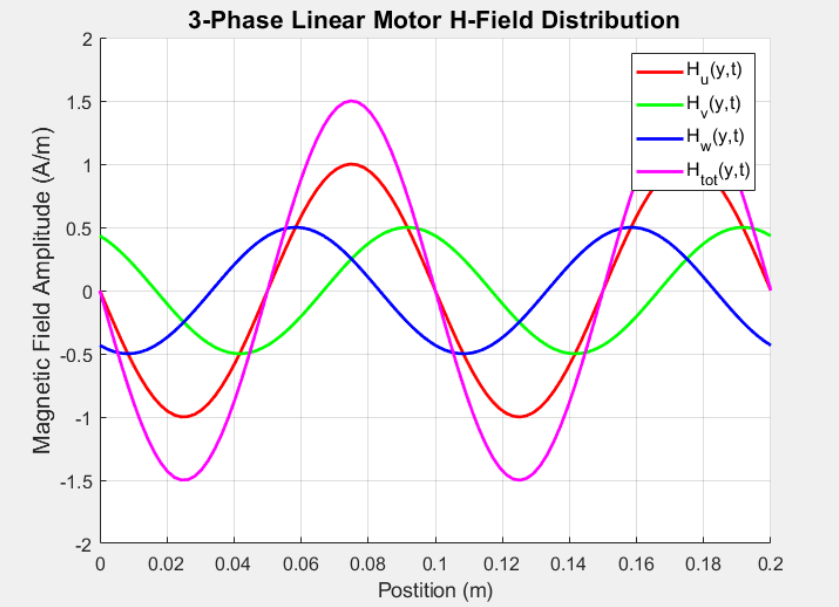

Fig. 2.13: 3-Phase Stator Fields and Total Stator Field – showing one instance in time how the three-phase fields (red, green, and blue) add up to produce the total stator field (pink)

As can be seen from Figure 2.13, the three-phase fields (red, green, and blue) add up to produce the total stator field (pink). A time evolution of the stator fields is plotted below in Figure 2.14 for different time instances to help visualize the travelling field.

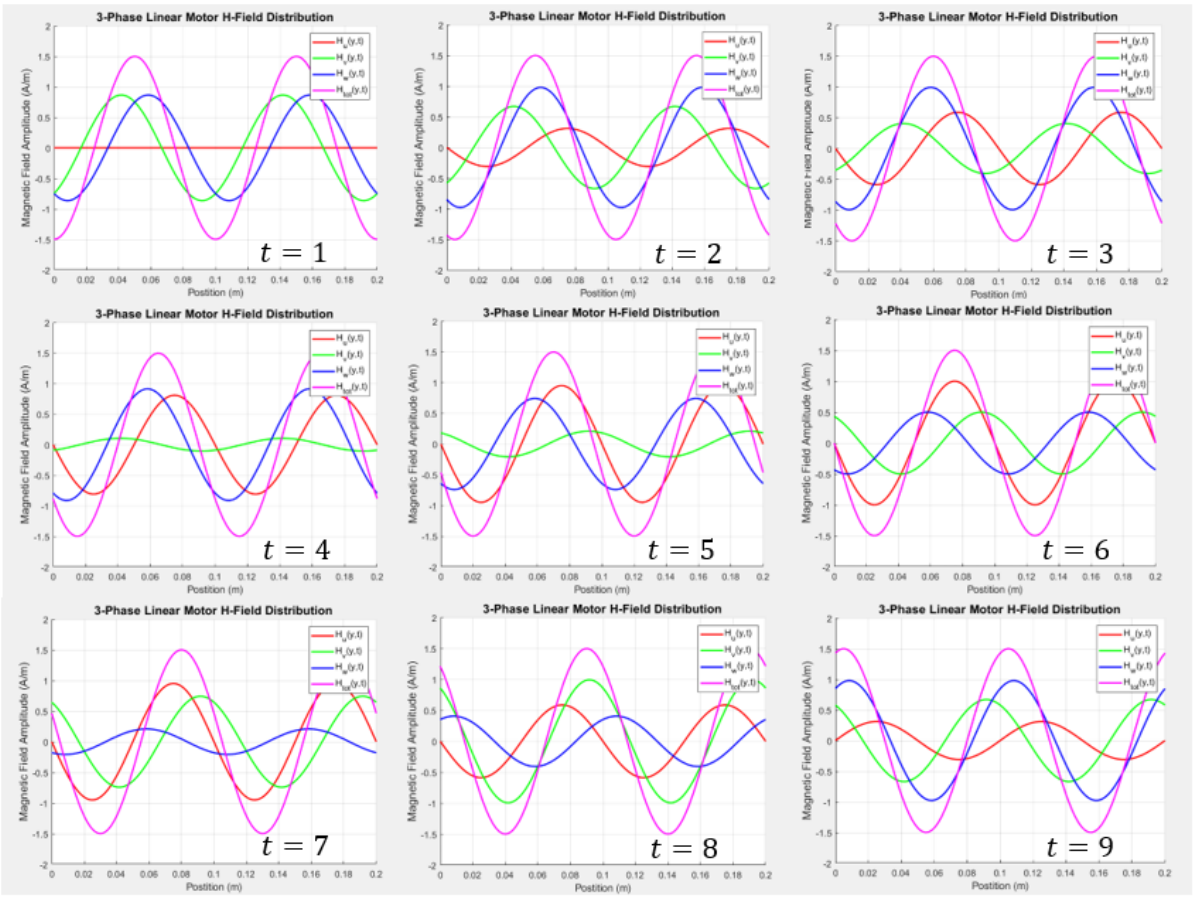

Fig. 2.14: 3-Phase Stator Fields and Total Stator Field – showing a progression of the system from t=1 sec to t=9 sec

As can be seen in Figure 2.14, the 3-phase fields are all plotted and the superposition shows the total field as a function of position and time. It can be seen that the 3-phase fields do not move in position, as they simply oscillate vertically in time. The total field only moves horizontally in position as it progresses towards the right side of the plots where no vertical oscillation is observed.

Now that the magnetic field strength of the travelling stator field has been quantified, it will be shown below how it interacts with the rotor to create thrust, as it is solely responsible for inducing the eddy currents which help generate a Lorentz thrust force. Interactions of this stator field with the rotor to induce currents used for thrust production, will be shown in the subsequent sections.

2.2.5 Synchronous Speed

The travelling stator field sweeps across the secondary with speed v_s. This is defined as the *synchronous speed* of the motor and is a key parameter for the motor. The motor's synchronous speed, or sync speed for short, is defined as the final speed reached by the motor for a given applied source frequency [21], [17], [22]. In the case of this thesis, the speed goal was specified as 500 km/h, so that is the sync speed to be used later in this thesis. The sync speed is often defined in its SI units, so 500 km/h is converted to 138.89 m/sec.

At the sync speed, there is no longer a contribution from the stator field and hence no counter-travelling field is produced by the rotor: its speed at this point, in principle, is the stator synchronous speed [17].

To derive an expression for this sync speed, the argument of the cosine in the total stator field expression can be set to one. This is the part of the equation which varies and therefore describes the speed of the field.

$$\cos\left(\frac{\pi y}{\tau_p} - \omega t\right) = 1 \tag{2.37}$$

If Eqn. 2.37 is solved for and rearranged, the following expression for the sync speed can be found.

$$\cos^{-1}(1) = \frac{\pi y}{\tau_p} - \omega t \tag{2.38}$$

$$0 + \omega t = \frac{\pi y}{\tau_p} \tag{2.39}$$

$$\tau_p \cdot \omega t = \pi y \tag{2.40}$$

$$\frac{\tau_p}{\pi} \cdot \omega = \frac{y}{t} = v_s \tag{2.41}$$

Performing the algebra and describing the expression in terms of its position and frequency yields a translation of space over time. This quantity is the synchronous speed velocity, v_s , of the motor and is shown below in simplified expressions, where the frequency of the stator field, f_s, is substituted for the angular frequency ω because the frequency of the stator field is often described in Hz rather than in rad/sec.

$$\frac{\tau_p}{\pi} \cdot 2\pi \cdot f_s = v_s \tag{2.42}$$

$$v_s = 2\,\tau_p\, f_s \tag{2.43}$$

This expression describes the speed of the travelling stator field of the motor.

As can be seen, the sync speed is directly related to the pole pitch of the motor, which will be seen to be a geometrical value given as a unit of length (usually in mm), and the frequency of the stator [17]. The fundamental principle behind asynchronous motors is that the electrical frequency of the stator field essentially sets the sync speed, which translates to an observable mechanical velocity [17]. In a linear asynchronous machine, this mechanical velocity corresponds to how fast the rotor will drive. Therefore, this equation is quite important and will be the key equation used in many sections of this thesis.

2.2.6 Poles and Pole Pitch

Maxwell's Equation, Eqn. 2.4, states that no isolated magnetic poles (magnetic monopoles) can exist. Therefore, every magnetic field must have two poles, a north and a south pole. This means that the magnetic poles created from the stator field will always develop in pairs. These pairs can be referred to as "*pole pairs*" and are one of the defining parameters of a motor (i.e, a motor is usually specified as being either 2-pole, 4-pole, 6-pole, etc.).

The fewer pole pairs a motor has, the less drag the motor experiences and therefore the more thrust it generates [17], [19]. Due to this property, it is desirable for motors to be designed with the minimum number of pole pairs, unless the application dictates otherwise. Normally, and in certain applications, motor constraints are fixed a priori, which makes designing the motor for fewer pole pairs not possible. However, this is not the case in this thesis and care will be taken to try and design for as few pole pairs as possible (e.g., a 2-pole or 1 pole pair motor).

The pole number of a motor can be defined by observing a sine wave function for a given stator field of a motor. As was seen, the stator field is approximated by a sine wave function and therefore has minimums and maximums that span the length of the stator. If the field is observed for the length of a generic linear motor, the poles of the motor can be observed. Figure 2.15 identifies the poles of a sine wave for a given linear motor.

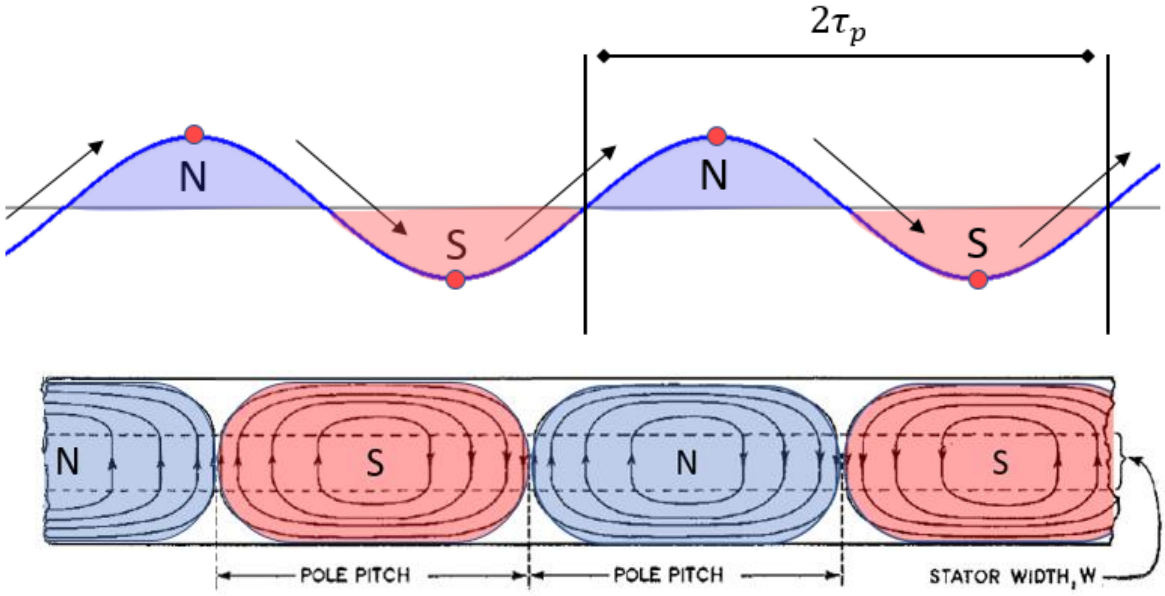

Fig. 2.15: Travelling stator field sine wave depicting pole pitch for 4-pole motor (above), and motor core depicting pole pitch similarly for a 4-pole motor (below)

As seen from the Travelling Stator Field Section above, this stator field will sweep the length of the stator. Figure 2.15 shows that there are several N and S indicators on the maximums and minimums

of the stator sine wave, respectively. These indicators represent the north and south poles of the magnetic stator field. Therefore, from the stator field shown in Figure 2.15, it can be seen that this motor has 4 magnetic poles, or 2 pole pairs, and would be classified as a 4-pole motor.

The pole pitch, τ_p, also shows up in Figure 2.15. The pole pitch is defined as the geometrical length for a single pole in a motor: it is the pole's "pitch" or length. Figure 2.15 shows that this stator field spans the length of the linear motor's stator producing the travelling field shown in blue, and that the pole pitch is roughly a quarter of the total length of the motor (i.e., the pitch or length of one pole). The length of the motor is directly related to the pole pitch, or vise-versa and therefore represents another key design parameter. If the length of the motor is known, the pole pitch can be determined if the pole number is also known. A simple formula for relating the pole pitch to the length of the motor can be seen below in Eqn. 2.44.

$$\tau_p = \frac{L}{2 \cdot p} \tag{2.44}$$

Where L is the length of the stator, and p is the pole number. Therefore, for a 2-pole motor, the pole pitch is half of the length of the stator; for a 4-pole motor, the pole pitch is a fourth of the stator's length and for a 6-pole motor, the pole pitch is a sixth of the stator length.

2.2.7 Slip

The travelling stator field created from the 3-phase excitation has a velocity called the sync speed, v_s. This velocity, as was seen in Eqn. 2.43, is directly related to the frequency of the stator field, f_s. This field sweeps across the rotor, which produces its own magnetic field that is equal and opposite to that of the stator field. This equal and opposite rotor field creates a repulsive force between the rotor and the stator that produces the main linear movement in the linear asynchronous motor. This fundamental thrust generation will be discussed in more detail in the Lorentz Force Section.

However, from this introduction, it can now be seen that the rotor has its own travelling field, complete with its own some speed and frequency defined as v_r and f_r , respectively. The speed and frequency of this newly created rotor field will, however, be different from that of the stator field. The rotor field will be slightly slower compared to the stator field due to a "delay" between the two fields. This delay in the fields can also be referred to as the *slip* of an asynchronous motor.

Therefore, it is from the differences in the two fields that the slip is defined. Put more accurately, the slip is defined as the difference between the synchronous speed of the travelling field produced by the stator and the actual mechanical speed of the rotor [17], [13], as shown below in Eqn. 2.45.

$$s = \frac{v_s - v_r}{v_s} \tag{2.45}$$

Thus, the slip is the difference in speed between the two fields and takes on a value between 0 and 1. A slip equal to 1 is defined as full slip and a slip equal to 0 means there is no slip. The slip is plotted below in Figure 2.16 against the moving rotor velocity to help better visualize its characteristics during operation.

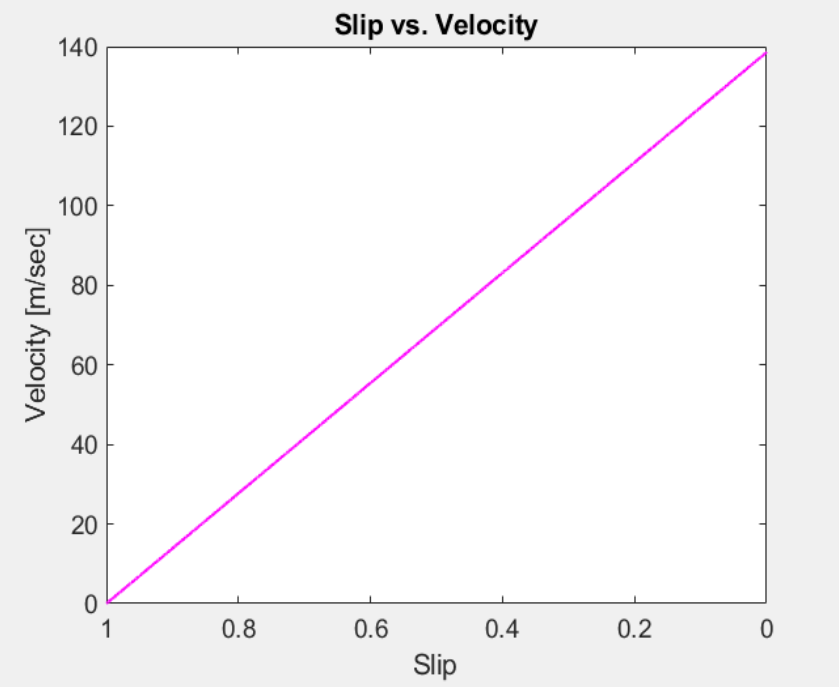

Fig. 2.16: Slip vs. Rotor Velocity – showing that when the sync speed is reached, the slip is 0, meaning the rotor should be at the same speed as the sync speed of the field. Likewise, for a slip of 1, the biggest difference between the rotor velocity and speed of the stator field is observed

As can be seen from Figure 2.16, a linear correlation is obtained between the slip and the rotor velocity during motor operation. It can be seen that for a slip of 1, the velocity of the rotor is 0 m/sec and when a slip of 0 is reached, the velocity of the rotor has reached the sync speed of 138.89 m/sec (or 500 km/h).

To elaborate, a slip equal to 1 corresponds to no movement and thus, the rotor is stationary with respect to the moving stator field. At this point, the biggest difference (i.e., largest slip) between the stator field velocity and the rotor's actual moving velocity is observed. When the slip is equal to 0, the rotor has reached the sync speed (i.e., the speed towards which it drives during operation) and no difference, or a small slip, between stator field velocity and rotor velocity is observed. In this case, the rotor moves at exactly the same speed as the synchronous field from the stator and there is no observable relative difference between the two.

With no reference place, the two fields would appear stationary, since relative to each other, they move at the same speed. Thus, the rotor can never move faster than the synchronous speed of the stator field. Once v_s is reached, the rotor stops accelerating.

Slip can be visualized in Figure 2.17, where a simple 2-Slot stator is displayed above a blade rotor in two scenarios: 1) for when the slip is equal to 1 and thus, the motor is stationary and 2) for when the slip is equal to 0 and the motor is moves at the sync speed.

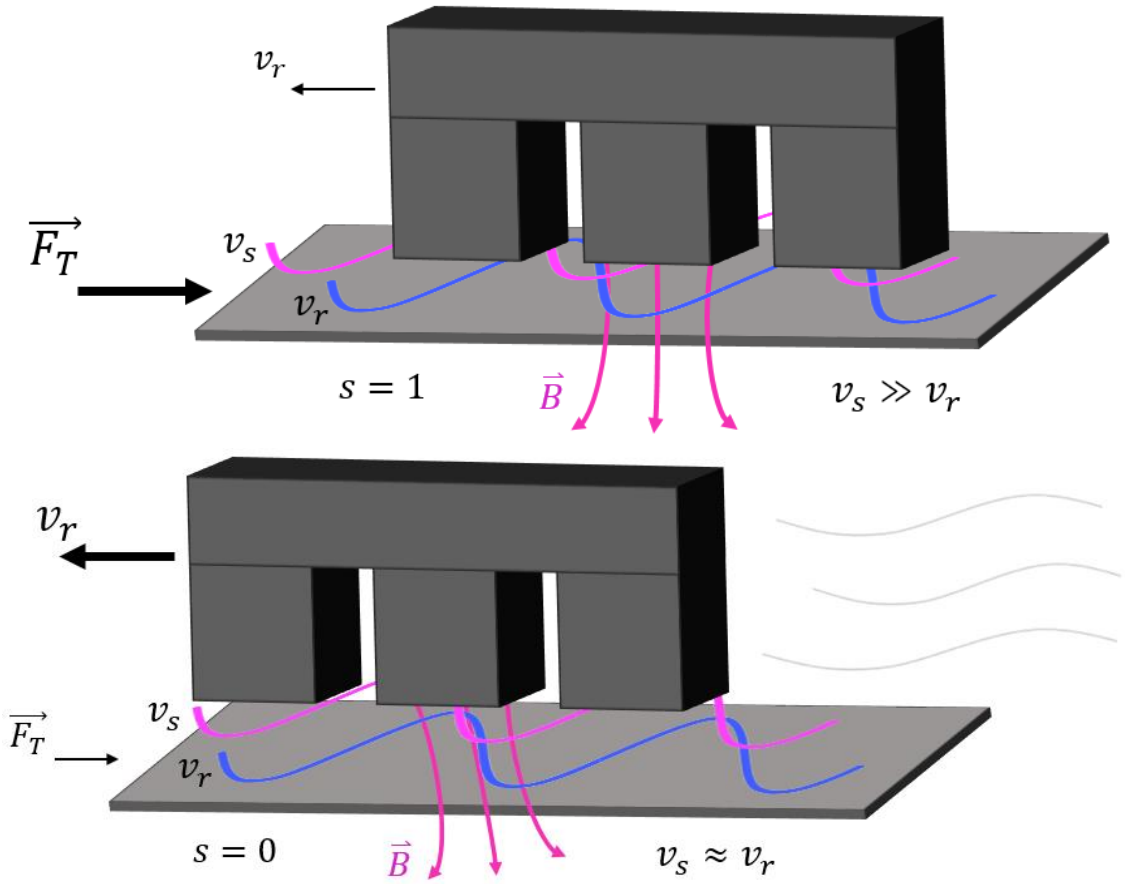

Fig. 2.17: Stator and Rotor of simple 2-Slot LIM – showing that when the motor operates at a slip close to zero, the LIM goes faster, but thrust production is lower. The stator magnetic field of speed v_s (pink), induces eddy currents in rotor, which generate a rotor magnetic field of speed v_r (blue)

Figure 2.17 shows that as the motor approaches the synchronous speed, less force will be generated but the velocity will be higher. To further understand this concept, a curve of the thrust is provided in the Lorentz Force Section. It will be seen that once the synchronous speed is reached, no more thrust is generated by the motor.

2.2.8 Power Factor

As was seen in the Polyphase Excitation Section, the 3-phase system was described in terms of the three currents, offset from one another by 120°. However, the configuration can also be described in terms of voltage. A similar phase diagram to Figure 2.18 can be seen below, where both the voltages and currents are now depicted with some angle separation between them.

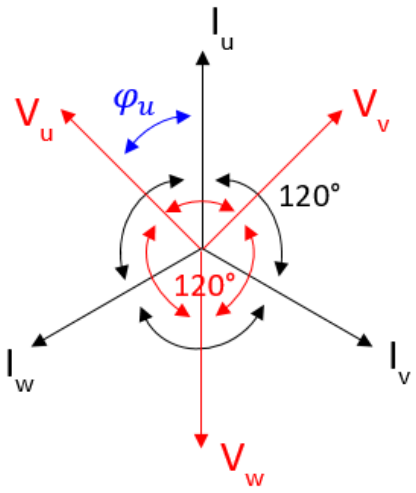

Fig. 2.18: 3-Phase Currents and Voltages, with equal 120° separation between phases, and φ angle separation between the current and voltage of the same phase

Figure 2.18 shows that both currents and voltages have a corresponding phase shift of 120° and an angle, φ (shown in blue), between currents and voltages of the same phase. The currents and voltages are shifted apart from each other by some angle because in AC inductive systems, the voltage is not in phase with the current. The cosine of this angle is called the power factor and is a measure of the system's efficiency, as it describes the ratio of the active power to the reactive power [17].

$$PF = \cos(\varphi) = \frac{\text{Active Power}}{\text{Reactive Power}} \tag{2.46}$$

Asynchronous motors tend to have a power factor around 0.8 [17]. Looking at Eqn. 2.46, the closer the power factor is to one, the more efficient the motor will be. This condition corresponds to a smaller angular separation between the voltages and currents. A power factor of one means the phase separation between the voltages and currents is zero (i.e., they are in phase), which means that all the energy supplied by the source is consumed by the load.

In a purely inductive coil, a phase shift of 90° corresponds to a power factor of zero. In this state, all the power in the system is reactive power, with no real power being dissipated. The inductor essentially absorbs all the power in the system on the positive swing and feeds it back into the system on the negative swing, so that no power is lost. In motor windings, the phase angle is not perfectly 90°, so there will always be some power dissipated in the system. This dissipation is due to electrical energy being converted to mechanical energy, which introduces losses into the system.

The windings will not be purely inductive anymore as there are some resistive losses in the windings. Thus, the positive power factor will be a positive value somewhere between zero and on. The inductor windings feed some energy back into the system on the down-swing, and absorb some energy on the upswing, however some energy is lost in the system during these swings.

The voltage drop across an inductor is at a maximum when the instantaneous current changes most rapidly and this occurs when it crosses the zero line. The voltage is then said to be "leading" the current, or stated differently, the current "lags" the voltage.

The power factor for the linear motor is defined below in Eqn. 2.47 as a function of the motor's design parameters [19].

$$PF = \cos(\varphi) = \cos\left(\tan^{-1}\left(\frac{\pi \cdot p_s \cdot g}{\mu_0 \cdot s \cdot \tau_p \cdot v_s}\right)\right) \tag{2.47}$$

Where p_s is the resistivity of the secondary, g is the air gap distance, s is the slip of the motor, v_s is the synchronous speed of the motor, and τ_p is the pole pitch of the motor. It is known from [19] that $\tau_p v_s$ is very large in high speed motors, meaning the air gap can be larger without increasing the power factor. To elaborate, if v_s increases by a factor of 10, g can also be increased by a factor of 10 with no observable change to the power factor. This property is very important because, as will be seen in the Motor Design Section, the distance of the air gap helps to define the motor's thrust and is quite difficult to reduce.

2.2.9 Slot and Winding Distribution

The travelling stator field is essentially a sine wave comprised of the sum of the three phase delayed currents. However, in reality, the created is not a perfect sine wave, since construction of a perfect sine wave is expensive and impractical. Therefore, the sine wave stator field is seen to be approximated by square waves [17].

Increasing the number of slots in the stator core improves the approximation because additional opportunities exist for the windings to interact and help "smooth" the stator field to make it more sine-like and gradual. Taking the FFT of the travelling stator field and observing the harmonics shows that keeping the stator field a sine-like function helps in the frequency domain as well. The fundamental frequency or first harmonic in the frequency domain represents the thrust force which moves the motor. The higher order harmonics act to disturb the fundamental and decrease performance of the motor in acting like a braking force by yielding other synchronous speeds towards which the motor will try to move.

The approach of using the windings and slots to help better approximate the sine wave stator field is called *distributed windings.* Approximations of sine waves can be seen below in Figure 2.19 for stator cores of increasing slot numbers: in summary, a higher slot number yields a better approximation.

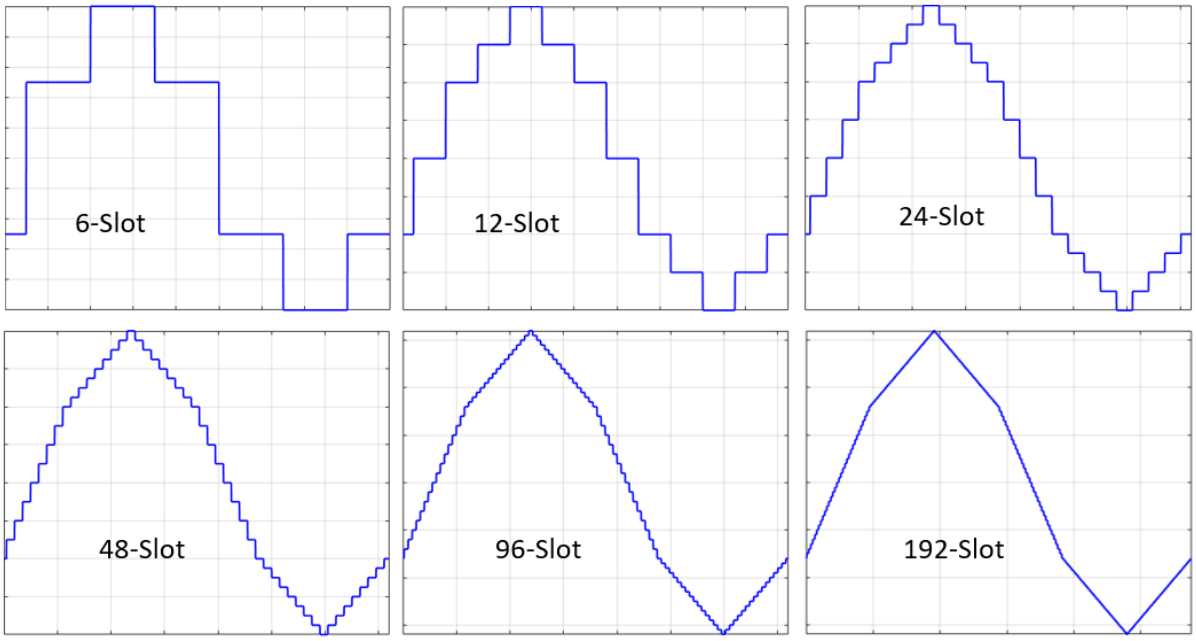

Fig. 2.19: Different Approximations for the Stator Sine Wave Distribution – showing that more slots yields a better sine wave approximation

Figure 2.19 shows that by using more slots in the stator core, a more sine-like approximation is obtained. However, after enough slots, the sine wave distribution does not improve further and actually begins to resemble that of a triangle waveform. To combat this, a left or right shift of a single slot winding for each phase can be performed. This is visually depicted for a sample 12-Slot model in Figure 2.20, where one slot winding of each phase is shifted to the right.

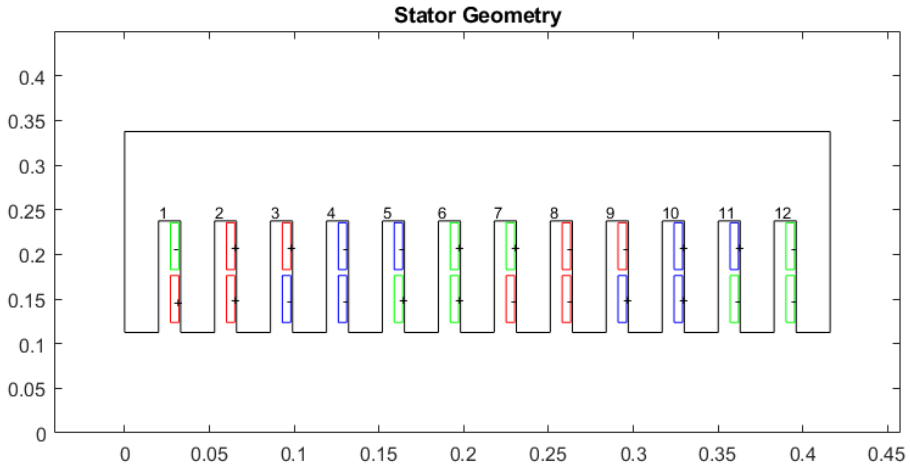

Fig. 2.20: Sample 12-Slot LIM Model – showing a right shift in the upper coils – which has the effect of better approximating the stator sine wave distribution

However, this shifting of the slots is generally quite hard to accomplish in the actual winding of the stator core and adds high complexity since the windings need to be split in half in this configuration and then somehow wound evenly again. This technique adds unbalanced resistances that result in an imbalance of the magnetic field at the ends of the motor. This shifting scheme is regularly performed in rotary motors because it is easier to wind the coils because the last slot is inherently next to the first slot. However, in the linear case, bringing the last coil all the way to the front of the motor for the shifted case requires an elaborate winding scheme and leads to a longer coil that unbalances the system. Nevertheless, this shifting scheme has the effect of better approximating the stator sine wave by rounding out the peaks, which can be visualized in Figure 2.21 for a 192-Slot model.

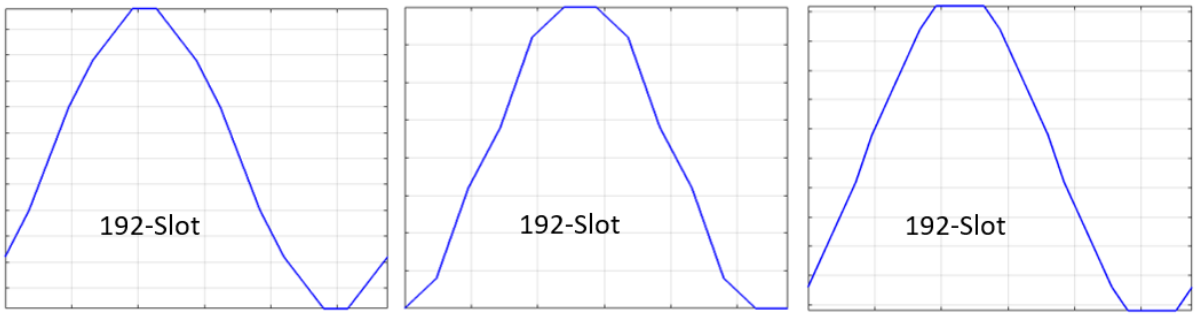

Fig. 2.21: 192-Slot stator sine wave approximation – showing that a shift in the coils helps to round out the sharp peaks in stator field, thus yielding a better approximation of a sine wave

Therefore, adding slots helps improve the approximation of the sine wave distribution for the stator magnetic travelling field, which in turn helps decrease other harmonics and improves the motor's overall efficiency and ability to obtain a higher driving thrust. As will be seen, the slots of the core and windings through them are a very important part of the motor design.

Having introduced the basics of the linear induction motor, specific concepts are now discussed in the following sections to help understand the theory around the LIM that guides the design.

2.3 Magnetic Flux Density

Eqn. 2.4 Gausses Law for Magnetism shows that no magnetic monopoles can exist.

$$\nabla \cdot \vec{B} = 0 \tag{2.48}$$

with $\vec{B}$ as the magnetic flux density in free space – defined as the product of the absolute permeability and the magnetic field strength;

$$\vec{B} = \mu \vec{H} \tag{2.49}$$

with μ being the absolute permeability comprised of the relative or material permeability μ_r, and the free space or vacuum permeability $\mu_0 = 4\pi \cdot 10^{-7}\ \mathrm{H/m}$ [15].

The flux is then defined as the number of magnetic field lines passing through some surface. Since the magnetic field lines begin and end on themselves, they are closed and do not terminate on a "magnetic charge" [15]. Therefore, the flux passing through some defined open surface area is defined as;

$$\Phi = \int_S \vec{B} \cdot d\vec{S} = B \cdot SA \tag{2.50}$$

The number of magnetic field lines passing through some surface area is defined as the net magnetic flux. The magnetic flux is measured in units of Webers. As the stator field is produced, this flux passes through and exists in-between the stator and rotor, or in the air gap of the LIM. This is the initial step of how the LIM's thrust is produced.

2.3.1 Magnetic Saturation

The magnetic flux is a product between the magnetic flux density, B, and the total surface area, SA, through which the flux passes. Therefore, if the flux should be increased, the only way to do so, is by either increasing the magnetic flux density, or by increasing the total surface area through which the flux passes. What is not evident by simply looking at Eqn. 2.50 is that the B-field can only be increased to a certain level: beyond this point, it is no longer possible it is no longer possible to achieve noticeable[3] changes in the flux by simply increasing the magnetic flux density, B.

This point is known as the *magnetic saturation flux density*, B_{sat}, and is dependent on the type of magnetic material used. The known physical limit for the magnetic saturation point of any magnetic material is usually around 1.8T [15], [17], [23]. Under special conditions, or for some rare materials, magnetic saturation values of 2.6T have been observed [23]. However, in general, this property is observed as a fundamental physical and theoretical limit on a material that cannot be surpassed.

As a result, to further increase the flux, one must increase the overall surface area through which the flux is allowed to pass. This means increasing the size of the stator so B_{sat} is not reached for a given input source. B_{sat} is therefore sought to be as large as possible for a given material as this has the effect of shrinking the size of the electric machine [23]. Otherwise, passing too much flux through a designated surface area can cause B to saturate to B_{sat}. This phenomenon can be seen in Figure 2.22, where magnetic saturation is observed for a simple soft iron stator core.

[3] The core will appear to not accept any more flux, however, increasing B after the saturation point will still slightly increase the flux, however diminishing returns will be observed, as asynchronous machines cannot be overloaded.

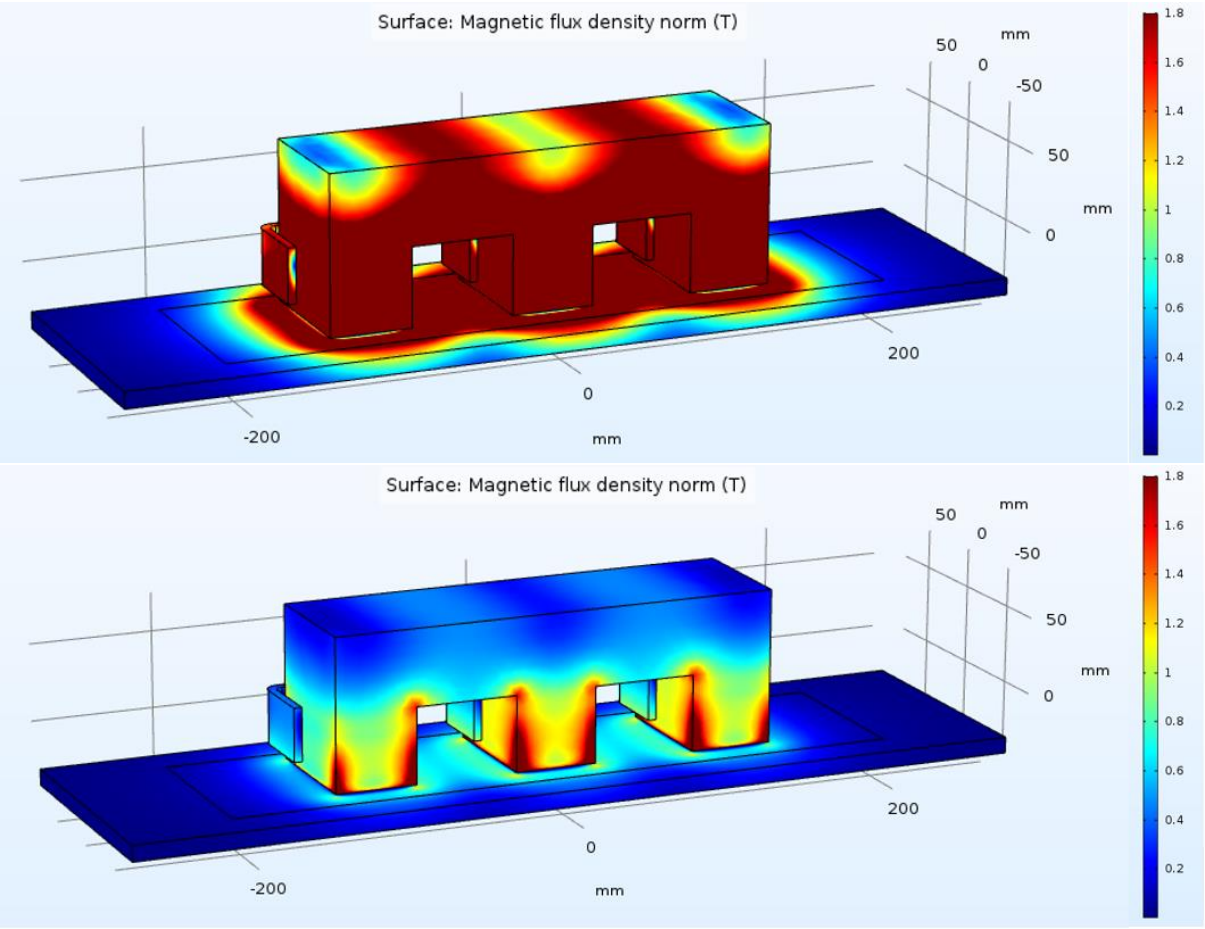

Fig. 2.22: Simplified LIM showing the magnetic saturation limit reached for a Soft Iron Stator Core. The stator core above is magnetically saturated, while the stator core below is not operating under magnetic saturation conditions.

The plot on top shows how the core saturates with a magnetic flux density point of 1.8T for a given input source. The below plot shows when the core is not saturated; this operating condition has been achieved by drastically lowering the input source. When operating below magnetic saturation conditions, the thrust produced will not be as large as it could be for higher input levels. When the core approaches saturation, the corners begin to saturate first due to their high field potentials. This behavior can be seen in the bottom plot where the corners of the stator core begin to saturate past 1.8T.

Conditions drawn from Figure 2.22 indicate that this linear motor stator core needs to be made much larger in order to support higher inputs and fluxes that would otherwise cause this current core to saturate. Otherwise, this core would simply produce less thrust for its current size. Less thrust correlates to a much lower motor efficiency because the machine does not produce an equivalent force relative to the applied input level. Thus, the core operates in a region implied by its name, *saturation*.

Saturation is not necessarily bad; it is a physical condition of the material describing what happens when too much flux is “pushed” through the stator core. The stator core will first try to react to this changing flux by accepting or supporting it. However, if the core is not large enough, it does not matter how much input is applied, it will saturate at B_{sat} for the given material.

As stated earlier, iron is usually deployed as the material of the stator core. Iron is a soft magnetic material, meaning the magnetic flux density, B, can be easily changed by applying small values of the

magnetic field strength, H [23]. This variation in the magnetic flux density in response to the magnetic field strength is described by a *BH curve* [23], [15]. The saturation level can be observed from a material's BH curve, where the input source is measured as the magnetic field strength, H. An example using soft iron's BH curve is shown below in Figure 2.23.

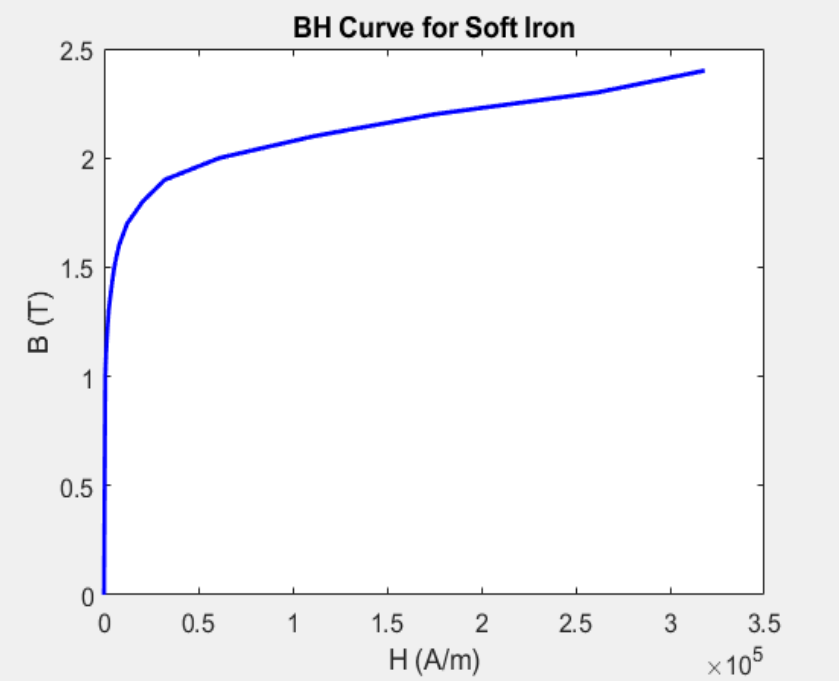

Fig. 2.23: BH Curve for Soft Iron Core Material

Observation of Figure 2.23 reveals that this soft iron material saturates around 1.8T as expected. The BH curve shows that towards the low input region of the curve, where the magnetic field strength input is minimal, small changes in the magnetic field strength, H, lead to rapid increases in the magnetic flux accepted by the core. The curve increases linearly in this region, but after this 2T soft "limit", one can see that the core rapidly begins to saturate. It is this point where even large changes in the magnetic field strength only produce minimal change in the magnetic flux accepted by the core. Eventually, the rate of increase on the magnetic flux density will be so small, that it won't appear to change at all. This is saturation of the iron core.

An analogy for understanding saturation is to imagine a pipe carrying a certain amount of fluid or water through it. If water flows through a certain portion of the pipe's cross-sectional area, then the pipe can support this amount of water just fine. However, if the amount of water throughout the pipe increases so that the water spans the entire diameter of the pipe's cross-section, the limit on the amount of water it can carry has been reached. The pipe will not be able to support any more water than what is being passed. Attempts to pass more water through the pipe will lead to the pipe expanding slightly to support a fraction of this change in the water level, and thus only a small increase is observed. Attempting to pass even more water will lead to the pipe bursting.

It is the same with magnetic saturation. When trying to pass too much flux through a too small surface area, the core saturates around B_{sat}, because the iron core material cannot handle this much flux passing through it. As the core saturates, the produced forces increase minimally and almost no additional force production is observed. Additionally, if the input level of the source continues to increase, then the core will heat up and eventually melt, as there is nowhere for the added flux to go but into heat dissipation.

Most magnetically permeable materials are non-linear, corresponding to a non-linear relative permeability value. Taking Eqn. 2.49 and solving for μ_r yields the following non-linear relative permeability.

$$\mu_r = \frac{\vec{B}}{\mu_0 \vec{H}} \tag{2.51}$$

This relative permeability using the soft iron BH curve example of Figure 2.23, is plotted below in Figure 2.24.

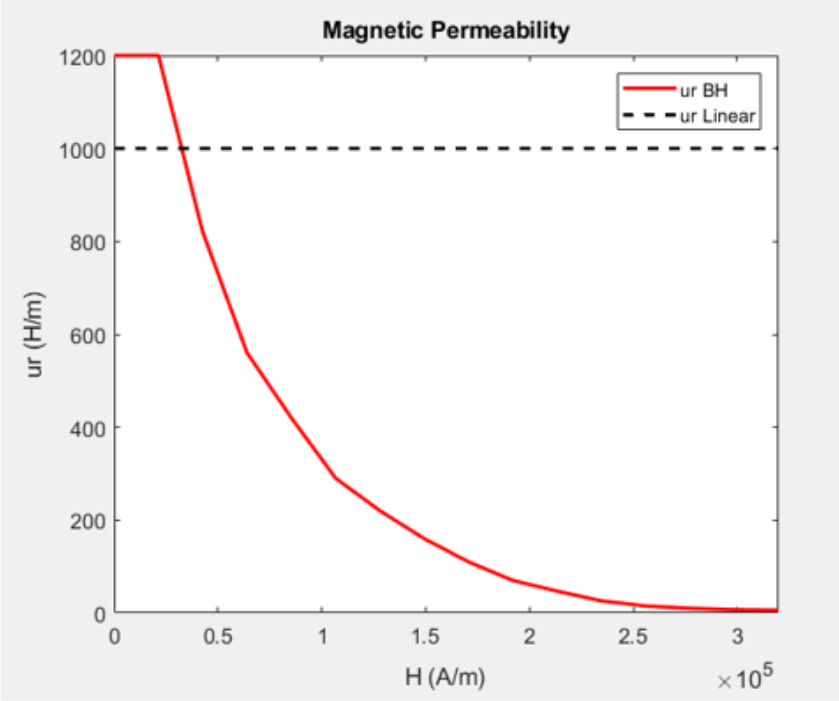

Fig. 2.24: Magnetic Permeability μ_r for Soft Iron Core Material – showing non-linear magnetic material, and linear magnetic material with μ_r=1000

Figure 2.24 indicates how the permeability drops off as the magnetic field strength input to the system increases and the core begins to saturate. As the core saturates fully, μ_r tends towards zero, which means that the magnetic field strength in the core increases, the permeability of the iron core decreases.

This property relates to materials or mediums of differing permeabilities, where it can be seen that materials supporting higher magnetic field strengths have lower permeabilities, and materials supporting lower magnetic field strengths have higher permeabilities. The relationship between magnetic field strength and permeability can be made clearer by examining the magnetic boundary conditions between two magnetically differing materials – iron and air. A sketch of a boundary between two materials can be seen in Figure 2.25 below [15].

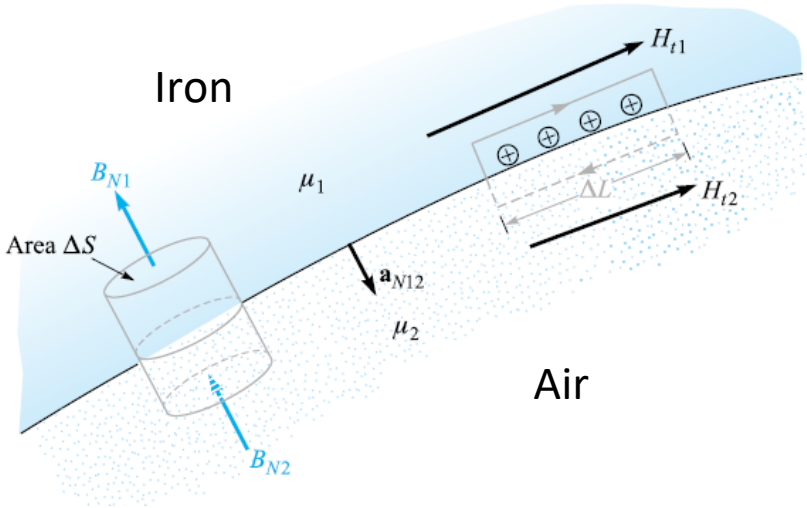

Fig. 2.25: Magnetic boundary between media 1 of iron and media 2 of air, having permeabilities of μ_1 and μ_2, respectively [15]

In Figure 2.25, a closed path is taken around a surface area ΔS, where the normal components of the magnetic flux densities of the two mediums are observed. Gauss's law for magnetism can be employed below in integral form to help more closely analyze what happens.

$$\oint_S \vec{B} \cdot d\vec{S} = 0 \tag{2.52}$$

From Eqn. 2.52, it can be seen that the normal components of each field must both sum to zero in order to satisfy Gauss's law for the magnetic field. This condition yields the following result of Eqn. 2.54.

$$B_{N1} \cdot \Delta S - B_{N2} \cdot \Delta S = 0 \tag{2.53}$$

$$B_{N1} = B_{N2} \tag{2.54}$$

This result states that the normal component of the two magnetic flux densities must be equal to each other [15]. Further analysis yields an expression for the normal components of the magnetic field strengths for the two mediums.

$$\mu_0 \mu_1 \cdot H_{N1} = \mu_0 \mu_2 \cdot H_{N2} \tag{2.55}$$

$$H_{N1} \cdot \frac{\mu_1}{\mu_2} = H_{N2} \tag{2.56}$$

From Eqn. 2.56, it is evident that if the permeability of medium 1 is larger, then the normal component of the magnetic field strength of medium 1, will also be larger. This corresponds to the field strength of the medium with the higher magnetic permeability essentially "pushing" the field from itself, to the medium of lower magnetic permeability. In iron, μ_r is often very large, with values around 5000 H/m, while air has a permeability of 1 H/m. This means that the normal component of the magnetic field strength in iron is 5000 times higher than that of air, which correlates to a strength or force 5000 times higher pushing the field from the iron core to the air around it.

2.3.2 Magnetomotive Force

It was mentioned above in the Motor Basics Section that iron helps constrain magnetic fields to paths of smaller distances. In this way, the field becomes stronger, however, it is not necessarily the longer path a field travels to enclose itself that decreases its strength. The path in air is usually a bit longer,

but only about three to five times as long as the path in iron. The main reason the field strength is much higher is the fact that fields in highly magnetically permeable materials are pushed or driven to less magnetically permeable materials and thus concentrate the field strength in these regions [13].

This force can be described as the Magnetomotive Force or MMF, and is best described by Ampere's Law, as the product of the magnetic field strength $\vec{H}$ and its closed path $d\vec{l}$.

$$\Theta = \oint_{(c)} \vec{H} \cdot d\vec{l} = \iint_S \vec{J} \cdot d\vec{S} = H \cdot L = \Phi \cdot \mathcal{R} = N \cdot I \tag{2.57}$$

Where Θ is the MMF [13], [21]. The MMF is a phenomenon that gives rise to magnetic fields. Electrons within the material itself oppose the magnetic field and create a force that can be observed as the MMF [13]. This opposing force "pushes" the field from materials with higher magnetic permeabilities to materials with lower magnetic permeabilities. In this manner, the iron core provides the MMF force necessary to drive the flux throughout its closed path. Note, flux does not flow as electric current flows through a circuit, it is rather a state of molecules in a material [13].

The MMF can also be described in other ways, as seen in Eqn. 2.57 above. The most appropriate form for this linear motor application is the turn number times the current, measured in ampere-turns (At).

Thus, it is clear why it is desirable to increase the flux passing through the stator core: flux is the main component of the MMF and by increasing the flux, thee MMF increases. It will be shown in the subsequent sections that the MMF is directly related to how the Lorentz Force is produced, which is the main parameter of interest in generating the thrust for this linear motor.

2.3.3 Reluctance and the Magnetic Circuit

It was stated above that the MMF is the force pushing or guiding the flux towards materials of lower magnetic permeabilities. However, the path that the flux takes, is defined differently; as a material's *reluctance*. Magnetic reluctance can be most easily thought of as a kind of magnetic resistance property, which essentially defines the path for the magnetic flux lines to follow inside of a magnetic material. Just as in an electric circuit, where the current takes the path of least electric resistance, in a magnetic circuit or path, the flux exists through the path of least magnetic resistance, or *reluctance* [15].

Rearranging Eqn. 2.57 allows the reluctance to be defined as the ratio of the MMF to the magnetic flux.

$$\mathcal{R} = \frac{\Theta}{\Phi} \tag{2.58}$$

The reluctance defines the path in which the flux exists, which is why flux paths are shorter through the magnetic material. If the μ_r of a material is higher, the reluctance will be lower and thus the path taken is shorter. This property can be seen if Eqn. 2.58 is manipulated to show the following;

$$\mathcal{R} = \frac{\Theta}{\Phi} = \frac{H \cdot L}{B \cdot S} = \frac{H \cdot L}{\mu H \cdot S} => \mathcal{R} = \frac{L}{\mu_0 \mu_r \cdot S} \tag{2.59}$$

From Eqn. 2.59, it can be observed that as μ_r of a magnetic material increases, the length of the path which the flux takes, L, decreases. Therefore, if the stator core is made of iron, the magnetic permeability will be higher in this material, meaning it can support higher magnetic field strengths. A higher magnetic field strength means that the MMF driving the field lines or flux will be much larger than in any surrounding materials and will force the field towards these materials of lower magnetic

permeabilities. The route is dictated by the iron's magnetic reluctance, which will favor paths of shorter lengths.

Not only can magnetic reluctance be explained from a field perspective, but the reluctance can also be explained by a circuit analogue. In this analogy, the entire linear motor is described by a corresponding magnetic circuit. The magnetic circuit can be constructed to detail the resistances and reactance's in the system and help determine the voltage levels supplied to the motor.

A simplified magnetic circuit for the primary stator core and stator windings with a passive aluminum "blade"-type secondary, can be seen below in Figure 2.26.

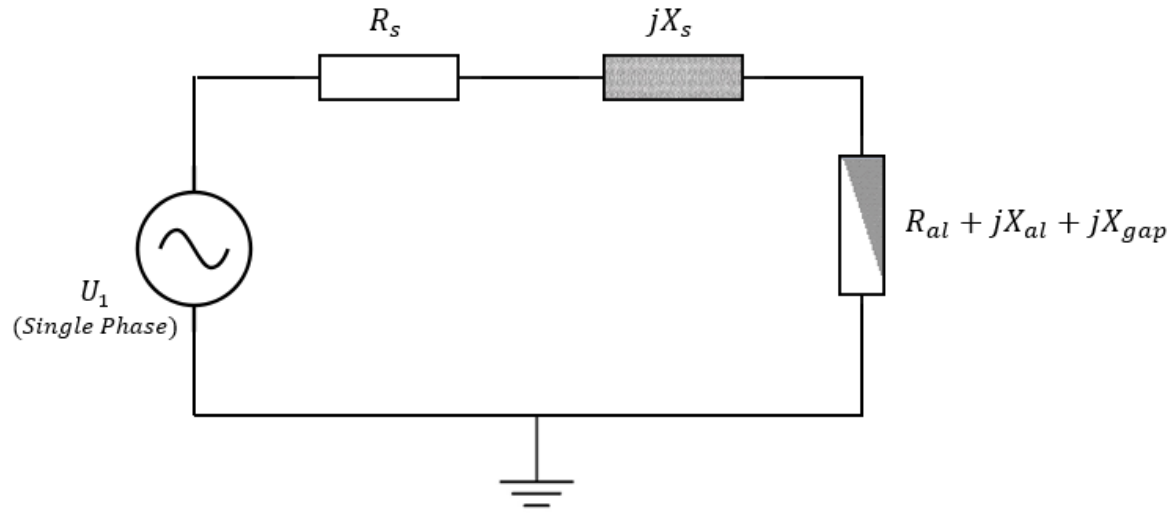

Fig. 2.26: Magnetic Circuit of the LIM showing Stator Winding Resistance, Rotor Reactance and Resistivity of Rotor for a single phase of the linear motor

Where R_s is the stator winding resistance, jX_s is the inductive stator winding reactance, R_{al} is the resistivity of the secondary aluminum rotor blade, jX_{al} is the inductive reactance of the aluminum rotor blade, and jX_{gap} is the reactance of the air gap (which can also be capacitive) [21], [13].

In 3-phase systems, it is best practice to calculate everything in terms of 'per phase'. Therefore, the source is represented as one phase of the system, U. The other phases, V and W, would be the same.

The rotary motor's equivalent circuit includes the rotor's mechanical rotating losses. The magnetic circuit for the linear motor on the other hand is much simpler, as these losses do not exist. However, the dominant losses in the linear motor are from the stray flux[4] losses of the motor, which often constitute a large percentage of the flux produced [13]. These stray flux losses do not contribute to overall thrust production of the motor and must therefore be minimized, while the useful or contributing flux should be maximized. A depiction of the stray flux compared to the useful flux can be seen below in Figure 2.27.

[4] Stray flux is defined as the flux which links one or two windings together, and acts just as the name suggests; stray. It can exist in air and usually encircles the coils. This stray flux leaks through all parts of the machine, and is unused in thrust production. The reason it is unused is that it does not generally pass near enough to the rotor to induce sufficient eddy currents into the rotor blade. Stray flux is sometimes referred to as leakage flux.

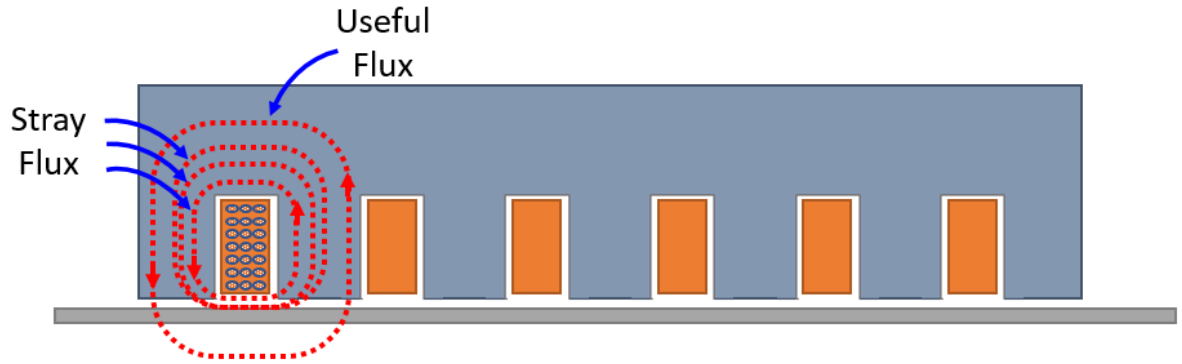

Fig. 2.27: Depiction of Stray or Leakage Flux, and the Magnetization or Useful Flux: Flux which contributes to Thrust Production by inducing eddy currents in the secondary – shown for simple 6-Slot Single-Sided LIM Variant

Observation of Figure 2.27 shows that the "Useful" flux penetrates all the way through the rotor, which ensures successful induction of the eddy currents. This penetration through the rotor distinguishes the stray flux from the useful flux, also referred to as the magnetization flux. The magnetization flux is responsible for thrust production and should be maximized where possible.

Stray flux losses are important to the overall design of the LIM, and can have large performance decreasing effects if not taken into account and mitigated. This will be seen later as the stray flux is actually a large contributor to the differences between analytical calculations and Comsol simulation results. Comparison of the two shows how the thrust and induced voltage results differ greatly. This disparity is due to the analytical calculations not incorporating stray flux losses, while the Comsol simulations do take these losses into account when simulating.

2.4 Faraday's Law of Induction

It was seen above that the travelling stator field is created by exciting the stator windings with a 3-phase source, where each input is out of phase from the other by 120°. Upon excitation of the windings, an electric potential develops across each coil winding and a corresponding current flows through them. From this point, the changing electric potential across the coil windings generates and sustains a magnetic field, and flux proportional to the turn number of the winding, exists around the coil. This phenomenon is described by Faraday's Law and is shown below in Eqn. 2.60 [15].

$$\mathcal{E} = -N\frac{d\Phi_B}{dt} \tag{2.60}$$

Where $\mathcal{E}$ is the electromotive force or EMF (proportional to an induced voltage drop across a coil), N is the turn number of that coil, and Φ_B is the flux around this coil. Eqn. 2.60 can also be interpreted in terms of flux. A change in flux over time produces a current that flows through a coil of N windings, which in turn generates an electric potential or EMF across those windings. The direction of the EMF is given by the negative sign in Eqn. 2.60 from Lenz's Law [15].

The stator windings or coils can be modeled as an inductor that stores energy in a magnetic field when current is passed through the coil. Changes in in the electric potential (or EMF) at the ends of the coil alter the amount of current flowing through the windings, which will produce a proportional change in the magnetic field as the inductor tries to resist this change in current [15]. Similarly, if the magnetic field changes over time, the field will collapse around the inductor and current will be induced in the windings of the coil. Therefore, when there is an electromotive force or EMF, induction is also present: this is Faraday's Law [15].

To elaborate, induction is a phenomenon concerning electric and magnetic fields whereby magnetic field changes produce electric fields, at the same moment and in the same place [17], [13].

Induction is therefore taking place in the motor due to the electric potential which is dropped across the stator windings. The EMF across the windings causes a proportional current to flow that produces the stator magnetic field according to Faraday's Law. This stator magnetic field varies in position, and sweeps across the length of the stator because the excitation is by a simultaneous 3-phase source.

As the travelling stator magnetic field sweeps across the stator, flux passes through and interacts with the rotor to induce eddy currents according to the Maxwell-Faraday Law of Eqn. 2.61.

$$\nabla \times \vec{E} = -\frac{\partial \vec{B}}{\partial \mathrm{t}} \tag{2.61}$$

Where the travelling stator field is defined as a time-varying magnetic field to the rotor, denoted here as $\partial\vec{B}/\partial \mathrm{t}$, and creates a corresponding electric field strength, $\vec{E}$, from Faraday's law [13], [15]. Since the electric field strength is proportional to the product of the medium's current density and its conductivity (i.e., by Eqn. 2.7), it is analogous to an electric current. Therefore, the stator's time-varying magnetic field induces currents in the conductive rotor secondary, herein referred to as *eddy currents*. These induced eddy currents lead to thrust generation in the LIM and help to realize the basic working principle behind an asynchronous motor: *Induction*, as is stated in the name of the motor; linear *induction* motor.

2.4.1 Eddy Currents

These eddy currents are induced from the EMF existing across a given stator winding. Once induced in the rotor by the travelling stator field, the eddy currents will in turn produce an equal and opposite magnetic field of their own. The generation of this field follows the same laws by which the eddy currents themselves were produced. However, the order is now reversed: while the induced currents were initially created by a time-varying magnetic field, now, the time-varying eddy currents produce a magnetic field. The resulting magnetic field is equal and opposite to the initial stator field from the source.

Thus, Eqn. 2.1 and Eqn. 2.2 sustain one another as is the case in a propagating electromagnetic wave. Additionally, just as the stator field is produced from 3-phase alternating currents, this newly created field from the eddy currents will also be 3-phase and alternating. These properties allow the rotor field to sweep the length of the motor like the travelling stator field does. This interaction of the traveling stator field to induce eddy currents in the rotor blade and the subsequent production of a corresponding magnetic field by the eddy currents can be seen in Figure 2.28 below.

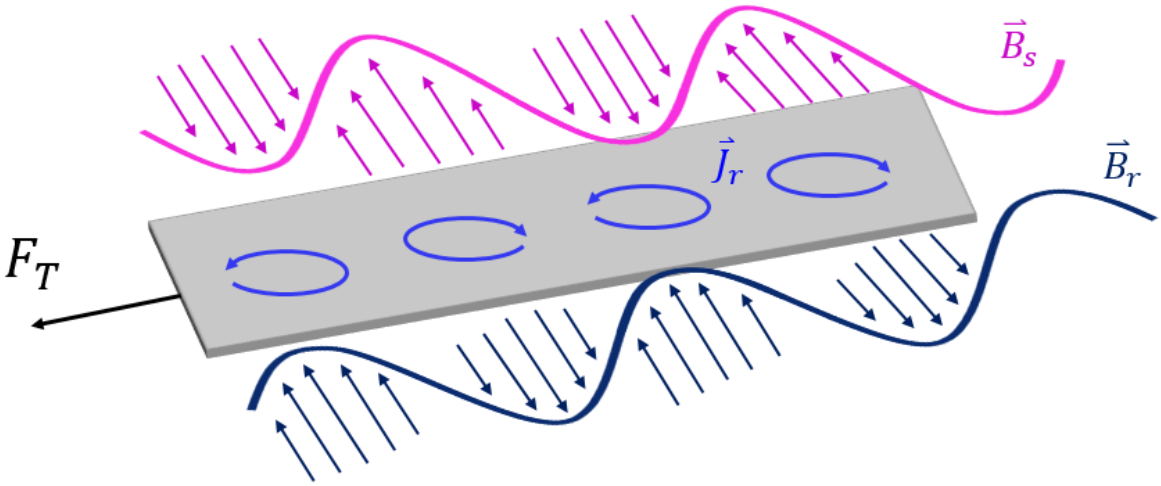

Fig. 2.28: Travelling Stator Magnetic Field (pink) induces eddy currents (light blue) in the rotor, which produce an equal and opposite rotor field (dark blue)

As can be seen from Figure 2.28, the travelling stator field, B_s (pink), sweeps past the rotor and induces eddy currents, J_s (light blue), which produce an equal and opposite magnetic field in the rotor, B_r (dark blue). These fields are self-sustaining as long as the source persists. A force (black), shown in Figure 2.28, acts on the plate to propel the motor.

2.4.2 Induced Stator Voltage

After having investigated eddy currents, it's possible to calculate exactly what the induced stator voltage is that induces these eddy currents. Quantifying the EMF, or induced voltage drop across the stator windings, makes use of Faraday's Law again.

$$\mathcal{E} = -N\frac{d\Phi_B}{dt} \tag{2.62}$$

From the equation, it is evident that the induced stator voltage, or EMF, increases with a corresponding increase in the turn number N of the windings. However, the EMF is a function of the time-dependent magnetic flux around the stator windings, therefore, the flux must first be analyzed.

Looking back at Eqn. 2.50, the magnetic flux is the product of the magnetic flux density and the surface area through which a number of flux lines passes. The magnetic flux passing through one phase of the LIM is calculated across its active surface area in Eqn. 2.63.

$$\begin{aligned}\Phi_B(t) = D\int_0^{\tau_p} B_x(y,t)\,dy &= D\int_0^{\tau_p} B_1 \cdot e^{j\left(-\omega t+\frac{\pi}{\tau_p}y+\varphi\right)}\,dy \\ &= -j\frac{\tau_p}{\pi}\cdot D\cdot B_1\cdot e^{j(-\omega t+\varphi)}\cdot\left[e^{j\pi}-1\right] = 2j\frac{\tau_p}{\pi}\cdot D\cdot B_1\cdot e^{j(-\omega t+\varphi)}\end{aligned} \tag{2.63}$$

Where D is the stack width, (i.e., width of the stator core); τ_p is the pole pitch; B_x is the magnetic flux density in the air gap, as a function of time and space directed vertically along the LIM; y is the position along the y-axis (direction of linear travel); φ is the phase shift of the magnetic flux density; and B_1 is the amplitude of the magnetic flux density. These parameters will be defined in more detail below in the Lorentz Force Section.

For the induced voltage, it is the pole pitch, instead of the length, over which the integration takes place. The total magnetic flux of the motor resides within one pole pitch: it flows into the rotor and comes back through the other pole pitch to the stator. Therefore, integration over the entire length of the motor, would result in zero flux captured because the total field contribution from pole pitch

pairs would cancel each other out, as they are the opposite of each other: Eqn. 2.4. To correctly determine the magnetic flux, integration must be performed over only one pole pitch and not the entirety of the motor length [22].

From Eqn. 2.63, the time derivative of the flux is then multiplied by the turn number, N, to get the total EMF or induced voltage of the stator windings, as seen in Eqn. 2.64.

$$\mathcal{E} = E_s(t) = -N\frac{d\Phi_B}{dt} = -N\frac{d\left(2j\frac{\tau_p}{\pi}\cdot D\cdot B_1\cdot e^{j(-\omega t+\varphi)}\right)}{dt} \tag{2.64}$$

Substitution of a sinusoidal frequency domain dependency, $j\omega_s$, for the time dependent derivative, d/dt, is performed in Eqn. 2.65 to help simplify the equation.

$$E_s(t) = -N\frac{d\Phi_B}{dt} = -N\cdot(j\omega_s)\cdot 2j\frac{\tau_p}{\pi}\cdot D\cdot B_1\cdot e^{j(-\omega t+\varphi)} \tag{2.65}$$

The stator induced voltage is a function of time and can be treated as a first order, differential equation with a particular solution equal to an exponential multiplied by some amplitude. This scaled exponential is then set equal to the stator induced voltage function to determine the amplitude of the induced stator winding voltage.

$$E_s(t) = N\cdot\omega_s\cdot 2\frac{\tau_p}{\pi}\cdot D\cdot B_1\cdot e^{j(-\omega t+\varphi)} \tag{2.66}$$

$$E_s(t) => E_1\cdot e^{j(-\omega t+\varphi)} = N\cdot\omega_s\cdot 2\frac{\tau_p}{\pi}\cdot D\cdot B_1\cdot e^{j(-\omega t+\varphi)} \tag{2.67}$$

Cancelling out the exponential function on both sides of the equation yields the amplitude of the induced stator winding voltage. After some additional algebra, a more elegant expression can be obtained.

$$E_1 = 2\cdot\omega_s\cdot\frac{\tau_p}{\pi}\cdot D\cdot N\cdot B_1 = 2\cdot v_s\cdot D\cdot N\cdot B_1 \tag{2.68}$$

The sync speed for the motor is substituted into Eqn. 2.68, and the induced stator voltage is quantified as a function of the sync speed, the stack or core width, the turn number, and the amplitude of the magnetic flux density. This induced voltage, or EMF, is observed across the stator windings, and as a consequence, the travelling stator field is produced. It is because the stator field *induces* eddy currents in the rotor that this motor is classified as a linear induction motor. The following section will show how the stator field interacts with this equal and opposite rotor field to create a time-average Lorentz Force between the stator and the rotor to generate thrust.

2.5 Lorentz Force

It was seen in the previous sections that the induction of eddy currents in the rotor leads to the generation of an equal and opposite magnetic field that is attracted to the stator magnetic field. The field produced from the induced eddy currents will be slightly slower than the stator field: the difference in speed is the slip. This slip delay is linear and always moving along the stator with the progression of the travelling field. The constant difference between the stator field and induced field of the rotor creates the opportunity for a magnetic force. Since the rotor moves at a speed slightly slower than the stator, it will always try to “catch up” and match the speed of the stator field (i.e., the sync speed) and will exhibit a sort of “chasing” behavior. As discussed in the Slip Section, once the

rotor reaches the sync speed, the force driving the rotor will drop off, causing it to stop accelerating. It is therefore evident that some force in the system causes the rotor to move towards the stator.

This force is the *Lorentz Force* and on a very low level, it is the force acting on moving charges as they travel through an electric and magnetic field [15]. The Lorentz Force exerted on moving particles in a magnetic field is detailed below in Eqn. 2.69.

$$\vec{F} = Q\left(\vec{E} + \vec{v} \times \vec{B}\right) \tag{2.69}$$

Where Q is the charge of the particle moving through an electric field strength, E, and magnetic flux density, B, at some velocity, v. The direction of the force is the cross-product of the velocity and the magnetic flux density, and is thus perpendicular to both v and B [15]. In a linear motor, the thrust generated is simply due to this Lorentz Force exerted on moving particles (i.e., eddy currents in the rotor) in the presence of an electric and magnetic field (i.e., stator travelling field).

The force acting on the rotor is the cross-product of the induced eddy currents and the stator magnetic flux density. The right-hand rule depicting the Lorentz Force is shown in Figure 2.29.

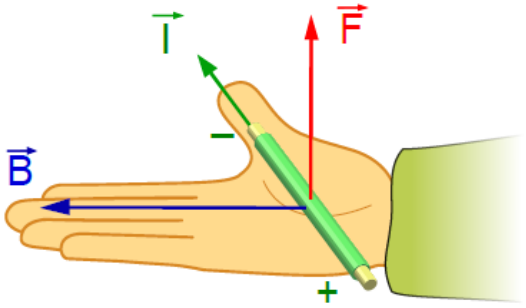

Fig. 2.29: Right Hand Rule for the Lorentz Force acting on a current carrying conductor – showing how the force produced (red) has a direction given by the cross-product of the magnetic flux density (blue) with the current (green), [18]

The combination of the stator magnetic field and the induced eddy currents in the rotor results in a torque that generates a thrust. In this manner, energy supplied from an electrical source is transferred to a linear mechanical motion, as described in the motivation for using an electric motor. The thrust produced by the motor can be seen more clearly by observing Figure 2.30, which depicts a sample 2-pole, 6-Slot linear motor above a conductive rotor plate.

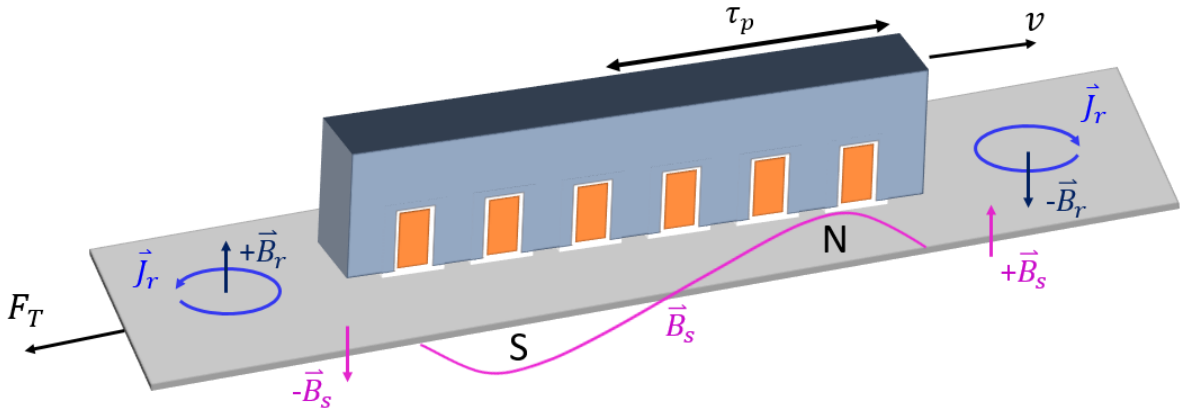

Fig. 2.30: 2-Pole 6-Slot Linear Motor Example – showing how when the stator field (pink) is produced from 3-phase excitation of the stator windings, the eddy currents (light blue) are created, thus, generating their own equal and opposite magnetic field (dark blue), thus creating a thrust force on the rotor, which moves the stator at a velocity v: assuming the rotor is fixed in place so it cannot move

As can be seen in Figure 2.30, as the stator field induces eddy currents, J, in the rotor, corresponding magnetic fields opposite in direction to the stator field are created from Ampere's Law. These magnetic fields then create the Lorentz force that moves the stator[5] at velocity v.

Another way to examine the Lorentz force is to look at a simpler picture of a magnet moving over a conductive plate in Figure 2.31. The magnet produces a DC magnetic field, so the field will remain constant. However, if the magnet is moved over some distance at a certain velocity, then the change in flux experienced by the conductive plate also changes. The fact that the magnet moves means that eddy currents will be induced in this plate by the flux lines of the magnet sweeping past the conductive plate. As seen, these eddy currents produce their own corresponding magnetic field relative to the changing flux from the moving magnet.

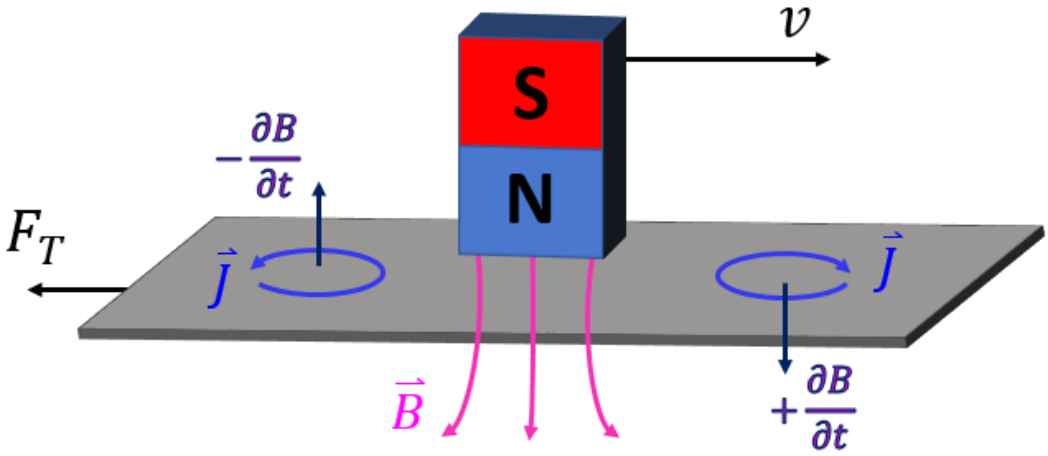

Fig. 2.31: Simple magnet showing induced eddy currents when thrust force exerted on magnet – or it is moving. approximated with a simple DC field. but then when you have a 3-phase AC "travelling" or moving field, the rotor will want to follow the stator, or in this case, the magnet.

Figure 2.31 shows that from the perspective of the conductive plate, as the magnet moves across the plate, there will always appear to be an increasing flux in the front of the magnet, and a decreasing flux behind the magnet. These fluxes this will act to "push" the plate from behind and "pull" the plate from the front, as the fields from the eddy currents try to align themselves with the slightly faster and continuously moving fields from the magnet. This scenario is similar to what happens to the rotor in the linear motor: the field from the eddy currents will always try to "catch up" to the faster time-varying travelling stator field.

This interaction of the eddy currents induced in the plate together with the source magnetic field is observed as the magnet sweeps across the aluminum plate at some velocity, v.

Understating how the Lorentz Force is developed in a linear motor, requires further investigation of the interaction between the induced eddy currents and travelling stator magnetic field. The combination of the stator magnetic field and the induced eddy currents gives rise to the Lorentz Force. Therefore, in order to quantify the thrust force produced by the LIM, Maxwell-Faraday's and Maxwell-Ampere's Laws must be deployed. These equations are the governing equations behind thrust production in the LIM.

[5] Note: in the entirety of this analysis, the rotor is the part of the motor assumed to be moving as the Lorentz Force acts on it to attract it to the stator. However, the part of the motor that moves can be reversed as it only depends on which part is fixed and which is left free. Therefore, either the rotor or the stator can be considered to be the moving part of the motor.

The following analysis is based on the methodology in [22], and Figure 2.32 is given as a layout of a sample double-sided LIM system to help put this scenario into context.

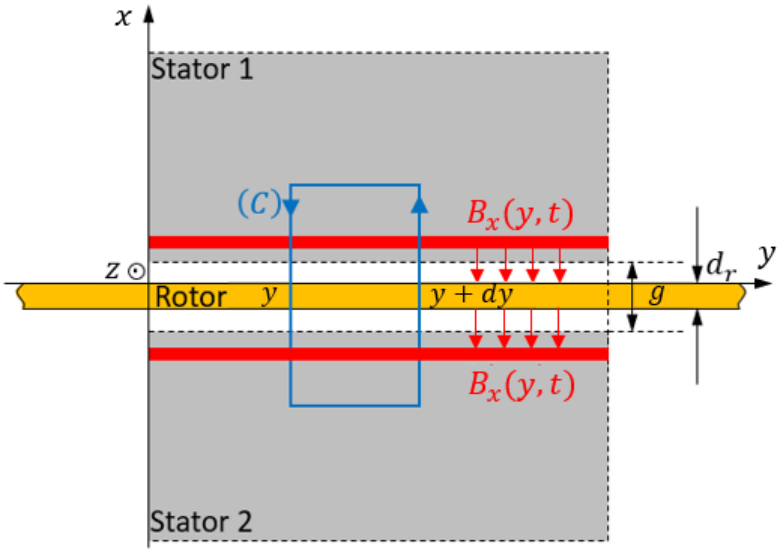

Fig. 2.32: Double-Sided LIM Scenario deployed to help develop Analytical Thrust Calculation [22] – showing induction of eddy currents from the two primary stator cores to the conductive rotor secondary

The travelling stator magnetic field is the starting point for the thrust force derivation.

$$H_{tot}(y,t) = \frac{6}{\pi} \cdot \frac{NI}{2g} \cdot \cos\left(\frac{\pi y}{\tau_p} - \omega t\right) \tag{2.70}$$

The total magnetic stator field in the air gap of the motor sweeps along the length of the stator to induce eddy currents in the rotor. It is important to have a high field concentration in the air gap so that as many eddy currents can be induced in the rotor as possible, since they are paramount for producing thrust in the motor.

The magnetic flux density in the air gap can be solved for to determine the amount of eddy currents induced in the rotor. The magnetic field strength of the stator field in Eqn. 2.70, can be converted to its corresponding magnetic flux density in the air gap through its constitutive relation.

$$B_x(y,t) = \mu \cdot H_{tot}(y,t) = \mu \cdot \frac{6}{\pi} \cdot \frac{NI}{2g} \cdot \cos\left(\frac{\pi y}{\tau_p} - \omega t\right) \tag{2.71}$$

The position-dependent magnetic flux incorporating these eddy currents can be seen if the magnetic flux density spans the entirety of the air gap. This relationship is given in Eqn. 2.72, where the eddy current density, J_z, is added to the equation for the position-dependent stator magnetic flux.

$$\frac{\partial}{\partial y} B_x(y,t) = \mu \cdot \left(\frac{6}{\pi} \cdot \frac{NI}{2g} \cdot \cos\left(\frac{\pi y}{\tau_p} - \omega t\right) + J_z(y,t) \cdot \frac{d_r}{g}\right) \tag{2.72}$$

As can be seen in Eqn. 2.72, the eddy current density must be multiped by the ratio of the rotor thickness to the total air gap length. This calculation takes the useable length of the air gap into account and determines how much space the induced current will encompass in the full air gap, as the total air gap in this case also encompasses the rotor plate.

These eddy currents must be incorporated into the above magnetic flux density equation because they originate from the magnetic flux as stated by Faraday's Law, before they are induced in the rotor. From Figure 2.29, it can be verified that J_z and B_x are orthogonal to each other.

The next step in the analysis is to quantify these eddy currents and solve for the magnetic flux density in the air gap. To do so, Eqn. 2.73 can be deployed to relate the induced eddy currents to the electric field strength.

$$J_z(y,t) = \sigma E_z(y,t) \tag{2.73}$$

These induced eddy currents, J_z , are a function of time and space and are connected to the electric field strength, E_z , through the conductivity of the rotor plate, σ. Now the electric field strength must be determined in order to solve for these currents and consequently, the magnetic flux density. Faraday's Law can be deployed again in Eqn. 2.74, to relate this electric field strength to the change in the passing flux.

$$\mathcal{E} = \oint_{(C1)} \vec{E} \cdot d\vec{l} = -\frac{d\Phi_B}{dt} \tag{2.74}$$

Where $C1$ is the closed curve over which the total electric components are summed and is perpendicular to the closed curve over which the magnetic field strength, C, is summed. Summing over this closed path C, yields the following equation relating the electric field strength to the magnetic flux density, as in [22].

$$\frac{\partial}{\partial y} E_z(y,t) = \frac{\partial}{\partial t} B_x(y,t) + v \frac{\partial}{\partial y} B_x(y,t) \tag{2.75}$$

Where it can now be seen that the magnetic flux density varies with position (i.e., along the length of the stator in the horizontal y-axis) and time.

With the expressions for the magnetic flux density in the air gap and the induced eddy currents, the system has been fully defined. Eqn. 2.72, Eqn. 2.73, and Eqn. 2.75, can be combined to find the magnetic flux density in the airgap. Combining the expressions yields Eqn. 2.76, which describes the behavior for the magnetic flux density in the air gap.

$$\frac{\partial^2}{\partial y^2} B_x(y,t) - \mu\sigma \cdot \frac{d_r}{g} \left[\frac{\partial}{\partial t} B_x(y,t) + v \frac{\partial}{\partial y} B_x(y,t) \right] = \mu \cdot \frac{6}{\pi} \cdot \frac{NI}{2g} \cdot \cos\left(\frac{\pi y}{\tau_p} - \omega t \right) \tag{2.76}$$

As seen from Eqn. 2.76, the combination of these equations leads to the creation of a second order non-homogenous differential equation. However, this is not a problem, because it is the particular solution of Eqn. 2.76, which has the form of a scaled exponential, that is of interest. The particular solution is given in Eqn. 2.77.

$$\underline{B}_x(y,t) = B_1 \cdot e^{j\left(\frac{\pi y}{\tau_p} - \omega t + \varphi\right)} \tag{2.77}$$

The particular solution for the magnetic flux density can then be substituted back into Eqn. 2.76 in order to obtain the amplitude of the magnetic flux density, B_1, and the phase shift, φ. After this substitution and reducing and simplifying the equations, the amplitude of the magnetic flux density can be expressed as in Eqn. 2.78.

$$B_1 = \frac{3\sqrt{2} \cdot \Theta}{\sqrt{\left(\frac{\pi g}{\mu}\right)^2 + (v_s - v_r)^2 \cdot \left(\sigma \cdot d_r \cdot \tau_p\right)^2}} \tag{2.78}$$

Where Θ is the MMF comprised of $(N \cdot I)$, g is the air gap distance, v_s is the sync speed, v_r is the mechanical speed of the rotor, σ is the conductivity of the rotor, d_r is the thickness of the rotor plate, and τ_p is the pole pitch.

The corresponding phase shift φ of the magnetic flux density can also be found and is shown below in Eqn. 2.79.

$$\varphi = \tan^{-1}\left[\frac{\pi g}{\mu \cdot \sigma \cdot d_r \cdot \tau_p \cdot (v_s - v_r)}\right] \tag{2.79}$$

Now that all parts of the magnetic flux density in the air gap have been solved for, the induced eddy current density can be substituted back into Eqn. 2.73 and Eqn. 2.75 to acquire an expression for the eddy currents induced in the rotor, as seen in Eqn. 2.80.

$$J_z(y,t) = \sigma \int \frac{\partial}{\partial t} B_x(y,t)\, dy + \sigma \cdot v \cdot B_x(y,t) \tag{2.80}$$

$$J_z(y,t) = -\sigma(v_s - v_r) \cdot B_1 \cdot e^{j\left(\frac{\pi y}{\tau_p} - \omega t + \varphi\right)} \tag{2.81}$$

At this point, the time-average Lorentz Force acting on the rotor can be described by the interaction of the varying stator magnetic flux density in the air gap with the eddy currents induced in the rotor, as shown in Eqn. 2.82.

$$F_{Thrust} = D \cdot d_r \int_0^L Re\{J_z(y,t) \cdot B_x^*(y,t)\}\, dy \tag{2.82}$$

The thrust is therefore the integral of the stator magnetic flux density conjugate along the rotor, B_x^*, multiplied by the induced eddy current density, J_z , and integrated over the length of the stator, L, and multiplied by the stator width, D, and rotor thickness, d_r .

Plotting the equation describing the LIM's thrust for every velocity through the motor's operational range (i.e., from 0 m/sec up to the sync speed) produces a curve that describes the linear motor's performance. This curve is called a linear motor's *thrust curve* and is the best method of describing how the motor will perform at every velocity during operation. The peak thrust for the motor and the velocity at which it occurs can be extracted from this curve. A generic thrust curve is plotted below in Figure 2.33 for the given driving direction, according to Eqn. 2.82.

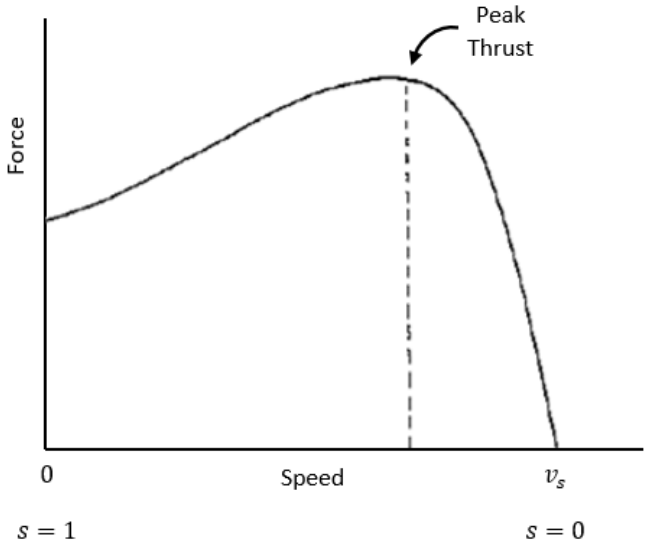

Fig. 2.33: Typical Thrust Curve showing peak thrust point near a slip of 0, where v_s is almost reached [13]

It can be seen from this curve that the peak thrust occurs when the rotor is almost at the sync speed. After this peak thrust point, the thrust falls off rapidly and at the sync speed, the thrust force is zero. The thrust goes to zero because when the rotor finally reaches the same velocity of the stator field, there is no longer any slip, or difference in the velocities of these two fields. If velocity increases beyond the sync speed, the motor will enter a regeneration region and it will act as a generator, which is undesirable in this application.

Thus, the process by which a linear motor produced thrust has been clarified. The Motor Design Section will show the linear motor in this thesis is designed to achieve the thrust required to propel a Hyperloop Pod to the desired sync speed.

2.6 End-Effects

End-effects are described as decreases or losses in the linear motor's performance due to the open-ended air gaps at the ends of the linear motor [19]. These air gaps constitute the biggest difference between rotary and linear motors and heavily influence the motor's thrust, power factor, and efficiency, all of which are reduced as a consequence of end-effects. End-effects do not exist in a rotary machine because there is never an "end", as the motor is circular and continuous. Therefore, the rotating stator field will always be continuously rotating without interruption.

However, in a linear motor, there is a "beginning" and an "end", which has the effect of "cutting off" the field at the motor ends. This interruption of the field means it is not a continuously travelling field anymore. Therefore, the field of the linear motor abruptly stops and starts at the beginning and ends of the motor instead of continuously flowing. End-effects lead to discontinuities in the stator field, and if not mitigated properly, can degrade design performance [19].

At low speeds, the end-effects are not significant and do not come much into play. However, at the higher speeds, they start to have a greater impact and become problematic [19]. At high speeds, the magnetic field distribution in the air gap, which was seen to be important for the overall thrust produced, is different at the ends of the motor, where the air gap is "open", more than in the middle.

The difference is due to the "entering" and "exiting" travelling stator fields having a different wave velocity when compared to the fields in the middle of the motor. The decay rate or attenuation of these "entering" and "exiting" fields is low, which allows them to interface with the thrust producing fields in the middle of the motor [19]. For instance, the entry-end-effect field decays rather slowly and is present along the entire longitudinal length of the air gap. This field significantly degrades performance by interfering with the phase distribution of the magnetic field in the air gap produced by the motor's main stator field.

One solution to this issue is to vary the frequency of the motor during operation. End-effects play a large role in the high-slip region of the thrust curve. Therefore, by always operating in a low-slip region, near the synchronous speed, these end-effects can be mitigated. Using a variable speed or frequency drive allows for this kind of operation. Additionally, the thrust is relatively small in this high-slip region, so operation is kept to the region of the thrust curve near the synchronous speed. Therefore, if the motor is operating near synchronous speed, end-effects should be minimized.

Another way to help further reduce the contribution of the end-effects is to adjust parameters such as the air gap distance, pole number, supply frequency, secondary resistivity, etc. However, it can be

that by tweaking these variables to reduce the influence of the end-effects, motor performance decreases. Therefore, a trade-off must be made when selecting and adjusting parameters.

End-effects can also be mitigated by altering the winding configuration. The main mechanism behind these end-effects is the non-uniform magnetic field distributions in the air gap, which lead to performance degradations because of the discontinuity between the beginning and end of the motor. A more gradual travelling stator field would help guide the transition from the end of the motor to the beginning. Therefore, for 3-phase excitation, proper winding techniques should be implemented to ensure symmetric and gradual phase distribution throughout the linear motor. Such techniques include increasing the number of slots or windings per phase of the stator: doing so yields a better approximation of the sine-like distribution of the travelling stator field. In this way, the disruption in the field seen from the end-effects is less and the field distribution in the air gap will appear less discontinuous to the secondary.

One final end-effect mitigation technique is to make the last teeth (i.e., the *end teeth*) on the beginning and end of the motor larger. Making the end teeth larger helps alleviate some of the end-effects by capturing more of the field. Capturing more of the field helps increase the overall thrust produced by adding more active surface area to the end teeth, which have been seen to saturate slightly faster than the other teeth in simulations.

2.7 Paschen's Law

Another important consideration for the motor, which introduces an additional challenge to overcome, is that it must also operate in the low-pressure environment of the tube. Operating in a low-pressure environment means there is an increased probability for voltage breakdowns within the motor. Voltage breakdowns can occur when operating at the high voltages needed to drive the motor in reduced pressure environments. The low-pressure environment or "near-vacuum" levels inside the tube help reduce air friction on the vehicles or Pods. Therefore, even if the motor works well in ambient pressure, this is no guarantee that it will also work well in the low-pressure environment of the Hyperloop tube.

To explain the problem further, a voltage breakdown is a discharge event that can occur between two conductive objects separated by a specific distance in a given medium, at certain pressures. A voltage breakdown can be defined as a conductive channel that is created by discharges between the two conductive objects. This discharge occurs when the electric field potential between the two conductive objects is high enough for a given separation distance or pressure in the medium. The product of the two, pressure and distance, is stated as pd, and represents a key quantity in the analysis. Once this product equals a specific value, a breakdown can occur.

Therefore, the pressure in the medium and distance act as a sort of insulation between conductive objects. They do not allow a connection, or channel, between the objects unless the conditions of the environment changed to support potential breakdowns. Such changes can include decreasing the pressure, decreasing the distance between the objects, or increasing the electric field potential between the objects. An example illustration of a few potential scenarios can be seen in Figure 2.34.

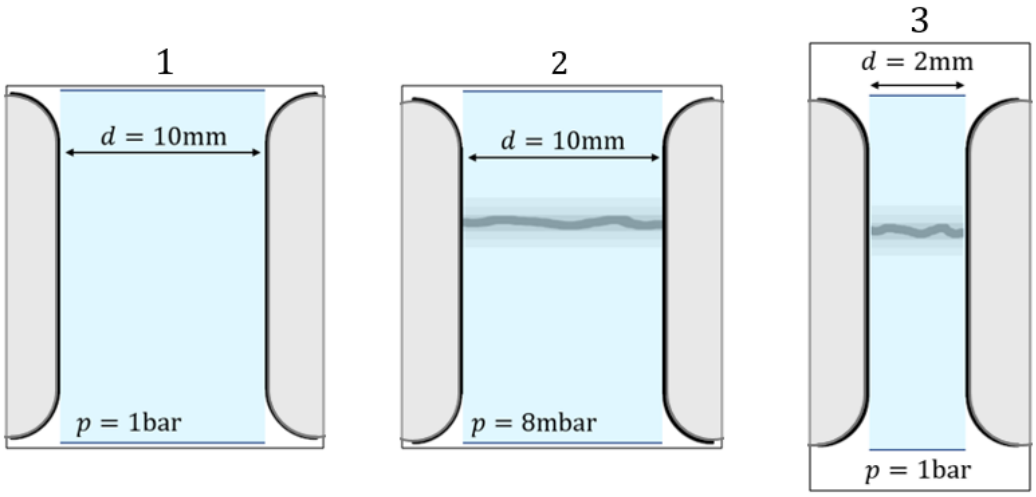

Fig. 2.34: Different scenarios for Paschen's Law in Air (light blue) – showing that if either the pressure or the distance is changed, voltage breakdowns can occur, as the effect of creating conductive channels between two conductive objects, depends both on the pressure of the medium and the distance between the objects

It can be difficult to quantify these effects analytically and most attempts only yield approximate results. Most analysis is performed experimentally and solving the derived analytical equations to explain these effects shows the differences in the two results. Nevertheless, estimates of the voltage breakdown point can be made to provide a general idea of where a possible breakdown can occur. Pachen's Law can be deployed in this endeavor to help analyze the voltage breakdown between two conductive objects of a certain separation distance, and to describe and quantify this level in given gaseous mediums. Eqn. 2.83 models this phenomenon and describes the voltage breakdown V_B, [24], [25].

$$V_B = \frac{B \cdot pd}{\ln\left[\frac{A \cdot pd}{\ln\left(1 + {}^{1}/_{\gamma_{se}}\right)}\right]} \tag{2.83}$$

Where p is the pressure of the medium, d is the distance between the two conductive objects in question, and A, B, and γ_{se} are all constants describing the ionization characteristics of the medium. A is the saturation ionization in the gas at a certain electric field strength, B is related to the excitation and ionization energy, and γ_{se} is the secondary ionization coefficient [25]. These values describe the medium's electron mobility and how ions are produced during the fundamental mechanism behind the discharge channel's creation, *avalanching*. This effect of avalanching is illustrated in Figure 2.35.

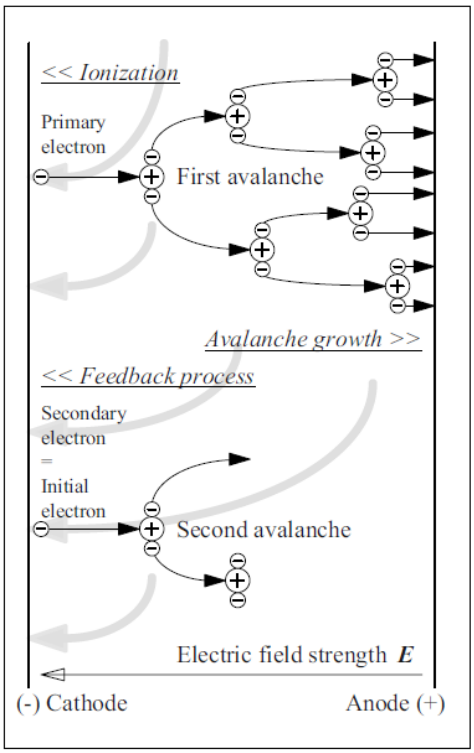

Fig. 2.35: Avalanching Effects depicted [24], where the Primary electron is the original or initial ionization event, from which the ionization events occur and avalanching follows if there is enough energy to do so.

Avalanching is best described as a process in which a number of free electrons in a transmission medium, subject to strong acceleration by an electric field, collide with other atoms and ionize them upon impact: a phenomenon otherwise referred to as *ionization* [24]. Ionization is a process by which an atom or a molecule acquires a negative or positive charge by gaining or losing electrons [24]. The acquisition or loss of electrons in this case is due to collisions with other atoms, molecules, or ions. After the initial ionization event takes place, the released electrons can collide with other molecules in the medium, which subsequently release additional electrons that accelerate and collide with other atoms. This cascading release of electrons is the avalanching effect.

These ionization values are key in explaining when a voltage breakdown occurs. However, obtaining these values is not straightforward and is generally accomplished experientially, which leads to wide variations depending on the source used. However, these variations make sense as the parameters greatly depend on the pressure, temperature, and chemical composition of the medium. Since air is most commonly taken as the medium of interest, and is the medium to be used in a Hyperloop-like system, it is instructive to study how these values differ over varying environments. Table 2.1 shows the values for the ionization parameters used in this thesis from [25], which seem to match up closely to those of [24].

Parameters used in Evaluating Voltage Breakdown (for Air)			
$p \cdot d$ [kPa-cm]	0.0133 – 0.2	0.2 – 100	100 – 1400
k	$2.0583 \cdot (pd)^{-0.1724}$	$3.5134 \cdot (pd)^{0.1599}$	4.6295
A [ionization/kPa-cm]	112.5		
B [V/kPa-cm]	2737.5		

Table 2.1: Ionization parameters used in Evaluating Voltage Breakdown (for Air) – for the given pd pressures distance range

Using these values in conjunction with Paschen's Law of Eqn. 2.83, over a specified range for pd, yields the curve in Figure 2.36 for air.

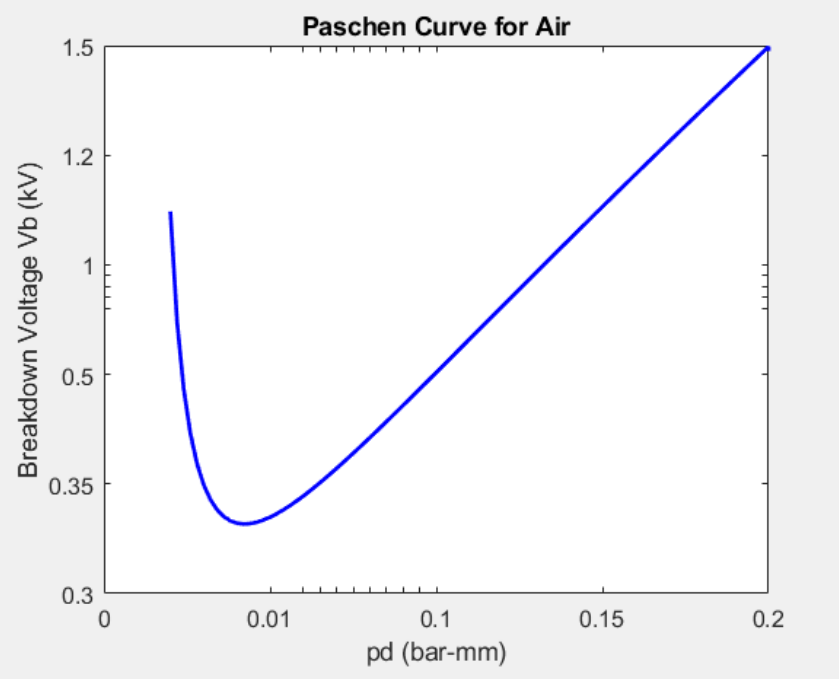

Fig. 2.36: Paschen Curve for Air showing there exists some Vbmin point on the curve – stating that any voltages below this point can never result in a breakdown event

Considering this breakdown effect, one might assume a reduction in the distance between objects or the pressure makes it easier for a voltage breakdown to occur. However, observation of the Paschen curve shows that this is not necessarily the case. In fact, there exists a minimum on the curve for which a breakdown can occur; this point corresponds to the optimum pd value for breakdowns to occur. This value is a minimum of the pd product and is denoted as $(pd)_{min}$ and shown below in Eqn. 2.84 [24].

$$(pd)_{min} = e \cdot \frac{k}{A} \tag{2.84}$$

This relationship states that for a given medium and any value of pd, there exisits a point where voltage breakdowns will not occur below the specified V_B [24]. One can then note this point as the minimum breakdown voltage in a given medium as V_{Bmin} [24].

$$V_{Bmin} = e \cdot k \cdot \frac{B}{A} = B \cdot (pd)_{min} \tag{2.85}$$

In air, this value is about 250-350V, for a given $(pd)_{min}$ value of around 9-13 bar-µm [24]. However, it can differ based on the values used for the ionization parameters because it is difficult to accurately capture all of air's dependencies on chemical composition and temperate. Nevertheless, it has been shown that 350V is a good approximation for the breakdown voltage of air at room temperature [24]. This means that for any given pressure or distance, no breakdowns can occur for potentials or voltages lower than this V_{Bmin} value in air.

Although V_{Bmin} indicates that there can never be any breakdown below 350V for any given distance or pressure, there can still be instances where other small partial or pre-discharges take place. Full voltage breakdowns should, however, not be confused with these pre-discharges, otherwise known

as corona discharges or arcing events [24]. These smaller pre-discharge events are sometimes observed even more often than full breakdown events.

To elaborate, arcing events can occur in scenarios when the potential difference between the two conductive objects is not strong enough to create the full breakdown discharge necessary to sustain a conductive discharge channel. In full breakdowns, a complete conductive channel is created between the two objects and will remain "open" for as long as the channel can be sourced. However, as soon as the field potential drops low enough, it stops supporting a full channel discharge and the channel will "close" and the breakdown discharge ceases to exist. Therefore, in pre-discharge events, the electric field potential's energy is not high enough to source this channel's creation.

When one of the objects is sharp or non-uniform, it can lead to large electric field potentials at the discontinuities or sharp area. In these instances, free electrons can escape the first conductor and move into the space around it. However, these free electrons do not have enough energy to create sufficient ionizations that would otherwise lead to avalanching and to the field breakdown or collapse that leads to the full discharge of the conducting channel. They simply escape from any sharp high potential edges and exist in the space around it, a phenomenon known as arcing or a corona event. The following figure taken from [24] shows the differences between pre-discharges or arcing and complete voltage breakdowns.

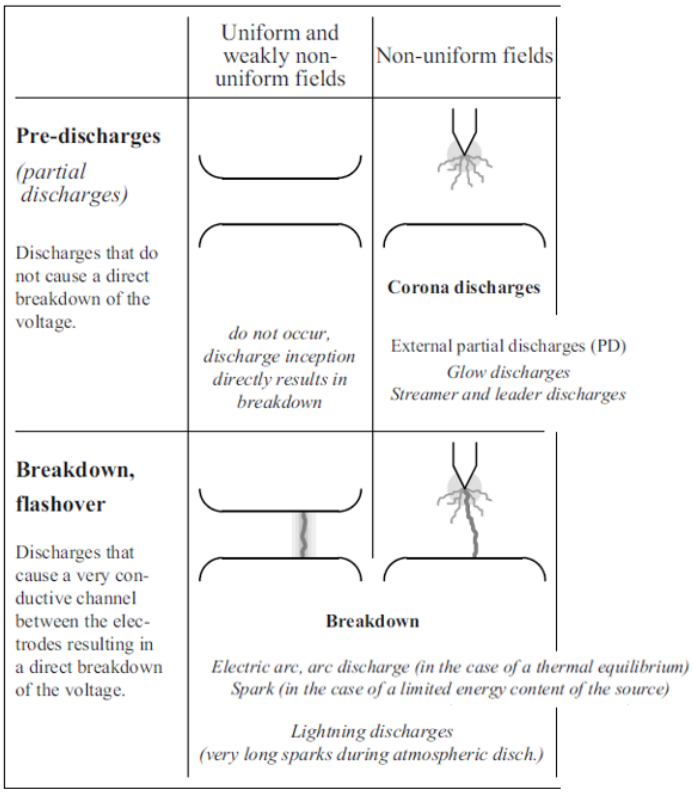

Fig. 2.37: Difference between a full Voltage Breakdown and Pre-dischargers for Uniform and Non-uniform Fields [24]

To state the difference in another way, partial and full discharges are defined by whether a constant conductive channel is created: this only occurs in the case of a full voltage breakdown discharge. Partial or pre-discharges, only occur as flashes of light as some charge carriers leave the first conductor. They have enough energy to become "free moving charge carriers" but no channel is created, so they most likely will not reach the second conductor. Either there are insufficient

molecules to form a full avalanche and create the channel, or the distance is too large between the two objects. Thus, a constant conductive channel is not created, as the energy from the electric field between the two objects is not strong enough.

For the LIM presented in this thesis, full voltage breakdowns can be mitigated and prevented, however, this does not mean that small arcing events or corona discharges won't take place during operation. To be realistic, some small arcing might occur, but it does not pose a huge threat for the motor itself. This arcing should not cause any damage to the core or windings, but may still introduce noise to any surrounding electronics on the Pod that have not been shielded properly against electromagnetic interference (EMI) created from the corona discharge. Therefore, these effects have to be measured and quantified in vacuum test chambers once the final motor has been fabricated.

3 Design

The design process for a linear induction motor is a methodology involving a theoretical framework, deploying equations and theory, complemented by some engineering experience. The design is finalized and validated using simulation tools, optimization methods and additional engineering intuition. A flowchart of this design process is shown in Figure 3.1.

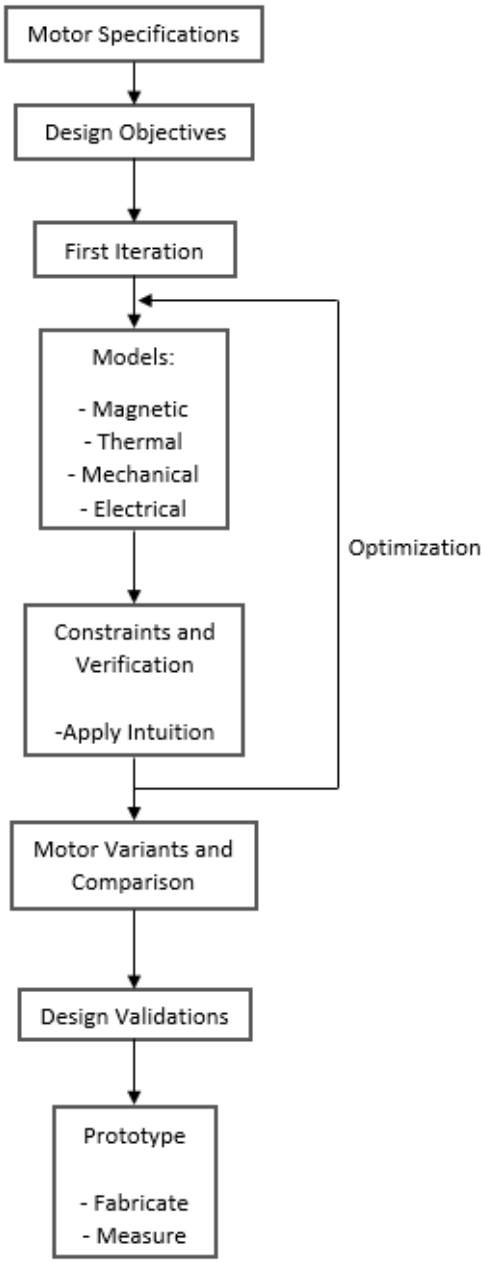

Fig. 3.1: Design Process Visualized in Flowchart

As in any engineering design, the process begins by defining basic goals or objectives. For this thesis, the goal of reaching a top speed of 500 km/h has been specified, which gives a starting parameter for the design. From here, a driving thrust force is defined, and the geometric design of the motor can begin.

The geometric design of the motor starts with some initial design parameters based on previous linear motor applications. That being said, it is difficult to quantify a basis or starting point since linear motors

of this application (high-speed and in a low-pressure environment) have never really been designed before. Nevertheless, a basic linear motor structure can be used to provide some initial intuitions about the fundamental operation or functionality of a linear induction motor. After this step, the design is improved to meet design specifications. This initial step provides an opportunity to become familiar with the simulation software of choice. The design of this motor relies on Comsol Multiphysics simulation software and uses the *Electric & Magnetic Fields* and *Eddy Current* solvers.

An example of a design criterion that makes this motor unique is the fact that the motor must operate at very high powers in a low-pressure environment. These conditions are ideal for creating high voltage breakdowns and arcing issues as discussed in the Paschen's Law Section above. However, these issues were addressed through proper coil insulation and reduction of the battery voltage to a low enough level to where arcing or breakdown is not possible. In addition to the high-power requirements, reaching the desired high speeds is also a non-trivial achievement.

There are also other design constraints, such as size, weight and manufacturing complexity, all of which have to be taken into account when designing the motor. Size is important in that the motor should consume as little volume as possible on the Pod. The Pod also needs to be able to mechanically support the stresses of the motor during operation, so the total weight is important. Lastly, the motor should be capable of being fabricated in a reasonable amount of time. This last concern relates to the winding configuration, as the winding scheme should not be too overly complex to construct.

3.1 Motor Configuration

The LIM to be designed is one a "double-sided short primary, single long stationary secondary" configuration. As the name suggests, in this configuration, the primary is the accelerating part of the LIM and the secondary is fixed in place (i.e., stationary). Therefore, the secondary can be incorporated into the Hyperloop tube track and thought of as the track itself. The primary can then be mounted onto the vehicle or Pod, which will then straddle the secondary as it accelerates along it. The primary is "double-excited", meaning it will be dual powered. Therefore, the primary will have two separate sources, each independently powering one corresponding side of the LIM separately. Examples of this LIM configuration can be seen in Figure 3.2, and additional images of the full configuration, also incorporating the electrical supply, can be seen below in the Electrical Design Section in Figure 3.40 and Figure 3.41.

It should be noted that the stator and rotor will be referred to interchangeably as the primary and the secondary, respectively, in this configuration.

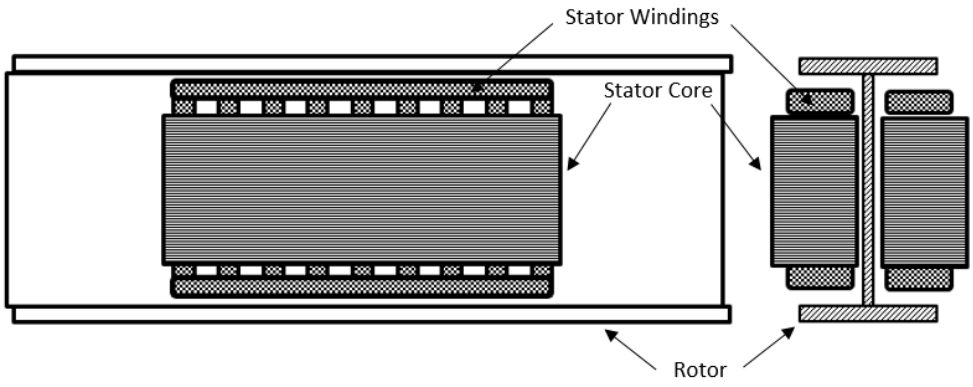

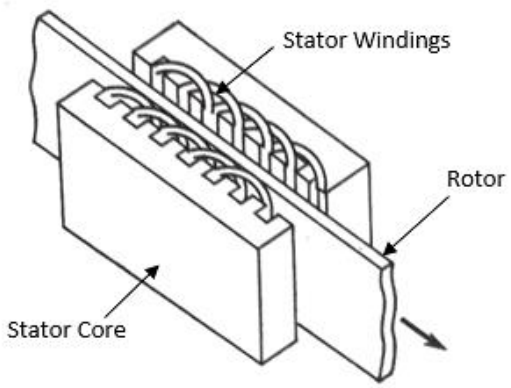

Fig. 3.2: Examples of Double-sided Short Primary, Single Long Secondary Configuration [21], [19]

As was stated in the Project Motivation, one goal of this thesis is to display the prototype motor at the *SpaceX Hyperloop Pod Competition* in Los Angeles, CA. In order for this to be possible, the motor will have to be designed around the same track that is inside of the Hyperloop tube at SpaceX. This I-beam track is shown in Appendix B.

Therefore, the SpaceX I-beam track geometry of Appendix B can also be considered as the secondary of this motor. The given I-beam track geometry thus becomes a fixed design constraint for the secondary and the design of the primary needs to fit accordingly within the inside dimensions of the I-beam. The complete specifications are shown below in Figure 3.3, with the critical dimensions highlighted in red as 4.17 in or 106 mm. With the I-beam as the secondary, it becomes clear why the primary was chosen to have the "double-sided short" configuration: it is the most optimal configuration for a "single long stationary" secondary.

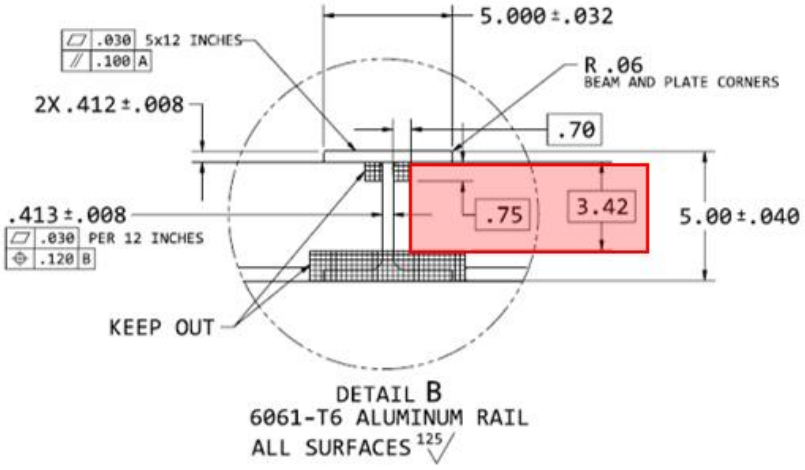

Fig. 3.3: SpaceX I-beam Track Geometry chosen as LIM Secondary [7]

It is however, important that the secondary also be conductive, as this is the working principle behind the induction motor. The secondary needs to allow induced eddy currents to flow through it. The secondary is made of Aluminum 60-61 T6, which is a very common aluminum material with a conductivity of roughly 2.5×10^7 S/m.

Unfortunately, the secondary inside of the SpaceX tube is not the optimal geometry for a secondary due to its minimized inside surface area. Electromagnetic principles show that larger surface areas lead to higher magnetic flux, which in turn gives rise to a stronger driving force! This property was discussed in the Magnetic Flux Density Section (Eqn. 2.50), where the flux produced is a direct product of the stator H-field and the active surface area of the stator.

Despite its minimized surface area, this secondary should still be adequate for producing the speed desired. The track was designed to support scaled down Pod capsules similar to the Pod that this motor will be mounted onto when finished. Additionally, this I-beam track has already been built, which is a major advantage and argument for using this I-beam geometry as the secondary, even if it is not the most optimal configuration.

3.2 Driving Thrust

Using this I-beam track as the secondary of the motor gives a length of 1.25 km for the secondary, as the SpaceX tube is 1.25 km long. To determine whether this secondary will be capable of propelling a prototype Pod to 500km/h, two calculations are performed. First, a trajectory calculation determines the thrust force required to move a Pod from a stationary position, to 500 km/h[6] or 138.889 m/sec. This speed is based on prototype Hyperloop pods weighing roughly 250 kg. Therefore, a Pod with a mass of 250 kg will be used in the design calculations here as well.

Second, a calculation is performed to derive the essential design parameter that dictates the Pod's propulsion, the driving thrust generated from the motor. This driving thrust can be equated to the Lorentz Force term derived in the Lorentz Force Section. Moreover, if the generated driving thrust is greater than or equal to the force required to move the Pod, then this secondary geometry is sufficient in propelling the 250 kg Pod to 500 km/h. Therefore, these two thrust forces, the *driving thrust generated from the motor* and *thrust required to move the Pod*, must be equated to one another in other to determine if the thrust level is indeed met.

3.2.1 Predicted Trajectory Profile

The following trajectory calculations determine the acceleration, time, distance, and maximum speed reached in using this I-beam track as the secondary. The first step in determining the necessary force required to propel a 250 kg pod to 500km/h, is to choose an acceleration time (e.g., 12.5 seconds) and perform a simple trajectory calculation.

$$v_f - v_i = a \cdot t \tag{3.1}$$

$$138.889\,{}^{m}/_{s} - 0 = a \cdot 12.5sec \tag{3.2}$$

$$a = \frac{138.889\,{}^{m}/_{s}}{12.5\ s} = 11.11\ m/s^2 \cong 1.13g \tag{3.3}$$

Accelerating over 12.5sec means that the Pod will experience an acceleration of approximately 1g. Likewise, the distance travelled along the SpaceX Hyperloop tube can be calculated to verify that there is enough distance to accelerate to top speed and then decelerate before crashing into the end of the tube.

$$d = v_i \cdot t + \frac{1}{2} \cdot a \cdot t^2 \tag{3.4}$$

$$d = 0 + \frac{1}{2} \cdot 11.11\ m/s^2 \cdot (12.5s)^2 = 868.05\ m \tag{3.5}$$

To ensure that there is adequate track remaining, roughly 4.5sec of braking time is used. Using this deceleration time and Eqn. 3.1 gives a deceleration of roughly 3g.

[6] It was stated in the Introduction Section that it would be a notable first step if this motor can reach speeds of about half of what is imaged for a full-scale Hyperloop system. This is how 500 km/h was chosen.

$$a = \frac{-138.889\,{}^{m}/_{s}}{4.5\ s} = -30.86\,\frac{m}{s^2} \cong -3.15g \tag{3.6}$$

The acceleration and deceleration profiles can be seen below in Figure 3.4. Note that constant acceleration and deceleration are assumed.

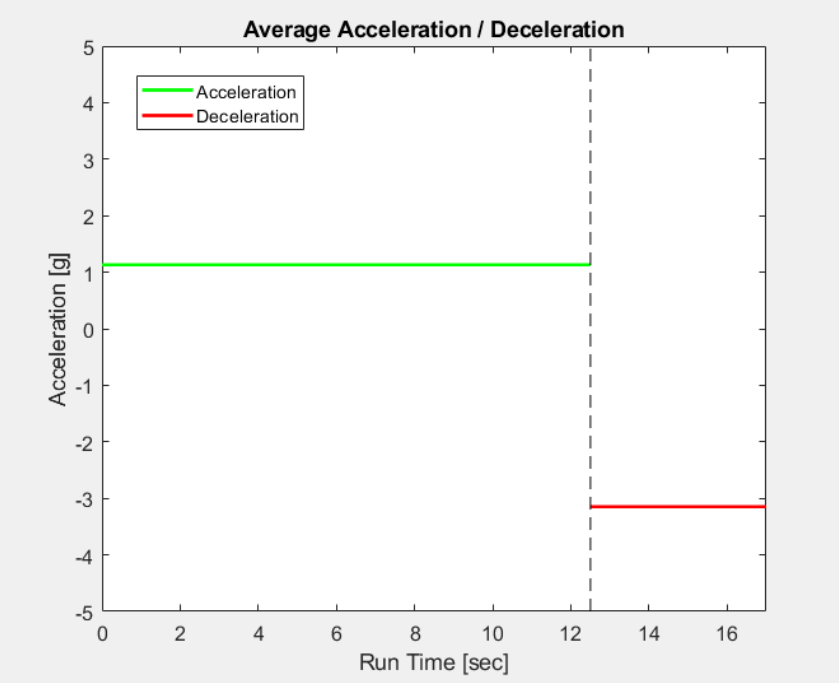

Fig. 3.4: Projected Acceleration and Deceleration Profiles – assuming constant acceleration and deceleration

The distance travelled while braking can be calculated in the same was as calculating the distance travelled while accelerating. After slightly rearranging Eqn. 3.4, it can be shown that a braking distance of roughly 313m is required during this braking period.

$$d = \frac{{v_f}^2 - {v_i}^2}{2 \cdot a} = \frac{0 - 138.889\ {}^{m}/_{s}}{2 \cdot -30.86\ {}^{m}/_{s^2}} = 312.5\ m \tag{3.7}$$

This calculation gives a total distance travelled of 1180.56m over a total run time of 17sec, which leaves approximately 70m of buffer remaining until the end of the tube is reached. A figure of the Hyperloop tube with these distances can be seen below in Figure 3.5.

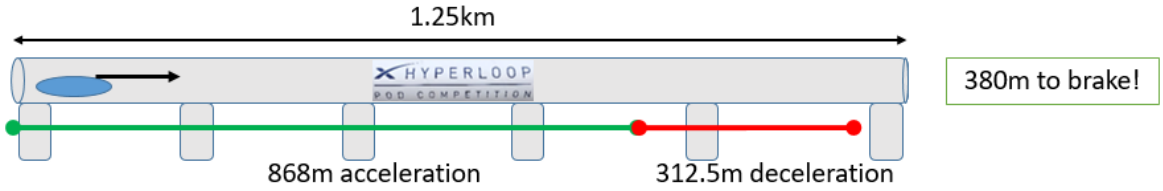

Fig. 3.5: SpaceX Hyperloop Tube Graphic showing Acceleration and Deceleration Distance Travelled

The kinematic trajectory plot in Figure 3.6 shows the velocity profile along the total travelled distance of 1.18 km and clearly indicates where the peak velocity of 500 km/h is reached. The projected runtime is also shown below in Figure 3.7.

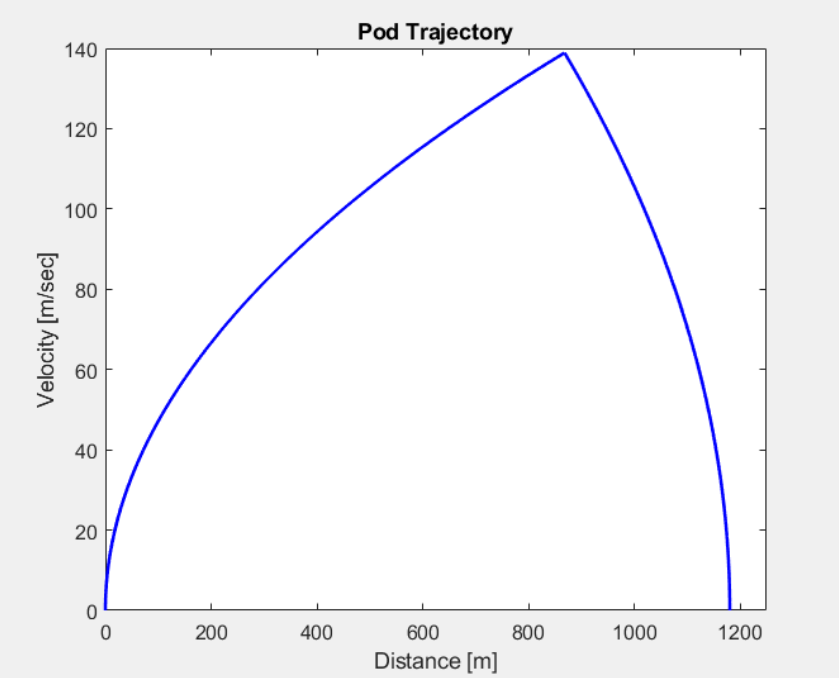

Fig. 3.6: Projected Pod Trajectory Profile showing Distance Travelled down the Hyperloop Tube

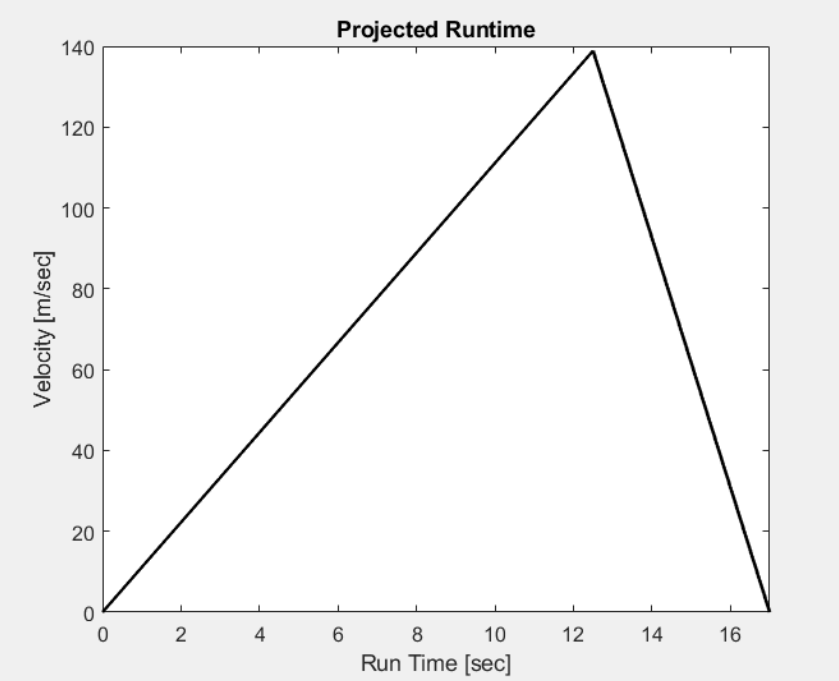

Fig. 3.7: Projected Pod Run Time Profile for Accelerating the Pod to 500 km/h over 12.5sec

Finally, the required mechanical force to accelerate the 250kg Pod to the final velocity of 500 km/h can be calculated using Newton's second law, $F = ma$, which states that the net force required to accelerate an object, is equal to the product of the object's mass and its acceleration.

$$F = 250\ kg \cdot 11.11\ m/s^2 \cong 2.778kN \tag{3.8}$$

Therefore, accelerating a 250kg prototype Pod at 1g over a 12.5sec time interval requires the LIM to produce a constant driving force of 2.778kN. This required force gives the necessary design value for Eqn. 3.9.

$$Lorentz\ Force := 2.778kN \tag{3.9}$$

To reiterate, if the LIM's secondary can generate a constant Lorentz Force of 2.778kN for 12.5sec, then the Pod will reach 500 km/h. Applying this force for longer than 12.5sec or generating an even greater force means that higher speeds can be achieved. The kinematic data from the above calculations is listed below in Table 3.1.

Kinematic Data	
Pod Acceleration to 500 km/h	11.11 [m/s²]
Braking Deceleration of Pod	30.86 [m/s²]
Total Acceleration Distance for 500 km/h	868.05 [m]
Total Braking Distance (500-0 km/h)	312.50 [m]
Total Run Distance	1180.55 [m]
Total Acceleration Time (0-500 km/h)	12.5 [sec]
Maximum Braking Time	4.5 [sec]
Total Run Time	17 [sec]

Table 3.1: Detailed Kinematic Data

3.3 Motor Design

Initial designs have the linear motor mounted on Swissloop's Pod from the previous year; "Escher" [26]. The primary reason for mounting the LIM on the existing chassis is that this Pod is already built and fully functioning. This Pod is complete with avionics, braking, and stability systems to help guide the Pod safely along the pre-selected I-beam secondary. A CAD rendering of the LIM mounted onto the Escher Pod is shown below in Appendix D.

However, if the chassis is to support this LIM, some additional design constraints must be defined. These constraints for the size and weight of the LIM are given by the Escher Pod. Table 3.2 lists these known design constraints.

The motor type shall also be a 2-pole motor because the lower the number of magnetic poles a motor has, the higher the thrust generation. Since no magnetic monopoles can exist (from Eqn. 2.4), the lowest number of poles a motor can have is limited to 2. This means the highest *thrust-drag* ratio is for a 2-pole motor. The LIM will therefore be constrained to a 2-pole motor configuration, which will be the driving factor influencing the design of the windings.

Initial LIM Design Constraints	
Speed Goal	500 [km/h]
Force Required	2.778 [kN]
Pole Number	2-Pole
Size Limits	1 (length), 0.2 (height), 0.08 (width) [m]
Weight Limit	80 [kg]
Power Limit	450 [kW]

Table 3.2: Initial Motor Design Constraints

The main constraints for mounting the LIM on the Escher Pod are the weight and size of the LIM. The weight constraints are important because the overall weight of the Pod should be around 250 kg, the value assumed for the trajectory calculations. In this manner, the weight is more of a limit on the maximum achievable speed, because the speed is dictated by the weight. The current Escher Pod consisting of the chassis and avionics, braking, and stability systems is about 100 kg. This setup leaves about 150 kg spare for the entire LIM system, which consists of the stator, battery source, and any other required DC/AC power electronics equipment.

The size constraints that the motor must satisfy are important so that the LIM physically fits onto the Escher Pod in the dedicated space for the motor. Given these dimensions, a space roughly 1m in length and 0.2m is height is available on the Pod. The LIM's width is also important because the LIM needs to fit within the I-beam's inner-most dimension, which was seen to be roughly 80 mm from Figure 3.3 above: given the "keep-out-zone" areas are taken into account. The implications of this width constraint will also be discussed in more detail in the Stator Core Design Section below, because the stator core width greatly influences the thrust generation of the motor.

The power limitations have been chosen to be around 450 kW. This value was selected as a trade-off between the battery design (both complexity and cost) and the power needed to produce thrust for speeds of 500 km/h.

Now that these constraints have been listed, the motor and its design constraints have become clearer. These constraints are for the most part fixed, however, there is some leeway for adjustment if the design values needed deviate slightly from these limits during the final design consideration (e.g., weight or power limits). Nevertheless, size constraints must be strictly adhered to, as there is finite space available on the Pod. In this manner, some of these "constraints" can be interpreted as "target specifications".

Before starting the design process, a simple linear motor concept was studied to gain intuition of how linear induction motor modelling is performed in Comsol. This simple model consisted of a basic magnetic iron core as the double-sided stator, with a simple 2-pole 3-phase winding configuration arranged to produce the travelling magnetic stator field. The stator fits in-between the I-beam secondary inner dimension, which acts as motor's rotor. Figure 3.8 shows this initial design concept and its dimensions. The inner dimension is approximated by a simple aluminum plate for simulation simplicity.

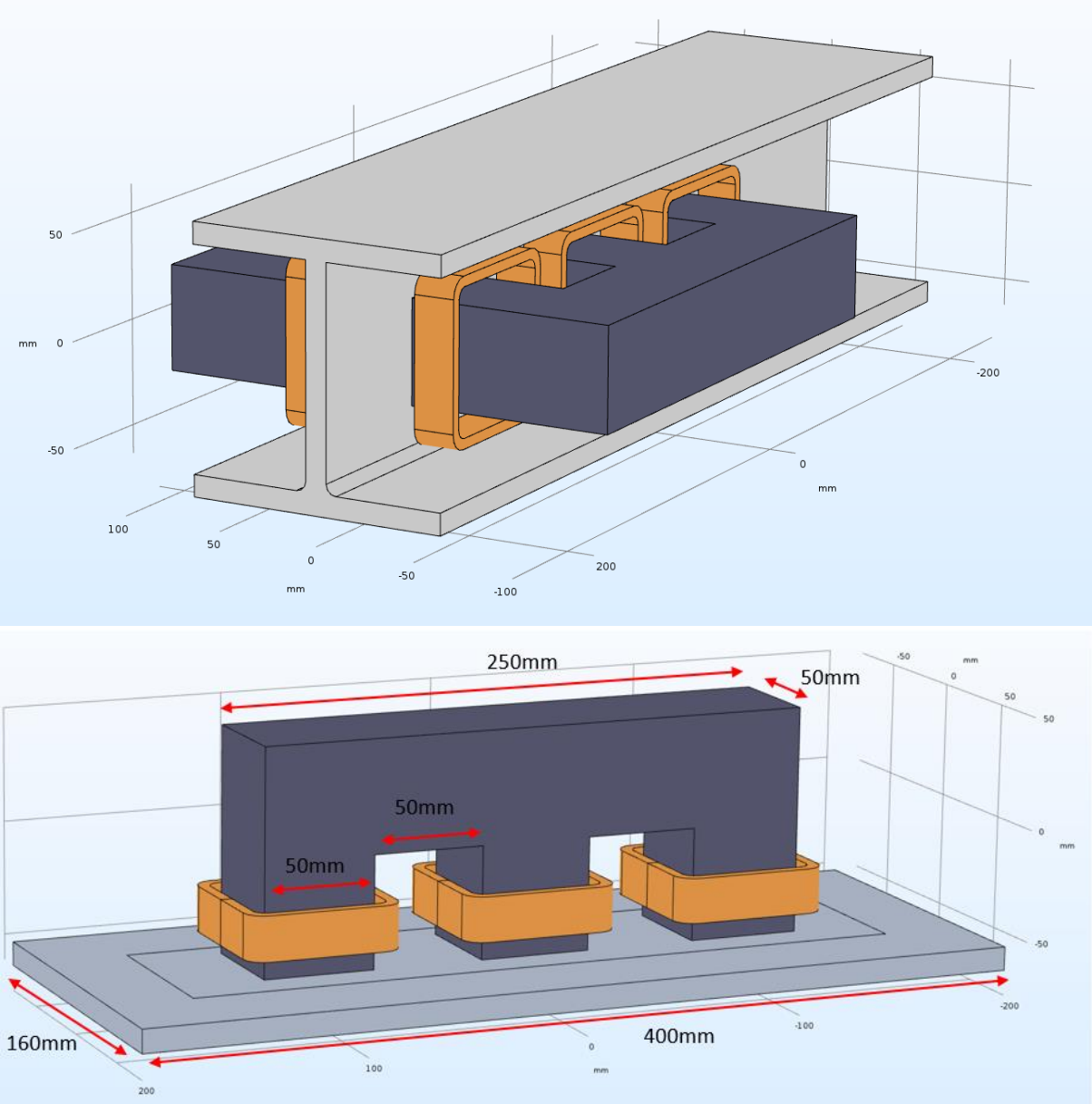

Fig. 3.8: Initial design concept acting as a starting point in the design process. Once enough intuition was gained by studying this simple model, the design process moved forward to further, more complex iterations.

As was seen in the Slot and Winding Distribution Section, the more slots the stator core has, the more sine-like the approximation for the travelling stator field. In examining Figure 3.8, one can see that this stator is quite basic with only 3 teeth and 2 slots – in a simple "E" configuration. Therefore, the stator field produced from such a design would clearly not be as efficient as a design with a greater number of slots. Additionally, the windings are approximated by coils, which are in turn specified in Comsol as a collection of many smaller windings. Appendix G shows how this is approximated in Comsol.

Such a simple model is insufficient for a motor to be used in this high-speed Hyperloop application, where speeds of 500 km/h are desired. Nonetheless, this model was important because it served as an initial step to see the operation and functionality of linear motors in Comsol. It also helped to demonstrate how varying certain parameters impact the final values, such as thrust production, core saturation, or induced voltage. Table 3.3 lists the intuitions gained during the study of this 2-slot concept.

Intuitions Gained from the Simple 2-Slot Model	
Parameter Varied	**Effect on the Thrust**
Air Gap	As one might imagine, the smaller the air gap distance, the greater the thrust force produced.
Active Surface Area	As the active width increases, the thrust produced increases. This property makes sense as the width or length (active surface area) is directly related to flux passing through some surface. Also, as seen in the Lorentz Force Section, the Stack Width is directly multiplied by the thrust produced.
Saturation	In order to avoid saturation of the iron core, one must increase the active surface area to a size large enough to handle the existing flux. The more the core saturates, the more it heats up and no additional thrust is produced.
Pole Pitch	The pole pitch is determined by the number of poles produced from the motor as well as by the winding scheme and slot number. However, in this simple design, one can manipulate the pole pitch by varying the length of the core, or more appropriately, the distance between the teeth. By adjusting the pole pitch, a maximum in produced thrust is achieved.
Turn Number	More turns in each winding produces more thrust. This is an intuitive result as the MMF is directly related to the turn number. However, there is also a higher voltage induced in the coil, which must be supported by the source. If this is not the case, the voltage level will drop to whatever can be supported by the source, and the thrust will then drop accordingly.
Slot Size	For the same wire cross-section, larger overall slot size allows for a greater number of turns in the slot, which increases the thrust production. More slots also mean that the stator field will more closely approximate a sine wave.
Yoke Height	The yoke height is not directly related to the thrust, however, it is important for saturation and heating considerations. Taller yokes will help dissipate more heat, however, they are larger because of the added material and will therefore be heavier. For saturation, if the yoke height is too small, the yoke will become saturated during operation, as there will be too much flux trying to pass through a small and limited space. On the other hand, if the yokes are too large, there is "unused" space which only adds more weight. There is a rule of thumb stating that the yoke height should be roughly proportional to the tooth width for an even distribution of flux field lines.
Input Current and Coil Cross-Section	As more current passes through the windings, a higher the thrust level is produced. This property is intuitive as the MMF is directly related to the input current. However, more current also means that the core and the coils will heat up at a faster rate. Additionally, as the current is increased to a high enough level, the resistance will increase drastically, and thrust production will actually decrease as the current level is unsupported by the winding cross-section. The smaller the cross-section of the coil winding, the higher the current density of the coil.

Table 3.3: Intuitions Gained from the Simple 2-Slot Model

Having gained sufficient knowledge from this initial 2-slot concept, more advanced models were then adapted and simulated to obtain a final 24-slot design with optimal performance. Subsequent slot variations were investigated, including 6-slot, 9-slot, and 12-slot variants with revisions and adaptions performed on each slot variation. Table 3.4 compares the parameters and specifications of the initial 2-slot concept design with the other investigated slot models.

Comparison of Slot Variations at Vsync of 138.89 m/s – Double-Sided LIM					
Slot Variation	**2-slot**	**6-Slot**	**9-slot**	**12-Slot**	**24-Slot**
Active SA [mm^2]	12500	33600	16480	52150	44660
Stack Width [mm]	50	80	40	70	55
Length [mm]	250	420	412	745	812
Core Height [mm]	100	100	130	120	225
Yoke Height [mm]	50	50	60	60	100
Slot Height [mm]	50	50	70	60	125
Slot Number	2	6	9	12	24
Pole Number	2	2	2	2	2
Pole Pitch [mm]	125	210	206	372.5	406
Final Frequency [Hz]	1111.12	330.69	337.11	186.43	171.05
Tooth Pitch [mm]	100	70	43	60	33
Slot Width [mm]	50	20	18	35	13
Tooth Width [mm]	50	50	25	25	20
Slot / Phase	0.5	1	1.5	2	4
MMF [At]	13859.29	19798.99	19798.99	14849.24	19798.99
Peak Input Current [A] / Phase	140√2	140√2	140√2	140√2	140√2
Turn Number / Phase	70	100	100	75	100
Maximum Thrust Produced at Vsync [kN]	0.31	1.38	3.63	2.94	4.69

Table 3.4: Comparison of Slot Variations at Vsync of 138.89 m/s – thrust values of double-sided LIM

Although these variations provided a great deal of information and insight in the stator design, ultimately only one could be chosen. The 24-slot model was selected as the stator design to be pursued because it is the option that guarantees performance for the required thrust level, while still not saturating under operation, which was the biggest problem for the other variants. Additionally, this variant still fits within the inner dimension of the I-beam. Given enough engineering time, some of the revisions to the other variations might also yield a LIM of similar performance.

The next few sections show what factors came into play when designing each section of the LIM, give general insights into the design decisions, and show how the final 24-slot design came to completion.

3.3.1 Primary – Stator Iron Core

The design of the stator comes down to two main aspects, the stator core, and the windings. The core's design was adapted from the intuitive 2-Slot model, while the winding design was much more complicated. It took several iterations to achieve the target performance from the windings, while still having them fit in-between the I-beam. The design of the stator core will be discussed first.

By following the intuition developed from the 2-Slot model, one can start with a basic yoke and tooth design and increase sizes until performance / target specifications are met. As stated previously, the 24-Slot model was chosen as the core design for this thesis. The core material was chosen to be iron stacks of M400-50A, which is a common iron core used in motor applications. The data sheet given in Appendix E details further information about the iron stacks.

Several parts of the stator make up the iron core. Deploying some engineering rules of thumb can help guide the basic geometrical design of these stator parts.

Teeth:

As seen earlier, the teeth can easily saturate from the flux passing through them. Therefore, for a given input, one should use as much surface area for the teeth as possible while still keeping the flux density of the teeth at a reasonable level, before saturation is reached. The teeth should be fully "loaded" with flux before increasing their size further. The larger the teeth, the more they should be loaded with flux. For example, if the teeth are large and only have a 0.2T magnetic flux density, then one should think about shrinking the overall size of the teeth until the average flux density through them is approaching a moderate saturation limit of roughly 1.8T. However, one should not over saturate the teeth past a limit of 2T, otherwise they will begin to overheat and the motor's efficiency will decrease. If this occurs, and additional input is needed to achieve a certain desired thrust force, then one must increase the teeth size so they can handle the higher flux density.

Yoke:

Similar to the condition for teeth saturation, the yoke height just needs to be large enough to handle the flux density passing through it. If the yoke is extremely saturated, it should be made larger. A general rule of thumb is that the yoke height should be roughly the same size as the tooth width. These two parameters do not have to be exactly equal; however, the ratio of the two should be as close as possible to one. This relationship helps create more gradually routed flux paths throughout the stator core. If the yoke is too large for instance, extra space in which the field lines "circle around" more, or aren't as evenly distributed because the reluctance begins to dictate the paths less accurately, might exist. If the yoke is too small relative to the tooth width, then the field lines might be more "compressed" and won't distribute as evenly. There is a tradeoff here, because the yoke should also not get so large that it weighs drastically more than the rest of the stator, including the windings.

Slot:

The slot needs to be wide enough to fit the needed turn number (which is needed for the MMF) inside of it for the given wire gauge. The given wire gauge is in turn based on the current density being driven through the windings. The slot should also not be so wide that there is more space than required. In general, the slot width should also be somewhat proportional to the tooth width. If there is inadequate space for the designed winding turn number, then the wire gauge will have to be reduced so that the desired turn number can fit inside the slot. In doing so, however, increases the

current density of the coils, which could have negative impacts on the thermal specifications of the motor. Therefore, target specifications and constraints should be clarified before designing.

Length and Width:

The active surface area is important for the thrust produced, as it is directly related to the MMF through the flux production. The width is especially important as it directly relates to thrust produced.

Pole Pitch:

A 2-pole motor is designed in this thesis. Eqn. 3.10, stated here again for reference with the pole pitch highlighted, describes what this classification means mathematically.

$$\tau_p = \frac{v_s}{2 f_s} \tag{3.10}$$

This states that the pole pitch of a 2-pole motor should be half the length of the motor. However, it is never exactly half, so finding the optimum point of a given pole pitch for the stator length requires some experimentation. For the simple 2-slot design concept of Figure 2.2, an optimization was performed to find the optimal length of the motor for the correct pole pitch, given a synchronous speed of 500 km/h. This optimal point can be seen in Figure 3.9, where a core length of 275mm yields the correct pole pitch.

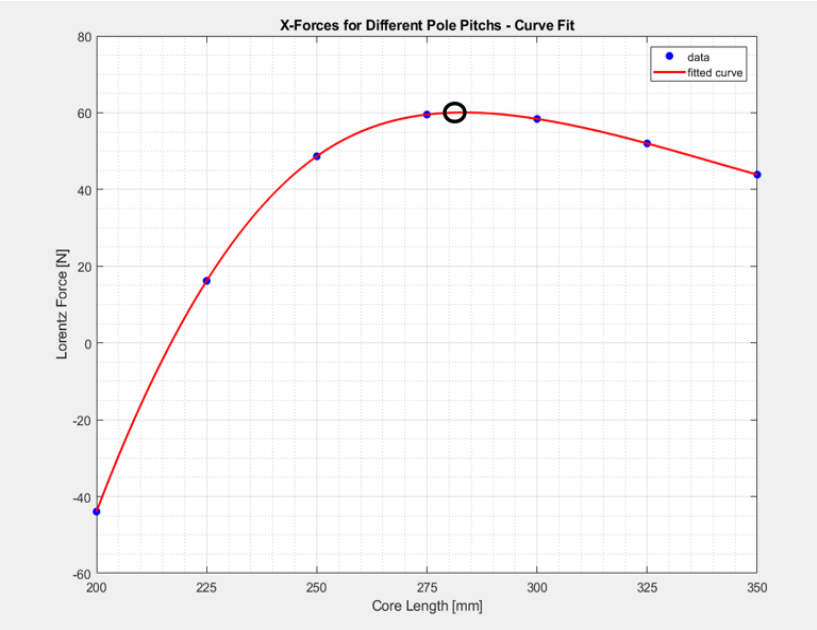

Fig. 3.9: Pole Pitch Variations from the initial 2-Slot design concept – showing how an optimized maximum point is achieved for the pole pitch of a given stator length.

A desired synchronous speed of 500 km/h correlates to a pole pitch of roughly 125mm for the stator frequency of 555Hz. This condition then translates into a core length of roughly 250mm, which was the initial design length of the stator core if the motor is taken as 2-pole. However, for this motor, an optimal core length of around 275mm for the given parameters is actually observed. This corresponds to a pole pitch of roughly 140mm, which was initially not the case. Therefore, it can be seen that although this parameter is usually not considered much in the design process, it should not be completely forgotten about, especially when designing motors of higher complexity.

The Motor Configuration Section indicated that the configuration of this LIM is one of a double-sided stator core. This arrangement has each core producing half of the necessary thrust to move the Pod, which corresponds to each side of the LIM producing roughly 1.4kN of thrust.

In addition to using more of the secondary's surface area to generate a higher thrust force, using a double-sided configuration, as opposed to a single-sided configuration, increases flux in the air gap by adding a second core. As seen in the Lorentz Force Section, a high flux concentration in the air gap induces more eddy currents in the secondary, which leads to greater thrust production.

The reason the magnetic flux density increases in the air gap when a second core is added is because the μ_r of the iron core, together with the MMF, act to push the fields from materials with higher μ_r to materials of a lower μ_r (i.e., air in this case). Therefore, the MMF guides the high field concentration from the iron core to the air. However, without a second core, the MMF drives the flux out of the iron core to the air along a longer path and below the secondary, where it is unusable. It is desirable to have a high field concentration only in the air near the rotor blade where it can contribute to thrust production. This location corresponds to the air gap where the flux can continuously produce eddy currents during operation. Field concentration pushed to air elsewhere around the motor is wasted below the rotor blade and does not contribute to the force production.

Properly guiding the flux is achieved by adding a second core below the rotor blade. Doing so adds a second side to the LIM that constrains the field to the air gap, since the MMF of the iron cores from both LIMs will now act to push the flux from the iron cores to the air. However now, the only place where the flux exists is in the air in-between the two cores. In this arrangement, the two iron cores act together to constrain the fields and produce a high magnetic flux density in the air gap.

Additionally, adding two cores helps further reduce the path length taken by the flux, since the magnetic field lines must "travel" back to close on themselves – Eqn. 2.4. A reduced path length will also slightly increase the flux density in the air gap, as less is "wasted" in the air beneath the rotor blade like in the single-sided case.

The reduction in path length can be seen again from Amperes' Law in its quasi-static integral form: the magnetic field strength is directly related to the path of the field.

$$\oint_{(c)} \vec{H} \cdot d\vec{l} = \iint_S \vec{J} \cdot d\vec{S} = N \cdot I \tag{3.11}$$

If no second core is added, the path taken by the magnetic field, $d\vec{l}$, will be longer than the path taken if a second iron stator core is added. Shortening the paths that the fields take to enclose back on themselves (i.e., the route the flux exists through around the windings and the core teeth), increases the magnetic field strength, $\vec{H}$ from the current density flowing through N windings, $\iint_S \vec{J} \cdot d\vec{S}$. An illustration of this explanation can be seen below in Figure 3.10.

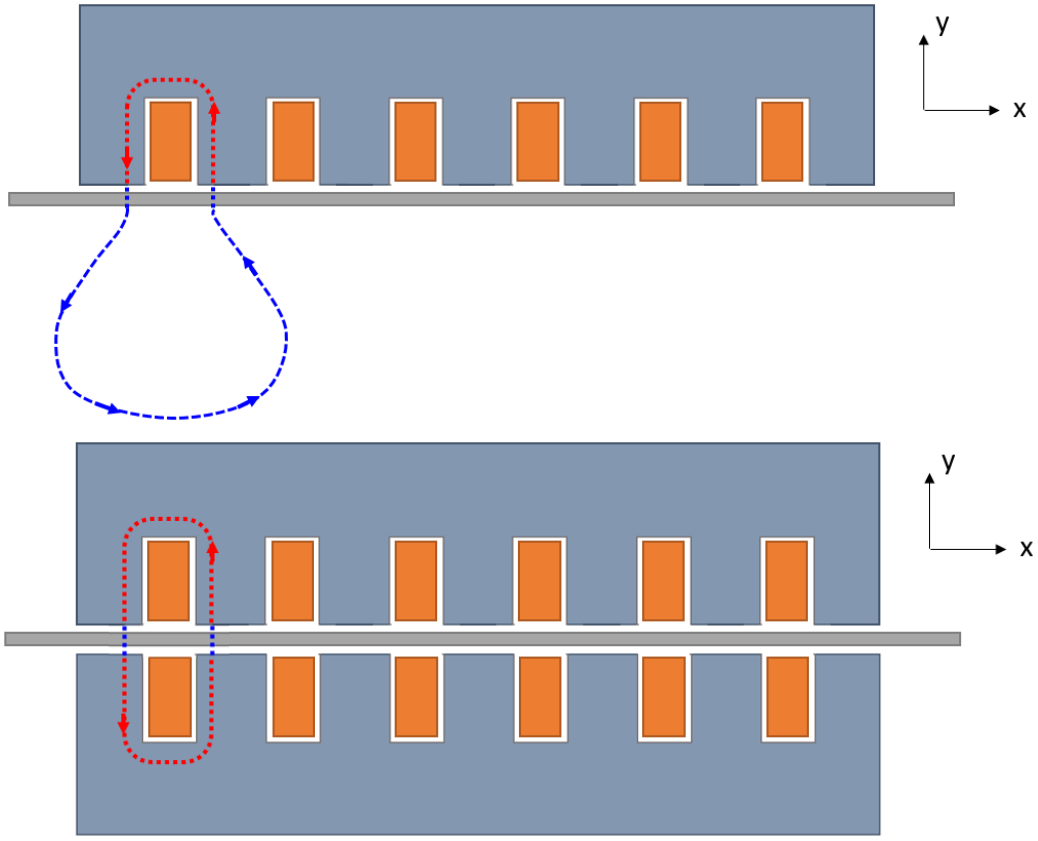

Fig. 3.10: Single-sided core vs. double sided core – the magnetic flux density is now constrained to the air gap and the paths which the flux exists are also shorter for the double-sided core. The path for the single-sided core is slightly exaggerated in blue help to demonstrate the point that the path is longer in non-magnetically permeable materials, as there is no MMF and thus no reluctance guiding the flux to a path of least magnetic resistance.

The portion of the closed path the flux follows through the air is shown in blue and the portion in red is through the iron core. The blue path is slightly exaggerated to help depict the more freely flowing flux lines that follow longer paths through non-magnetic materials. Nevertheless, in the top image, where no second core is present, the path through air is essentially "wasted" below the rotor blade because the flux in this region does not induce the desired level of eddy currents in the rotor. However, in the bottom image where a second core is present, the same input does produce the desired behavior.

To summarize, it is desirable to constrain the flux density to the air gap where it can be used to contribute to thrust production. Flux existing too far below the rotor is unusable, and does not contribute to thrust production. Adding a second iron core below the blade "completes" this circuit and further constrains the field to the air gap.

Adding a second core on the opposite side of the track also helps balance the magnetic forces in the system. It does this by adding a sort of symmetry, as there will always be an equal Lorentz force "pushing" on both sides of the secondary.

The stator has a *toothed* configuration. In this arrangement, the stator is comprised of "teeth", which are extrusions from the yoke, allowing the armature windings to be wound around them. When the windings are excited, these teeth accept the flux passing through them. To support the windings, small notches at the end of each tooth are made to help hold the windings in place. These notches in the teeth can be seen below in Figure 3.11 – taken from the technical drawing for the final LIM design of Appendix F.

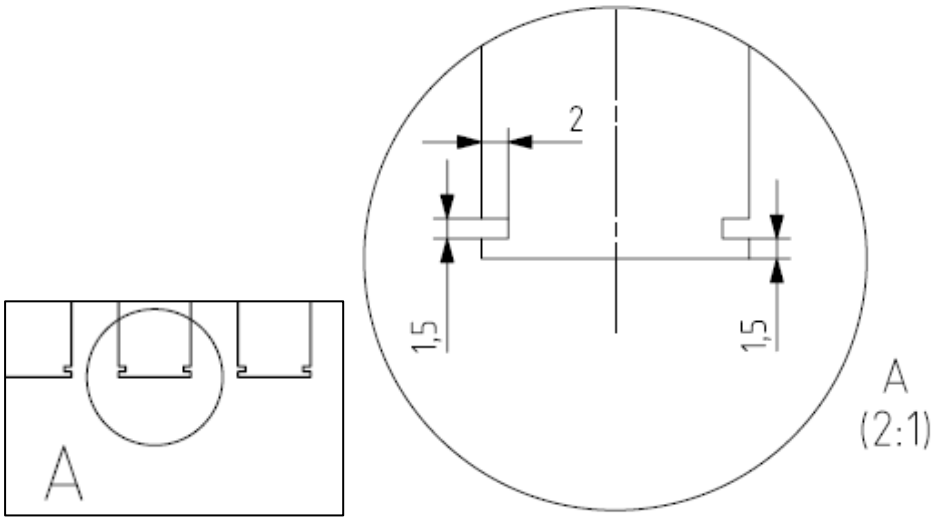

Fig. 3.11: Projected Pod Trajectory Profile showing Distance Travelled down the Hyperloop Tube – Appendix F

3.3.2 Primary – Stator Windings

The windings were much more difficult to design than the stator core because the SpaceX I-beam was used as the secondary. For a given winding design, it had to be verified that the core would fit in-between the I-beam's inner most dimension. The inner-most spacing constraint has the greatest impact on the winding heads that protrude from the stator teeth of the core. The winding heads are shown here in Figure 3.12, for a double-sided LIM around an upside T-beam[7] track, where the necessary space is allocated for the winding heads.

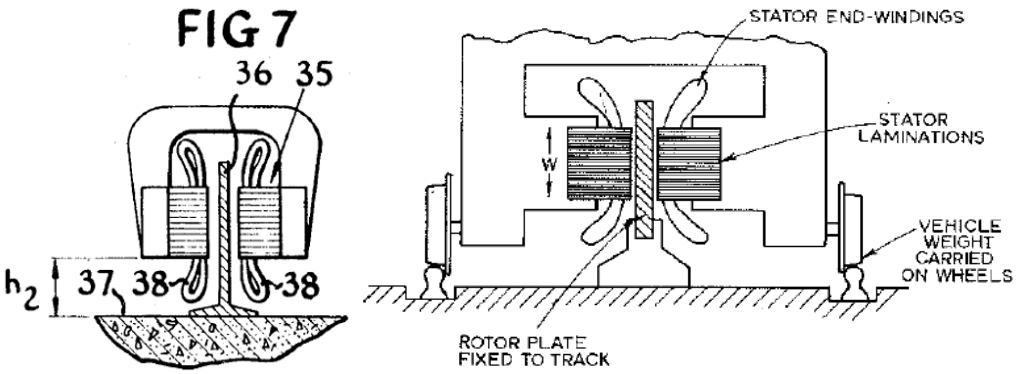

*Fig. 3.12: U.S. Patent of Linear Induction Motors for Vehicle Propulsion – showing that there should necessary space provided for the winding heads; detailed on the left as **38** [12], [13]*

As a rule of thumb, the amount of space for the winding head height should be roughly the same length as for the designed width of the slots in the stator. For the stator core in this thesis, the slot width is designed to be 125 mm, implying that a corresponding spacing of 125 mm should be provided on both sides of the LIM for the winding heads.

If the available spacing given by the I-beam's inner dimension from [7] (i.e., 86 mm) is used to calculate the useable width for the stator core, then it can be seen that at most 62 mm remains for the stator core width. This distance is calculated assuming that the given winding head height tolerances of 25 mm (12.5 mm for each winding head height) has already been subtracted. However, the required heights for the winding heads could be slightly larger than the 25 mm given by the rule of thumb value. It is also desirable to have some air spacing in-between the winding heads and the top of the beam.

[7] The upside T-beam is thought to be the optimal secondary for the double-sided linear induction motor.

This extra space provides some tolerance for error and ensures that the winding heads will not contact the top of the beam during operation. Therefore, to be safe, the width of the stator core is set to 55 mm, leaving about an extra 3.4 mm on each side of the stator core for the winding heads.

It was seen previously that the width of the stator core directly influences the amount of thrust produced by the motor. By using the I-beam as a secondary, one of the major parameters dictating the LIM's driving thrust is limited by the inner spacing of this I-beam. The magnetic flux density has a limit of around 2T; therefore, if flux, the key driving parameter in thrust production, should increase by a noticeable amount, the active surface area of the stator core must also increase. However, as seen here, the core is limited in width by the constraint of the I-beam inner spacing. The only other way to increase the flux noticeably is to increase the length of the stator core, which unfortunately cannot be made incredibly long. As a good approximation, given the material and weight of the stator core, the limit on the length can be set to 1 m. It is not evident that there exists some theoretical limit on the flux produced, a conclusion that can be seen below in Eqn. 3.13.

$$\Phi = \int_S \vec{B} \cdot d\vec{S} = B \cdot SA = B \cdot W \cdot L = 2\ \mathrm{T} \cdot 0.055\ \mathrm{m} \cdot 1\ \mathrm{m} \tag{3.12}$$

$$\Phi_{LIMIT} = 2\ \mathrm{T} \cdot 0.055\ \mathrm{m} \cdot 1\ \mathrm{m} = 0.11\ \mathrm{Wb} \tag{3.13}$$

This limit on the flux is a key reason why using the I-beam provided by SpaceX as the secondary rotor for this LIM is not an optimal decision. However, for reaching speeds of 500 km/h, this already constructed secondary will be sufficient for this first prototype LIM.

Continuing the design process with this flux constraint in mind, a winding scheme that fits inside the I-beam was found after several design iterations. Since the stator core has a toothed configuration, the windings will wrap around each of the teeth to produce the flux. This configuration of how the stator teeth are wound, is known as the *winding diagram*. The final winding diagram for the 24-Slot LIM can be seen in Figure 3.13.

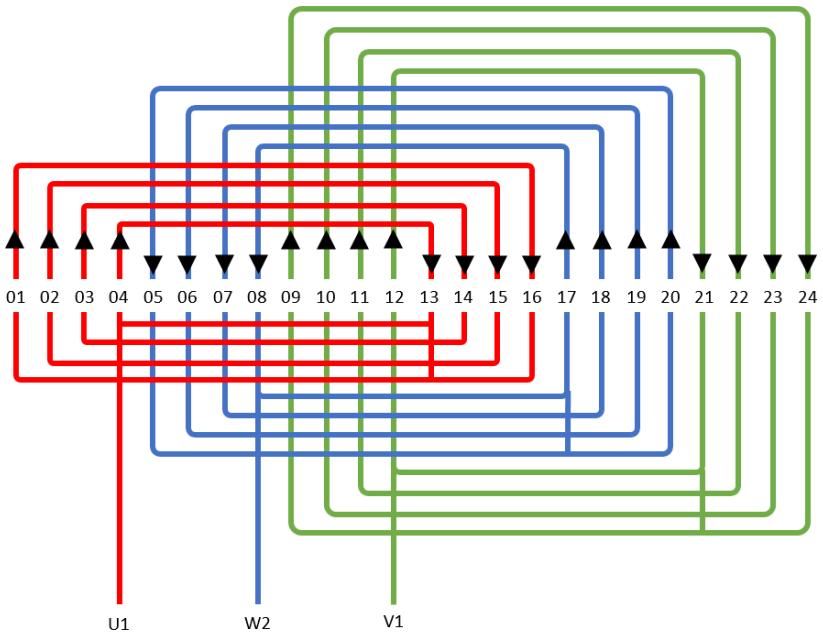

Fig. 3.13: 24-Slot Stator Winding Diagram for a Parallel Star (Wye) Configuration

This winding diagram assumes 4 slots per phase for the chosen 24-Slot design, which guarantees a 2-pole motor. The 24-Slot LIM with the 3-phase windings highlighted, can be seen below in Figure 3.14.

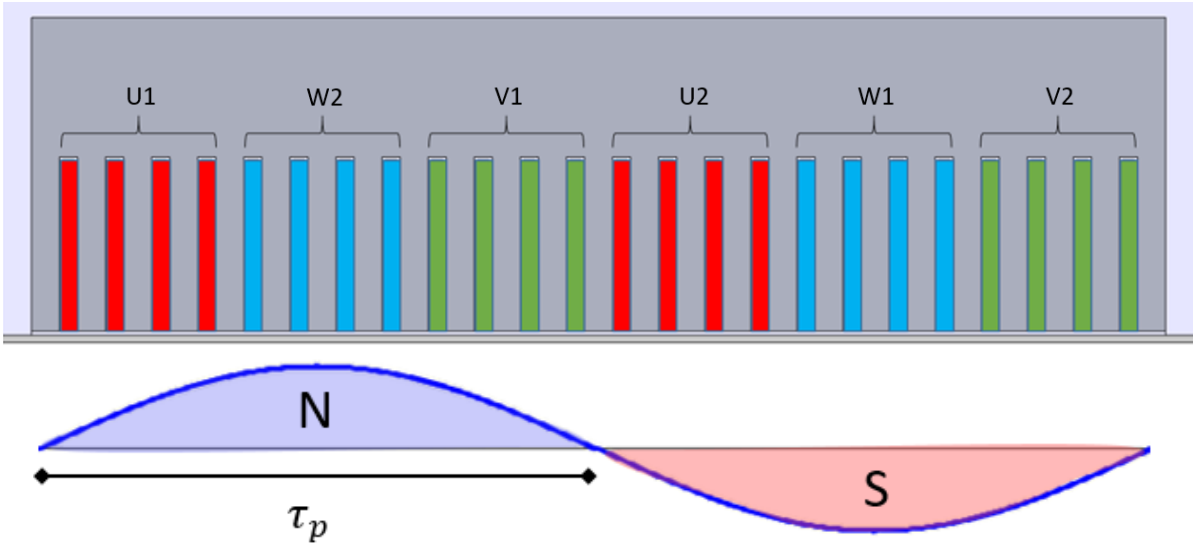

Fig. 3.14: 24-Slot LIM (above) – showing the 3-phase 4 slot/phase winding configuration to be designed, and corresponding pole pitch (below): the pole pitch is roughly half the length of the motor, validating the 2-pole design

Figure 3.14 depicts the windings and shows the 4 slots/phase configuration. The design is split up into 4 slots/phase to create a more uniform stator field, while still providing a 2-pole design for a 3-phase input excitation. The pole pitch from the resulting stator field is shown as half the length of the motor in the bottom portion of Figure 3.14.

As seen in the Slot and Winding Distribution Section, the motivation for increasing the slot number in the motor design is to help better approximate the sine wave input to the stator. Since the number of slots in the motor dictates how well the sine wave is approximated, the more slots there are, the better the windings approximate the sine wave. Therefore, having 4 slots/phase helps provide a better approximated stator field. The stator field for this 24-Slot design can be seen below in Figure 3.15.

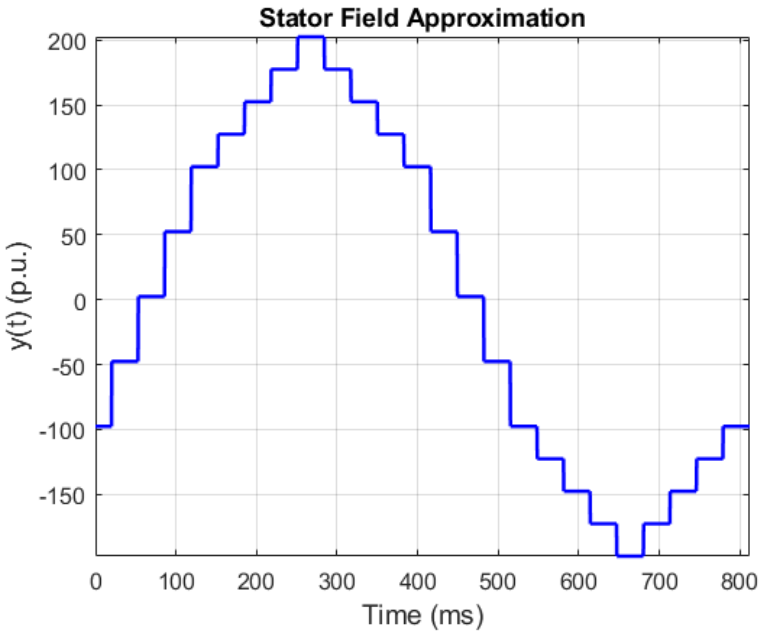

Fig. 3.15: Approximated Stator Field from 24-Slot LIM 4 slot/phase

Figure 3.15 shows that the 24-Slot 4 slot/phase gives a well approximated sine wave by the windings of the stator. There are some slight inconsistencies, though: there is a peak at the maximum and

minimum not present in an actual sine wave, and the zero crossing should be perpendicular, instead of parallel as depicted in Figure 3.15.

By taking the FFT of this approximated sine wave, it becomes clear that the less the stator field resembles an ideal sine wave, the more heavily the higher order harmonics weigh in. However, in this 4 slot/phase configuration, the stator sine wave yields an FFT with a very strong first-order harmonic, or fundamental frequency, meaning other harmonics or frequencies are no longer significant. Without this strong fundamental frequency, the generated stator field would be very noisy and would generate irregular movement during driving. The FFT of this 24-Slot model can be seen in Figure 3.16 below.

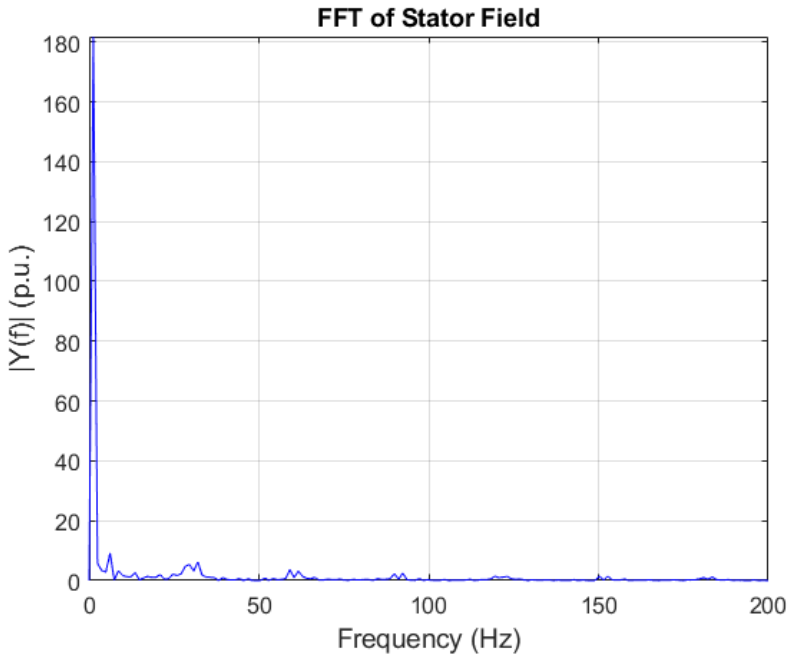

Fig. 3.16: FFT of Stator Field – showing very strong fundamental frequency, while all other higher order harmonics are attenuated down

Additionally, it was also seen that for a 2-pole motor, there should be one pole pair corresponding to a positive and negative direction for each phase of the motor. Thus, for a 2-pole motor, there can only be two U phases, two V phases, and two W phases: this case is shown here in Figure 3.14, and yields one pole pair, which validates the initial design specifying a 2-pole motor.

The LIM is then connected in a Star or Wye connection, meaning each of the phases is connected together at one end to give a parallel connection [17]. Therefore, the U, V, and W phases should be connected at U2, W1, and V2. This configuration is depicted in Figure 3.17, which details the equivalent star or wye circuit of a single phase of the motor.

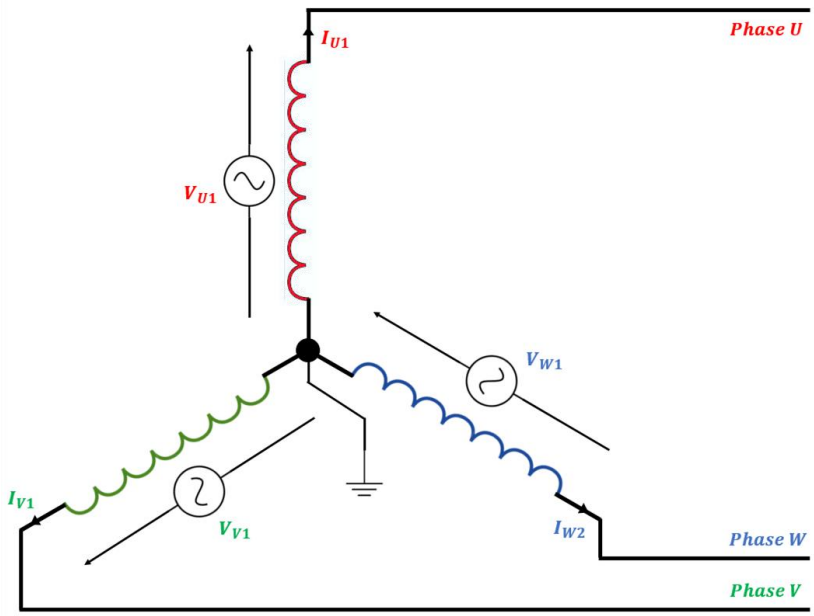

Fig. 3.17: Star / Wye Connection for a Single Phase of the 3-Phase 24-Slot LIM System

Finally, the coils of each phase are made from copper of a certain cross-sectional diameter. The diameter of the windings directly dictates how much current can pass through them. Once the turn number and current is chosen based on the MMF needed to provide the required thrust, a coil cross-section large enough to ensure that the current does not burn the windings can be selected. To determine the appropriate winding size, one must first determine the current density passing through each of the coils. To find the current density, the overall winding system must be analyzed. Figure 3.18 shows the final winding system for a single phase of the LIM, given the 4 slots/phase configuration.

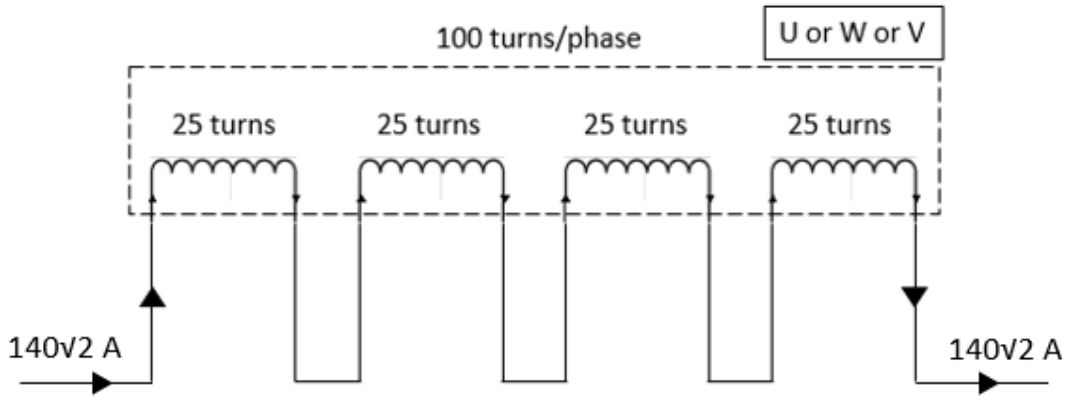

Fig. 3.18: 24-Slot LIM Winding Scheme for 4 slot/phase configuration for a Single Phase – showing roughly MMF of roughly 20000 At is achieved

From this illustration, it can be seen that the MMF of roughly 20000 At is indeed achieved for this 4 slot/phase LIM configuration;

$$\Theta_{LIM} = N \cdot I_p = \left(25 \text{ turns} \cdot 4 \frac{\text{slots}}{\text{phase}}\right) \cdot 140\sqrt{2}\, A = 19798.99\, At \tag{3.6}$$

This 4 slot/phase configuration states that each slot of the LIM will support 25 windings for each phase; however, the full coil will appear to have 100 windings, as each coil is connected in series, which effectively sums the turn numbers.

From this overview, the current density for each coil can be approximated by looking at one slot of the 24-Slot LIM. The approximation uses the assumption that 25 coils will pass through a single slot and carry roughly 200A, as the coil cross-section of this configuration is visualized in Figure 3.19.

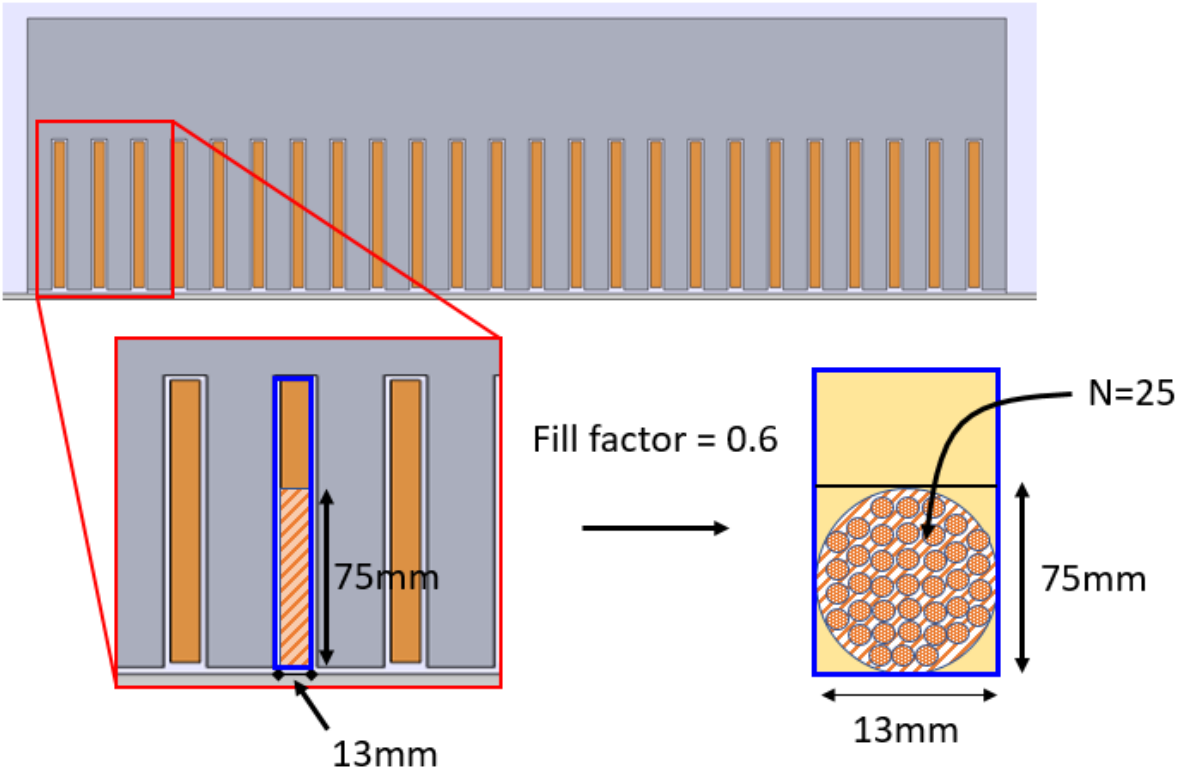

Fig. 3.19: 24-Slot LIM – showing the method of approximating the current density of the winding coils

Given the current specification of about 200 A/phase, and the turn number of each coil through a slot of a given cross-sectional surface area, the current density of the coils can be found from Eqn. 3.14.

$$J_c = \frac{N \cdot I}{SA \cdot FF} = \frac{25 \cdot 140\sqrt{2}\ A}{125\ \text{mm} \cdot 13\ \text{mm} \cdot 0.6} = \frac{4949.75\ A}{75\ \text{mm} \cdot 13\ \text{mm}} = 5.076 \frac{A}{\text{mm}^2} \tag{3.14}$$

Here, N is the turn number of each coil, I is the peak current through the coil as determined by the MMF required, SA is the useable cross-sectional area of the slot through which the coil will pass, and FF is the fill factor, which from manufacturing considerations was found to be 0.6, as it determines how much space is useable to wind the coils in the slots.

From this analysis, it can be seen that a current density of roughly 5 A/mm^2 passes through the large coils of N smaller windings. Although this value appears a bit high to be passed through these coils for the 12.5sec acceleration phase, this current density is actually found to be nominal after discussions with the manufacturing team responsible for the stator windings. Temperature analysis of these coils is shown below in the Temperature Considerations Section. A wire diameter of AWG-4, or 5.19 mm can be chosen based on the available space in the slot. In particular, it is desirable to have the largest winding size for the given 25 turn number count that fits within the useable slot cross-sectional dimensions, so to support the high currents passed through the coils as best as possible. This condition corresponds to a winding of cross-sectional area of approximately 21.1 mm^2.

The windings of the stator have been approximated as coils of N smaller windings in Comsol. This approximation simplifies the geometry to a copper coil, where the surface area can have a certain number of windings in a specific configuration (e.g., parallel or series). Comsol doesn't distinguish

between the number of smaller wires inside this large coil, which means care must be taken to ensure that the designed turn number of smaller windings will in reality fit inside a specified cross-section of the coil. A generic coil of N windings is shown in Figure 3.20 similar to how a coil in Comsol is depicted.

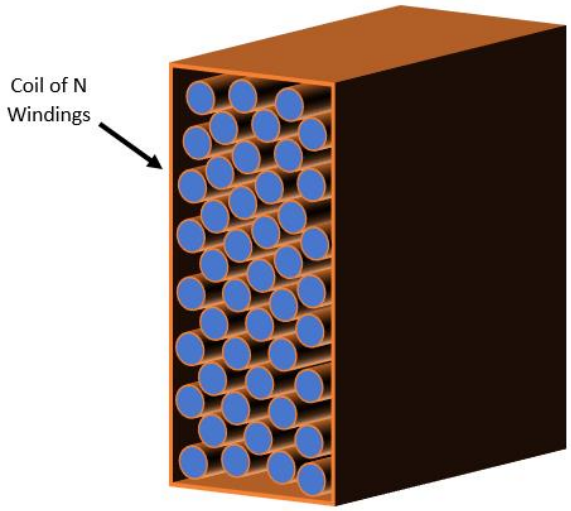

Fig. 3.20: Coil Geometry comprised of N windings similar to that which is approximated in Comsol

In this way, Comsol calculates the influence of this coil of N turns. Additional analysis of Comsol's computation is seen in Appendix G below.

3.3.3 Secondary – Aluminum I-Beam

As discussed, the secondary of the LIM will be the same I-beam geometry used by SpaceX in their Hyperloop tube in LA. Consequently, no design efforts were deployed in designing the secondary. However, using I-beam as the secondary still required some analysis.

One interesting point to investigate was the penetration depth of the magnetic stator field through the 10.465 mm thick Aluminum 6061-T6 I-beam. It can be shown that if the frequency of the produced stator field is low enough, it will penetrate through the aluminum I-beam secondary. This detail is important, as the motor's driving operation functions best when one stator field penetrates through the I-beam to reach the corresponding stator on the other side of the I-beam. When the stator field from one core penetrates the I-beam and reaches the opposite core, the magnetic field line "paths" (as stated from Ampere's Law) close on themselves and both cores are said to be "coupled" to each other[8].

If the stator field frequencies are too high, the fields will not penetrate through the I-beam, and the two cores are said to be "decoupled". In other words, when the path from one stator core does not reach the second stator core, the stator fields will not encompass both cores and will operate individually. At higher frequencies, the fields do not penetrate well through the entire material and instead stick to the surface of the material. In this case, field energy is "lost" in the plate as it is absorbed and dissipated as heat.

[8] The stator configuration is one of a double-sided configuration. This means that the two stators drive optimally when acting together to generate the necessary force to push against the secondary, thus propelling the Pod. To do so, the two cores must operate in a synchronized manor, which requires each respective field to penetrate through the I-beam and reach the other corresponding stator. This condition is achieved if the skin depth at all frequencies of operation is larger than the thickness of the I-beam.

This phenomenon can be further analyzed by looking at the skin depth for all frequencies of driving operation, which corresponds to a frequency range from 50Hz to approximately 171Hz[9]. The performed validation observed variation in skin depth distances across this frequency range.

The skin depth for a given material can be seen below in Eqn. 3.15, assuming low frequencies[10] [15].

$$\delta = \sqrt{\frac{2\rho}{\omega\mu}} \tag{3.15}$$

Where ρ is the resistivity of the material, ω is the frequency of operation, and μ is the magnetic permeability. A plot of a frequency sweep of the skin depth from 0Hz to 171Hz can be seen below in Figure 3.21.

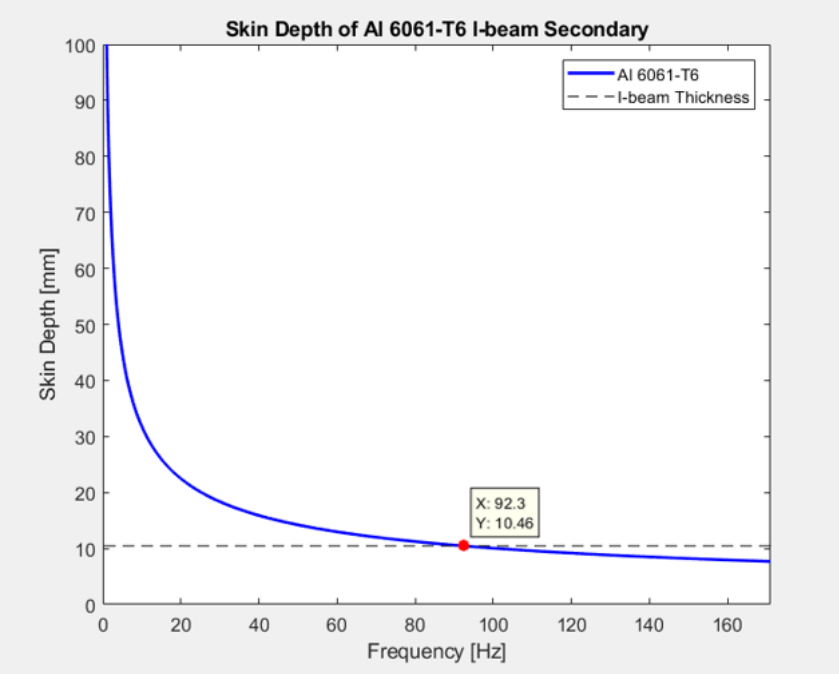

Fig. 3.21: Skin Depth Penetration Distance of Aluminum 6061-T6 I-beam Secondary

As shown, below frequencies of roughly 20Hz, the curve asymptotically approaches infinity.

A more interesting curve for operational frequencies of 50Hz through 171Hz, which are the frequencies through which the motor will sweep during its acceleration period, is shown in Figure 3.22. Table 3.5 lists some key values within this range.

[9] 171.047 Hz corresponds to the synchronous speed of the motor: 138.89 m/s for a pole pitch of 0.406m.
[10] The approximation holds if the frequency of operation is lower than $1/\rho\varepsilon$ for a given material.

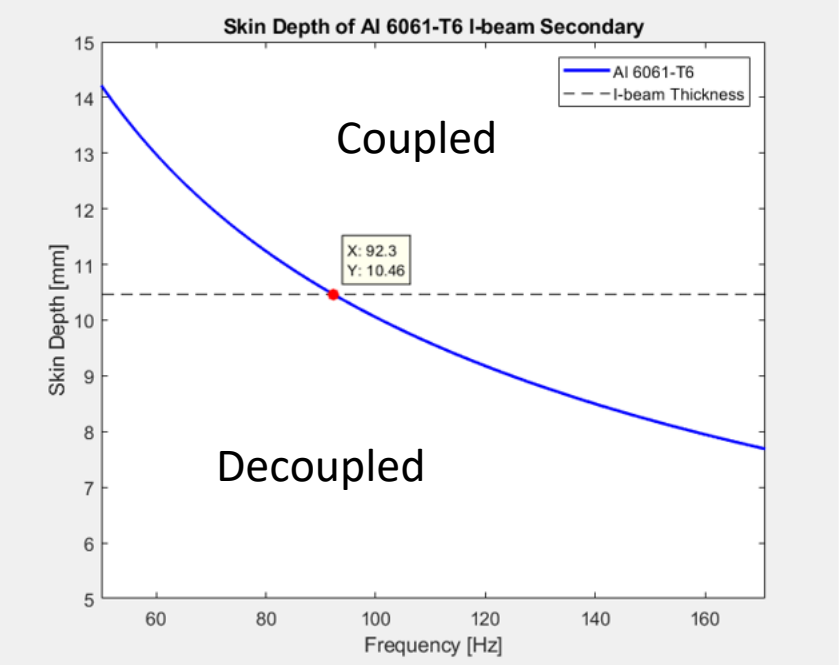

Fig. 3.22: Skin Depth Penetration Distance of Aluminum 6061-T6 I-beam Secondary for Frequencies 50Hz through 171Hz showing coupled and decoupled regions

Skin Depth – Penetration Distances	
Frequency [Hz]	**Skin Depth [mm]**
50	14.217
92	10.481
93	10.425
171	7.688

Table 3.5: Key Values for Skin Depth Penetration Distance of Aluminum 6061-T6 I-beam Secondary

From 50Hz to 171Hz, the penetration depth ranges from 14.22mm (at 50Hz) to 7.69mm (at 171Hz). At about 93Hz, the penetration depth is less than the thickness of the aluminum I-beam, so any further increase in frequency causes the two cores to decouple from one another.

The decoupling boundary is depicted in Figure 3.22 as a black dotted line. At low frequencies above this line, the two sides of the LIM will be magnetically coupled to each other and below this line at the higher frequencies, the penetration distance is too short to penetrate all the way through the aluminum, so the two sides will be magnetically decoupled.

Thus, with regard to skin depth, for about half of the frequency range of operation, the cores will be decoupled from one another. Since coupling guarantees that the cores' produced fields complement each other, extra care that the fields still accompany one another and do not fight against each other must be taken beyond this decoupling point of 93Hz. The main way to ensure complementary behavior is by verifying that the produced fields point in the same direction as one another during all points of operation. This configuration ensures that the moving fields support each other and will also be synchronized to each other during the decoupling region of operation. Coupling of the fields ensures a greater synchronization between the fields, as illustrated below in Figure 3.23.

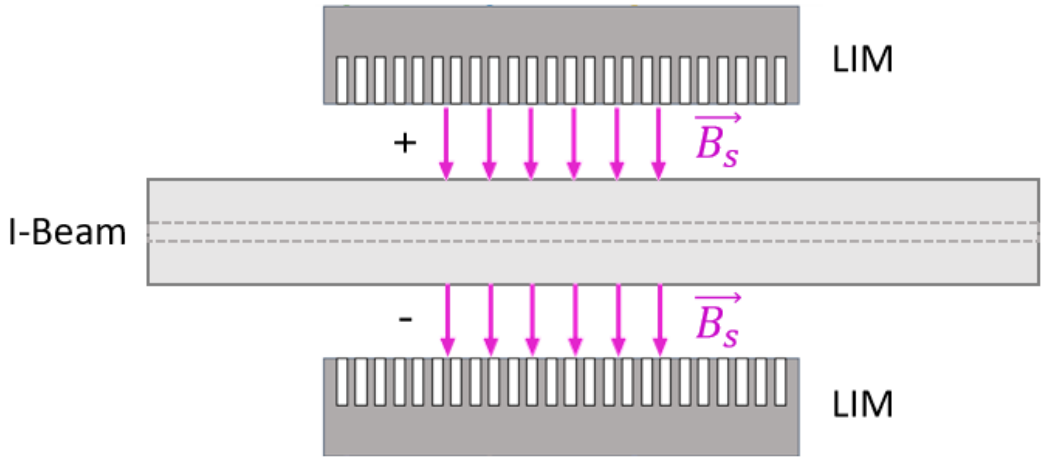

Fig. 3.23: Showing coupling I-beam, fields should be same orientation so motor thrusts are working together not against each other – reinforcing the thrust or complementing.

The I-beam was modelled in Comsol to simulate the effects of the secondary as close to reality as possible. The modelled I-beam in Comsol can be seen below in Figure 3.24.

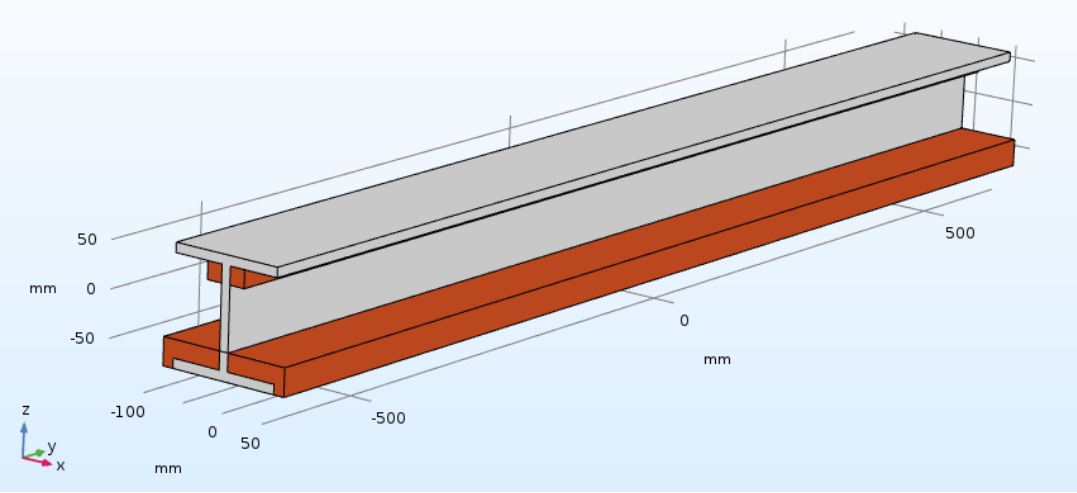

Fig. 3.24: I-beam with "Keep-out-Zones" Modelled in Comsol – CAD of each motor prototype can be inserted into this design to see exactly how it fits in the I-beam dimensions

After modelling the complete I-beam, the 3D simulation was very computationally heavy, as Comsol places very fine mesh elements in the edges/corners of the I-beam during discretization, even when taking symmetries. Instead, and for the entirety of the simulations, the I-beam was modelled as a single aluminum plate with the same length as the inner dimension (106mm) of the I-beam. Doing so greatly reduced the run time and complexity during simulations in Comsol.

3.3.4 Air Gap

Analysis and theory indicate that a smaller air gap yields a stronger thrust force [17], [21], [13]. Therefore, the closer the double-sided stator cores are to the rotor I-beam, the smaller the air gap will be, and thus the greater the thrust produced. Nevertheless, determining the right air gap for the motor design was aided by performing a parametric sweep of varying air gap distances shown in Figure 3.25, which further validated this smaller air gap ansatz.

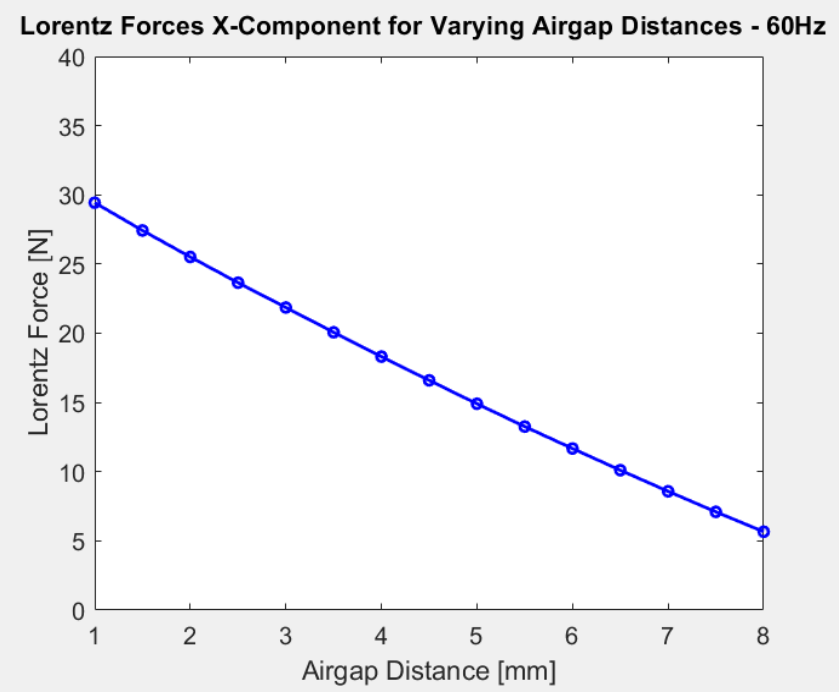

Fig. 3.25: Air Gap Parametric Sweep showing X-Component of Lorentz Force (Driving Force) vs. Distance, for a frequency of 60Hz. It can be seen that as the air gap distance decreases, the generated Lorentz force decreases.

This parametric sweep was performed for the 2-slot model concept, but the intuition gained from the study still holds. In this model, the turn number, N, is equal to 10 turns and the current through the windings, I, is set to 50A for a constant frequency of 60Hz. This is a very low power configuration, meaning the produced thrust levels will in turn be very low. However, in examining Figure 3.25, the idea that smaller air gaps lead to higher thrust forces produced, is again held true.

Ideally, the air gap is at a minimum so that eh LIM is as close to the I-beam as possible. However, due to mechanical tolerances and constraints, very close distances cannot be chosen. Specifically, the I-beam secondary for the SpaceX tube comes in sections, and at the interfaces of these sections, tolerances of +/- 1mm have been reported and observed. Therefore, as a precaution to ensure that while driving between these interfaces, the LIM does not make contact with the beams, a 3mm spacing from the I-beam is chosen. This is a moderate compromise between mechanical feasibility and adequate electromagnetic field performance.

However, this does not mean that the air gap used in the design calculations is 3mm. In the double-sided case, the air gap is actually defined as the distance from one LIM stator core to the other. In other words, the air gap is actually much larger, as can be seen below in Figure 3.26. The true air gap is comprised of both 3mm gap distances, as well as the rotor blade thickness of 10.465mm, and is therefore 16.465mm.

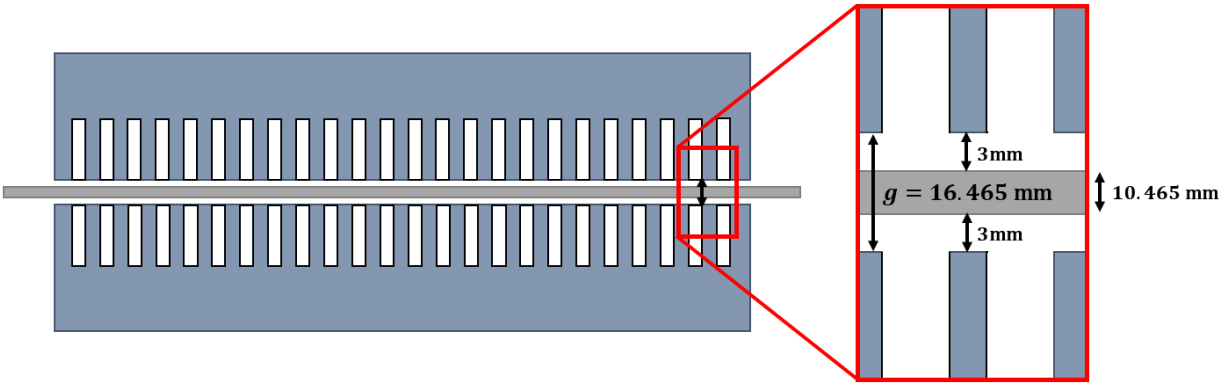

Fig. 3.26: Double-Sided 24-Slot LIM showing the full air gap distance of 16.465mm, with windings omitted

Thus, it can be deduced that linear motors require large air gaps, which is a conclusion also stated in [19], [13], [21].

Rotary motors do not require air gaps as large, a property that constitutes one of the main negative aspects of a linear motor. For this reason, it is sometimes advantageous to use permanent magnet (PM) or synchronous linear motors. PM linear motors generate higher field strengths in the air gap when compared to induction or asynchronous machines, thereby enabling operation in larger air gaps through an increased overall field strength in the air gap.

In the Comsol simulations, the air gap was modelled as a separate geometric object, defined by a finer mesh, which was needed because the air gap is always much smaller than the rest of the motor. In this way, the simulations yield more accurate results. A screenshot of the mesh produced for a single side of the 24-Slot variant can be seen below in Figure 3.27 – which shows the finer mesh in the air gap compared to the rest of the model.

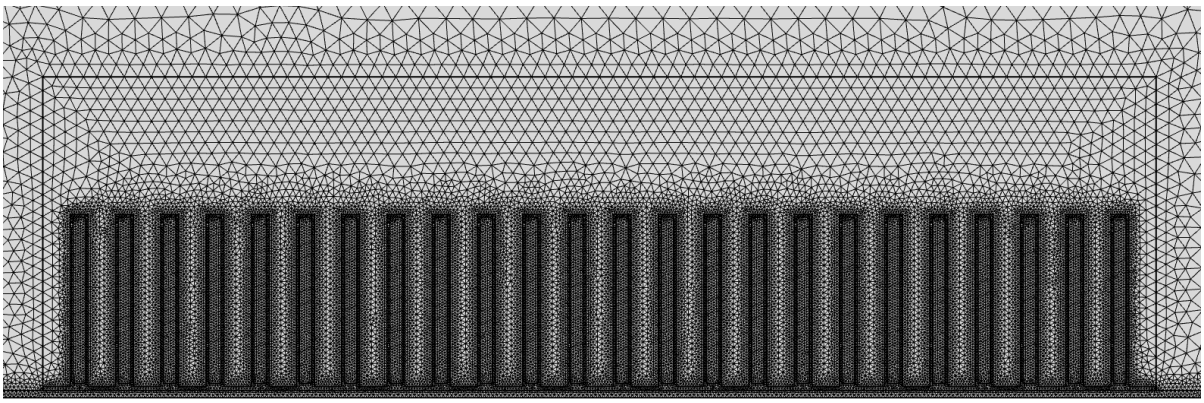

Fig. 3.27: Mesh of Symmetric 24-Slot Comsol model showing very fine mesh created in the air gap

Finally, considering all the points listed in the preceding sections, an optimized 24-Slot revision was reached, and a final design specified. The final optimized 24-Slot design is detailed in the following section.

3.4 Final Model

The final design presented in this thesis is a 24-Slot Double-Sided 2-pole LIM. The model was designed according to the processes laid out in the previous sub-sections and is the results of several design iterations and revisions. Simulations were performed in 2D in Comsol to reduce the computational time and complexity relative to 3D simulations. The final 2D Comsol CAD model can be seen below in Figure 3.28 with the according dimensions given in the technical drawing Appendix F.

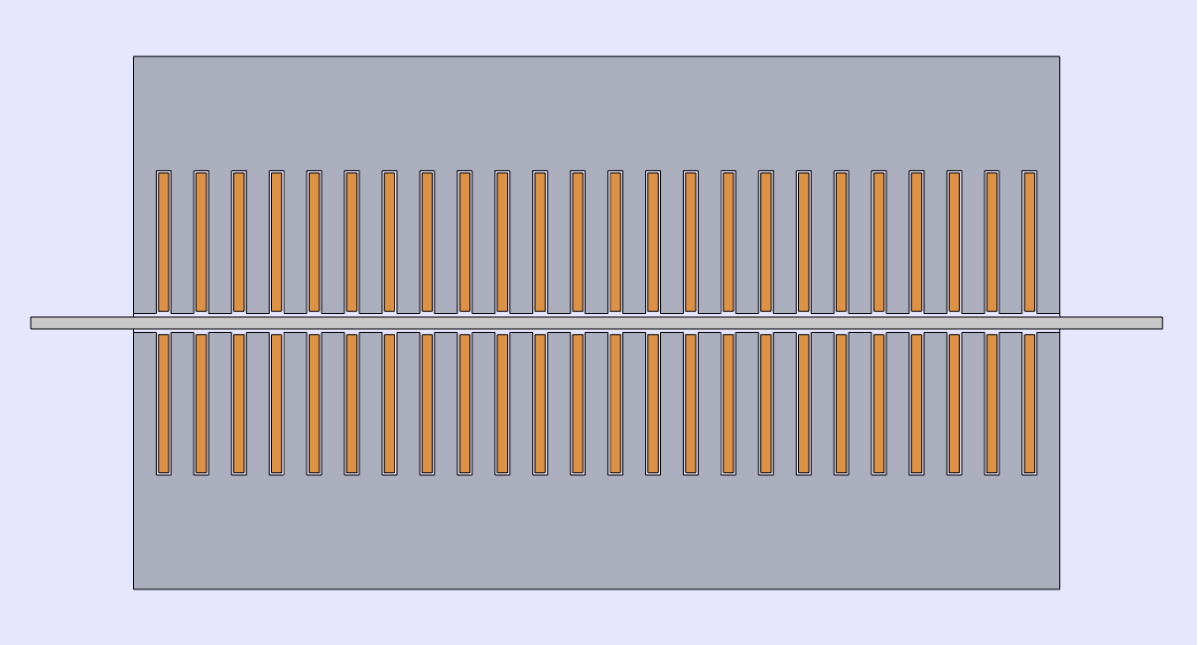

Fig. 3.28: Final Double-Sided 24-Slot LIM model modelled in Comsol

Additionally, by using a symmetry point in the middle of the single aluminum plate (modeled as the I-beam), the need to model and simulate the full double-sided LIM in Comsol was eliminated. Instead, simulating half of the LIM is sufficient, as the thrust produced from a single-side of the LIM can simply be doubled to find the correct complete double-sided result. A single-side of the 2D LIM model in Comsol can be seen below in Figure 3.29.

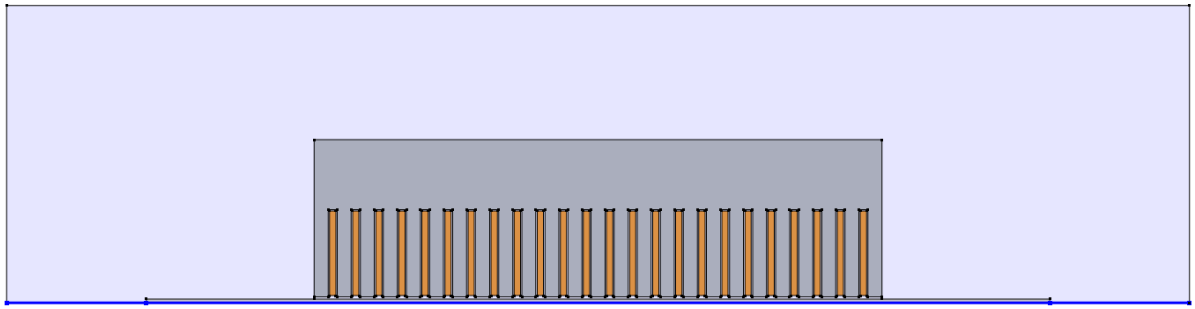

Fig. 3.29: 24-Slot LIM shown as 2D simulation in Comsol with a symmetry taken on the x=o plane (I-beam middle) – the bottom blue boundary is a PMC boundary, while all other boundaries in the simulation are magnetic insulation boundaries

This figure shows a blue boundary line on the bottom of this model running beneath the I-beam plate. This is a perfect magnetic conductor (PMC) boundary, which sets the tangential component of the magnetic field strength, H, and the current density, J, to zero. This PMC boundary accurately models the second half of the LIM. By creating this boundary, the magnetic flux lines are continuous across it, as this correctly models reality in the case of a double-sided LIM.

The rest of the boundaries in the simulation are all set to magnetic insulation boundaries. These boundary conditions set the tangential components of the magnetic potential, A, to zero.

As can also be seen in the simulation, the rotor is taken as some “shorter” than reality rotor. This is because Comsol cannot simulate the entire 1.25 km long I-beam blade. However, it is also not necessary to simulate a full-scale rotor blade in these simulations. It will be seen in the subsequent sections that velocity or distance travelled, can be modeled differently in Comsol.

As was seen in the previous sections, there exist limits to both the magnetic flux density (fundamental material limit) and the active surface area (limit of the stator core width due to the I-beam secondary). From these limits, the magnetic flux produced by this 24-Slot LIM can be found from Eqn. 3.16.

$$\Phi_{LIM} = 2\ \mathrm{T} \cdot 0.055\ \mathrm{m} \cdot 0.812\ \mathrm{m} = 0.0893\ \mathrm{Wb} \tag{3.16}$$

The flux produced does not seem to be that far off from the fundamental limit for this secondary, as was seen in Primary Windings Section above. The MMF was also found from Eqn. 3.17.

$$\Theta_{LIM} = N \cdot I_p = \left(25\ \mathrm{turns} \cdot 4\ \frac{\mathrm{slots}}{\mathrm{phase}}\right) \cdot 140\sqrt{2}\ A = 19798.99\ At \tag{3.17}$$

The MMF of this motor is then seen to be 20,000 At. This is the MMF which will guide the flux in order to produce the necessary thrust to move the LIM. The magnetic reluctance of the motor can be then found as the ratio of the MMF to the magnetic flux.

$$\mathcal{R}_{LIM} = \frac{\Theta_{LIM}}{\Phi_{LIM}} = \frac{19798.99\ At}{0.0893\ \mathrm{Wb}} = 221713.2\ \mathrm{H}^{-1} \tag{3.18}$$

Now that many of the design specifications have been determined, a full list of parameters for the 24-Slot LIM are listed below in Table 3.6.

Final Design Parameters for 24-Slot LIM		
Description of Parameter	**Symbol**	**Value**
Surface Resistivity of the Secondary Conductive Plate	ρ_r	2.857*10^-8 [Ω*m]
Thickness of Secondary Rotor Plate	d_r	10.465 [mm]
Air gap distance between the Primary Cores	g	16.465 [mm]
Stator Field Synchronous Velocity	v_s	138.889 [m/sec]
Final Frequency of Stator Field	f_s	171.047 [Hz]
Turn Number	N	100 [Turns]
Peak Input Current	I_p	140√2 [A]
Stack Width or Stator Core Width	D	0.055 [m]
Stator Length	L	812 [mm]
Pole Pitch	τ_p	406 [mm]
Tooth Width	t_w	20 [mm]
Slot Width	s_w	13 [mm]
Tooth Pitch	τ_t	33 [mm]
Slot Number	N_s	24 [slots]
Maximum Thrust Produced	T_{max}	4.69 [kN]
Mass of Stator	m	80 [kg]
Permeability of Iron Core	μ_r	5000 [H/m]
MMF Produced	Θ_{LIM}	19798.99 [At]
Reluctance of Stator Core	$\mathcal{R}_{LIM}$	221713.2 [1/H]
Flux Produced	Φ_{LIM}	0.0893 [Wb]

Table 3.6: 24-Slot LIM Final Design Parameters

3.5 Electrical Design

It was stated above that an electric motor is defined as a device that takes electrical power as an input and produces mechanical motion as output. In a linear motor this motion is transferred in a linear direction, hence its name. Therefore, some source of electrical energy is needed to supply power to the LIM.

The following section will describe the methods chosen to electrically power the LIM. Lithium-ion polymer (Li-Po) batteries were chosen as the electrical source due to their high capacity and power density, as compared to conventional Lithium-ion (Li-Ion) batteries. As a drawback, the chosen cells chosen are susceptible to lower pressures. This poses a problem since this motor needs to operate in a low-pressure environment, as was defined as one of the main characteristics of a Hyperloop-like system. Therefore, a sealed container will have to be designed and constructed to support these cells in an airtight environment.

Finally, high-powered inverters are chosen to convert the DC voltage of the Li-Po batteries to 3-phase AC voltage. This AC voltage is then supplied to the motor to produce the necessary travelling stator field required to generate a Lorentz Force capable of moving the Pod.

3.5.1 Power

To determine the source for to electrically powering the LIM, one can look at the power needed to move the Pod. By taking the force required to move the Pod (i.e., the 2.778kN calculated in the Trajectory Section), and relating it to the mechanical power needed, one can determine the required power. Relating this force to a mechanical power, requires it be multiplied by the final velocity [13] of 500 km/h.

$$F_m \cdot v_f = P_{mech} \tag{3.19}$$

$$P_{mech} = 2.778kN \cdot 138.889\,{}^{m}/_{s} = 385.8\ kW \tag{3.20}$$

After choosing a relatively modest electric motor efficiency term, the necessary input electrical power needed to output this mechanical power can be found.

$$\text{efficiency} \coloneqq \eta = 0.93 \tag{3.21}$$

$$\frac{\text{Mechanical Power}}{\eta} = \text{Electrical Power} \Rightarrow \frac{385.8\ kW}{0.93} \cong 414.84\ kW = P_{elec} \tag{3.22}$$

Therefore, using an efficiency of 93%, this LIM prototype requires a minimum electrical input power of approximately 415kW to reach a top speed of 500 km/h in 12.5sec. The electrical and mechanical powers can be seen below in Figure 3.30 as linearly increasing curves for the power throughout the run. This relationship is due to a constant thrust force being assumed for the duration of the run.

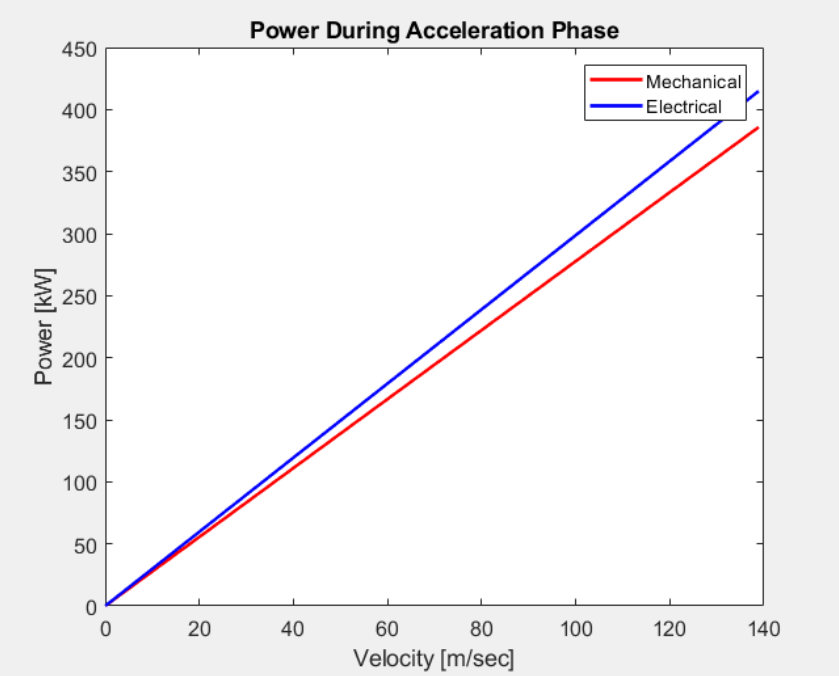

Fig. 3.30: Mechanical and electrical powers during the acceleration phase of the run – showing an electrical power of about 415kW is consumed by the end of the run, in order to reach 500 km/h

The total energy needed for the run can also be calculated as the effective electrical power multiplied by the total acceleration time.

$$E = P_{elec} \cdot t \cdot \left(\frac{1\,h}{3600\,sec}\right) = 414.84\,kW \cdot 12.5\,sec \cdot \left(\frac{1\,h}{3600\,sec}\right) = 1.44\,kWh \tag{3.23}$$

It is also recommended to have at least 10 times the required capacity for safety concerns and operating flexibility. This condition would require the electrical source to be capable of providing around 14.40 kWh.

Using this electrical power, the remaining electrical design parameters needed for the LIM, such as the required driven voltage and current draw of the LIM, are determined. For this analysis, Figure 3.31 is created to depict the corresponding powers for each stage in the LIM's electrical design.

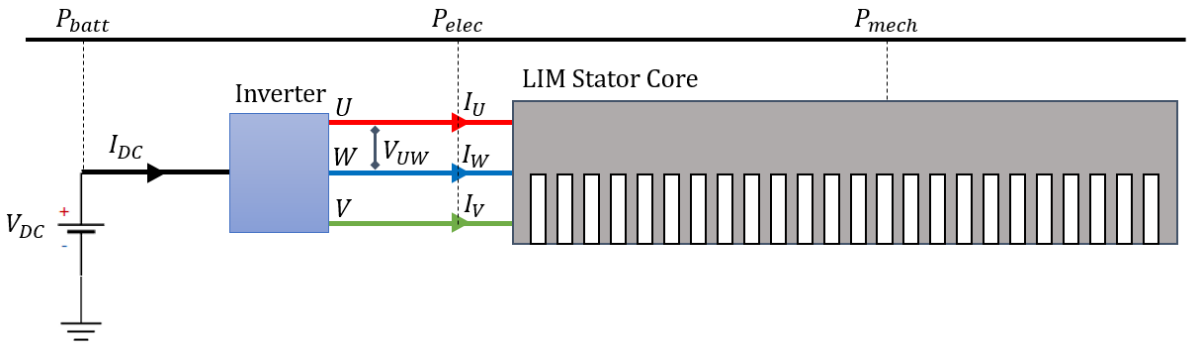

Fig. 3.31: Different Power Levels seen in the LIM system

As can be seen from Figure 3.31, each stage in the LIM electrical design is depicted by a different power parameter, where each of these powers are defined below.

$$P_{batt} = V_{DC} \cdot I_{DC} \tag{3.24}$$

$$P_{elec} = \sqrt{3} \cdot V_{UW} \cdot I_U \cos\varphi \tag{3.25}$$

$$P_{mech} = F_m \cdot v_f \tag{3.26}$$

P_{mech} and P_{elec} were both already found above as 385.8 kW and 414.8 kW, respectively. However, the source power, P_{batt} must still be determined and is an important parameter because the source must be capable of driving the LIM to the P_{mech} level found in Eqn. 3.26. The LIM will try to draw the requisite power from the supply, however, if the amount needed is unavailable, the estimated trajectory of 500 km/h over 12.5sec will not be reached, and the LIM will operate on a lower level.

To find the P_{batt} required by the LIM, the inverter efficiency is required. A value of roughly 99% for maximum power output is found from [27]. P_{batt} is then calculated as roughly 417 kW.

$$P_{batt} = \frac{P_{elec}}{0.995} = 416.926\ kW \tag{3.27}$$

With the required battery source power, the corresponding voltage level for the battery can be determined. The MMF discussed in the Motor Design Section requires roughly 200A/phase of current supply to generate the 2.778 kN of necessary thrust force for the LIM to reach 500 km/h. This MMF constraint then fixes the input current from the battery. Therefore, the DC input current sourced from the battery should be at least 200A. The corresponding voltage drop[11] required to sustain the power level of the battery source can now be determined. To find this voltage, one can use the electrical power formula.

$$V_{DC} = \frac{P_{batt}}{I_{DC}} = \frac{416.93\ kW}{140\sqrt{2}\ ADC} = 2.105\ kVDC \tag{3.28}$$

Eqn. 3.28 shows that an induced voltage of approximately 2kV is required to drive the LIM for 12.5sec to 500 km/h. However, this is not ideal as finding a portable high-density power source to supply this much voltage would be impractical. Decreasing the induced voltage needed to supply the LIM requires further analysis and inspection of the winding configuration of the LIM.

As seen from Faraday's Lawn, the number of turns, N, is directly related to the induced voltage across a set of coils. The relationship is rewritten here for clarity.

$$\mathcal{E} = -N\frac{d\Phi_B}{dt} \tag{3.29}$$

Here, $\mathcal{E}$ is the electromotive force or EMF and it is proportional to an induced voltage. By increasing the number of turns in a coil, more voltage will be induced across its windings. Therefore, if it is desired to reduce the coils' required voltage drop, the number of turns in a coil should be reduced. However, it was seen that the turn number is also directly related to the MMF; therefore, by decreasing the turn number to reduce the induced voltage drop across the coils, the MMF also correspondingly decreases. A smaller MMF decreases the amount of thrust produced and is undesired and actually counterproductive to the central point of this thesis.

Thus, if the number of turns in a coil is increased for the purpose of increasing thrust, then the voltage supplied by the electrical source must also increase to support this level. This relationship is well known as most high-powered motor applications, such as trains or wind turbines, all supply high voltages in the kV range.

[11] This voltage drop is also the induced voltage required by the LIM's coils to drive the desired MMF. If this level is not reached, the MMF will drop to a voltage level that can be sustained.

The tradeoff is that one needs a large number of turns to support a high MMF, however, a lower number of turns are required to provide a lower induced voltage drop. Therefore, an "effective turn number" can be introduced which is effectively the turn number seen by the MMF, but not what is actually wound in each coil. This effective turn number should therefore be maximized to provide a high MMF, while the actual turn number should be minimized to induce a lower voltage drop. To achieve this, the coils can be split into a certain number of smaller parallelized coils, each of which requires a lower induced voltage drop. At the same time, the overall MMF must stay the same: it is the product of the current and the turn number, so this ratio of current to turn number must stay the same. Therefore, the current must also increase as it will now be split across each of the parallelized coils. Without a current increase, the MMF would decrease accordingly.

Since all of the coils are now in parallel and have a smaller turn number, they will have a lower induced voltage drop that together will be equivalent across the coils. Additionally, the MMF should stay the same, provided that a correct value of current has been chosen. For the 24-Slot LIM, this splitting is performed and the winding diagram shown above in Figure 3.18 is slightly altered to support this change. This new parallelized configuration to support a lower induced voltage is shown below in Figure 3.32.

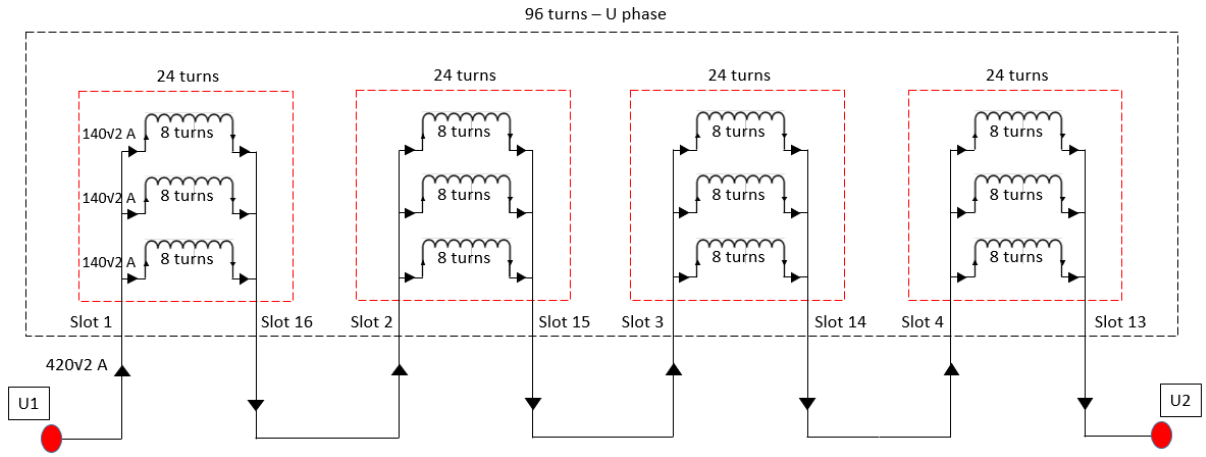

Fig. 3.32: Creative winding Idea to parallelize the windings to reduce the induced voltage dropped across the coils, while still keeping the same MMF – seen for a single phase, U, of the LIM

It can be seen from Figure 3.32, that keeping a symmetric configuration requires three parallelized windings of 8 turns each. In this way, the MMF of this design is kept almost equivalent to the previous MMF. This new MMF is analyzed and calculated below in Eqn. 3.30.

$$\Theta_{LIM} = N \cdot I_p = \left(8 \text{ turns} \cdot 4 \frac{\text{slots}}{\text{phase}} \cdot 3 \text{ parallel coils}\right) \cdot 140\sqrt{2}\, A = 19007.03\, At \tag{3.30}$$

The new MMF produced is 19007.03 At, and the percent difference between the two MMF's is listed in Eqn. 3.33.

$$\text{Percent Difference} = \frac{|\Theta_1 - \Theta_2|}{(\Theta_1 + \Theta_2)/2} \times 100 \tag{3.31}$$

$$\text{Percent Difference} = \frac{|19798.99 - 19007.03|}{(19798.99 + 19007.03)/2} \times 100 = \frac{791.96}{19403.01} \times 100 \tag{3.32}$$

$$\text{Percent Difference} = 0.0408163 \times 100 = 4.08163\ \% \tag{3.33}$$

It can be seen that by implementing this new winding scheme, the percent difference between the two MMF values is about 4%.

It can be seen that the MMF is slightly lower now because the equivalent turn number is also slightly lower: the effective turn number has decreased from 100 turns to 96 turns. However, 100 turns cannot be achieved by parallelizing the coils into three groups. Therefore, this slight 4% decrease is a non-avoidable design trade-off.

Reducing the turn number from 25 turns to three parallel windings of 8 turns, produces a 702 VDC voltage drop across the coils instead of 2kV. However, it can also be seen that the current had to be increased correspondingly by three-fold to compensate for this lower induced voltage change. These changes are seen in Eqn. 3.34 and Eqn. 3.35.

$$V_{DC} = 2.105\ kVDC/3 = 701.9\ VDC \tag{3.34}$$

$$I_{DC} = 140\sqrt{2}\ A \cdot 3 = 420\sqrt{2}\ A \tag{3.35}$$

If the induced voltage must be decreased, the windings can be parallelized to support a lower induced voltage.

Therefore, this V_{DC} should be the voltage that the electrical source can supply, which also gives a corresponding new I_{DC}. The new peak current to be supplied by the electrical source is shown below in Eqn. 3.36.

$$I_{DC} = \frac{P_{batt}}{V_{DC}} = \frac{416.93\ kW}{702\ VDC} = 593.969\ A\ DC \tag{3.36}$$

This states that the required current will now be about 600A, which is a design trade-off to make for a lower induced voltage. This larger current matches up with the required MMF needed for 200A/phase. Therefore, the electrical source will have to be large enough to support both this current level as well as the new induced voltage level dropped across the parallelized coils. The source must provide this voltage level at a minimum, but should ideally be a bit higher. If the source cannot provide the necessary voltage drop across the coils needed for the constant driving thrust, then lower velocities or accelerations will be achieved because there will be insufficient power to reach these higher levels.

An estimate of the drawn current during the run, based on these solved powers, is seen below in Figure 3.33, where the final current level of approximately 600A is sourced by the end of the run.

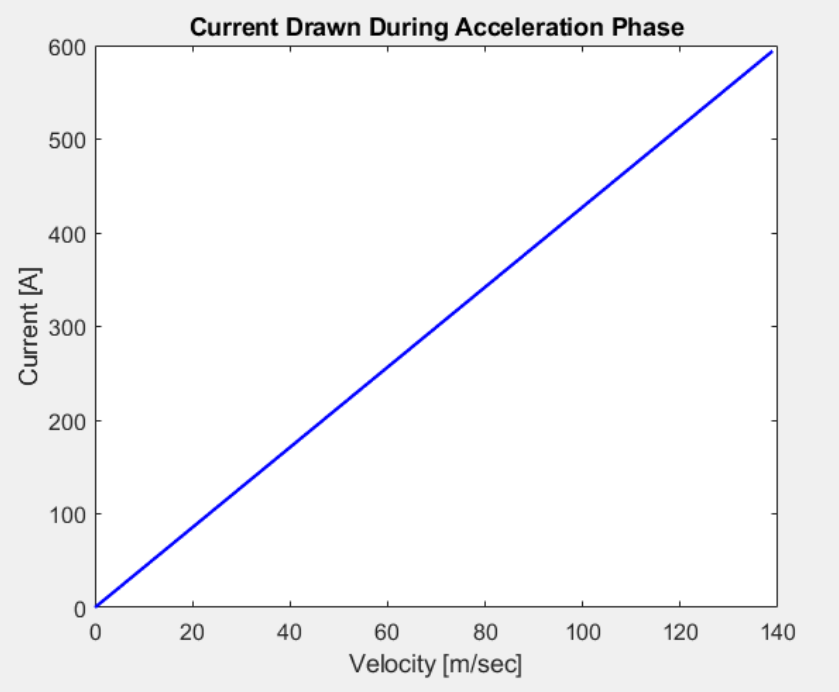

Fig. 3.33. The current to be supplied from the electrical source during motor acceleration

The simulation ends on the final value of 593.969 A, which means it will almost reach the designed 600A level. Providing an electrical source to support these specifications will be shown in the next section.

It was also discovered above that V_{Bmin} for air is roughly around 330V to 350V [24]. This means that for any voltage below this breakdown minimum, there can never be any pressure or distance product which causes a breakdown. Therefore, if the DC source or battery voltage level is set to 350 VDC, the issue of breakdown and discharges is eliminated.

To further reduce the induced voltage drop and to meet this minimum voltage breakdown level, this 702 VDC source can be split into two separate sources, each capable of supplying 351 VDC at the needed 600A current. Splitting up the source like this is acceptable since there are two sides of the LIM and each side will supply half of the required thrust. Together they will produce the full 2.778kN of thrust needed to reach 500 km/h.

Finally, the power factor of the LIM can be found as roughly 0.6, by using Eqn. 3.25 above.

$$PF = \cos\varphi = \frac{P_{elec}}{\sqrt{3} \cdot V_{UW} \cdot I_U} = \frac{414.84\ kW}{\sqrt{3} \cdot 698.42\ VDC \cdot 420\sqrt{2}\ ADC} = 0.577 \tag{3.37}$$

This then corresponds to a phase angle φ between the voltage and current of 54.736°.

$$\varphi = \cos^{-1}(0.577) = 54.736° \tag{3.38}$$

Now that the electrical power specifications have been determined, an electrical power source capable of providing the high currents and voltages required by the motor can be chosen. The source should be able to provide the high powers while supporting a relatively high voltage level.

3.5.2 Batteries

Two custom built 351.5 VDC Li-Po batteries provide these high-power levels, by supplying the high current draw and high voltage needed to drive the LIM. Each battery configuration is a 95S-4P design

(95 cells in series with 4 submodules in parallel) of SLPB7646143 cells from Malesta. Together the full 190S-4P battery configuration has a total voltage of 703 VDC and is capable of supplying currents above 600A. This meets both of the electrical design constraints listed above for the voltage and current required to drive the LIM. A table of the specifications of the individual cells from Malesta is shown in Table 3.7 below.

Malesta SLPB7646143 Cell Specifications	
Nominal Voltage	3.7 [VDC]
Cell Dimensions	Thickness: 7 [mm] Width: 46 [mm] Length: 144 [mm]
Cell Mass	106.5 [g]
Cell Capacity	5 [Ah]
C Rating	30C
Max Continuous Discharge Current	150 [A]
Power Produced	555 [W]
Energy Stored	18.5 [Wh]
Internal Resistance	1.2 [mΩ]

Table 3.7: Malesta Li-Po Cell Specifications

Each battery will be separated into five submodules of a 19S-4P configuration. Three parallel cells will be connected in series via a CUPAL connection element onto which the cell's connection tabs will be laser welded. CUPAL is a metal composite material consisting of aluminum and copper often used in wiring applications to save costs and weight over traditional pure copper, while still having the conductive advantages of pure copper. To connect the submodules, an end-element, also made out of CUPAL, will be used and an aluminum connection will be fixed onto it. CAD models of the Malesta cells, submodules and complete battery packs are shown below in Figure 3.34 and Figure 3.35.

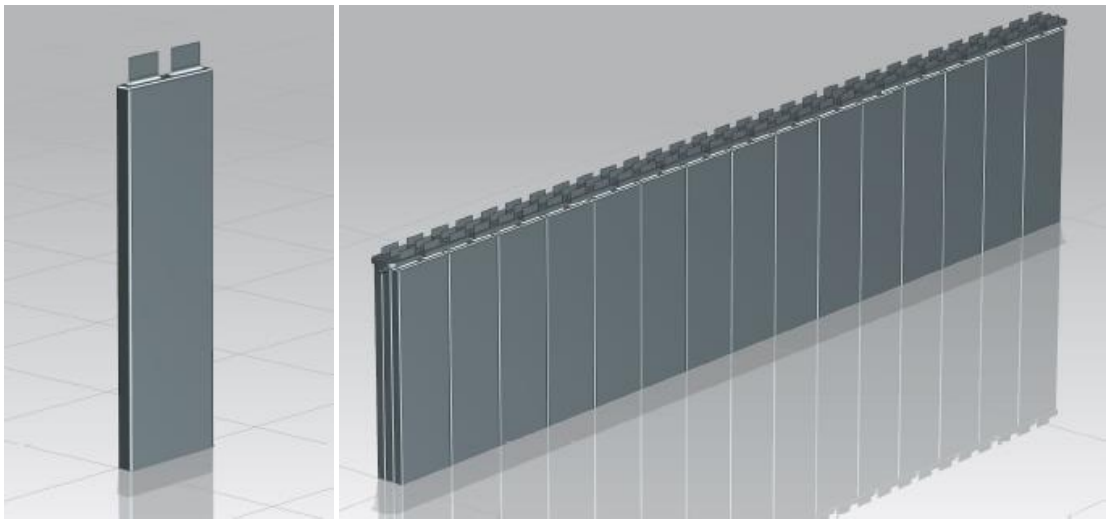

Fig. 3.34 Single Malesta Cell [left], and 19S-4P submodule [right] – both modelled in CAD

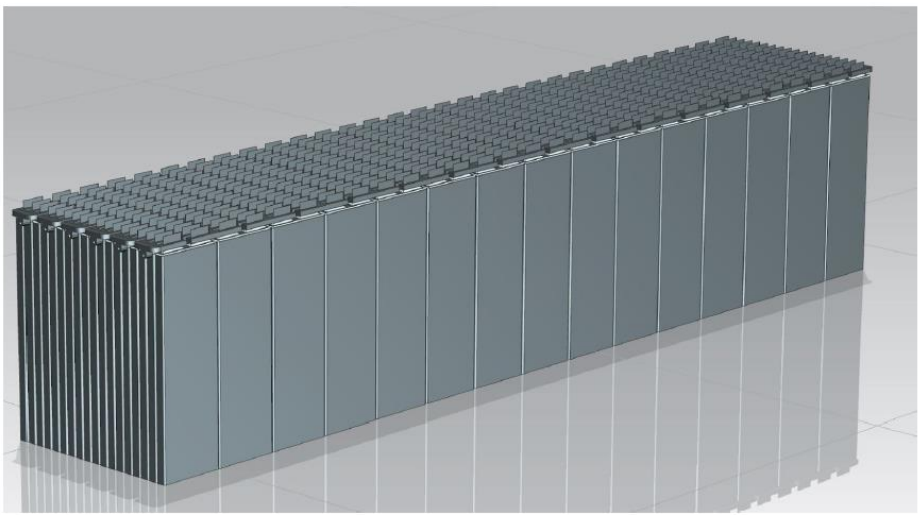

Fig. 3.35: One of the custom built 95S-4P batteries modelled in CAD

The complete battery specifications are listed below in Table 3.8.

Assembled Battery Specifications	
Total Cells	380
Cells in Series	95
Cells in Parallel	4
Battery Mass	40.47 [kg]
Battery Voltage	351.5 [VDC]
Number of Battery Packs	2
Total Number of Cells	760
Total Mass	80.94 [kg]
Total Voltage	703 [VDC]
Continuous Current Supply	30C or 600 [A]
Peak Current Supply	35C or 700 [A] ≤ 1sec
Total Capacity	20 [Ah]
Total Power Produced	421.8 [kW]
Total Energy Stored	14.06 [kWh]

Table 3.8: Malesta Li-Po Full Battery Specifications

The weight of a single 95S-4P battery configuration is 40.47kg, as it is comprised of 380 Malesta Li-Po cells. Therefore, the total weight of the190S-4P battery is then 80.94kg. This is computed by multiplying the mass of an individual cell (106.5g) by the number of series and parallel cells, as seen in Eqn. 3.39.

$$m_{tot} = m_i \cdot S \cdot P = 106.5\ \text{g} \cdot 190 \cdot 4 = 80940\ \text{g} \tag{3.39}$$

Both batteries together are capable of supplying a total power output of 421.8kW. Although the required power output from the batteries is around 415kW, the batteries are still capable of supplying a bit more (i.e., 422 kW). This then gives a power-to-weight ratio for the combined batteries of 5.21 kW/kg, which is comparable to some turbojet engines, as shown below in Eqn. 3.40.

$$Power\text{-}Weight\ Ratio = \frac{421.8\ kW}{80.94\ kg} \cong 5.21\ kW/kg \tag{3.40}$$

The performance of the batteries can be seen in Figure 3.36 below where the current draw and voltage drop during the 12.5sec acceleration phase of the run is depicted. Additionally, Figure 3.37 shows the power and energy drawn from the batteries during the run.

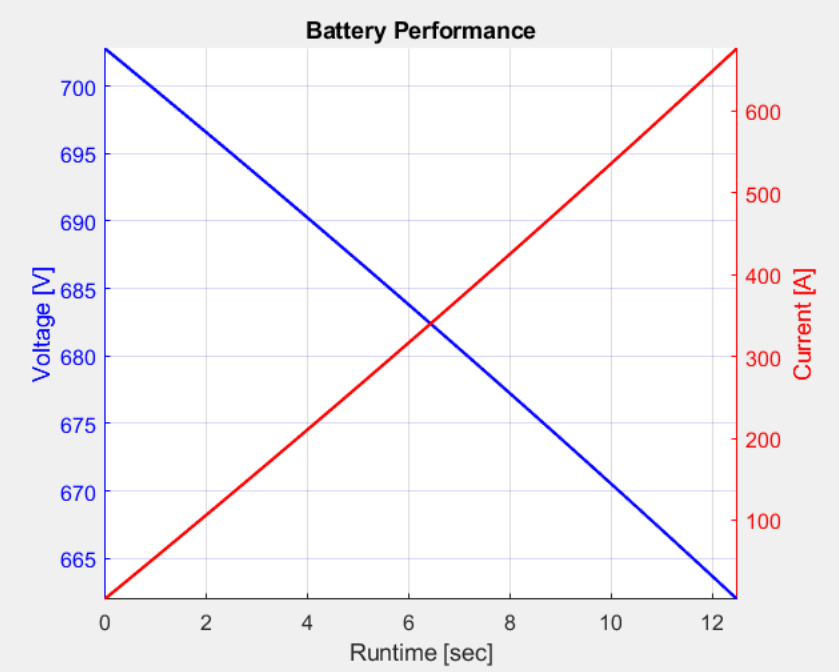

Fig. 3.36: Battery Performance Voltage Drop & Current Drawn

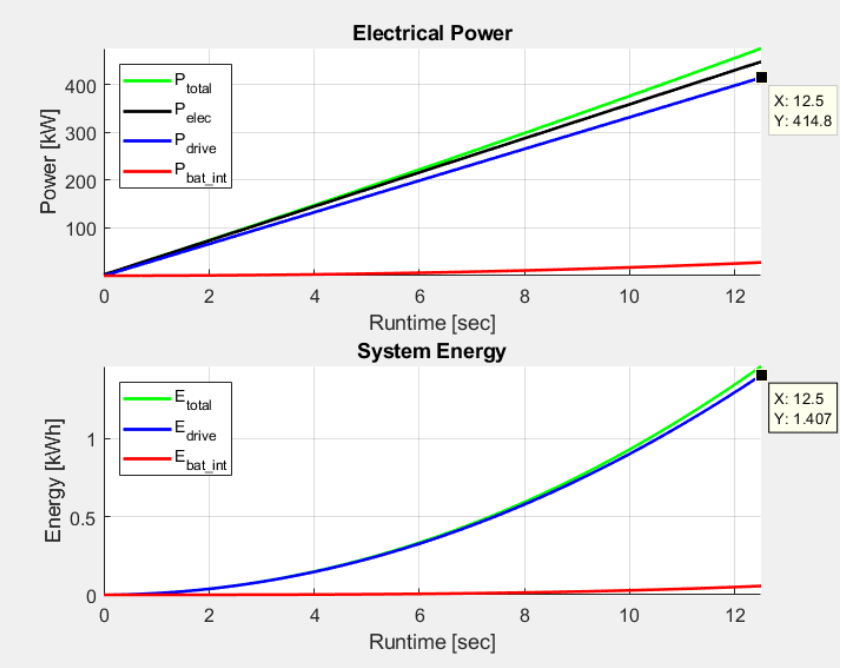

Fig. 3.37: Battery Performance – Electrical Power and System Energy

These results were calculated using the Malesta cell specification data, meaning these estimates are more precise than the previous trajectory calculations as they encompass the actual effects in the cells. These effects include internal resistance, heating losses, and discharge rates, and should therefore more accurately depict the cells function during the run.

It can be seen that the energy drawn from the batteries during the entirety of the run is 1.4Wh, which is almost exactly what was calculated for the energy consumption of the run. This is a good sign that validates the design and confirms the results of the above kinematic calculations. This results also shows that these batteries should provide a significant source of energy for the Pod during the run. Additionally, the voltage drop during this time is minimal, as the final voltage level after the 12.5sec interval is 662 VDC: only about 41V dropped during acceleration time.

Since it is known that the LIM will be mounted onto the Escher 2017 Swissloop Pod and this current LIM prototype does not levitate the Pod, the wheel speed can be calculated in revolutions per minute (RPM) as seen below in Figure 3.38.

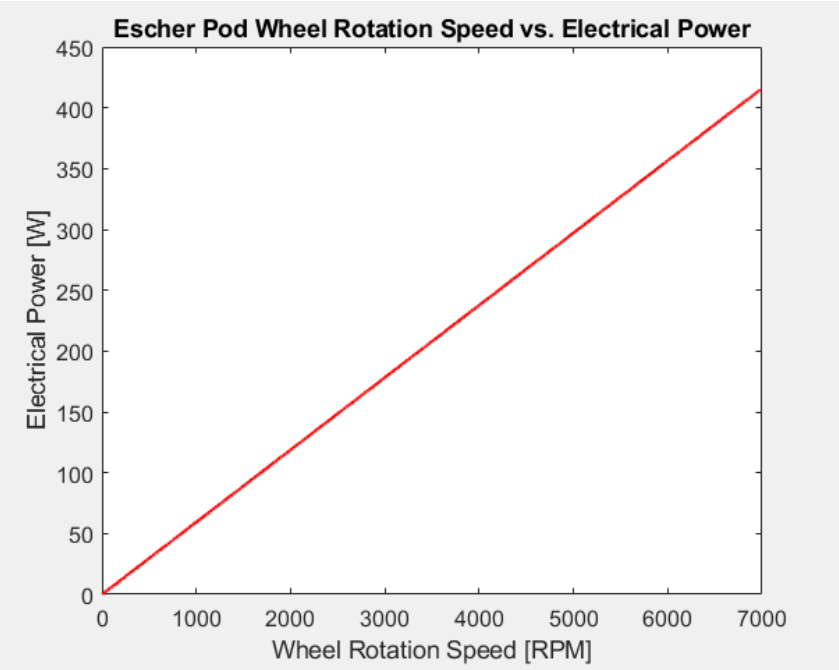

Fig. 3.38 Rotational Speed in RPM of the Escher Pod's Wheels experienced if double-sided LIM is mounted on and a top speed of 500 km/h is reached

To calculate this wheel speed in RPM from the produced velocity of the motor, Eqn. 3.41 is deployed.

$$\Omega\,[\mathrm{RPM}] = \frac{v_r}{r_w} \cdot \frac{60}{2\pi} \tag{3.41}$$

Where v_r is the speed that the rotor experiences (from 0 to 500 km/h), and r_w is the radius of the Escher wheels at 0.19m. Therefore, one can see the wheel rotational speed denoted by Ω in RPM.

Levitation would be ideal in further reducing the friction on the wheels, especially since it was laid out as one of the key principles behind the overall Hyperloop technology. However, for the speeds of the scaled down prototypes, and for design simplicity, the LIM of this thesis will not levitate. Therefore, wheels are indeed needed on the Escher pod. It can be seen that the wheels experience about 7000 RPM during this 12.5sec acceleration period. It is interesting to note, that this is well within the limits

of the wheels, as they were designed to withstand speeds of 10,500 RPM [26], which is about 1.5 times the maximum operating conditions seen in this run.

3.5.3 Inverters

To control the LIM and convert the DC voltage to 3-Phase AC voltage, UNITEK Bamocar D3-700 200/400 inverters will be used [27]. Figure 3.39 shows an image of this inverter.

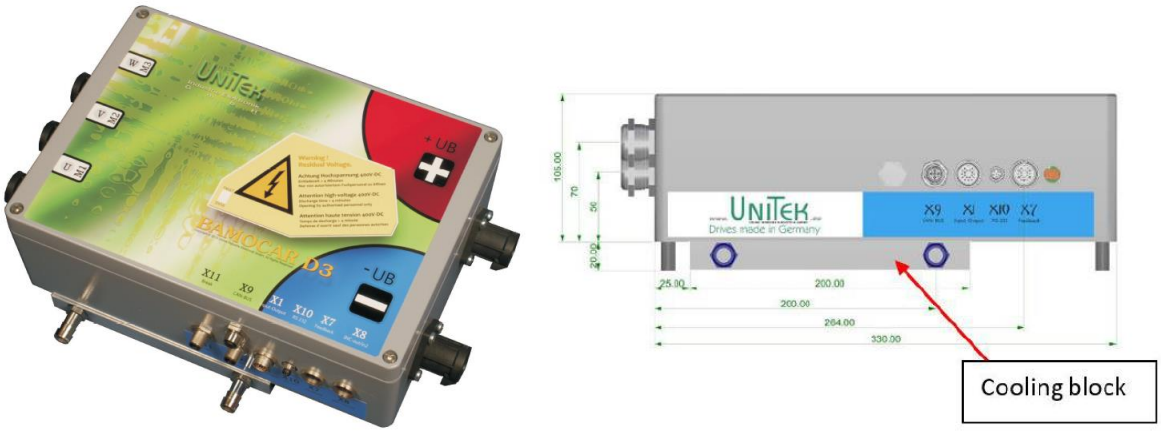

Fig. 3.39: BAMOCAR D3-700 Inverter used to convert DC voltage from Batteries to 3-Phase AC Voltage [27]

Figure 3.39 shows how the inverter cooling block dissipates heat from the high-voltage and high currents being used. There is an option to water cool the aluminum block if needed. However, for the 12.5sec acceleration time during which this inverter will be in operation, additional water cooling should not be necessary, as confirmed by engineers at UNITEK. Table 3.9 lists the technical specifications provided by UNITEK for the inverters.

Technical Data BAMOCAR D3-700 -(400)	
Rated Supply Voltage	24 to max. 700 [VDC]
Rated Output Voltage	3x450 [VAC]
Continuous Output Current (RMS)	200 [A_{RMS}]
Peak Output Current	400 [A_{peak}]
Maximum Dissipation Power	4 [kW]
Clock Frequency	8 to 16 [kHz]
Level Over Voltage	800 [VDC]
External Fusing	250 [A_{RMS}]
Weight	6.8 [kg]
Dimension	403 (height) x 250 (width) x 145 (depth) [mm]

Table 3.9: BAMOCAR D3-700 (200/400) Technical Specifications [27]

The technical data indicates that the inverters can handle a continuous RMS output current of 200A and have an internal fuse that blows at 250A. For the experimental purposes of this thesis, this current setting can be bypassed to allow for higher currents to flow. After speaking with engineers at UNITEK, this was deemed possible for the application of this thesis, since operational time is only 12.5sec.

To control the AC power supplied to the stators, an 8kHz pulse width modulation (PWM) signal is used as a clock rate to control the insulated-gate bipolar transistors (IGBTs), which act as very high speed electronic switches in the inverters. Construction of the stator field is accomplished by discretizing and approximating a sine wave. This discretization is performed by switching these high-power transistors (IGBTs) on and off very fast and in a controlled way. Using a PWM signal, sampling at 8kHz to construct the sine wave, should be sufficient to construct a reasonably clear sine wave input. This sampling frequency is also the maximum clock rate that can be used while still allowing the maximum current possible to pass through the inverters. Higher clock rates will have aliasing effects on the output of the IGBTs that will act to decrease the current being supplied to the motors.

Using two inverters and two batteries power to each side of the LIM is supplied independently. The inverters use control feedback to verify that each side of the LIM is being powered symmetrically. This feedback ensures that each side of the LIM is the same as the other and that synchronization between the fields takes place so that power is not supplied in an unbalanced fashion.

To power the double-sided 24-Slot LIM, two batteries will be connected to two inverters, each of which supplies approximately 350VDC to the inverters. This DC voltage is then converted to 3-phase AC voltage, which is then supplied to each corresponding side of the LIM. This configuration can be seen in Figure 3.40 and Figure 3.41 below.

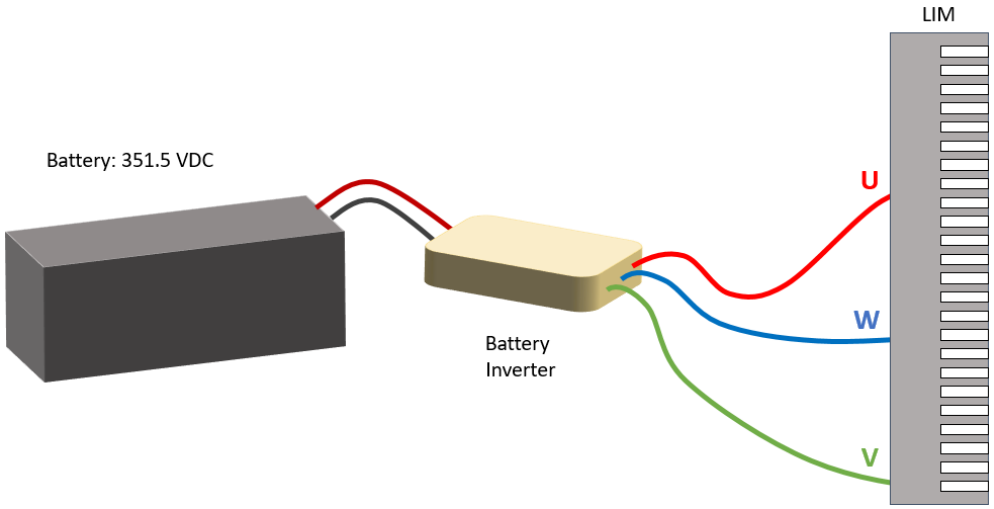

Fig. 3.40: Single Side of LIM Electrical Configuration

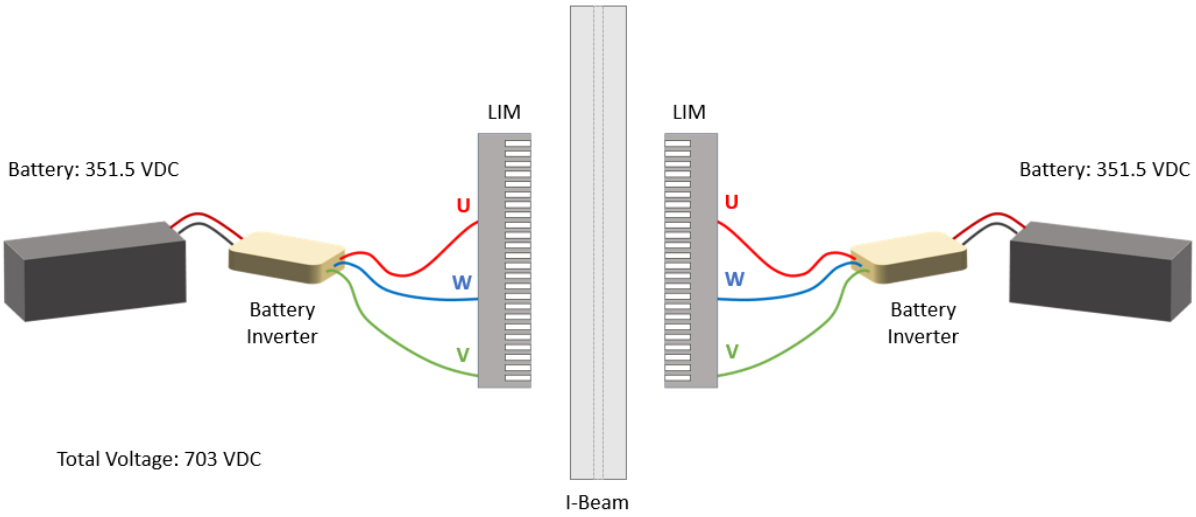

Fig. 3.41: Complete LIM Electrical Configuration

Additionally, by varying the width of the pulses, or the 'on' time of the IGBTs, one can also dictate the frequency of the input sine wave, and therefore the speed of the motor because the frequency of the stator field is directly related to its velocity – Eqn. 2.43. This property leads to the use of a variable frequency drive (VFD), which allows one to sweep through a range of frequencies. Every frequency provides a different synchronous speed and thus a new optimized peak thrust value.

Using a VFD and programming the motor inverters allows for continuous operation at a maximum thrust value by sweeping through a range of frequencies. This optimum on the thrust curve is denoted in the generic thrust curve of Figure 3.42 where a stable optimal point on the curve is specified. The inverters will be programmed to try and always "land" as close to this point as possible.

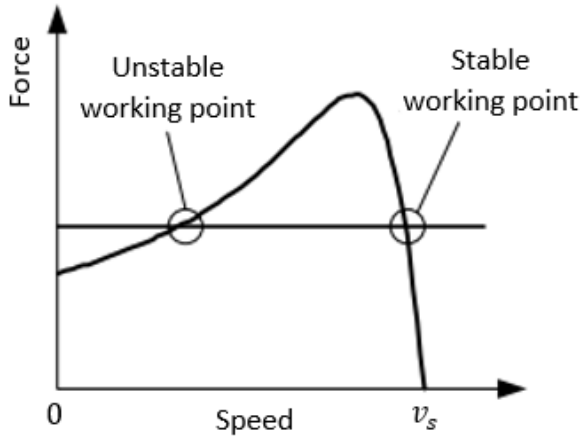

Fig. 3.42: Generic Thrust Curve – showing stable and unstable thrust points to choose in frequency inverter programming

The point on the right of the curve is in a more stable working region than the corresponding thrust point on the left side of the curve. In fact, the point on the left is in an unstable working region when the speed adjusts itself during the frequency sweep because the shape of the curve to the right of the peak will not change significantly whereas the curve on the left side will. Therefore, once this thrust point on the right has been found, the inverters can be programmed to maintain this point so as to not drastically alter performance. Programming these inverters for the frequency sweep requires noting the discrete frequency points desired in the sweep. It is important to choose the frequency that yields the correct synchronous speed value for each thrust curve.

For each thrust curve, the inverters should be programmed at the same thrust level for each varying frequency curve. Doing so yields a constant thrust during acceleration. Once this frequency sweep is performed by the inverters, the LIM experiences a constant thrust. Thrust curves at various frequencies are shown in Figure 3.43 where the frequency sweep takes place and the constant thrust level of 2.778kN for the 12.5sec acceleration period from 0 km/h to 500 km/h is sustained.

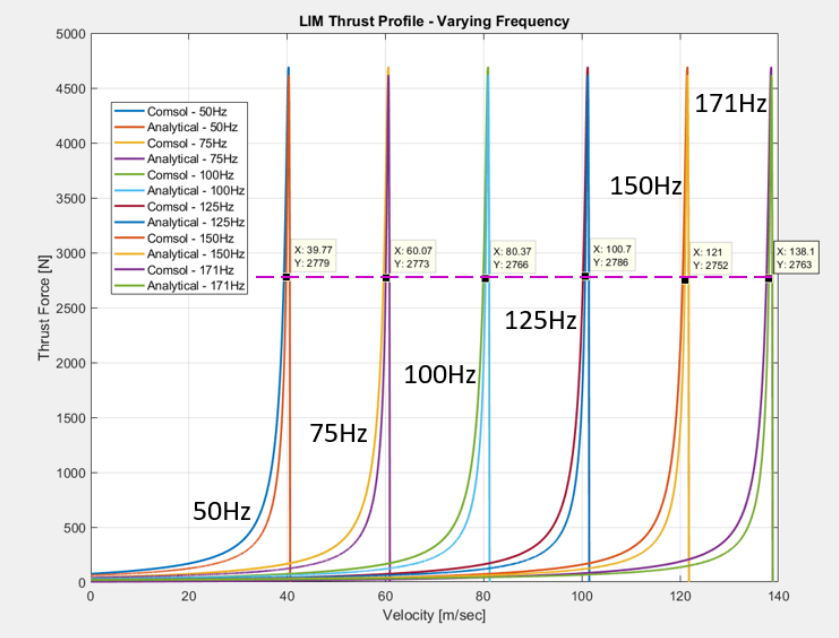

Fig. 3.43: Various Thrust curves of the 24-Slot LIM – showing how during the frequency sweep from 0Hz to 171Hz, or correspondingly from 0 km/h to 500 km/h, a constant thrust level is experienced for the entirety of the run

For each frequency, there is a corresponding thrust curve. And on each curve, a data cursor has been placed to select the point closest to the required 2.77kN thrust force. However, it is not always the case that the frequency inverter samples the curve at the necessary sample rate that yields exactly 2.778kN. As can be seen on the above plot, the data cursors get close to 2.778kN; however, they may not land exactly on that point so the inverters have to be programmed to select the point closest to the desired thrust level.

For each frequency, the motor inverters will sweep through the corresponding thrust curve in an attempt to find the constant thrust force for every velocity during operation. Figure 3.44 below shows how the corresponding thrust levels might vary for the given frequency inverters as they try to select the thrust level closest to 2.778 kN.

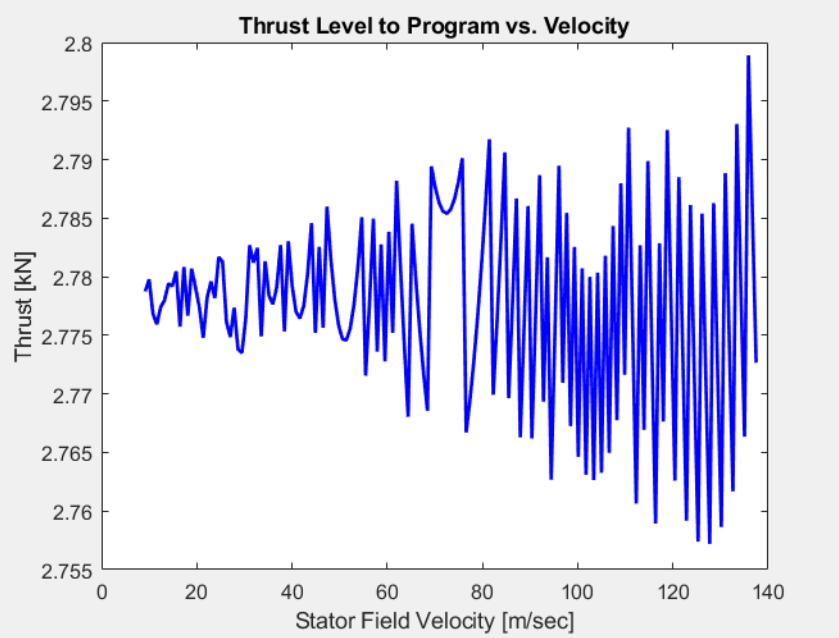

Fig. 3.44: Thrust level centering around 2.778 kN level for each corresponding frequency or velocity point – showing the points to program in the inverters to achieve near constant thrust production

Figure 3.44 shows that the inverters will search for the desired thrust level, but will never land exactly on the 2.778 kN point. However, the inverters will come close enough for steady driving performance, as these variations in the curves are so small they will not disturb the motor. For higher velocities, the difference between the ideal 2.778kN thrust point and the value found by the inverters becomes greater.

Figure 3.45 shows the resulting discrete frequency points plotted relative to the velocities they are supposed to yield. These discrete frequency points are plotted for every velocity seen by the motor during operation, excluding velocities under 10 m/sec.

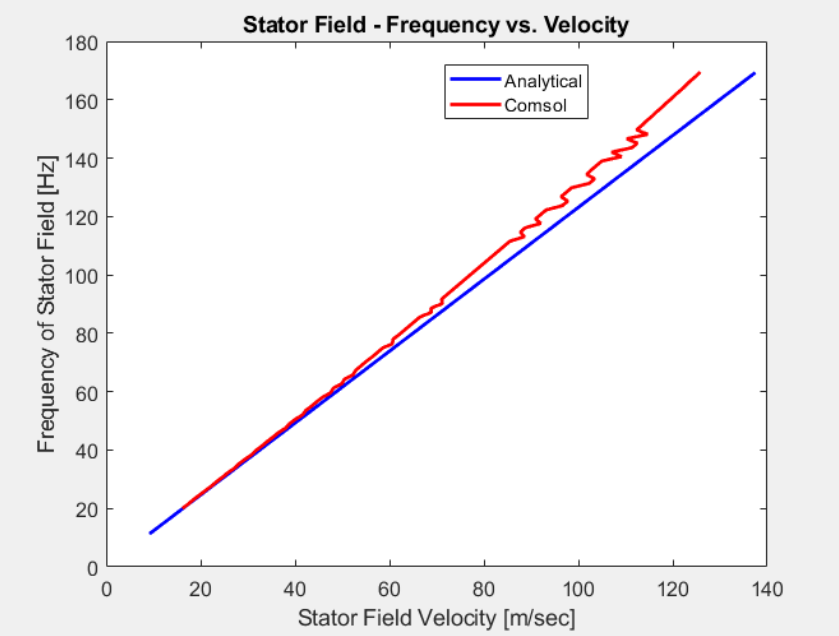

Fig. 3.45: Stator field velocity vs. frequency – shows how the inverters are programed according to this curve. The correct frequency is chosen for every velocity which is seen during the acceleration period. This ensures optimum performance as the inverters will choose values close to the peak thrust for each corresponding thrust curve or frequency

If the frequency inverters follow this curve, then the motor should sweep through this frequency range and for each frequency, choose the optimal point on the thrust curve. Moreover, for every thrust profile, the motor will always operate at a point close to synchronous speed for that specific frequency. This corresponds to always operating in a region near the peak thrust, where the motor thrust is optimized for a given input.

As can be seen, there are some discrepancies between the Comsol results and the analytical results shown in Figure 3.45. This difference can be traced back to the stray flux that is once again not incorporated in the analytical model, however is considered in the Comsol simulations. The stray flux causes the thrust curves to change shape relative to the velocity, meaning that as the thrust curves increase in frequency, the curve tends to widen more. This widening causes the frequencies to drift further apart and explains why the Comsol curve tends to arc up for the higher frequencies.

3.6 Motor Fabrication

The manufacturing process of the 24-Slot Double-Sided LIM design of Appendix F consisted of two steps. The first was to produce the stator iron core stacks, and the second was to wind the stator. The manufacturing of the primary took around 1.5 months and was accomplished through an Industry Partner, *Gebrueder Meier AG,* in Regensdorf, Switzerland. Since the rotor will be the SpaceX I-beam, no manufacturing had to be performed for the secondary. The 24-Slot LIM fully manufactured can be seen below in Figure 3.46.

Fig. 3.46: Manufactured 24-Slot LIM Stator from Gebrueder Meier AG *in Regensdorf, Switzerland*

Using iron core stacks removes the self-induction that would occur in a solid piece of iron and lead to several problems including overheating and oversaturation if not mitigated properly.

Since iron is a conductive material, it receives and conducts the eddy currents induced by the stator coils and are also present in the secondary. However, the issue of conductivity is a more of an issue for the stator because the fields inducing these eddy currents come from the stator and exist near and all around it. Inducing eddy currents in a solid stator core can lead to build-ups of current and heat, as there is nowhere for them to be released to in most cases. Thus, solid cores can lead to faster saturation and overheating, and even generate Lorentz forces oriented in directions other than the desired one.

However, splitting the core into several thin isolated iron sheets or segments, called *laminated stacks* [17], can help to mitigate these effects. An insulating layer coats these thin iron sheets, which should

lie as parallel to the magnetic flux produced from the stator as possible. The core is then built up of these insulated layers, or “stacks”, which act as a barrier to restrict induced eddy current flow in narrow loops within the thickness of each single lamination [17]. In this manner, the stacked core will not be nearly as conductive as a solid core: it will actually have close to zero conductivity when using these laminated stacks. A sketch of these laminated iron stacks can be seen below in Figure 3.47.

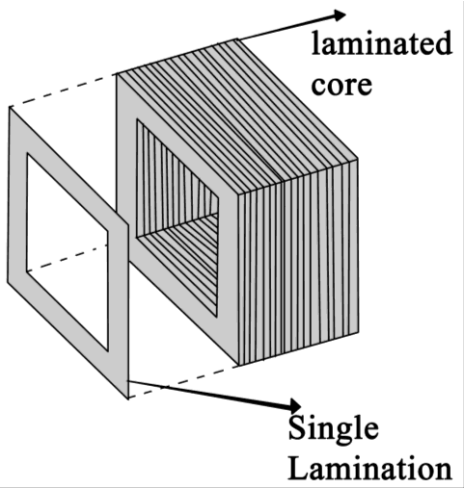

Fig. 3.47: Example of iron core laminated stacks [18]

Using iron core stacks splits the core into these thin segments or slices of iron and laminates them together with a non-conducting oxide layer in-between the core stacks. Since the total flux passing through the core is the product of the magnetic flux density and the surface area, reducing the surface area also reduces the area in which eddy currents can flow. Therefore, the flux passing through each iron slice is much smaller than the total flux passing through a solid iron core. The surface area for conducting eddy currents is much smaller and almost negligible when using stacks. Additionally, any small eddy currents induced in the iron stacks do not add together to contribute to some total force or current collection. Instead they are merely smaller individual currents induced on each iron slice that have little influence; thus, using this stack configuration ensures that the core is not as sensitive to these eddy currents anymore. A diagram of the eddy currents in a solid core compared to those in the iron core stacks is shown in Figure 3.48.

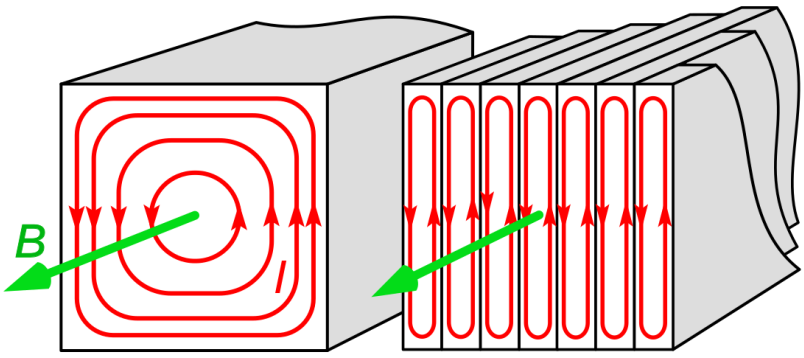

Fig. 3.48: Induced eddy currents shown in red in a solid iron core compared to iron core stacks – the iron core stacks are made from thin laminations which are parallel to the B- field in green with an insulation layer between them to help further reduce the induced eddy currents [18]

Figure 3.48 shows that the iron core stack splits the eddy currents into smaller induced currents that do not add up or contribute to some higher value, which would otherwise, in the solid core case, yield a very strong and undesired Lorentz force.

Splitting up the currents also acts to reduce the overall heat produced. If iron core stacks are not used, the iron core could even melt if it were one solid piece of iron, due to the high level of current induced from the nearby coils. Generally, more flux passes through the core than through the secondary, so if a solid core is used, all the input current is essentially self-induced in the core. Additionally, since the power dissipated in a system is proportional to the square of the current, breaking up a solid core into narrow laminations, significantly reduces the power losses in the core. Thus, this design employs laminated core stacks.

Securing these iron stacks together requires creative ideas. Some ideas involve the use of clamps or fixtures to hold the stacks together. In this thesis's design, they are precisely glued together, which should be sufficiently as long as they are not exposed to very high temperatures. While it is more difficult to manufacture the stator from iron core stacks than from a solid core, it is a necessary step because the motor would not function otherwise with a solid core. The process of manufacturing these stacks is more of a chemical than mechanical process. The individual stacks need to be well laminated with an oxide layer, so that the core stacks don't create conductive channels between them in which larger eddy currents can then be induced.

It is important that the oxide layers between each stack cannot be "breached" because if this occurs, the core, or any connecting stacks, will be conductive again. Therefore, extra precaution must be taken to prohibit the flux from penetrating the laminations by ensuring that the stacks are not electrically connected while securing them together, which could happen if portions of the oxide lamination layer are scratched off [17].

Mounting holes have been designed in the yoke of the stator core to mount the LIM on the Escher Pod. The LIM will be supported mechanically to the Pod chassis throughout operation by mounting bolts fitted through these mounting holes. Therefore, the bolts fixing the LIM to the Pod must be capable of attaching the LIM efficiently to the chassis. The mounting fixture drafted up for this purpose is shown below in Figure 3.49: the LIM is shown in light blue, mounted onto the Escher Pod.

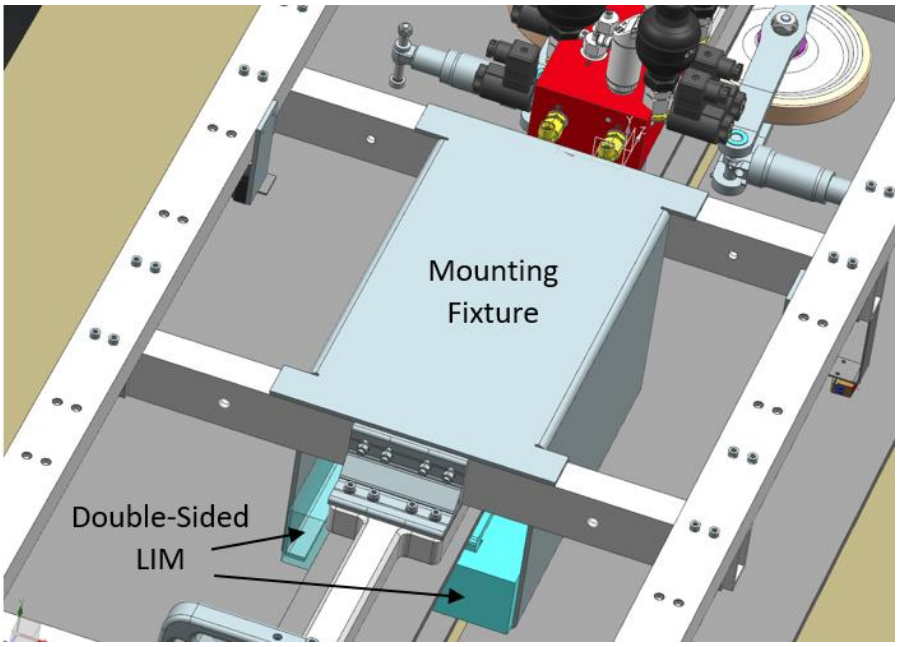

Fig. 3.49: LIM mounted onto the Escher Pod, held in place by a mounting fixture

3.7 Temperature Considerations

With the high powers the motor uses to accelerate to high speeds, it is an interesting exercise to perform a short temperature analysis to quantify the thermodynamic effects and temperature changes experienced by the motor during its operation.

Estimating the temperatures in the motor, is important because the motor will operate with little to no thermal convection or air cooling in the low-pressure environment once the air is pumped out of the Hyperloop tube. The heat generated in a motor is usually transferred via convection to the medium surrounding the machine (i.e., air); however, in the low-pressure environment of the Hyperloop tube, there is less air to facilitate this heat transfer. Thus, heat transfer in the motor will occur solely by conduction or radiation.

Quantifying the temperature change that the motor experiences during the 12.5sec accelerating period uses heat transfer or energy equilibrium equations. The calculations focus on the temperature change experienced by the coils, as these high currents flow through them during operation, and experienced by the core around which these coils are wrapped.

Eqn. 3.42 is deployed to analyze the change in temperature seen in the coils.

$$Q = m \cdot \Delta T \cdot c_t = I^2 \cdot R \cdot \Delta t \tag{3.42}$$

$$R = \rho \frac{l}{SA} \tag{3.43}$$

Where Q is the heat content or energy transfer in Joules, I is the supply current to the LIM, R is the resistance of the coils, m is the mass of the coils, c_t is the specific heat value for copper, Δt is the duration of operation time, and ΔT is the absolute change in temperature experienced. The resistance, R, is comprised of the copper coil's resistivity ρ, multiplied by the length of coil, l, divided by its cross-sectional area, SA.

Given a copper coil resistivity of $1.68 \cdot 10^{-8}\ \Omega \cdot \mathrm{m}$, a specific heat value of $390\ \mathrm{J}/kg \cdot K$, a coil mass of $1.067\ \mathrm{kg}$, a total RMS input current of 420A passing through a cross-sectional area of $2.11 \cdot 10^{-5}\ \mathrm{m}^2$, and a length of coil of $16\ \mathrm{m}$, the heat transfer is calculated as follows.

$$R = (1.68 \cdot 10^{-8}\ \Omega \cdot \mathrm{m}) \cdot \frac{16\ \mathrm{m}}{2.11 \cdot 10^{-5}\ \mathrm{m}^2} = 12.74\ m\Omega \tag{3.44}$$

$$\Delta T = \frac{I^2 \cdot R \cdot \Delta t}{c_t \cdot m} = \frac{420A^2 \cdot 12.74\ m\Omega \cdot 12.5\ sec}{\left(390\ {}^{J}/_{kg \cdot K}\right) \cdot 1.067\ kg} = 67.51\ K \tag{3.45}$$

The temperature change experienced by the coils is large due to the high currents being passed. Heat transfer effects for the stator core are analyzed similarly and performed below using Eqn. 3.46.

$$Q = m \cdot \Delta T \cdot c_t = l \cdot \Delta t \tag{3.46}$$

Where Q is the heat content or energy transfer in Joules, c_t is the specific heat of the core, l_s are the losses in the iron stator core, m is the mass of the core, Δt is the duration of operation in seconds, and ΔT is the absolute change in temperature. ΔT is then calculated using Eqn. 3.47.

$$\Delta T = \frac{l_s \cdot \Delta t}{c_t} = \frac{400\ {}^{W}/_{kg} \cdot 12.5sec}{457\ {}^{J}/_{kg \cdot K}} = 10.94\ K \tag{3.47}$$

The values for the specific heat, c_t , and the losses, l_s , in the stator core are obtained for the M400 iron core used in this LIM from Appendix E. As shown, the core does not experience as large of a temperature increase as the coils do. The main reason why the core does not heat up much from this heat transfer is that the iron core is essentially acting as a large heatsink for the coils, dissipating the heat from them and dispersing it evenly throughout the iron core. Significantly heating up this iron core would require a much longer operational time. Therefore, the temperature change observed is manageable and will not negatively influence the motor's functionality or performance during the 12.5sec operation time.

Assuming the motor is initially at room temperature (i.e., 293 K), the final temperature for the coils and the core can be calculated.

$$\text{Coils:} \quad \Delta T = 67.51\ K = T_f - T_i \Rightarrow 67.51\ K = T_f - 273\ K \tag{3.48}$$

$$T_f = 293\ K + 61.51\ K = 360.51\ K \tag{3.49}$$

$$\text{Core:} \quad \Delta T = 10.94\ K = T_f - T_i \Rightarrow 10.94K = T_f - 273\ K \tag{3.50}$$

$$T_f = 293\ K + 10.94\ K = 303.94\ K \tag{3.51}$$

The final temperatures for the core and coils, converted to Celsius, are shown below.

$$\text{Coils:} \quad 360.51\ K - 273.15\ K = 87.36\ ℃ \tag{3.52}$$

$$\text{Core:} \quad 303.94\ K - 273.15\ K = 30.79\ ℃ \tag{3.53}$$

The final temperatures of the coils and the core after 12.5sec of operation are seen to be $87.36\ ℃$ and $30.79\ ℃$, respectively. If the temperature changes were larger, for example, due to longer continuous motor operation or an increase in input current, then other cooling methods or mitigation techniques would have to be applied so that the motor would not overheat or melt during operation.

4 Results

After the final simulations, the results of the double-sided 24-Slot LIM can be analyzed. The desired thrust force of 2.778kN is met and an even higher peak thrust has been achieved. This larger thrust provides a safety margin in case the performance of the LIM decreases after manufacturing, which is common since simulation results always differ from real world measurements. Therefore, the fact that this 24-Slot variation produces almost twice the required thrust in simulation is a good indicator that after fabrication, the desired results can still be obtained even after some performance decreases.

In addition to the Comsol simulations, an analytical calculation for the thrust was performed in Matlab using the thrust calculations in the Lorentz Force Section above, and in [22]. This analytical model attempts to calculate the effects of the LIM in order to provide an alternate approach to solving the problem. The models can be compared and validated to make sure the results are consistent and correct. The results from this analytical model are compared to the Comsol simulation results in the following section, and are seen to match very well.

The final design specifications for a single-side of the 24-Slot LIM can be seen in Table 4.1. To obtain the full double-sided results for the thrust, the peak thrust can simply be doubled.

LIM Final Design Specifications – Single-Side of LIM	
Pole Number	2
Slot Number	24
Weight	80 [kg]
LIM Stator Core Dimensions	Length: 812 [mm] Width: 55[12] [mm] Height: 225 [mm]
Peak Thrust Produced	2.345 [kN]
Thrust-Weight Ratio	2.989

Table 4.1: Performance specifications for 24-Slot LIM – showing only specifications from a single-side of the LIM

Given that the peak thrust produced is 2.345 kN for a single side of the LIM, which weighs approximatively 80kg, the thrust-to-weight ratio can be calculated to be almost 3. This is the same peak thrust-to-weight for the Space Shuttle.

$$Thrust\text{-}Weight\ Ratio = \frac{2.345\ kN}{80\ kg \cdot 9.807\ {}^{m}/_{s}} = 2.989 \cong 3 \tag{4.1}$$

This thrust-to-weight ratio means that the LIM can move objects three times it weight, which is very impressive for a first prototype LIM presented in this thesis.

4.1 Double-Sided 24 Slot 2-Pole LIM

As stated above, the thrust curve of a linear motor is the best method of describing the motor's performance because it shows which velocities produce the greatest thrust and thus, in which region

[12] The width of the motor is actually 53.35 mm due to the stacking factor of 97%: $55\ \text{mm} \cdot 97\% = 53.35\ \text{mm}$.

the motor should be programmed to operate in. The thrust curve for the 24-Slot double-sided LIM can be calculated over the operational range of velocities that the LIM experiences. The calculation is performed according to Eqn. 2.82 and is listed here again for reference as the time-average Lorentz Force acting on the rotor [22].

$$F_{Thrust} = D \cdot d_r \int_0^L Re\{J_z(y,t) \cdot B_x^*(y,t)\}\, dy \tag{4.2}$$

The results of the analytical thrust calculation can be seen below in Figure 4.1, with the Comsol results plotted alongside for comparison.

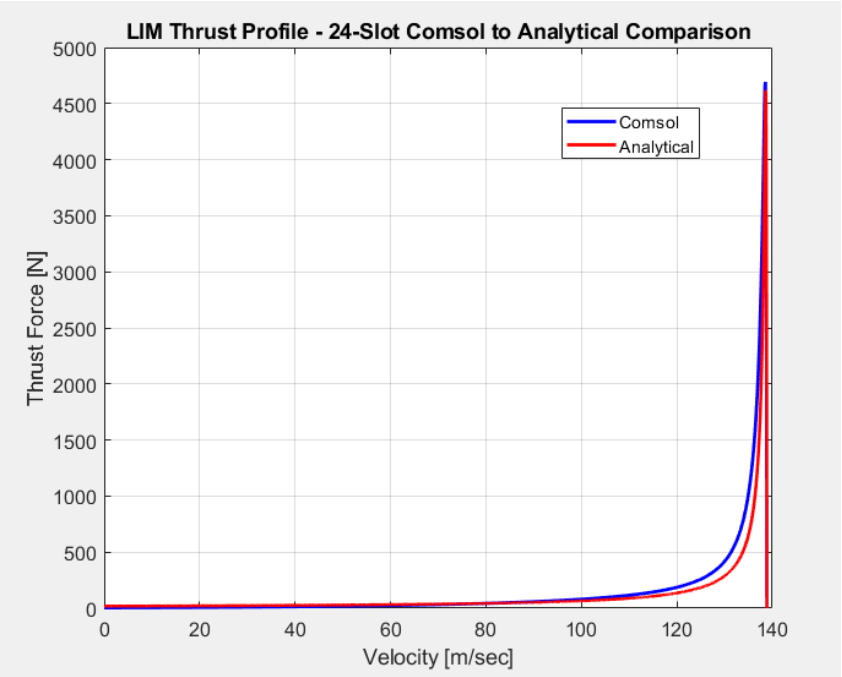

Fig. 4.1: 24-Slot Double-Sided LIM Final Design Thrust Curve for v_s = 500 km/h – showing good agreement between the Comsol simulation and the Analytical calculation

The LIM must generate 2.778kN to reach 500 km/h within 12.5sec. Plotted in Figure 4.1, is the thrust curve for the total double-sided LIM, where the required thrust force of 2.778kN is met and even surpassed. It can be seen that the Comsol results match up well with the analytical model. This comparison is a great sanity check and shows that the models are consistent, despite the fact that separate approaches have been taken to analyze and solve the problem.

The thrust point on the curve equal to 2.778kN occurs close to the synchronous speed, which is expected because this point produces the highest forces on the rotor. Therefore, the motor must operate in a region close to the synchronous speed in order to obtain the desired thrust point.

The induced voltage for the LIM can also be obtained for both the analytical and Comsol models, and is plotted in Figure 4.2 from the calculation of Eqn. 4.3, which is listed here again for reference.

$$E_1 = 2 \cdot v_s \cdot D \cdot N \cdot B_1 \tag{4.3}$$

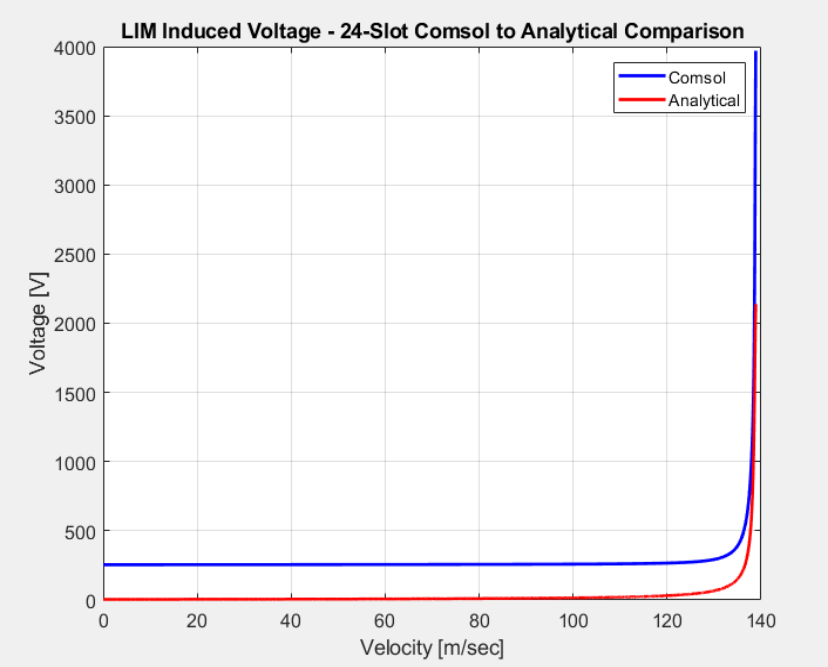

Fig. 4.2: 24-Slot Double-Sided LIM Final Design Induced Voltage Curve for v_s = 500 km/h – showing large inconsistencies between the Comsol simulation and the Analytical calculation

In this plot, it can be seen that the Comsol and analytical models for the induced voltage are much less in agreement than they were for the thrust curves. This difference is attributed to the stray flux in the motor, which is not taken into account in the analytical modeling, however is added to the calculations solved in the Comsol simulations. Adding a stray flux component to the analytical model is complex and time-consuming and is out of the scope of this thesis.

However, it is believed that these differences due to the stray flux of the motor only influence the induced voltage and not the thrust. The thrust does not depend on the stray flux because it is only a function of the contributing flux, which is comprised of the input current and turn number needed for the MMF. The induced voltage on the other hand is exactly a consequence of the stator windings where the voltage is induced across the coils. The current driving the MMF or thrust is linked to this voltage, which must be maintained at a certain "level" to the drive motor. However, this would not be depicted in the above thrust curves. Therefore, any stray flux around the windings of the stator will directly affect the induced voltage drop, but not influence the thrust produced from the contributing flux.

Additionally, in this 24-Slot LIM model, the stray flux is believed to be very high due to the influence of the large air gap. Any flux that is not stray flux has to reach all the way from the core on one side of the I-beam to the core on the opposite side. This long path that must be traveled by the flux decreases the amount of contributing flux that reaches the rotor and would increase the stray flux inducing more voltage around the windings of the stator since this flux does not leave the stator, it just encircles it. For the 16.465 mm air gap, the amount of stray flux is believed to be almost double the contributing flux. Figure 4.2 shows that the Comsol results incorporating the stray flux give almost double the total flux given by the analytical model. Therefore, these discrepancies between the two curves seem to make sense.

From here, the corresponding magnetic flux density of the LIM stator core can be plotted to help visualize the magnetic properties/effects in the stator, as is shown in Figure 4.3 below.

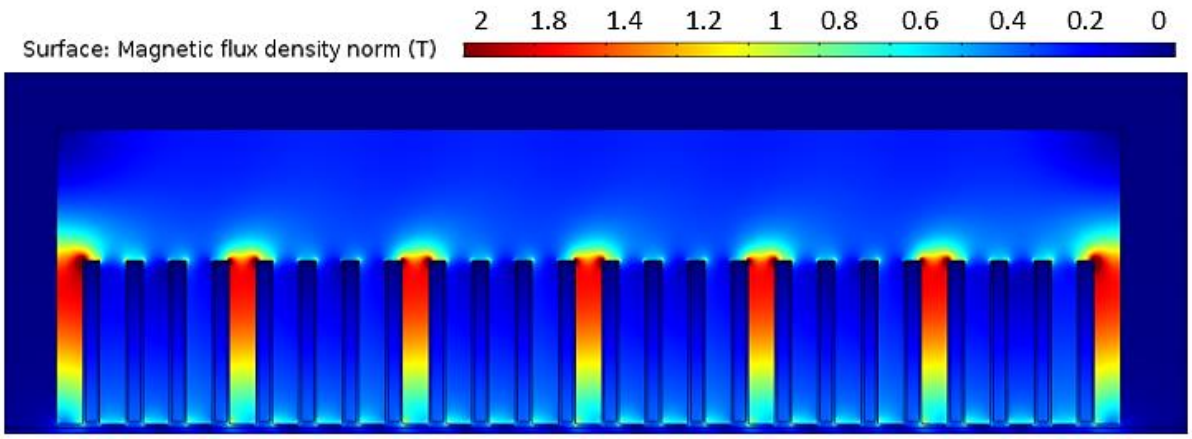

Fig. 4.3: Magnetic Flux Density Norm plotted in Comsol – showing how several teeth begin to saturate first, with the highest field concentration at the corners of the slots

Figure 4.3 shows that the normal component of the magnetic flux density yields a very consistent field pattern throughout, despite every fourth slot saturating more than the yoke or other slots around them. This behavior is due to the 4 slots/phase winding distribution where every fourth slot sees both the beginnings and ends of the phases; thus, high concentrations of flux density will build up in these regions faster and lead to saturation.

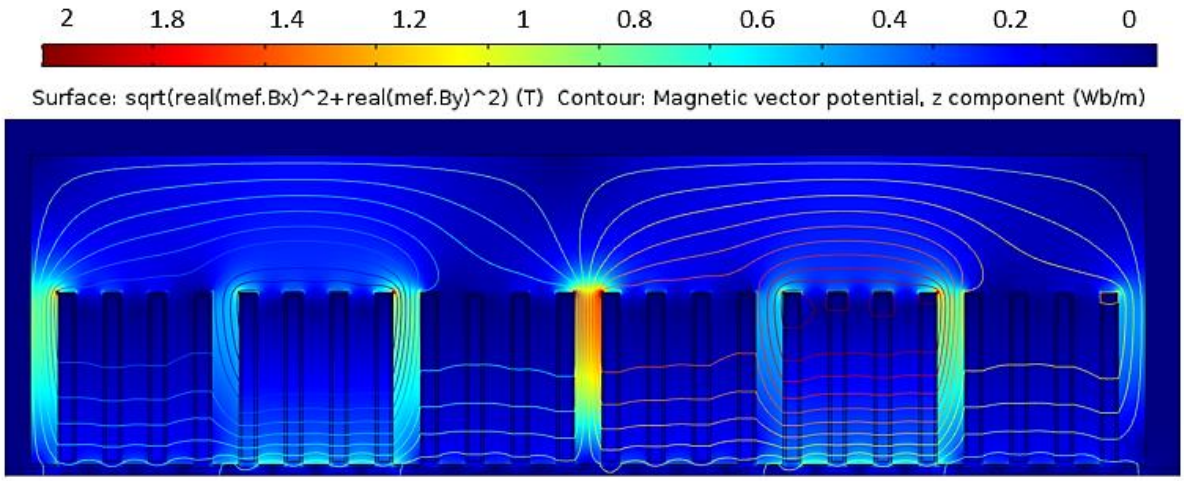

Fig. 4.4: Magnetic Flux Density Plotted in Comsol for a single-side of the LIM – showing an evenly distributed field pattern, with the flux lines superimposed on the plot to depict the pole pitch of the motor: validates 2-pole design

Figure 4.4 shows that the pole pitch of the motor is indeed about half the length of the stator core, as is expected in a 2-pole motor. It also shows that good saturation levels are obtained for the LIM stator core despite the high operating powers achieved. This behavior verifies that the core will be able to withstand the necessary power levels and will not oversaturate or yield other undesirable effects that might otherwise occur if the core was not properly designed.

As stated earlier, a symmetry was taken along the middle of the I-beam to simplify the simulation complexity and time in Comsol. However, some simulations were also performed on the full model to compare the results of the full model with those of the symmetric model. Two plots of the magnetic flux density given for the full model can be seen below in Figure 4.5.

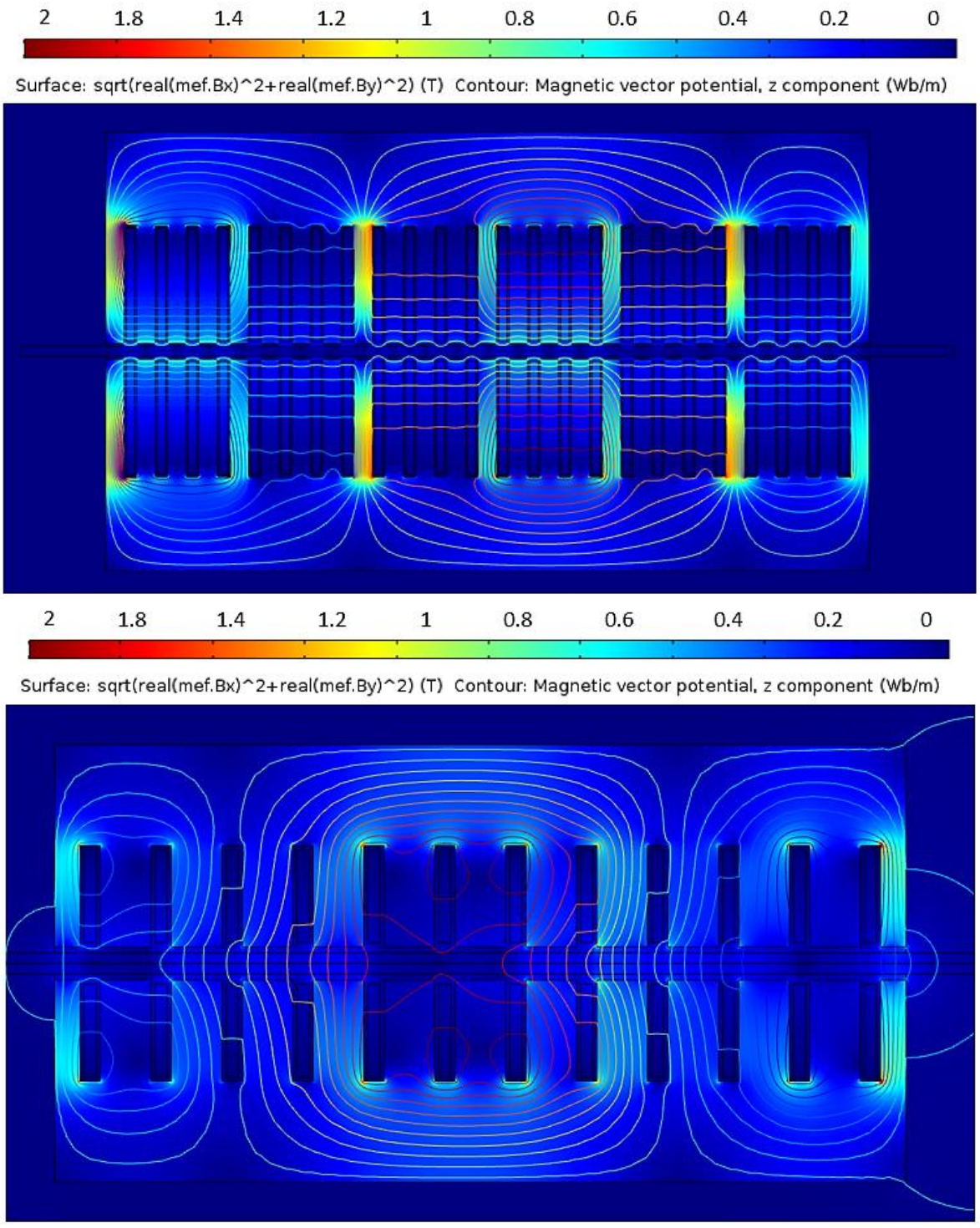

Fig. 4.5: Magnetic flux density plot for the full double-sided 24-Slot LIM – showing coupling (below) vs decoupling (above) scenarios; the above plot is most likely where operation will occur.

The image on top shows the motor operating close to the synchronous speed. The operating frequency will be higher at the synchronous speed and corresponds to the motor operating in a decoupling region. The image below depicts an operating point further away from the synchronous speed in the coupling region, and thus for a lower frequency. Here, the fields penetrate all the way through the aluminum I-beam secondary as a result of the lower frequency.

When comparing the two Comsol models (symmetric and full), it is evident that the two models match each other quite perfectly when the thrust curve results are doubled for the symmetric model. This

consistency is shown in the thrust plot of the 24-Slot LIM in Figure 4.6 below, where the full and symmetric models are plotted for the synchronous speed of 500 km/h.

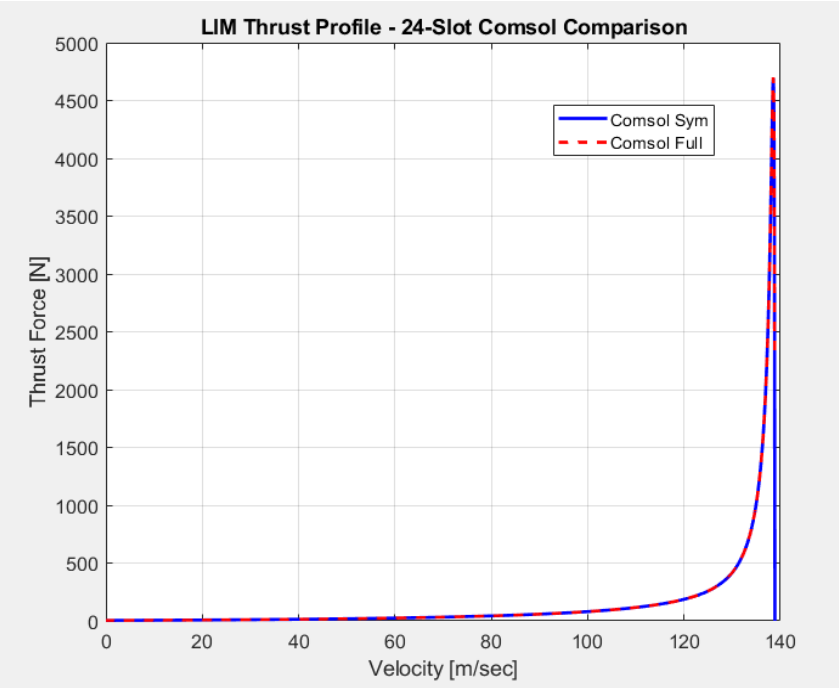

Fig. 4.6: 24-Slot Double-Sided LIM Final Design Thrust Curve for v_s = 500 km/h – showing almost exact agreement between the Comsol symmetric single-sided and full double-sided simulations

As can be seen, the two thrust curves are practically identical and no distinguishing features can be observed between the two curves.

Since the Comsol simulation results for the thrust match the analytical results well, the Comsol results can be taken as reliable. The lift force for the LIM is computed in Comsol and plotted below in Figure 4.7. Calculating the lift force analytically is much more complicated than calculating the thrust, so the results for the lift are those provided solely by Comsol.

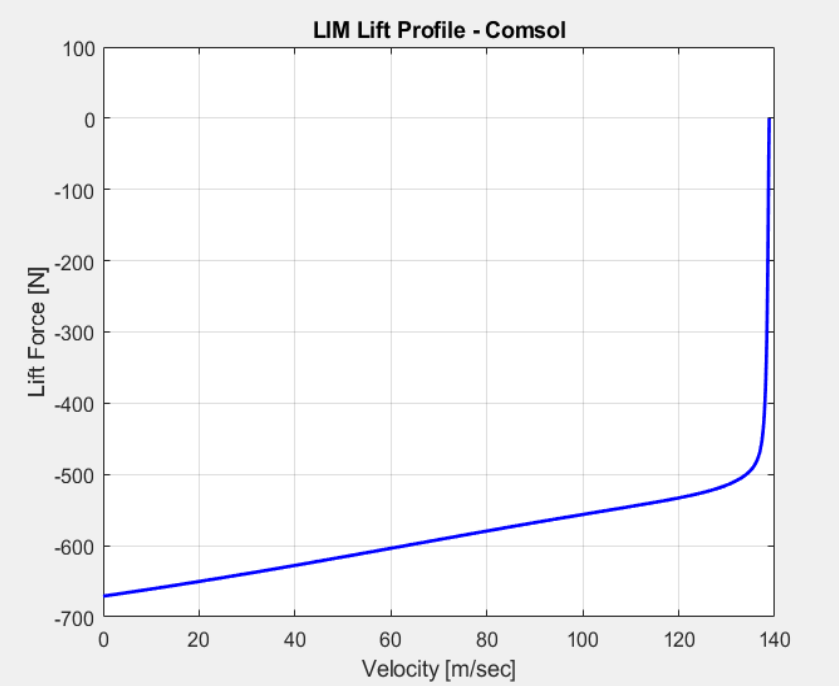

Fig. 4.7: 24-Slot Double-Sided LIM Final Design Lift Curve for v_s = 500 km/h – showing that the lift forces generated close to the synchronous speed are almost zero, while during the low-speed operation, the lift forces are the greatest

It can be seen that the lift curve is almost opposite the thrust curve in that the lift generates the highest forces when the slip is greatest. When the motor approaches the synchronous speed, the lift force asymptotically approaches zero. The initial forces generated from a stationary position or in the low velocity region are greatest because when the LIM starts up at very low speeds, the generated magnetic fields from the rotor are so strong that they actually repel or push directly against the stator and produce a levitation or lift force. However, as the LIM accelerates to higher velocities, the lift decreases and near the synchronous speed there is almost no lift force generated by the LIM. The lift force decreases because the magnetic field strength begins to drop off as the LIM accelerates: the slip is reduced so the difference in the speeds become smaller, and the LIM moves at almost the same speed as the stator field. Since there is no difference in the field speeds, no forces are produced.

Also, since it is desirable to operate close to the synchronous speed to achieve the highest thrust force, the motor will naturally operate in a low lift region, meaning almost no levitation forces will be experienced. There could perhaps be some initial forces observed during the LIM's startup, however, these need to be measured and quantified to determine if they are problematic. When the LIM is mounted onto the Pod, these lift forces are directed away from the I-beam and thus add higher mechanical stresses that the LIM mounting fixture would have to support, which is undesirable.

As a note, the magnetic flux density plots show that the teeth seem to saturate faster than the rest of the core. Full saturation is undesirable; however, the teeth do saturate a bit, relative to the rest of the core and will therefore most likely be the first components to heat up. This heating was already discussed in the Temperature Considerations Section, which confirmed that the temperature increases were below an amount that would make the LIM inoperable. The corners of the slots are seen to heat up as well, however, this was also expected since high field potentials or concentrations tend to build up there as well.

5 Summary

This thesis focuses on the design and manufacturing of a 24-Slot Linear Induction Motor. The motor meets the design specifications laid out in the beginning of the thesis and achieves the main goal of reaching 500 km/h while fitting around the SpaceX I-beam secondary. The motor was also designed to operate in a low-pressure environment, making it suitable for a prototype LIM to be used as the main propulsion mechanism for Hyperloop-like systems. The motor has not been measured/tested yet due to time constraints, however, testing, characterization, and validation of the motor will continue after the thesis, and appropriate findings will be documented in a supplementary paper.

5.1 Project Challenges

One of the first challenges encountered during this thesis was the large lift forces observed relative to the thrust forces. In the concept 2-Slot design, the observed lift forces were repeatedly orders of magnitude greater than the produced thrust forces. In this manner, the motor acted more like a magnet repelling its own magnetic field, than a linear motor driving itself. However, this behavior was only observed in the 2-Slot stator, and was the main motivation to shift to a stator with more slots. After subsequent design iterations and simulations, this effect disappeared and the subsequent linear motors functioned as expected.

When taking into account the end-effects of the linear motor, the end teeth were extended to try and mitigate the observed performance losses. Designing the outer teeth of the core to be slightly larger and not placing any coils around them helped the core capture more of the field that would otherwise be “lost” in the air. This behavior is illustrated in Figure 5.1 by a plot of the magnetic flux density for the concept 2-Slot motor, where a 2D simulation shows how the end-effects of the motor can be drastic: most of the field is lost in the air.

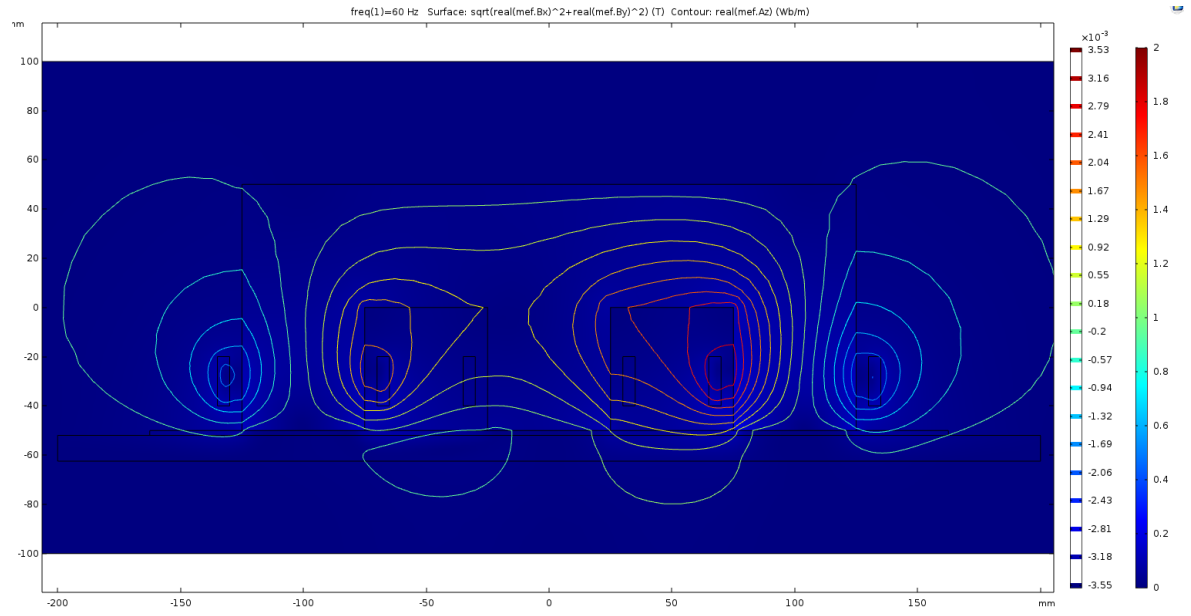

Fig. 5.1: Magnetic Flux Density of the 2-Slot Concept – showing how the field escapes the LIM due to the end-effects of the motor: to mitigate these effects, coils should not be placed on the outside of the motor, and the end teeth should be made larger to capture more of the external fields

The winding design, and how to effectivity fit the winding heads inside the tight inner dimension of the I-beam, were also difficult challenges in this thesis. As seen in the winding design portion of this thesis, what can be practically manufactured and wound is much different from what theoretically

works in simulation. The coils had to be redesigned over several iterations because although each proposed configuration worked in simulation, the coils could not be physically wound. Nevertheless, a compromise between simulation and reality was finally reached.

Additionally, it took longer than desired to accurately represent the stator windings in the Comsol simulations; this step was by far the most difficult part of the simulations. Determining exactly how to excite the windings in Comsol, and how Comsol recognized the coils was non-trivial. Appendix G shows how Comsol configures and calculates the windings of a multi-turn coil.

One other main challenge throughout the simulation portion of this thesis was figuring out how to vary the velocity of the rotor secondary in Comsol. This variation was needed to produce accurate thrust curves over the range of velocities experienced by the motor during the run. Since this behavior is very difficult to implement and solve in Comsol, a "trick" was employed to mimic this velocity action.

Looking at the real motor, it can be acknowledged that movement comes from the varying frequency of the stator field, as velocity is directly proportional to the velocity (or frequency) of the travelling field from Eqn. 2.43. The actual movement comes from the difference in the velocity of the induced field and the velocity of stator field: otherwise known as the slip. Therefore, the slip must somehow be introduced into the equations that Comsol solves so as to mimic this velocity action. In other words, Comsol must be made to think the motor is stationary, when in reality and from the equations, it will not be.

Observation of the equations that Comsol solves reveals the areas to manipulate. The magnetic vector potential equation Comsol solves is shown below in Eqn. 5.1.

$$\vec{J}_s = \nabla \times \left(\frac{1}{\mu}\nabla \times \vec{A}\right) - j\omega\mu\sigma\vec{A} \tag{5.1}$$

Where $\vec{A}$ is the magnetic vector potential, $\vec{J}_s$ is the surface current density, μ is the permeability of free space, σ is the conductivity of the aluminum 6061-T6 secondary I-beam, and ω is the frequency of the travelling field. Eqn. 5.1 indicates that ω would be the exact parameter to vary over the range of velocities the rotor experiences because the velocity of the rotor is directly proportional to the frequency of the travelling field, from Eqn. 2.43.

However, this frequency term cannot be varied easily in Comsol. Therefore, another route must be explored. Eqn. 5.1, shows that the frequency shares the same contribution as the conductivity of the rotor, as the two share the same location in the equation and will have the same impact when varied. Therefore, changing the conductivity of the rotor relative to frequency is analogous to changing the frequency of the rotor field itself.

By changing the conductivity of the rotor, σ, one can mimic the movement in Comsol. Eqn. 5.2 models this behavior where σ_n is the new conductivity that is multiped by a ratio of the slip. Here however, the slip is in terms of frequencies instead of velocities, as was previously shown in Eqn. 2.43. For a linear motor, though, frequency and velocity are more less the same.

$$\sigma_n = \frac{f_s - \frac{v_r}{2\tau_p}}{f_s} \cdot \sigma \tag{5.2}$$

The conductivity of the secondary can then be varied relative to the frequency of the travelling field. Figure 5.2 shows the conductivity of Eqn. 5.2 versus the rotor velocity.

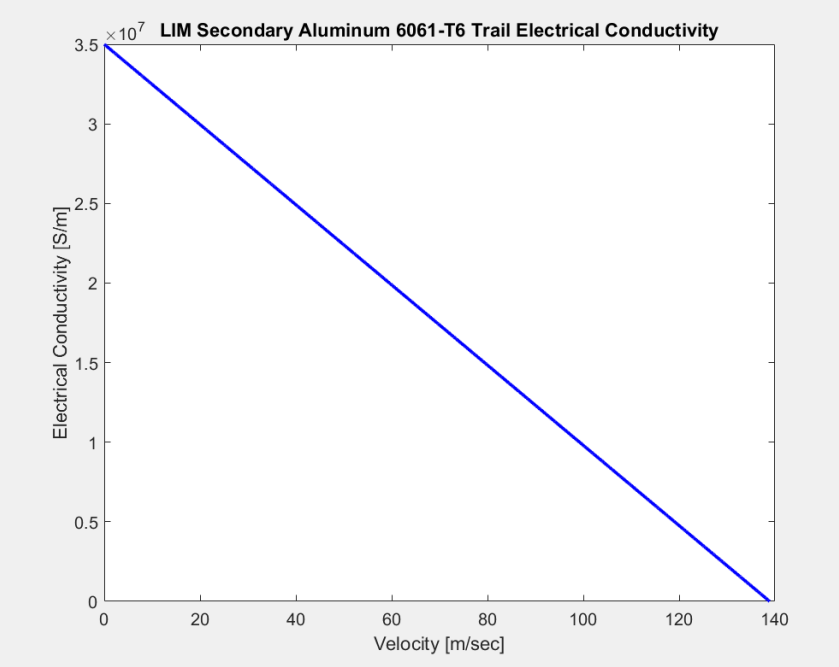

Fig. 5.2: Sigma Variation to Mimic Frequency Sweep in Comsol Simulations

5.2 Outlook

As mentioned, the linear motor of this thesis still needs to be tested to see how well the measured values match the simulated results. Several other tasks must be completed before this motor can be fully operational and integrated onto a Hyperloop Pod. To elaborate, the motor control algorithms to control the inverters must be programmed to sweep though the range of frequencies in order to provide an optimal, constant thrust progression. Efficient and dedicated programming will yield very powerful drivetrain performance.

Additionally, the structure and chassis of the Escher Pod must be strong enough to support the LIM. Additional mounting fixations or even a new chassis may need to be developed to support this LIM. However, once an appropriate chassis is found, the LIM can be mounted and tested in high-speed test runs in the Hyperloop tube at SpaceX. Prior to testing at SpaceX, low-speed runs to validate and tune the motor can take place at the Dübendorf testing facilities here in Switzerland.

It will also be beneficial to test the motor's operation in a vacuum chamber before testing in the SpaceX tube. These tests will show how much, if any, arcing occurs in a low-pressure environment.

Finally, a second prototype will most likely be developed after characterizing this initial prototype and seeing the areas where the performance can be improved.

Additional next steps include conducting a feasibility study for the overall Hyperloop system to determine the optimal track geometry. Such a track would be deployed in full-scale Hyperloop systems. It was shown that the SpaceX I-beam is a non-optimal geometry for the secondary due to the confined inner dimensions. Scaling up these systems for fully-fledged Hyperloop systems around the world is the end goal and perhaps descendants of this prototype LIM design will even one day be used to support passenger and cargo transportation around the world.

5.2.1 Design Improvements

The biggest design constraint of the motor is the width of the stator due to the limited space in-between the I-beam. Therefore, the main design improvement to be made is the removal of one of the tops of the I-beam track, thereby creating a longer "T-beam" track. This change would allow for increased active surface areas of the stator and allow more thrust to be generated from the motor. Additionally, perhaps it is later determined that linear induction motors of a short primary and long secondary track configuration are not ideal for a Hyperloop-like system.

For instance, it may be the case that the primary and secondary are swapped or reversed. In this case, the rotor blade would be mounted to the vehicle or Pod, and the primary would be married to the track. It is known that having the primary aboard the Pod is not optimal for larger scaled up systems. Factors making this primary configuration suboptimal include 1) bringing the energy to power the motor aboard the pod capsules, thus adding mass and requiring more energy 2) added pod capsule costs: placing the primary in each pod significantly drives up the overall value and maintenance cost of each pod. However, it could also be the case that designing a complex track infrastructure to support the required high-powers over long distances would also be expensive. Therefore, a feasibility study is needed to discover an optimal and efficient configuration for such a system.

Nevertheless, the working principles and motor theory for linear motors is more or less universal and thus the fundamentals learned in this thesis can be directly applied to optimized linear motor configurations later. For example, the configuration proposed by Elon Musk in the Hyperloop Alpha Whitepaper suggests having the linear accelerator or primary coil windings fixed at various "accelerating" stations in the low-pressure tube with secondary rotors contained in each Pod capsule. This configuration can be seen below in Figure 5.3 and is similar to the one used in Hyperloop One's system.

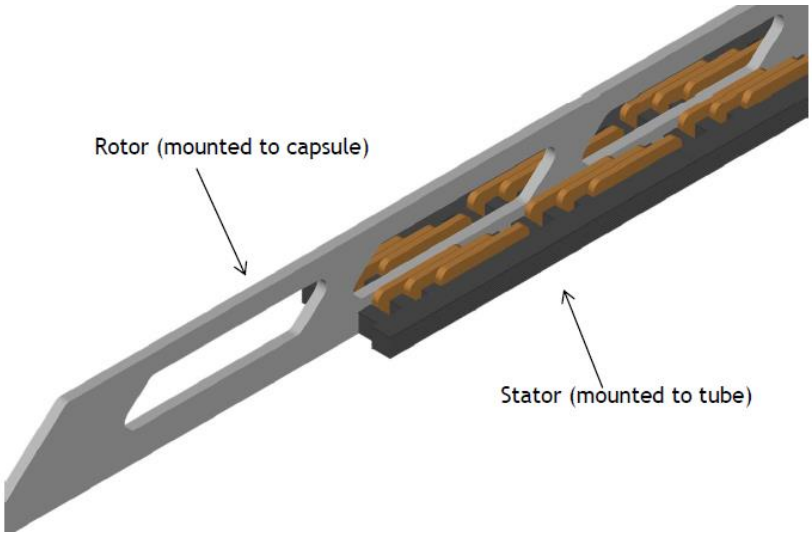

Fig. 5.3: Rotor and Stator Concept Proposed by Elon Musk [5]

Having the rotor blade on the Pod and the stator mounted to the track may perhaps be the more feasible and power efficient way to build the motor because additional power to account for the motor does not need to be brought aboard. However, the reversed configuration shown in this thesis was a useful first step because it fostered the development of a strong intuition into the working principles of a LIM. With some engineering work, the LIM design of this thesis could simply be reversed to match this configuration. The prototype LIM designed in this thesis has been an impressive first step towards a sustainable linear motor eventually capable of reaching speeds of 1,000 km/h.

6 References

[1] H. G. Schwartz, M. Meyer, C. J. Burbank and M. Kuby, "Ch. 5: Transportation. Climate Change Impacts in the United States: The Third National Climate Assessment," 2014. [Online]. Available: https://nca2014.globalchange.gov/report/sectors/transportation.

[2] R. Chin, "Solving transport headaches in the cities of 2050," BBC, 2013. [Online]. Available: http://www.bbc.com/future/story/20130617-moving-around-in-the-megacity. [Accessed 2018].

[3] "THE OECD ENVIRONMENTAL OUTLOOK TO 2050. Key Findings on Climate Change," Organization for Economic Co-operation and Development (OECD), 2012.

[4] C. Höft, P. Armstrong and M. Berger, "Abstract: Hyperloop Transportation Technologies Risk Report," Münchener Rückversicherungs-Gesellschaft, München, 2017.

[5] E. Musk, "Hyperloop Alpha," Hawthorne, 2013.

[6] "Beach Pneumatic Transit," nycsubway.org, 2012. [Online]. Available: https://www.nycsubway.org/wiki/Beach_Pneumatic_Transit. [Accessed 2018].

[7] SpaceX, "SpaceX Hyperloop Track Specification, Revision. 13.0," Space Exploration Technologies, Hawthorne, 2017.

[8] M. Jufer, "Swissmetro - Introduction," 1999.

[9] M. Jufer and A. Cassat, "Collaboration with the Korean Railroad," 2010.

[10] M. Jufer and N. Wavre, "Le Moteur Linéaire: Développement Théorique et Applications," Lausanne.

[11] "Facts & Frequently Asked Questions," Hyperloop One, [Online]. Available: https://hyperloop-one.com/facts-frequently-asked-questions. [Accessed 2018].

[12] E. R. Laithwaite, "Linear Induction Motor for Vehicle Propulsion". England Patent US3585939A, 22 June 1971.

[13] E. R. Laithwaite, Propulsion without Wheels, English Universities Press, 1970.

[14] "LINEAR MOTORS OVERVIEW," ETEL, [Online]. Available: http://www.etel.ch/linear-motors/overview/. [Accessed 2018].

[15] W. Hayt and J. Buck, Engineering Electromagnetics, New York: McGraw-Hill, 2012.

[16] C. Timperio, "Inertial Navigation System using Magnetoquasistatic Field Data to Improve Non-Line-of-Sight (NLoS) Communication," ETH Zürich, Zürich, 2016.

[17] J. Pyrhönen, T. Jokinen and V. Hrabovcová, Design of Rotating Electrical Machines, John Wiley & Sons, 2008.

[18] M. Larsson, "Electric Motors for Vehicle Propulsion," Linköpings Universitet, Linköping, 2014.

[19] S. Yamamura, Theory of Linear Induction Motors, 1st ed., Wiley, 1972.

[20] S. Chevailler, "Comparative Study and Selection Criteria of Linear Motors," École Polytechnique Fédérale de Lausanne, Lausanne, 2006.

[21] M. Jufer, "Chapitre 12: Champ Tournant et Bobinage," in *Électromécanique*, Lausanne, Presses Polytechniques et Universitaires Romandes, 2004, pp. 283-287.

[22] J. Smajic, "Theory of Linear Induction Motor (LIM)," Zürich, 2018.

[23] W. Soong, "Chapter 3: Magnetic Materials," University of Adelaide, Australia, 2016.

[24] A. Küchler, High Voltage Engineering, Berlin: Springer Vieweg, 2018.

[25] E. Husain and R. S. Nema, "Analysis of Paschen Curves for Air, N2 and SF6 Using the Townsend Breakdown Equation," *IEEE Transactions on Electrical Insulation,* Vols. EI-17, no. 4, 1982.

[26] C. Timperio and I. Besler, "Swissloop Pod: "Escher"," Zürich, 2017.

[27] UniTek, "Manual, Digital Battery-Motor-Controller, BAMOCAR-D3 for AC Induction Motors," Leutenbach.

Acknowledgements

I would like to thank Prof. Dr. Jasmin Smajic, Prof. Dr. Juerg Leuthold, Prof. Hon. Dr. Marcel Jufer, and Dr. Marco Zahner for their valuable discussions, suggestions, and help in providing both theoretical insight and practical background which was needed in the research and development of this project. I would also like to thank D-ITET and Gebrüder Meier AG for financially sponsoring this thesis.

Lastly, I would like to thank my friends and family for their continued support throughout this thesis, as well as all of the members of the Swissloop team for their help in various aspects of this project, it has been a pleasure to work with you all.

This page is intentionally left blank.

Appendix A: Why Linear Motors?

With all of the current hype around linear motors and the Hyperloop, one of the most common questions asked is, “Why linear motors?” People want to know why this concept has not been pursued earlier if linear motors are indeed as great as described. They wonder why rotary motors are still used if linear motors are better, and what in particular makes the linear configuration better.

The main reason linear motors are considered to be better than conventional rotary motors is due to their higher efficiency: a linear motor does not experience the frictional losses that a rotary motor experiences. To elaborate further, in a rotary motor, the rotor is excited from the rotating stator field and spins according to the direction of the moving field. The rotor then turns an axial, which is connected to wheels that spin and move a vehicle. In an optimized linear motor, on the other hand, there is no need for wheels. If designed properly, a linear motor can levitate, and the losses due to rolling friction from wheels are completely removed from the equation. By eliminating the moving parts, the major source of losses in the system at higher speeds is removed.

The moving parts of a rotary motor also require regularly scheduled maintenance, which is another point in favor of linear motors. However, why then, if they are so much better than rotary motors, have linear motors not already been implemented? The answer to this question is that linear motors require a dedicated track. Rotary motors used in conventional train systems already all use a standardized track. Currently, there has been no industry standard adopted for linear motors for use in Hyperloop-like systems. Establishing one would require a complete redesign of existing train tracks, which would be a huge infrastructural undertaking.

Additionally, friction losses only become significant at speeds above 500 km/h, which conventional train systems do not experience, as they stay under 400 km/h. Therefore, until now there has not been a need to further reduce this rolling friction. In some areas like Japan, Korea, and Europe, where innovation is a driving motivator, construction of specialized tracks has begun. However, it will take a long time until the entire train system is replaced with linear motors.

Although it may seem advantageous to use linear motors because the reduced rolling friction at higher speeds increases efficiency, their use would require a complete redesign/rebuild of current transportation infrastructure. Even building a completely new system dedicated to linear motors, such as the Hyperloop, would be an expensive endeavor. Therefore, if a new system is to be developed, an industry standard for linear motors must be established and the right driving force i.e., a need from the public, must be cultivated. If this is accomplished, then perhaps one day a Hyperloop-like system will be a reality.

This page is intentionally left blank.

Appendix B: SpaceX Hyperloop Subtrack Technical Drawing

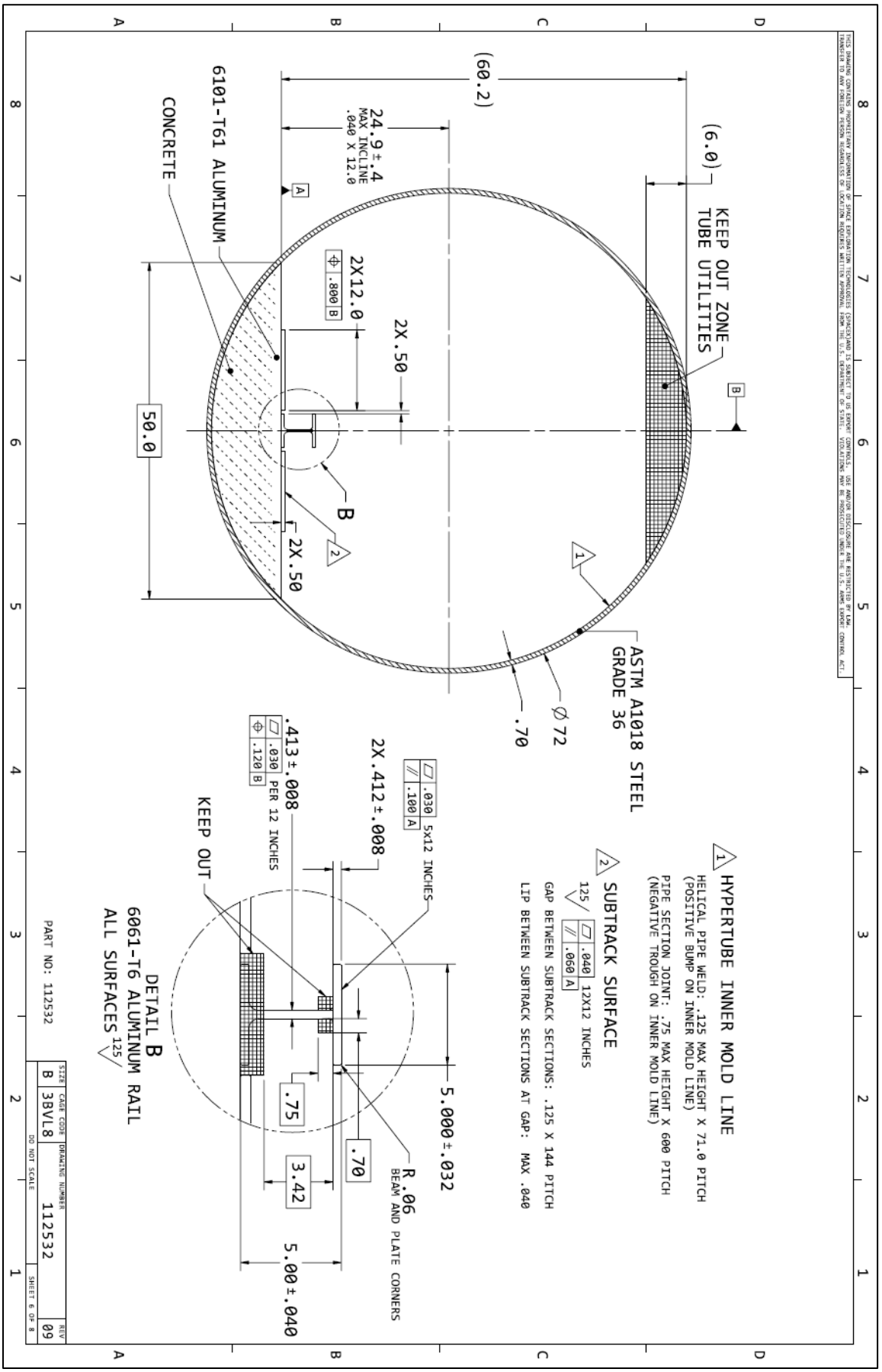

This page is intentionally left blank.

Appendix C: Swissloop Test Track – Dübendorf Testing Facilities

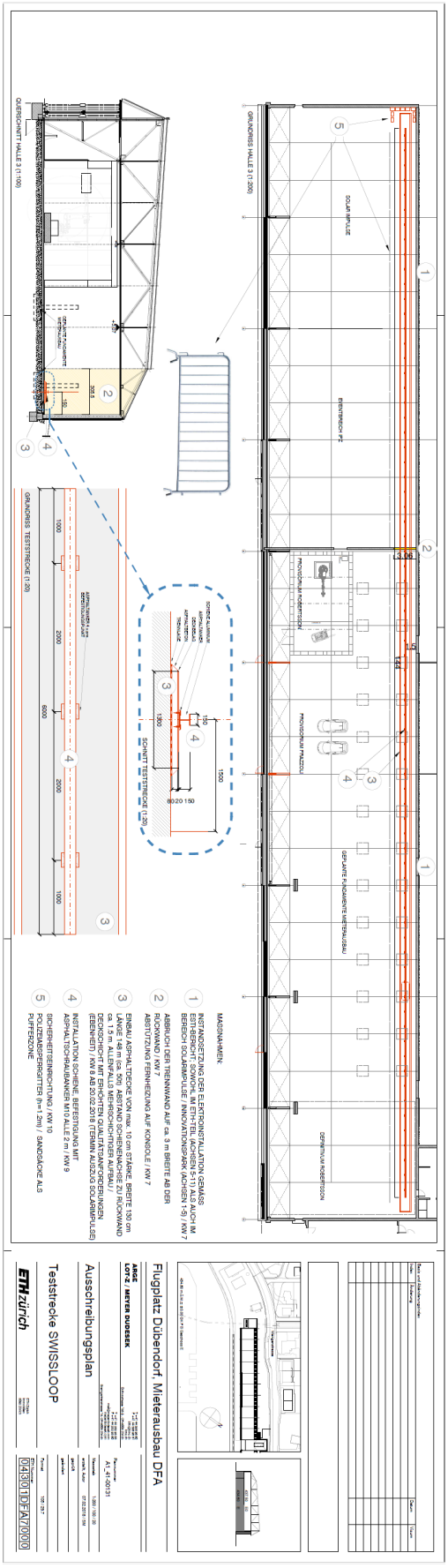

This page is intentionally left blank.

Appendix D: Escher Pod with Double-Sided 24 Slot LIM

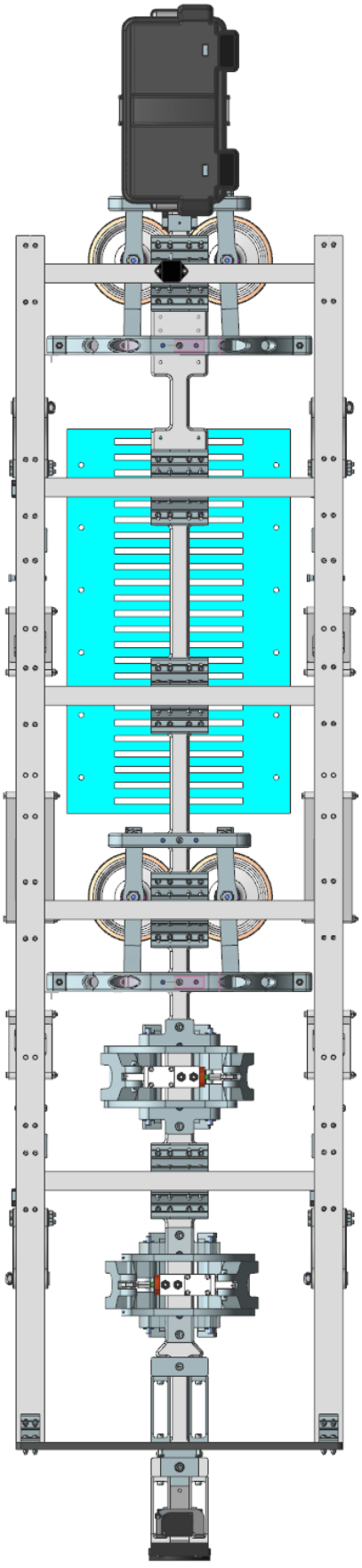

This page is intentionally left blank.

Appendix E: M400-50A Iron Core Material Data Sheet

C.D. Wälzholz

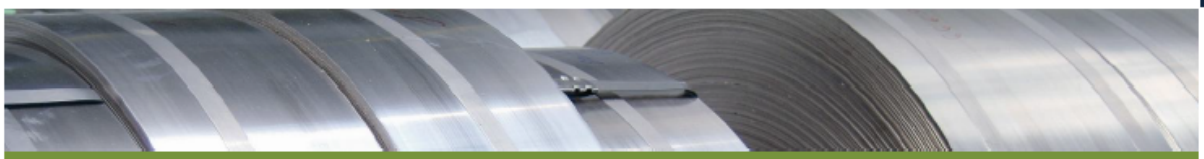

Werkstoffdatenblatt Elektroband — **M400-50A** nach EN 10106
Material data sheet Electrical steel strip — *M400-50A acc. EN 10106*

Magnetische Werte
Magnetic values

	P 1,0$_{50Hz}$ [W/kg]	P 1,5$_{50Hz}$ [W/kg]	P 1,0$_{400Hz}$ [W/kg]	P 1,0$_{700Hz}$ [W/kg]	P 1,0$_{1000Hz}$ [W/kg]
Mittelwert *mean value*	**1,54**	**3,68**	-	-	-
min.	1,46	3,50	-	-	-
max.	1,62	3,86	-	-	-

	J 2500 [T]	J 5000 [T]	J 10000 [T]		
Mittelwert *mean value*	**1,57**	**1,67**	**1,79**		
min.	1,55	1,65	1,76		
max.	1,60	1,70	1,82		

Mechanische Werte
Mechanical values

	Rm [N/mm²]	Rp0,2 [N/mm²]	A80 [%]	HV	
Mittelwert *mean value*	**420**	**310**	**30**	**130**	
min.	380	250	24	110	
max.	450	340	35	140	

Die hier angegebenen magnetischen Kennwerte sind als typische Produktionswerte anzusehen und können nicht garantiert werden.
The above listed magnetic properties should be considered only as typical production values, and can not be guaranteed.

Anisotropie max. [%] *Anisotropy max. [%]*	± 12	**Wärmeleitfähigkeit [W/mK]** *Thermal conductivity max. [W/mK]*	29,64
Stapelfaktor min. *Stacking factor min.*	0,97	**Wärmeausdehnungskoeffizient α $10^{(-6)}$/K bei 20°C** *coefficient of thermal expansion α $10^{(-6)}$ /K at 20°C*	12,08
Biegezahl min. *Number of bends min.*	5	**spezifische Wärmekapazität [kJ/kg*K]** *specific heat capacity [kJ/kg*K]*	0,457
Dichte [kg-dm³] *Density [kg-dm³]*	7,75	**elektrische Leitfähigkeit [S/m]*10⁶** *electric conductivity [S/m]*10⁶*	4,14
		spezifischer elektrischer Widerstand [µOhm*m] *specific electrical resistance [µOhm*m]*	0,350

Ansprechpartner / *contact person* : Daniel Dunker
Telefon / *phone* : +49(0) 2331-964-2412
E-Mail / *e-mail* : ddunker@cdw.de

C.D. Wälzholz KG / Feldmühlenstr. 55 / 58093 Hagen / Deutschland / www.cdw.de Stand: 2014

This page is intentionally left blank.

Appendix F: LIM Technical Drawing: 24 Slot 2-Pole

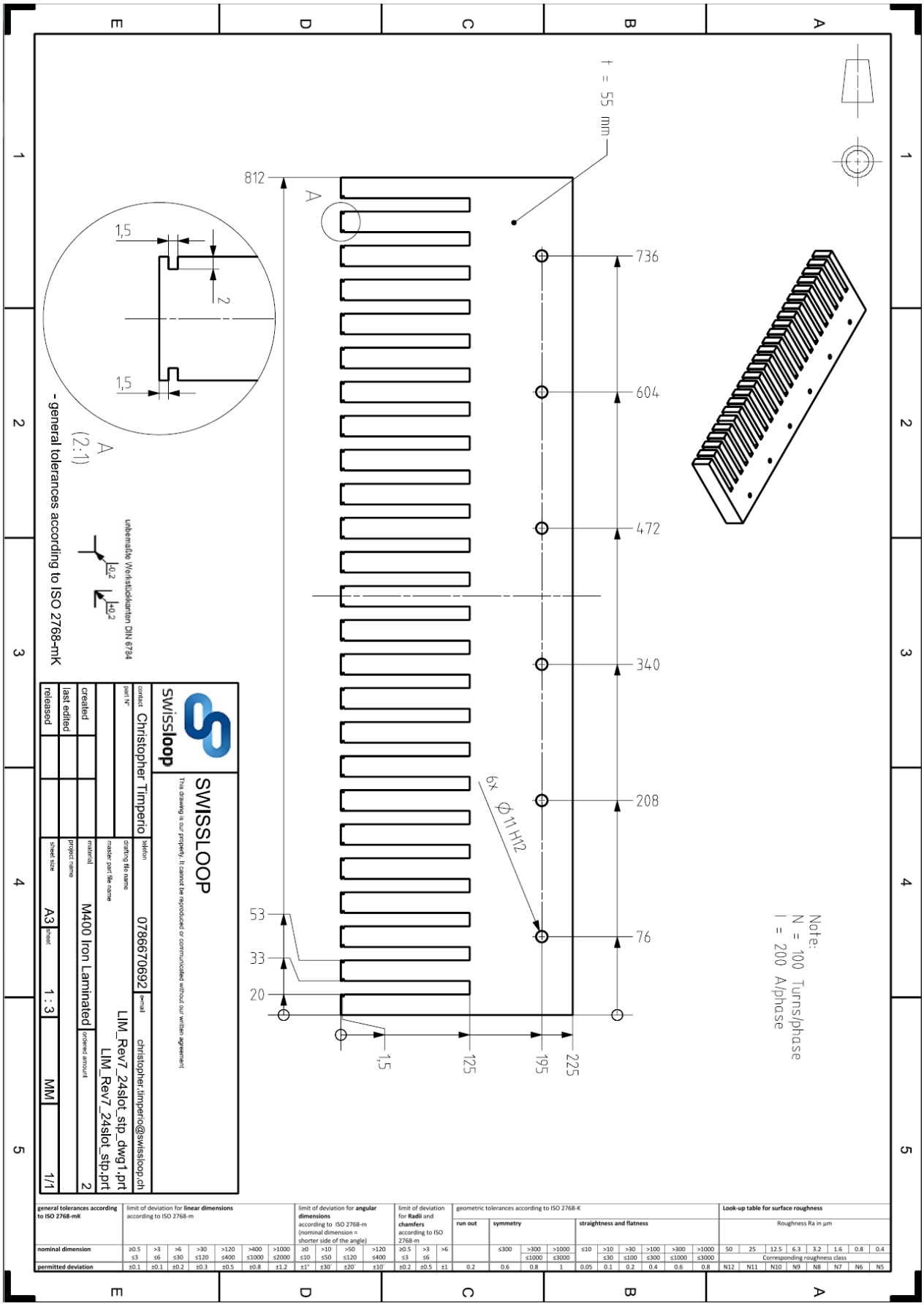

This page is intentionally left blank.

Appendix G: Comsol Multi-turn Coil Geometry Arrangement